Extragalactic X-ray Binaries

Black holes and Neutron Stars in Centaurus A

by

Mark J. Burke

A thesis submitted to
The University of Birmingham
for the degree of
DOCTOR OF PHILOSOPHY

Astrophysics and Space Research Group
School of Physics and Astronomy
The University of Birmingham
September 2013

Abstract

This thesis presents research into the X-ray binary population of NGC 5128 (Centaurus A). The two principle investigations focus on the identification of black hole candidates, which can be identified by their long term variability and spectral properties. We demonstrate this with what we believe is our best example; a source that faded over two months of observations and displayed cool disc thermal-dominant spectra when at high luminosities – similar to the Galactic black hole X-ray binaries. The main result of this research is that the population of black hole X-ray binaries is more pronounced in the dust lane of the galaxy compared to in the halo. The explanation of this result, based around the mass of the donor stars required for systems to emit at the observed luminosities, may also explain the long noted effect of a steepening of the X-ray luminosity function in early-type galaxies at a few 10^{38} erg s^{-1}; an effect that increases with the age of the stellar population.

Finally, relatively frequent 'snapshot' Chandra observations of the NGC 5128 were used to investigate the two known ultraluminous X-ray sources. These are transient systems and were observed at luminosities $1 - 10\%$ of their peak, in the regime frequented by the Galactic X-ray binaries. This presented an exciting opportunity to study the lower luminosity behaviour of these systems in an effort to determine the mass of the accreting compact object. The results of the spectral analysis point towards accretion powered by a stellar, rather than intermediate mass black hole. The long term variability of these sources is reminiscent of several of the long period Galactic X-ray binaries.

... and other sources may exist.

Fred Hoyle, writting about the recent discovery of extrasolar X-ray sources.

Galaxies, Nuclei and Quasars (Harper Row, New York, 1965)

To family, friends, and everyone. In that order.

Acknowledgements

I have often heard people state a preference for acknowledgements that are short, concise passages that thank the bare minimum of people. The thinking goes that this allows for the maximum potency of the gratitude, and that thanking too many people demonstrates insincerity, and is disrespectful to those who contributed the most help. I understand this opinion, but I disagree. I believe that help, in whatever form or quantity, deserves thanks. Further, as this document is quite clearly the pinnacle of my formal education, it is just as important to thank those that laid important foundations as those who helped hoist the uppermost flagpole. Therefore, I'm not going to worry about the length of these acknowledgements.

I came to Birmingham in September 2008 to start a PhD investigating the Galactic X-ray binaries. After two and a half years, I was pretty miserable. I felt that my options were to either quit the PhD, or follow through to the completion of a thesis in which I would have no pride. Taking my feelings to the school, they offered extra funding for me to perform similar research assuming that another supervisor could be found from the astronomy staff. Almost no-one wanted to risk having a student that might not be able to complete a PhD in two years. It is at this point that I come to my first thanks, and these go to Somak Raychaudhury, who took over as my PhD supervisor in May 2011. I suspect that taking me on board was against his better judgement, but I hope that I have shown his initial faith in me to have been well placed. To suddenly find myself working for someone who treated me with respect, gave unflinching encouragement (even when I made stupid mistakes!) and has such a well grounded and genuine enthusiasm for all astronomy was incredibly motivating for me, and helped make my job a joy. Thank you.

My next thanks go to Ralph Kraft. Not long after I switched supervisor, Ralph suggested to Somak that I analyse the X-ray binaries in Cen A (my eventual project!). This work was long over due, as the six 100 ks Chandra observations were taken in 2007, and the X-ray binaries had not been studied in any detail. This was the best opportunity to study X-ray binaries in early-type galaxies so far, and a science project that I have only dented with this thesis; there's still loads more that could

be done with these data alone! So my first thank you to Ralph is for letting me join his collaboration, and offering me this great project, which I have really enjoyed.

I need to extend further thanks to Ralph, who arranged for me to visit the Harvard-Smithsonian Center for Astrophysics over four months in 2012. This was a great experience, and I really loved working at such a fantastic facility. It was very rewarding, educational and enriching to be part of such a diverse and thriving research institute, if only for a short while. Everybody doing a PhD in astronomy should get the chance to do this, but very few are lucky enough. Ralph dedicated a huge amount of time to my supervision while I was in the US, and we typically had a couple of two hour meetings each week where we would really push the project forward. During these meetings Ralph also managed to convey a great deal to me about good practice as a researcher, and that I should remember to prioritise the science. He also educated me in the nuances of baseball and the history of the Red Sox. For all of this and more, thanks.

I must extend many thanks to Tom Maccarone, who has also given me a generous amount of his time, advice and patience. He was always more than happy to help improve my understanding and to talk about all the science we could do. He has also been tremendously encouraging, particularly with my recent job hunting. It has been a pleasure to collaborate with Tom, and I hope to do so again.

For all the help and discussion he provided for the ULX paper, I thank Roberto Soria. It was great to be able to e-mail questions to an expert and get such incredibly detailed (and rapid!) replies. I am also grateful for his patience during the achingly slow submission of the paper.

I wish to express my thanks to all of my collaborators in the Cen A VLP, particularly Nicola Brassington for much help early on. Many thanks go to Martin Hardcastle, Jo Goodger, Greg Sivakoff, Bill Forman, Christine Jones, Kristin Woodley, Steve Murray, Jouni Kainulainen, Mark Birkinshaw, Judith Croston, Dan Evans, Marat Gilfanov, Andres Jordan, Craig Sarazin, Rasmus Voss, Diana Worrall and Zhongli Zhang.

Thanks to other academics who have had involved discussions with me. Thanks to Will Farr, Andrea Prestwich, Jeff McClintock, Chris Done, Jeanette Gladstone, Dong-Woo Kim and Pepi Fabbiano. I hope I haven't forgotten anyone.

I thank my viva examiners, Professors Phil Charles and Trevor Ponman for a fun, educational and humbling discussion. They have submitted many comments that have improved the readability

and quality of this thesis. Thanks also to Ian Stevens, who chaired the proceedings.

Thanks also to other staff at Birmingham who have given me words of advice over the years, specifically Ilya Mandel, Andreas Freise and Alberto Vecchio from the astronomy group. I have immense gratitude for the pastoral support afforded me by Professors Ray Jones and Pete Watkin, especially during the change in supervisors, but also before this time.

I feel that three postdocs need to be singled out for special thanks, and they are Alastair Sanderson, Ewan O'Sullivan and Robin Barnard. Thanks to Al for introducing me to *R*, as well as miscellaneous help and discussions about science and statistics over the years. Thanks to Ewan for helping me get to grips with Chandra data analysis, for lots of advice, wisdom and, specifically, for subbing me rent for a few days when I first arrived in America. Thanks to Rob for many illuminating, entertainingly gesticulated discussions on X-ray binaries during my time at the CfA. It was really fun to talk to someone else who is as interested in X-ray binaries as I am every day, whether in the office, the coffee shop or the pub.

A humongous thank you to Viscount David Stops, who takes time out from managing his vast estates and presiding over the local disputes of the peasant-folk to manage our computer systems and provide IT support. He is undervalued and vital. Many's the time I have asked him to install some new software for me or had a hair-brained scheme with the computers that has eventually come to nothing, but he has helped out nonetheless. Cheers, David.

I thank my fourth year project supervisor from LJMU, Ivan Baldry, who taught me much about managing and manipulating data that I still live by today.

The day-to-day experience of a PhD student involves working in an office with lots of other PhD students (and post docs, on occasion). It is fortunate, and all the more rewarding, when these people form friendships and a camaraderie that extends beyond the department door. I am grateful for their support and friendship, and thank them for the fun we had both inside the office and beyond, where we drank, ate, watched films, danced, karaoke'd, partied and occasionally played sports. These are Samuel George, Paul 'LG33 of Doom' Fulda, Rory O'Smith, Chris 'Mistakio' Collins, Trevor Sidery, Ben Aylott, Konstantinos, Chiara, Ludo Carbone, Mike Holynski, Mat 'Quintessentially' Turnbull, Ria Johnson, Mathis Baumert, Ole Kock, Nadine Mayer, Gemma Whittaker, and the late Charlotte Bond[1]. I also thank Dan Reed and Natasha Jackson-Booth for their advice and help early on.

[1]Though she would argue that she arrives exactly when she means to.

My undergraduate days in Liverpool were happy, which meant that I was able to work very hard on my studies. For this I have to thank my friends during my time there. Together we revised, drank and did student-type things together. Thanks to Sam Wedge, Rob, Dan, Maya, Nick, Sue and Nat.

Going further back, it would be completely wrong of me not to thank my physics teachers at Woldgate school, Mr Jones and Mr Pinchin. I regularly recall to colleagues the amount of help that they were willing to give their students, often after school or during lunchtimes, and I now realise how fortunate I was to have two such dedicated and enthusiastic teachers back then. In particular I remember that due to being rather clumsy, I had to retake one of my AS level practical exams not once, but twice! One occasion actually resulted in me knocking the whole apparatus off the bench, which I found very frustrating! I remember both giving me extra opportunities to practice my practical work, and without that crucial step I would not have achieved the A-level grades that I did, and wouldn't be receiving a PhD certificate in December. I further thank the rest of Woldgate school, as there were many, many more teachers who really helped me during my time there, particularly in the maths and history departments. Thanks.

For the sake of my sanity, I occasionally want to hang out with people who wouldn't touch physics or astronomy with a barge-pole, and I have a great group of friends with which to do that. In other news I thank Jack, Will, Ben and Adam.

Thanks to Claire for being part of my life, and making the last two years two of the best. The world is all the more exciting for sharing the experience of exploring it. My work was always the reason I get up in the mornings, and now you're my reason to go home.

I thank my family for the love and support that they have given me over the years. Specifically for the huge amount of maths help that Dad gave me, especially during the summer of 1998, and the blind, unwavering belief that I will always succeed that Mum has in me. I also acknowledge the huge influence from both of the grandparents that I knew. Both Nan and Gran were tremendously determined souls, and I invariably think about them every time I decide to tackle something difficult.

Contents

List of Figures

List of Tables

Motivation and Overview

This thesis documents research into extragalactic X-ray binaries, carried out at the University of Birmingham and the Harvard-Smithsonian Center for Astrophysics.

We know of around 20 black hole X-ray binaries in our galaxy, the Milky Way, and around ten times as many systems containing neutron stars. Due to the observed differences in behaviour depending on the mass of the companion stars, these sources are typically divided into high- and low- mass X-ray binaries. The latter are associated with older stellar populations such as the bulges of the Milky Way and Andromeda galaxies, as well as ancient globular clusters. Early-type galaxies are dominated by older stellar populations, so they provide the ideal laboratory for studying low mass X-ray binaries.

Centaurus A (Cen A) is our nearest large early-type galaxy, and should possess the largest collection of low mass X-ray binaries that can be studied in detail using current observatories. Indeed, it is now well-established that there is a large X-ray point source population consisting of hundreds of sources emitting above a limiting luminosity of 10^{36} $\mathrm{erg\ s^{-1}}$. The Cen A Very Large Project, a series of six 100 ks *Chandra* observations made over two months in 2007, allows us to explore the X-ray properties of the galaxy in unprecedented depth. In other early-type galaxies the larger distance coupled with shorter observations mean that the available data is of much lower quality than we have for the Cen A sources. For example, if we wish to examine the spectral and timing behaviour of sources in other early-type galaxies, then this has proved to be possible only for the very brightest sources, which are above the typical luminosities observed from sources in the Milky Way. For Cen A, we are able to study sources in detail that emit in the luminosity regime frequented by many of the most-studied Galactic X-ray binaries.

Cen A also contains two transient Ultraluminous X-ray sources (ULXs), which is unusual as most ULXs are observed to be persistent and reside in late-type galaxies. ULXs are sources that emit at-or-above the Eddington limit for a $10\mathrm{M}_{\odot}$ black hole. This is interesting because the observed mass distribution of Galactic black holes is peaked at $\sim 8\mathrm{M}_{\odot}$, and supermassive black holes are

hundreds of thousands of times more massive, and found at the centre of most galaxies. Primarily, ULX research concentrates on resolving the mass of the compact object. We wish to resolve whether they are powered by stellar mass BHs in some new and non-isotropic emission state, or 'intermediate' mass black holes (IMBHs) of hundreds to thousands of solar masses; the existence of which would bridge the gulf between the compact stellar remnants and supermassive black holes. The existence of IMBHs would have wide-reaching implications across astrophysics, from stellar population synthesis to gravitational wave astronomy.

Overview

Chapter 1

The first part of Chapter 1 introduces the need for accretion physics to produce bright extra-solar X-ray sources, and discusses our theoretical understanding of accretion discs. The second half of the chapter outlines a contemporary view of Galactic X-ray binaries. Much of the first half of the chapter contains important theoretical results and derivations that introduce the physics needed to discuss accretion discs in the context of extragalactic X-ray binaries, and so this material can be found in any texts that summarise accretion. The theoretical considerations come mostly from equations in the standard text, Frank et al. (2002) as well as Melia (2009) and Lewin & van der Klis (2010). Important results are occasionally explored by use of graphical illustrations of physically plausible scenarios.

Chapter 2

Chapter 2 contains the most requisite background information for this thesis, detailing the current state of understanding in the field of extragalactic X-ray binaries. This begins with a discussion of the X-ray binary populations in late-type and early-type galaxies, before a brief foray into globular cluster black hole sources, and then introduces ultraluminous X-ray sources to the reader. Finally, Centaurus A (NGC 5128) is discussed, with emphasis on previous X-ray binary studies.

Chapter 3

This chapter familiarises the reader with the Chandra X-ray observatory and X-ray spectral analysis. The text establishes a requisite understanding of *Chandra*, the ACIS detector and the underlying techniques used in the thesis.

Chapter 4

Chapter 4 has been published in the Astrophysical Journal, volume 749, page 112 (Burke et al., 2012). This paper details the discovery of a black hole candidate in the dust lanes of Centaurus A. This source is a transient candidate that varied by over two orders of magnitude, with spectra reminiscent of Galactic black hole X-ray binaries in the thermal dominant state. The proximity of Cen A means that this is one of the best analogues to Galactic X-ray binaries discovered in an early-type galaxy, or indeed beyond the Local Group of galaxies. This work utilised the Cen A Very Large Project (VLP), which consists of 6×100 ks of *Chandra* ACIS observations taken over two months in 2007. This black hole candidate declined from $\sim 2 \times 10^{38}$ erg s^{-1} to beneath the detection limit during this time.

I performed the data reduction, analysis, produced all plots and wrote this paper, with the exception of the analysis of IMACS data, which was performed by Kristin Woodley. Collaboration and PhD supervision took the form of discussing the scientific interpretation of the results and iteratively refining the wording of the paper prior to submission.

Chapter 5

Chapter 5 has been published in the Astrophysical Journal, volume 766, page 88 (Burke et al., 2013). This chapter concerns a wider detailed spectral study of the X-ray point sources in Centaurus A. This uses the VLP to perform a more substantial study of X-ray binaries. A further three transient black hole candidates are identified in the sample, and all of the candidates are coincident with the dust lane. To reach the observed peak luminosities requires larger period systems, and therefore more massive companions. It is argued that the dust lane, where star formation is more active, possesses companions massive enough ($\sim 1 M_{\odot}$) for black hole transients to reach luminosities $\sim 10^{38}$ erg s^{-1}, while the stellar population of the Cen A halo is dominated by stars $\gtrsim 12$ Gyr old. Further to this, our thermal states show tentative evidence of the apparent gap in the mass distribution of compact

objects.

Note that figures 5.1 & 5.2 were not included in the published paper, but are included here for completeness. An appendix containing an example spectral fit, and output of the ciao tool *glvary*, is also included.

I performed the data reduction, analysis, produced all plots and wrote this paper, with the exception of the optical investigation of source 50, which was performed by Kristin Woodley. Collaboration and PhD supervision took the form of discussing the scientific interpretation of the results at length using an online wiki, and iteratively refining the wording of the paper prior to submission.

Chapter 7

Chapter 7 is in press with the Astrophysical journal. This paper outlines the behaviour of the two known ultraluminous X-ray sources in Cen A from 2007 to the present day. A series of snapshot *Chandra* observations caught the ULXs in outburst, but at significantly sub-Eddington luminosities. The available evidence suggests the presence of accreting stellar mass black holes in these systems, rather than intermediate ($> 1000\ \mathrm{M}_{\odot}$) mass black holes.

I performed the data reduction, analysis, produced all plots and wrote this paper, with the exception of the use of, and text pertaining to Starburst99, which was carried out by Roberto Soria. Further collaboration and PhD supervision took the form of discussing the scientific interpretation, and iteratively refining the wording of the paper prior to submission.

Chapter 1

Accretion Physics and Galactic X-ray Binaries

1.1 Accretion Theory

1.1.1 Accretion onto Compact Objects

Five decades ago the discovery of the first extra-solar X-ray sources, towards the Galactic centre, posed a problem for astronomy (Giacconi et al., 1962). The ratio of X-ray flux to optical flux of these objects was found to be ≈ 1000 (Sandage et al., 1966), while in contrast the X-ray component of solar emission makes up $\sim 10^{-6}$ of the total bolometric luminosity (e.g. Judge et al., 2003). The need for an efficient and powerful origin for this emission lead to the idea that the brightest sources, such as Sco X-1, were binary star systems possessing a a neutron star (Zeldovich & Guseynov, 1966; Shklovsky, 1967) accreting a stream of material from an old donor star. Making minimal assumptions about the properties of the object, one can show that accretion onto a neutron star can be ≈ 20 times as efficient as nuclear fusion reactions, and that the more compact the accretor, the more efficient this process. These sources were confirmed as binaries for the first time by Webster & Murdin (1972), who measured the orbital period of Cyg X-1 from the radial velocity curve of the optical counterpart, and Schreier et al. (1972), who observed X-ray eclipses from the highly inclined Cen X-3.

This thesis will mostly concern itself with systems that contain black hole (BH) or neutron star (NS) accretors, both of which are exotic stellar remnants. Black holes are massive objects that are so compact, so gravitationally attractive that no light can escape from within them. The size of a black hole, which is to say the spatial extent from which light cannot escape, is defined by the Schwarzschild radius r_{Sc}, where

$$r_{Sc} = \frac{2GM}{c^2} \approx 3\frac{M}{\mathrm{M}_\odot}\ \mathrm{km}, \tag{1.1}$$

which is sometimes refered to as the 'gravitational' radius. BHs are remnants that have a mass greater than the Tolman-Oppenheimer-Volkoff limit (Tolman, 1939; Oppenheimer & Volkoff, 1939), which is the point at which the remnant gravitational force is no longer balanced by short-range neutron-neutron repulsion, and therefore dictates the maximum possible mass of a NS. This is highly dependent on the (unknown) equation-of-state, but is thought to be $\sim 3\mathrm{M}_{\odot}$ (e.g. Heiselberg & Pandharipande, 2000). In the same way, NS are always more massive than white dwarf systems, which are beyond the scope of this thesis. The minimum NS mass is determined by the Chandrasekhar limit (Chandrasekhar, 1931), currently thought to be $\sim 1.0 - 1.4\mathrm{M}_{\odot}$, depending on the composition of the remnant.

Eddington

A useful quantity to define is the so-called Eddington limit. This is the maximal isotropic luminosity an accreting compact object should be able to produce from spherical accretion. This is known as the Eddington luminosity L_{Edd}, and is the point at which the gravitational force pulling material towards the centre of the compact object is balanced by the outwards force from radiation and accretion is halted. Consider a compact object of mass M, which will exert force F_g on proton of mass m_p at radius R

$$F_g = \frac{GMm}{R^2}. \tag{1.2}$$

The luminosity L of the source has flux f at R and exerts a force S on one electron with Thomson cross-section σ_T of

$$\begin{aligned} S =& \frac{f}{\sigma_T c^2} \\ =& \frac{L}{4\pi R^2 \sigma_T c^2}, \end{aligned} \tag{1.3}$$

and because the electrons can be thought of as 'dragging' the proton by the Coulomb force, equations 1.2 & 1.3 can be equated to find the Eddington luminosity

$$\begin{aligned} L_{Edd} =& 4\pi\sigma_T G M m_p c^2 \\ \approx& 1.3 \times 10^{38} \frac{M}{\mathrm{M}_{\odot}}. \end{aligned} \tag{1.4}$$

It is often useful to discuss the luminosity of a given source as a fraction of L_{Edd}.

Roche-Lobe Overflow

Roche lobe overflow is a mechanism for material to accrete from a star onto a compact object. The donor evolves to the point where it expands, the surface spilling over the inner-Lagrangian point in the equipotential between the two stars and falling onto the compact object. For an accretor (primary) mass M_1, donor (secondary) mass M_2, separated by distance a, Kepler's law shows that

$$P_{orb} = \sqrt{\frac{4\pi^2 a^3}{G(M_1 + M_2)}}. \tag{1.5}$$

A test particle in the coordinates of the co-rotating frame of the binary system, with origin at the centre of mass, will experience three significant accelerations; gravitational attraction from both stars and a centrifugal acceleration given by

$$\vec{a_c} = -\vec{\omega} \times (\vec{\omega} \times \vec{r}), \tag{1.6}$$

where r is the displacement from the centre-of-mass of the system. Each acceleration will be equal to the derivative of the potential $\vec{a} = -\vec{\nabla}\Phi$, the combined potential is given by

$$\Phi = -\frac{GM_1}{|\vec{r} - \vec{r_1}|} - \frac{GM_2}{|\vec{r} - \vec{r_2}|} - \frac{1}{2}\vec{\nabla}(\vec{\omega} \times \vec{r})^2. \tag{1.7}$$

When one considers a radius r that is not so small as for a test mass to just orbit the one star, nor so large such that the binary potential approximates a point, the equipotential connects the two binary components in the classic 'figure-of-eight' shape, known as the Roche lobes. Of particular interest is the so-called inner Lagrangian point L_1, directly between the two stars, and from which matter from a suitably evolved companion can pass before accreting onto the compact object.

Material passing through L_1 possesses angular momentum and cannot simply land on the primary directly. Instead, the plasma travels to the side of the compact object, into an orbit. Matter is essentially pushed through L_1 by the radiation pressure of the secondary, at which point it has two major components to its velocity, viewed from the non-rotating frame. The first is the velocity from rotation of the system $v_\perp$, perpendicular to the binary axis, away from the primary. This can be considered in terms of classical circular motion, with a test mass at L_1 a distance b from the primary, moves with the binaries angular frequency ω and therefore $v_\perp \sim b\omega$. Perpendicular to the binary axis, the material will have velocity $V_\parallel$ from being pushed through L_1. This velocity willl therefore be

less than the sound speed of the gas c_s, which for normal stellar envelope temperatures ($c_s \propto \sqrt{T}$, Frank et al., 2002) means that $v_\parallel \lesssim 10 \text{ km s}^{-1}$. By contrast, given that $P_{orb} = \omega/2\pi$ and equation 1.5, it can be demonstrated that $v_\perp$ is much larger than $v_\parallel$ (Figure 1.1). It is clear that $v_\perp \gg v_\parallel$, even for long period binaries of comparable, low mass.

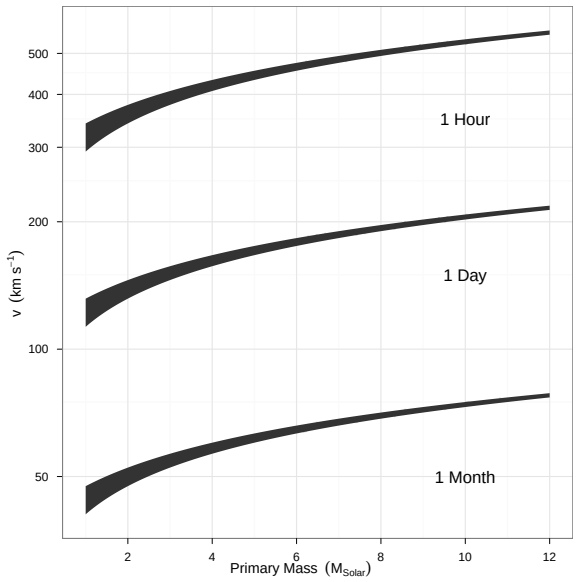

Figure 1.1 The variation of perpendicular velocity $v_\perp$ with compact object mass. The ribbons represent different binary periods, the width of each ribbon shows the effect of secondary mass M_2 in the range $0.5 - 1.5\text{M}_\odot$.

After leaving L_1, the material circularises around the compact object at distance R_{circ}. We can calculate the distance from the primary by assuming a Keplerian orbit for matter travelling with instantaneous velocity v_θ. From angular momentum conservation

$$\begin{aligned} R_{circ} v_\theta &= b v_\perp \\ &= b^2 \omega \\ R_{circ} \sqrt{\frac{GM_1}{R_{circ}}} &= \frac{b^2 2\pi}{P_{orb}} \\ R_{circ} &= \left(\frac{4\pi^2}{GM_1 P_{orb}^2} \right) b^4 \end{aligned} \tag{1.8}$$

and in units of binary separation we can then simplify using Kepler's law,

$$\begin{aligned} \frac{R_{circ}}{a} &= \left(\frac{4\pi^2}{GM_1 P_{orb}^2} \right) a^3 \left(\frac{b}{a} \right)^4 \\ \frac{R_{circ}}{a} &= (1+q) \left(\frac{b}{a} \right)^4 \end{aligned} \tag{1.9}$$

to put R_{circ} in terms of the mass ratio and binary separation. Assuming reasonable values, typically $R_{circ} \approx 0.3 - 0.5a$, many orders-of-magnitude larger than the radius of compact objects (10^6 cm in the case of NSs).

Wind-powered Accretion

High mass X-ray binaries, which possess donor stars in excess of $\sim 10\ \mathrm{M}_{\odot}$, tend to have larger periods than LMXBs, varying on timescales of many days. The donor stars reside well within their Roche lobes, and tend to be early-type O- or B-stars and the accretion process powered by out-flowing material in a strong stellar wind (e.g. Psaltis, 2006). For some sources, such as neutron star Be binaries (Maraschi et al., 1976), the compact object is in an extremely elliptical orbit that passes through the surrounding ejecta of rotating B-emission stars at periastron. This circumstellar material is accreted, resulting in sudden outburst from the system.

Disc Structure

The stream of material that circularises into orbit of the compact object eventually spreads out due to viscous forces (see Pringle, 1981, for review of disc structure theory). These forces arise from shear viscosity, and the chaotic motions of gas elements. Taking any two adjacent infinitesimal rings of material in the disc, there will be a torque exerted between the two. The net torque between the two rings will depend on the differential between the angular velocities Ω', and the viscosity ν of the disc. This can be expressed in terms of the surface density Σ, viscosity ν,

$$\tau_o \sim -2\pi\Sigma\nu R^3\Omega'. \tag{1.10}$$

Intuitively, it is easy to see that a rigid disc, with $\Omega' = 0$, will have no shear viscosity between adjacent annuli. Assuming that the motion of each ring is Keplerian, the angular velocity $\Omega(R)$ decreases with increasing distance from the centre of the compact object. Material from an inner ring will impart angular momentum to the outer ring, causing the inner ring to slow down and spiral inwards while the outer ring spreads out beyond R_{circ}. We are ultimately interested in the energy dissipated by the disc as radiation. To do this we must assess the amount of energy converted to kinetic and thermal energy, and how much may be radiated away. Consider infinitesimal annuli at R and $R + dR$; the net torque τ_o acting on the ring at R is

$$\tau_o(R) - \tau_o(R + dR) = \frac{d\tau_o}{dR} dR \tag{1.11}$$

and the power $\Im$ exerted by the sheer viscosity

$$\begin{aligned}\Im =& -\Omega\frac{d\tau_o}{dR}dR \\ =& -\left[\frac{d}{dR}(\tau_o\Omega) - \tau_o\Omega'\right]dR\end{aligned} \tag{1.12}$$

where $\frac{d}{dR}(\tau_o\Omega)$ is the transfer of rotational energy through the disc. However, it is $\tau_o\Omega'$ that is of interest, the dissipation that results in heating of the disc. As each annuli has a surface area (top and bottom) of $2(2\pi R)dR$, so the dissipation rate per unit surface area $D(R)$ is (the substituting equation 1.10)

$$\begin{aligned}D(R) =& \frac{\tau_o\Omega'}{4\pi R} \\ =& \frac{1}{2}\nu\Sigma(R\Omega')^2\end{aligned} \tag{1.13}$$

However, to assess this as astronomers we need to express $D(R)$ in terms of observable quantities, for which the accretion rate $\dot{M}$ shall suffice. Starting from the conservation of angular momentum

$$R\frac{d}{dt}(\Sigma R^2\Omega) + \frac{d}{dR}(R\Sigma v_R R^2\Omega) = \frac{1}{2\pi}\frac{d\tau_o}{dR} \tag{1.14}$$

and setting the time derivative to zero then substituting using equation 1.10

$$\begin{aligned}R\Sigma v_R R^2\Omega =& \frac{1}{2\pi}\tau_o + C \\ -\nu\Sigma\Omega' =& \Sigma(-v_R)\Omega + \frac{C}{R^3}\end{aligned} \tag{1.15}$$

we can calculate the constant C by recalling that $\Omega' \to 0$ at the surface of the compact object, and so with Ω being Keplerian at the stellar surface (radius R_s)

$$C = -\frac{\dot{M}}{2\pi}\sqrt{GMR_s}. \tag{1.16}$$

Consider that material will have velocity in the radial direction towards to compact object v_R, then a steady accretion disc shall accrete at a rate of $\dot{M} = 2\pi R\Sigma(-v_R)$. Substituting 1.16 and $\dot{M}$ into 1.15 and rearranging to obtain

$$\nu\Sigma = \frac{\dot{M}}{3\pi}\left[1 - \left(\frac{R_s}{R}\right)^{1/2}\right]. \tag{1.17}$$

One can return to the expression for $D(R)$ (1.13), which will be important when considering the predicted disc spectra in §1.1.2. With the first part of the equation, $\nu\Sigma$, now expressed in terms of

quantities measurable through observations, it is only remains to recall that

$$\begin{aligned} R\Omega' =& -\frac{3}{2}R(GM)^{1/2}R^{-5/2} \\ \frac{1}{2}(R\Omega')^2 =& \frac{9}{8}\frac{GM}{R^3} \end{aligned} \tag{1.18}$$

and Equation 1.13 becomes

$$D(R) = \frac{3GM\dot{M}}{8\pi R^3}\left[1-\left(\frac{R_s}{R}\right)^{1/2}\right]. \tag{1.19}$$

The geometrically thin disc is optically thick ($\tau \gg 1$) the emission from an individual disc annulus must be blackbody in nature. Therefore one can equate the blackbody emissivity of a given effective temperature T_{eff} with the dissipation rate from the disc

$$\begin{aligned} \sigma_B T_{eff}^4(R) =& D(R) \\ T_{eff} =& \left(\frac{3GM\dot{M}}{8\pi R^3\sigma_B}\left[1-\left(\frac{R_s}{R}\right)^{1/2}\right]\right)^{1/4} \end{aligned} \tag{1.20}$$

which is used to describe the predicted spectrum in §1.1.2.

Having described the dependence of temperature and surface density on radial distance, it is now possible to collect these together with other well known descriptions of physical quantities to get a generic description of accretion disc properties. The pressure in the disc will be a combination of the gaseous and radiation pressures acting at a given point

$$P = \frac{\rho k T_c}{\mu m_p} + \frac{4\sigma}{c}T_c^4 \tag{1.21}$$

and also

$$= c_s^2 \rho \tag{1.22}$$

and assuming a that the disc is thin ($H \ll R$)

$$H \approx c_s\left(\frac{R^{3/2}}{\sqrt{GM}}\right) \tag{1.23}$$

leaving the viscosity ν and opacity τ as the remaining unknown physics, and once a prescription for these is specified it is possible to solve the above equations to a full, simple analytic description of accretion discs.

The velocity of the plasma fluctuations will be limited by the local sound speed c_s and the vertical height of the disc H, from which we arrive at the famous α prescription of viscosity,

$$\nu \equiv \alpha c_s H \tag{1.24}$$

first considered by Shakura & Sunyaev (1973), and their disc description in terms of the surface density Σ, mass accretion rate (in units of 10^{16} g s^{-1}) $\dot{M}_{16}$, radial distance from the centre of the compact object (units of 10^{10} cm) R_{10}, central temperature T_c, density ρ and the numerical factor f, where $f^4 = 1 - \sqrt{R_1/R}$. Assuming also that the optical depth τ is described by Kramers' law ($= 5 \times 10^{24} \rho T_c^{-7/2}$ cm^2 g^{-1}) the disc solution is

$$\begin{aligned}
\Sigma =& 5.2\alpha^{-4/5}\dot{M}_{16}^{7/10} m_1^{1/4} R_{10}^{-3/4} f^{14/5} \text{ g cm}^{-2} \\
H =& 1.7 \times 10^8 \alpha^{-1/10} \dot{M}_{16}^{3/20} m_1^{-3/8} R_{10}^{9/8} f^{3/5} \text{ cm} \\
\rho =& 3.1 \times 10^{-8} \alpha^{-7/10} \dot{M}_{16}^{11/20} m_1^{5/8} R_{10}^{-15/8} f^{11/5} \text{ g cm}^{-3} \\
T_c =& 1.4 \times 10^4 \alpha^{-1/5} \dot{M}_{16}^{3/10} m_1^{1/4} R_{10}^{-3/4} f^{6/5} \text{ K} \\
\tau =& 190 \alpha^{-4/5} \dot{M}_{16}^{1/5} f^{4/5} \\
\nu =& 1.8 \times 10^{14} \alpha^{4/5} \dot{M}_{16}^{3/10} m_1^{-1/4} R_{10}^{3/4} f^{6/5} \text{ cm}^2 \text{ s}^{-1} \\
v_R =& 2.7 \times 10^4 \alpha^{4/5} \dot{M}_{16}^{3/10} m_1^{-1/4} R_{10}^{-1/4} f^{-14/5} \text{ cm s}^{-1}
\end{aligned} \tag{1.25}$$

which is displayed for clarity in figure 1.2. An important result is that the disc is indeed thin ($H \ll R$) and optically thick ($\tau >> 1$). As well as the thinness of the disc being demonstrated by H/R using the equations 1.25, I demonstrate that this is so to large radii in figure 1.2; the height of the disk reaches ~ 1.5 the radius of a NS at a distance of $\approx 1000\ km$ from the centre of the compact object.

1.1.2 Disc Emission and Comptonisation

Thin Disc Spectra

The optically thick nature of thin accretion discs means that the emission is blackbody limited. Given equation 1.20, it can be assumed that the disk is a series of annuli emitting as blackbodies characterised by a range of temperatures across the disc away from the compact object (where $T \propto R^{-3/4}$). This means that the emission at a given radius can be expressed in terms of the Planck function

$$B_\nu = \frac{2h\nu^3/c^2}{e^{\frac{h\nu}{kT}} - 1} \tag{1.26}$$

which has units of energy/area/time/frequency/angle. The form of the integrated emission, which we can expect to observe as the source spectrum, can be considered as the superposition of blackbodies at all annuli into a so-called multi-color disc blackbody (herein disc blackbody). This flux F_ν observed

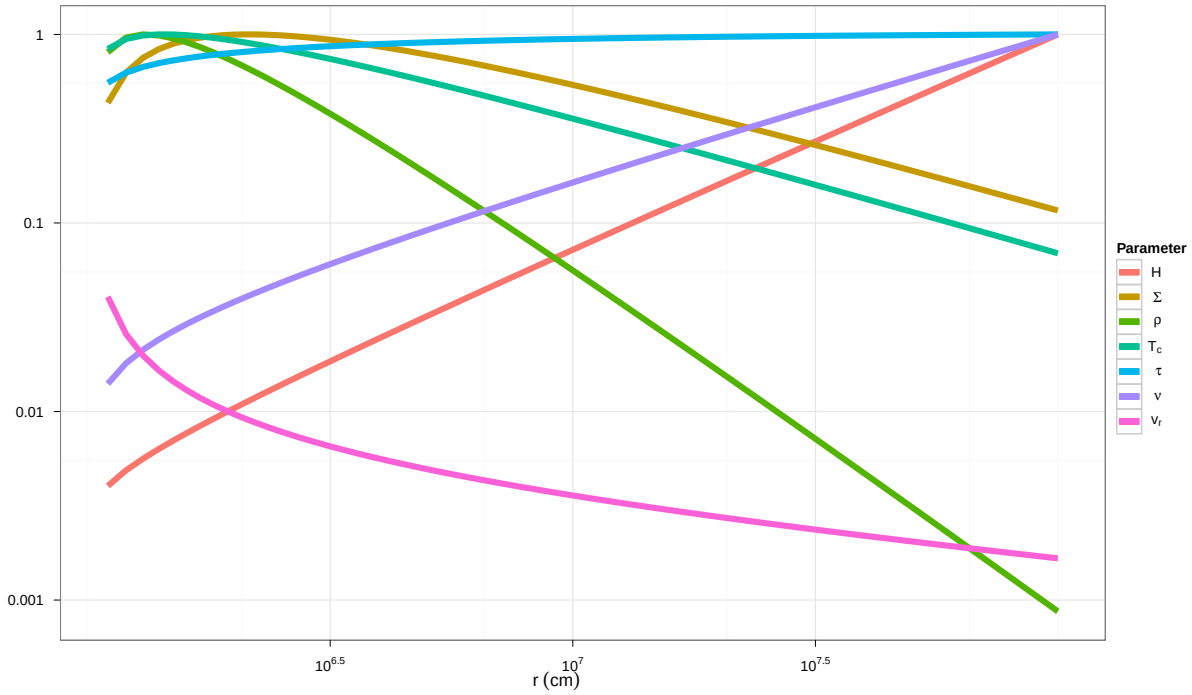

Figure 1.2 Structure of Shakura & Sunyaev disk spanning 11km to 1000 km from the centre of a NS-like compact object that has 1.4 $M_\odot$ and radius of 10 km, accreting at 10^{17} g s^{-1}, maximal values all normalised to unity. The maximal values in this span of r; $H \sim 1.5 \times 10^6$ cm, $\Sigma \sim 4.5 \times 10^4$ g cm^{-2}, $\rho \sim 4.2$ g cm^{-3}, $T_c \sim 2.4 \times 10^7$K, $\nu \sim 8.9 \times 10^{11}$ cm^2 s^{-1} and $v_R = 1.6 \times 10^7$ cm s^{-1}.

in the solid angle $\ominus(R)$ subtended by the observer at distance D is

$$\begin{aligned} d\ominus &= \frac{2\pi R dR \cos i}{D^2} \\ F_v &= \int_{R_s}^{R_{out}} B_\nu d\ominus(R) \\ F_v &= \frac{4\pi h\nu^3 \cos i}{c^2 D^2} \int_{R_s}^{R_{out}} \frac{RdR}{e^{\frac{h\nu}{kT(R)}} - 1}. \end{aligned} \tag{1.27}$$

From this, the approximate spectral shape can be revealed by looking at the frequency extremes at the inner and outer radii of the disc. In the low frequency (Rayleigh-Jeans) limit, the spectrum beneath the peak frequency of the blackbody emission characterised by the effective temperature of the outer edge of the disc, $h\nu \ll kT(R_{outer})$, is approximated by

$$\begin{aligned} B_\nu &\approx \frac{2kT(R)\nu^2}{c^2} \\ F_\nu &\propto \nu^2, \end{aligned} \tag{1.28}$$

while the spectrum above that of the blackbody peak of the inner disc, $h\nu \gg kT(R_s)$, will be Wien-like

$$B_\nu \approx \frac{2h\nu^3}{c^2} e^{-\frac{h\nu}{kT}}$$
$$F_\nu \propto \nu^3 e^{-\frac{h\nu}{kT}}, \tag{1.29}$$

and for the disc itself, between the inner and outer edge, the spectrum shall approximately follow

$$F_\nu \propto \nu^{1/3}. \tag{1.30}$$

Equations 1.28,1.29 & 1.30 can be put together for their respective energy regimes to obtain the complete spectral shape of thermal emission from an optically thick thin disc (Figure 1.3).

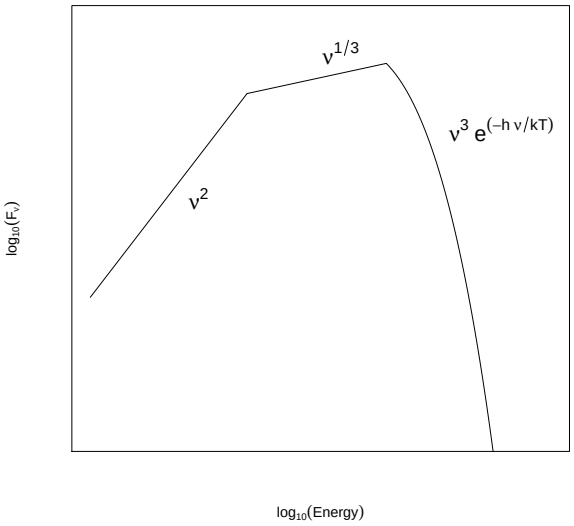

Figure 1.3 Approximate spectral shape of thermal emission from a thin disc.

Emission from Compton scattering in a thermal medium

Inverse-Compton scattering is where photons are scattered off high-energy electrons to shorter frequencies. This process is 'inverse', because it is in contrast to the more familiar laboratorical Compton-scattering where photons experience a net energy loss and momentum is imparted to the electrons (see Rybicki & Lightman, 1986, for a thorough treatment). When discussing photons that traverse a cloud of material, gaining energy ΔE, it is useful to define the Compton y parameter

to gauge the extent of the change experienced by the photon over the whole cloud. Therefore it considers the energy change per scattering averaged over all angles $\hat{E}$, and the total number of scatterings N experienced in the cloud, such that

$$y \equiv \hat{E}N. \tag{1.31}$$

Here, N is the supremum of the optical depth τ ($\tau < 1$) or its square τ^2 ($\tau > 1$),

$$\tau \sim \rho \frac{\sigma_T}{m_p} D, \tag{1.32}$$

the product of the electron scattering opacity in ionised Hydrogen ($\sigma_T/m_p = 0.4 \text{ cm}^2 \text{ s}^{-1}$) and the amount of material the photons traverse, along length D. For a thermal distribution of electrons,

$$\hat{E} = \frac{E}{mc^2}(4kT - E), \tag{1.33}$$

for initial photon energy E traversing a cloud of temperature kT. We assume circumstances where $4kT \gg E$, so

$$y \equiv \frac{4kT}{mc^2}\text{Max}(\tau, \tau^2). \tag{1.34}$$

For the purposes of this thesis and the discussion of black hole X-ray binary spectral states, it is sufficient to understand that the emergent spectrum will follow a power law up until the temperature of the electron distribution, after which point the spectrum falls off exponentially. The intensity I of emergent radiation between energies E_i and E_f will therefore be described by

$$I = I_i \left(\frac{E_f}{E_i}\right)^{-\Gamma} \tag{1.35}$$

below kT, and

$$I = I_i \left(\frac{E_f}{E_i}\right)^{3} e^{-x} \tag{1.36}$$

above kT, where $x \equiv h\nu/kT$. Rybicki & Lightman (1986) show that spectral index, Γ, is related to the Compton y parameter as

$$\Gamma - 3 = -\frac{3}{2} \pm \sqrt{\frac{9}{4} + \frac{4}{y}} \tag{1.37}$$

1.1.3 Outburst behaviour

X-ray binaries can be divided into groups based on their long term behaviour. There are persistent systems, seemingly always in outburst, and there are transient systems, that may outburst on

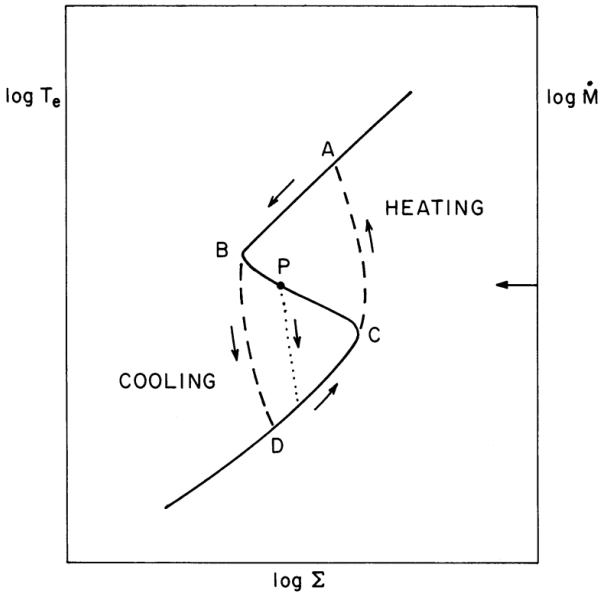

Figure 1.4 Schematic of the duty-cycle behaviour resulting from the Hydrogen ionisation instability. As described in the text, an accretion disc on branch **DC** will increase in temperature and density until the ionisation jump and thermal runaway (**CA**), which then decreases in density and temperature until a jump due to reionization (**BD**). Path **BC** is unstable, and a perturbation will cause the disc to jump to either **AB** or **DC**. Taken from Smak (1984).

timescales of a months to years before returning to a quiescent state. The favoured explanation for this outburst behaviour is based around the so-called disc instability mechanism (DIM).

At low accretion rates, the material flowing towards the compact object is neutral hydrogen and therefore optically thin as the electrons are bound to their parent atoms. When the temperature at a given annulus of the disc reaches the ionisation point of hydrogen (~ 6500 K) the number of free electrons increases and the optical depth becomes extremely sensitive to the temperature of the annulus, with a small increase in T_c leading to a large increase in τ. This means that the temperature of the annulus rises as more photons are absorbed, which increases the opacity further in a thermal runaway until all of the Hydrogen is ionised. The thermal instability then triggers viscous instabilities. The larger temperature raises the accretion rate through that annulus (Eq. 1.25), so the material in the disc within this annulus races away, decreasing the density of the flow, and in turn, the optical density. The material cools, and eventually Hydrogen can recombine in a cooling thermal runaway. This cyclic behaviour, of course, will effect adjacent annuli of the disc, particularly if the difference between the accretion rate of the ionised and neutral material is large, so the whole disc experiences the limit-cycle behaviour (see Figure 1.4). This has been successful in explaining the lightcurves (Figure 1.5) of accreting white dwarfs in dwarf novae (Cataclysmic variables, CVs)

(Smak, 1984). In the case of NS or BH containing X-ray binaries, this is not as clear-cut. While the lightcurves have the predicted fast rise from the onset of the instability, the decay is typically quasi-exponential (see review by Lasota, 2001). The decay shape is attributed to irradiation of the outer disc by the luminous inner regions, preventing Hydrogen from recombining, which reduces the disc and is observed as an exponential decay in the lightcurve. In turn, the disc cools and reduces the irradiating power until the outer disc temperature can dip below the Hydrogen recombination point and the runaway cooling can occur (van Paradijs, 1996). This cooling is slowed because of the region still irradiated, and so the lightcurve experiences linear decline.

Persistent behaviour is therefore the result of a steady state that keeps the temperature above 6,500 K. Initially ignoring the effects of irradiation, and approximating equation 1.20 far from the compact object as

$$T_{eff}^4 \approx \frac{3GM\dot{M}}{8\pi\sigma R^3} \tag{1.38}$$

and setting $T_{eff} = T_{H^+}$, the Hydrogen ionisation temperature, an approximate critical mass accretion rate $\dot{M}_{crit}$ separating the persistent and transient regimes can be derived. The orbital period correctly predicts persistent/transient nature for CVs. For X-ray binaries, the effects of irradiation have to be taken into account, stabilising the disc at lower accretion rates (reducing $\dot{M}_{crit}$).

King et al. (1996) considered three scenarios for the evolution of binary periods that lead to transient or persistent behaviour, based on the resulting mass transfer rate. For Roche lobe overflow to occur from the secondary either the lobe itself must shrink – as a result of angular momentum losses – or the star must expand to fill its lobe during the course of normal stellar evolution. As a third option, King et al. (1996) also considered the case for when the secondary has marginally evolved off the main sequence but the Roche lobe has shrunk to the stellar surface. In the former scenario, the angular momentum losses cause the system to retard to small periods after the onset of mass transfer, while the second scenario allows for the binary to move to larger periods on a timescale equal to the main sequence (MS) lifetime of the donor. The key parameter in determining which of the scenarios takes precedence is the mass of the primary, as for a larger mass the angular momentum losses will take longer to affect the orbital period of the system, giving the secondary more time to evolve off the MS.

Assuming that the secondary has had time to leave the MS, then the binary period will have increased, and it can be shown that for LMXBs with $P > 2$ days, the $\dot{M}$ will always be less than $\dot{M}_{crit}$, and all such systems should be transient. This is because $\dot{M}_{crit}$ has a greater dependency on P than the global accretion rate does, as $\dot{M} \propto P^{0.9} m_2^{1.47}$ while $\dot{M}_{crit} \propto m_1^{2/3} P^{4/3}$ (Webbink et al., 1983; King, 1988). However, a great number of transient sources have $P < 2$ days, and so these must be the systems for which angular momentum is lost to the extent that Roche lobe shrinks on a shorter timescale than that of the donor's evolution.

The dependence on the primary mass is useful in the context of the type of compact object, BHs being more massive than NSs. Fundamentally, secondaries need to be more evolved for less massive primaries in order for transient behaviour to occur. For transience, King et al. (1996) estimate that at the onset of transfer the mass of the donor as fraction of the main sequence mass M_{MS} needs to be $< 0.25 M_{MS}$ for NS primaries, while $< 0.75 M_{MS}$ for BHs. Therefore, for NSs to be transient the secondary has less time to evolve (as angular momentum loss takes place on a shorter timescale) to a more evolved state than required for black holes. This points to black holes more readily existing in transient X-ray binaries, in good agreement with observation. Compared to NS LMXBs, a far larger proportion of known BH LMXBs are transient (McClintock & Remillard, 2006).

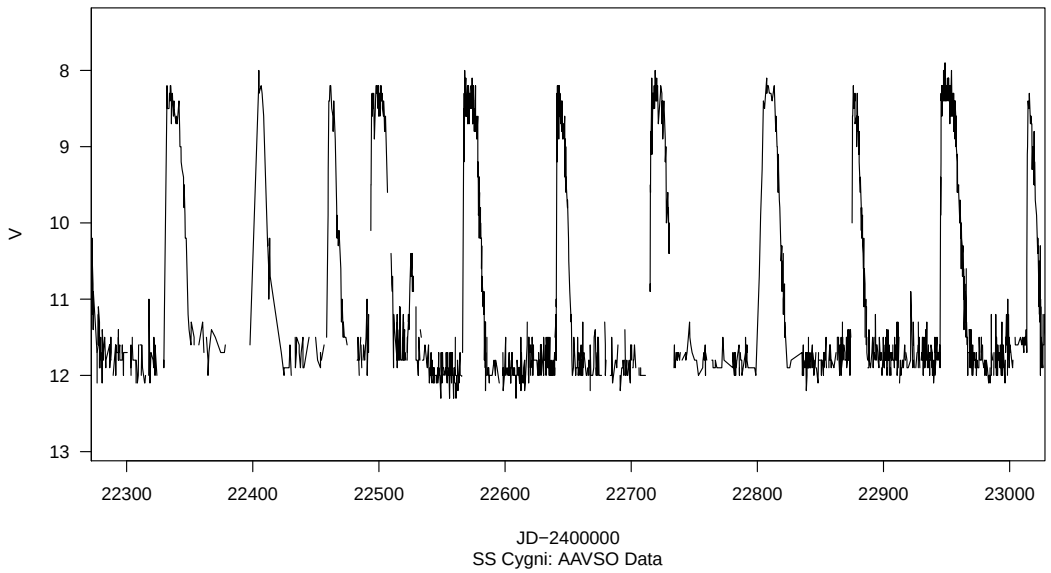

Figure 1.5 Lightcurve of SS Cygni showing limit cycle behaviour, using data obtained from the American Association of Variable Star Observers (AAVSO)

1.2 Galactic Sources

1.2.1 Accretion onto stellar mass black holes

This section shall outline our current understanding of BH XBs in terms of temporal and spectral behaviour, derived mostly from studying the Galactic sources. In the Milky Way there are at least 15 confirmed BH XBs with low mass ($< 2\mathrm{M}_{\odot}$) secondaries (LMXBs) and 3-5 sources with high mass ($> 10\mathrm{M}_{\odot}$) companions (McClintock & Remillard, 2006). It is unlikely that every Galactic BH XB has been discovered, and new identifications are ongoing (e.g. Muñoz-Darias et al., 2013). These systems have a small orbital separation and would fit inside the orbit of Mercury around the sun, as illustrated in figure 1.6. The 15 BH LMXBs are all transients (see § 1.1.3), while the HMXBs are persistent sources and this is likely because they are continually accreting material ejected from their companions as a stellar wind (§ 1.1.1). The LMXBs tend to spend a lot of time accreting in quiescent states at L_x $10^{32} - 10^{34}$ $\mathrm{erg\ s^{-1}}$ before experiencing outbursts lasting weeks-months that peak at luminosities $\sim 10^{38}$ $\mathrm{erg\ s^{-1}}$. Exceptionally, the so-called Galactic micro-quasar, GRS 1915+105, sprang into an extremely volatile outburst in 1992 that is still precipitating, while GX339-4 never truly reaches quiescence, though does experience dramatic variability.

The spectral behaviour can be summarised by utilising hardness ratios, a long-standing tool that underpins most X-ray spectral research. A hardness ratio, or X-ray colour, is usually the ratio of intensity in one energy band to that of another, with lower energies are referred to as 'soft', while higher energies referred to as 'hard'. Typically, the hardness ratio is defined with a hard numerator and soft denominator, but various other definitions exist. Hardness ratios are mission-dependent in that the bands chosen depend on the bandwidth and spectral resolution of the instrument, which varies on a mission-by-mission basis. This means that it is often not possible to compare hardness ratios from different missions, which is a disadvantage discussed in § 4.3. The hardness ratio is particularly useful for poor quality data, where full spectral fitting is inadequate, but also for quickly diagnosing the spectral state of both BH and NS XBs.

BH XBs experience two main spectral states. An outburst from BH LMXB GX339-4 is presented in figure 1.7, observed using the *MAXI* instrument on the International Space Station. The plot to the left shows the intensity lightcurve (over the bandwidth of the instrument, 2-20 keV) as a function of MJD, while the plots to the right show the corresponding variation of intensity with

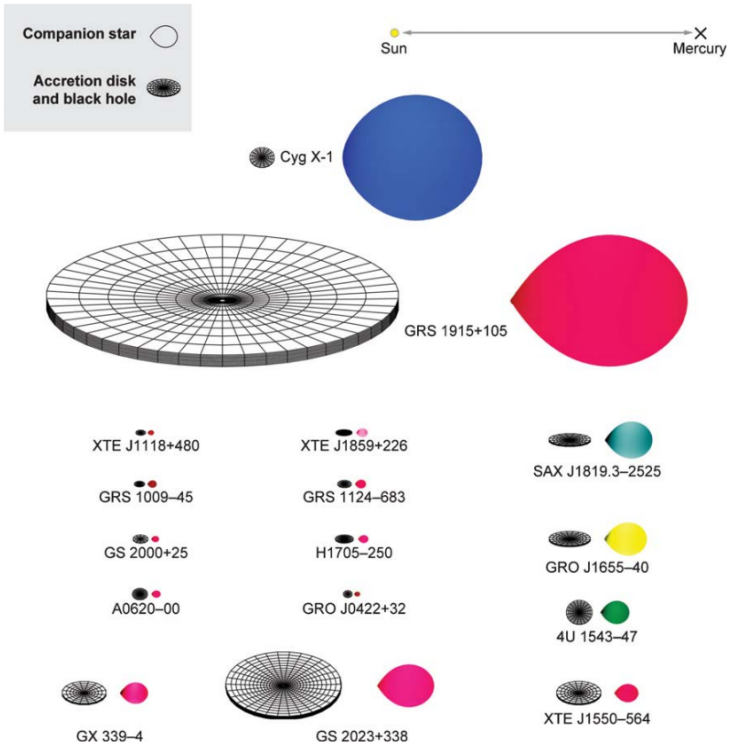

Figure 1.6 Galactic BH XBs, from Remillard & McClintock (2006)

spectral hardness. The spectrum is at its hardest at the start of the outburst, and increases in brightness over ≈ 50 days. The broad-band intensity is still increasing after MJD 55300, but the spectrum starts to soften at this point, which continues until after the intensity peaks and the source stays around a constant intensity in a soft state for a large portion of the outburst. The intensity slowly decreases and eventually the spectra start to harden again, and canonically this would then be followed by descent into quiescence, the spectra remaining hard (as stated above, GX339-4 never quite reaches quiescence). Historically, an observational bias resulting from being more likely to see source in a relatively bright, soft state and the hard, usually less luminous state led to a belief that the states were dichotomous in intensity, and therefore became known as the high-soft and low-hard states, respectively.

It is now generally accepted that there are three canonical BH XB outburst states (McClintock & Remillard, 2006). Far from being dichotomous in intensity, it is more the case that the sources evolve hysteretically around a 'loop' in intensity-hardness (IH) space. It has been shown that the softer state is well described as emission dominated by a disc blackbody (§ 1.1.2), with the characteristic shape presented in figure 1.3, but with a very weak power law component also present to high energies.

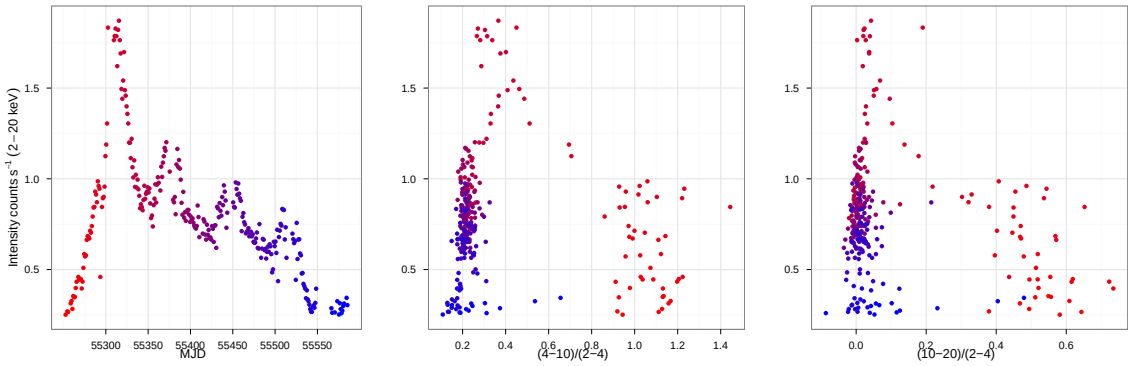

Figure 1.7 Behaviour of GX 339-4 over one outburst, using data obtained from the *MAXI* (see Mihara et al., 2011, for mission overview) all-sky monitor on board the International Space Station. Left is the outburst lightcurve, binned to one day. The two plots to the right show the classic X-ray hardness behaviour with intensity. Uncertainties not shown for clarity.

Crucially, spectral fitting has been used to recover the inner temperature of the disc, which has been shown to evolve with luminosity along $L_x \propto T^4$ (Davis et al., 2006), a key prediction of accretion disc theory (§ 1.1.1). Therefore, it is likely that we are observing an optically thick, geometrically thin accretion disc, and it has subsequently become de rigour to refer to the high-soft spectra as the *thermal dominant* state. This disc blackbody typically has an inner disc temperature of $\lesssim 1$ keV, though can be larger. Galactic source thermal states are displayed for contextual purposes in figure 4.6.

The assumption that the disc extends down to the innermost stable circular orbit during the thermal dominant state allows a determination of the black hole mass, based on the measured maximum disc temperature and luminosity (Gierliński et al., 1999),

$$L_{disc} = \frac{\pi \sigma G^2 M^2 T_{max}^4}{6 c_o^4 f_{col}^4 c^4}, \tag{1.39}$$

where M is the mass of the compact object, f_{col} is a colour temperature correction (see Shimura & Takahara, 1995), σ is the Stefan-Boltzman constant and $c_o \sim 0.1067$. The disc luminosity L_{disc} recovered from spectral fitting results is further modified by relativistic effects close to the black hole (Gierliński & Done, 2004). This necessitates the need for a modification factor, $g(i, a)$, which is a function of both the spin of the black hole a, and the inclination of the system i such that $L_{observed} = g(i, a) L_{disc}$. Zhang et al. (1997) evaluated $g(i, a)$ at a handful of inclinations for both non- and maximally-spinning BH. In Chapter 5, these relationships are used to show mass ranges in $L_x - kT_{in}$ space for thermal dominant state sources in Cen A.

During the emergence from quiescence, and the eventual decline towards the end of the outburst, the spectrum is dominated by a hard component. This is often refered to as the hard power law state, as the spectra are well-fit by a power law of $\Gamma \sim 1.6 - 2.0$, which extends to very high energies (> 100 keV). The exact accretion geometries producing this emission are still debated, but there is consensus that some form of inverse-compton process is taking place, with low energy photons scattered to higher energies (§ 1.1.2). The predominant concept is that the accretion flow becomes optically thin, so that the energy in the disc at that point does not thermalise. The large temperature of the protons in this flow leads to the disc expanding perpendicular to the plane of accretion. The typical spectra peak at over 100 keV, before showing a steep decline at high energy as expected for seed photons scattering off a hot thermal medium of electrons.

It is desirable in terms of understanding accretion phenomena across the full mass range of compact objects, to try to tie the states together. Esin et al. (1997) demonstrate a feasible synergy between an advection-dominated accretion flow (ADAF) and the optically thick, Shakura & Sunyaev style disc. During a low accretion rate in quiescence, the disc is truncated at a large radius; the small density of the material leading to the inner regions being dominated by an ADAF. The truncation of the disc means that few disc photons are intercepted by the flow. The hard spectra peak at ≈ 100 keV, suggesting that the flow is warm, and as the disc starts to edge closer to the compact object the number of photons being intercepted by the ADAF increases. This increases the amount of comptonisation and cools the flow, in good agreement with observations showing a softening of the high energy peak with larger L_x (Ibragimov et al., 2005). More of the disc starts to extend into the flow, until a critical point at which the disc extends down to the innermost stable circular orbit (ISCO). At this stage, the exposed disc dominates the spectrum as a thermal multicolour disc blackbody, a tenuous cloud of electrons above the disc giving the spectrum a weak comptonised component to high energies. If the high energy tail in the steep power law state is produced from up-scattered disc photons, then the power law description of the tail should be modelled with a low energy cut-off to correctly recover the parameters of the disc from the continuum emission. This usually reveals a partially truncated disc, i.e. the inner disc temperature is smaller than in the thermal state. A thorough review of this description, and possible alternatives to the hot inner flow geometries, are discussed in detail by Done et al. (2007).

There are two further key observational features distinguishing the thermal state from the power

law state. In the power law state, there is a rapid variability that is not seen in the thermal state. As well as this, it is now well established that there is radio emission associated with the power law state that again is not present at other times (e.g. Fender et al., 2004). It is thought that this emission is the result of a beamed jet of material, perpendicular to the accretion flow, that somehow becomes quenched as the spectra transition to the thermal state. A good correlation exists between the radio and X-ray luminosities (see Fender, 2006), suggesting a direct link between the properties of the accretion disc and the jets.

The third canonical BH state is the *steep power law* (aka 'very high') state (which one can surmise is the soft peak shown by GX 339-4 in figure 1.7). The spectra here is a superposition of both a strong thermal and non-thermal components, that can be modelled with a power law of $\Gamma > 2.4$ (steeper than in the hard state) and disc blackbody. The power law and steep power law states are also distinct at higher energies, the former experiencing a high energy cut-off at ~ 100 keV that is not present in the latter (Grove et al., 1998). While the steep power law state is dominated by a soft component, the high energy tail can carry as much as a third of the bolometric luminosity.

1.2.2 Accretion onto neutron stars

Neutron stars differ from black holes in that they possess a physical surface. The remaining energy of the accretion flow must be surrendered at this surface, rather than disappearing beyond an event horizon. The surface is thought to give rise to at least two observed phenomena. Firstly, most NS systems exhibit X-ray bursts, which are occasional rapid rises in the light curve, followed by an exponential decay lasting tens to hundreds of seconds, thought to be caused from the build up of material on the surface of the neutron star to the point of nuclear ignition (For a review of X-ray burst research, Strohmayer & Bildsten, 2006). The physical surface also gives different spectral characteristics; the energy that would disappear into the event horizon of a black hole is now released and emission from a boundary layer is always present, which has a thermal quasi-blackbody spectral shape (Gilfanov et al., 2003), which has been demonstrated using Fourier-resolved spectral analysis (Revnivtsev & Gilfanov, 2006). The boundary layer facilitates a change in angular momentum between the keplerian motion of the disc and the (slower) rotation of the surface. The gravitational energy E_G released by the time the material is at the NS surface is

$$E_G = \frac{GM\dot{M}}{R_s}, \tag{1.40}$$

but the luminosity of the disc $\sim E_G/2$ (integrating the dissipation rate in equation 1.19 over both sides of the disc), so the power dissipated in the boundary layer is also $\sim E_G/2$. The boundary layer will be optically thick, so the emission will thermalise, and then escape from a region of the disc out to a radial distance of $\sim H$. The emitting area is therefore the product of the surface area and scaleheight $2(2\pi R_s H)$ and will emit as a blackbody of temperature T_{bl}, where

$$4\pi R_s H T_{bl}^4 = \frac{E_G}{2}, \tag{1.41}$$

which for a canonical NS gives $T_b \sim 3 \times 10^7$ K, or ≈ 2.6 keV in X-ray terms. Example spectra from one of the brightest NS LMXBs, GX 17+2 are displayed in figure 1.8. The temperature of the blackbody component ranges from $\sim 2.5 - 3.5$ keV.

Classifications and Behaviours

A bimodality in the behaviour of sources in the population of Galactic X-ray binaries was first confirmed by Hasinger & van der Klis (1989), who used EXOSAT data to illustrate distinctive spectral and timing behaviours (For review, van der Klis, 2006). Two main catagories of source emerged, the Z track sources, which follow a characteristic 'Z' shape in X-ray color-color diagrams, and 'Atoll' sources, which spend most of their time in a state that shows large fractional variability. Z track sources move through this behaviour in about a day, whereas Atoll sources take around a month – similar to black hole XBs. Here is a short précis of the Z track and Atoll behaviours.

It is now clear that Z track sources comprise the six brightest NS LMXBs in the Milky way, with luminosities all in excess of 10^{38} erg s^{-1}. There are three branches to the spectral evolution in hardness-intensity diagrams for these sources. Having previously discussed BH XB behaviour, it seems reasonable to approach the NSs from a similar vantage point, in terms of phenomenology. The three branches describe a hard 'horizontal' state, a softer 'flaring' state and a 'normal' branch that marks a steady transition from the brightest hard state to the lowest luminosity soft state. Of the six classic sources (GX 17+2, Cyg X-2, Sco X-1, GX 340+0, GX 5-1 and GX 349+2), there are two distinct types of 'Z', grouped by the relative size of the horizontal and flaring branches; 'Sco-like'

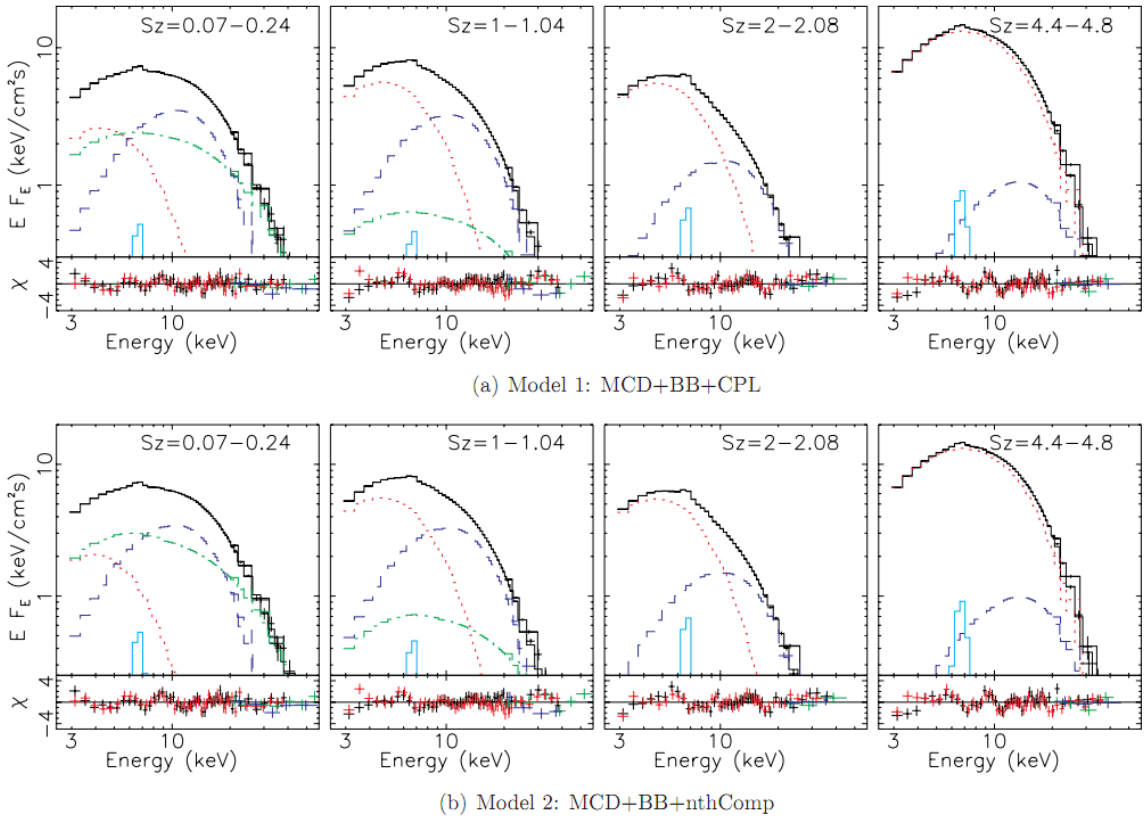

(a) Model 1: MCD+BB+CPL

(b) Model 2: MCD+BB+nthComp

Figure 1.8 RXTE spectra from an example Galactic NS LMXB, GX17+2, fitting a multi-color disk blackbody (red), a blackbody (blue) and some weak comptonised emission (green), and strong Fe-line emission (Light blue). T_{in} and T_{bl} are in the range $\sim 1.6-3.0$ keV and $\sim 2.5-3.5$ keV, respectively. Figure taken from Lin et al. (2012), who used two different descriptions of the comptonisation.

sources that have large flaring branches and almost no horizontal branch, and 'Cyg-like' sources that have pronounced horizontal branches, which harden at lower luminosities. For the Sco-like sources, the flaring branch the source exhibits a rapid and repeated increase in luminosity, increasing from the least luminous state to peak brightness in a matter of minutes. In Cyg-like sources, the flaring is negligible and the softer branch more complicated; a wide number of behaviours exist that are beyond the scope of this thesis.

The majority of low mass X-ray binaries are Atoll sources, which have luminosities $\leq 10^{38}$ erg s^{-1}. Broadly speaking, their behaviour is much more similar to that of the BH XBs than that of the Z sources, spending most of their time in a soft state that becomes harder as the luminosity decreases (giving rise to the so-called 'bannana' branch). The source will often remain at low luminosity in the hard state for some time, and if it is a transient (such as Aql X-1), then the source returns to quiescence from there.

Arguably the most important advancement in our understanding over the last ten years has come from the discovery of the first transient Z source, XTE J1701-462 (Homan et al., 2007), which was observed over a 600 day outburst. While there are exotic sources that at various times have undergone transient behaviour and later reached possibly super-Eddington luminosities, such as Cir X-1, XTE J1806-246 and Ser X-1, XTE J1701-462 was important because it displayed both Z source behaviour at higher luminosities and Atoll behaviour at lower luminosities before returning to quiescence. Not only that, but the source also showed transitions between the different types of Z behaviour (Lin et al., 2009; Sanna et al., 2010), which is shown in figure 1.9.

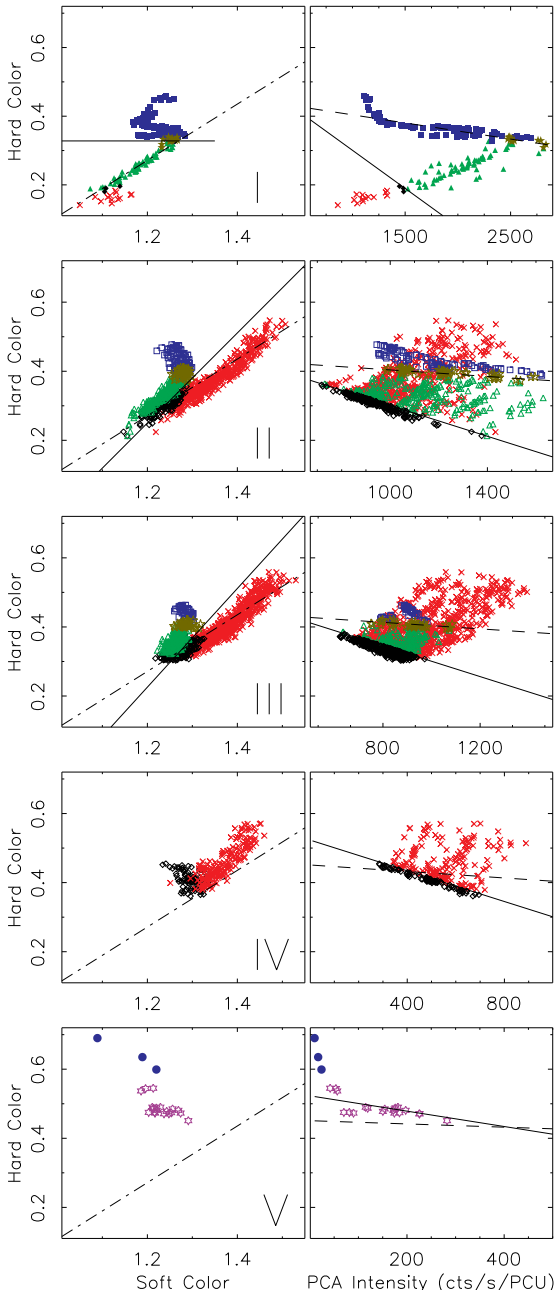

Figure 1.9 RXTE color-color and hardness-intensity diagrams for XTE J1701-462, taken from (Lin et al., 2009). From top–bottom, the source transitions between Cyg-like behaviour, Sco-like behaviour and eventually evolving into the atoll banana states.

Chapter 2

Extragalactic X-ray Binaries

2.1 Introduction

This chapter concerns the state of extragalactic X-ray binary research. Detailed studies of X-ray binaries outside of the Milky Way have only come about comparatively recently, thanks to the unprecedented spatial resolution, energy resolution and collecting area of the *Chandra* and *XMM Newton* observatories. Work carried out prior to this epoch made use of the surveys carried out by the *Einstein* and *ROSAT* observatories. During the 1980s the reasonable suspicion that X-ray binaries exist in other galaxies was confirmed (Long & van Speybroeck, 1983; Fabbiano, 1989), and non-nuclear sources brighter than a $10\mathrm{M}_{\odot}$ BH accreting at Eddington ($\gtrsim 10^{39}$ erg s^{-1}) were discovered, which became known as Ultraluminous X-ray sources (ULXs).

Before thrusting into a discussion of the sources, it is worth considering what makes the study of XBs in other galaxies attractive. While the modern observatories are excellent, practically the data will be of lower quality (fewer counts) than the Galactic data, simply because of the immense distances between galaxies. To give the reader some quantitative, albeit anecdotal understanding of this effect, observations using the RXTE PCA of Galactic XB Sco X-1, located a mere 2.8 kpc away, were able to detect $\sim (4-8)\times 10^{3}$ s^{-1}. In contrast, a similar source located at the distance of Centaurus A ($3.7-3.8$ Mpc) would have a measured intensity with Chandra of $\approx 5\times 10^{-3}$ s^{-1}, a change over six orders of magnitude! So why study extragalactic X-ray binaries?

There are three main motivations for the study of extragalactic XBs. The first reason, and that most arresting of scientific attention, is the discovery of new phenomena. ULXs (and now Hyper-luminous X-ray sources [HLXs]) are the stand out example of this; sources that are difficult to explain under the existing accretion paradigm without invoking the presence of a very massive primary. A more prosaic rationale is that the large distances of the galaxies leads to luminosity measurements having a far smaller statistical uncertainty, as the distance is more constrained (compare, for example,

Galactic sources with distance 7 ± 4 kpc with extragalactic sources at a distance of 4 Mpc, with the extent of the galaxy < 0.1 Mpc). Further, most of the sources in the Milky Way are located in the direction of the Galactic bulge, behind a large absorbing column, and many galaxies will be at an extended angle away from the Galactic plane, where absorption is a much less significant problem. Finally, the study of X-ray binaries in different galaxies allows for numbers of X-ray binaries to be assessed in terms of their environment or parent stellar population; what are the conditions that favour the production of particular flavours of XB?

2.2 Population Studies

Most research into populations of sources has focussed on use of X-ray luminosity functions (XLFs) to characterise the XB population[1]. In its simplest form, this is merely a cumulative count or census of the number of sources at a given flux level. This treatment is attractive because it allows consistent comparison between XB populations in a straightforward way and allows for the number of XBs in to be formulated in a statistical sense, the density of background sources (distant AGN) is well known (Moretti et al., 2003). As discussed above, extragalactic astrophysics often involves working with the low count regime, and in such circumstances counts would be converted to luminosity based on an assumed spectrum. This is a limitation of the technique because it can greatly over/under-estimate the true flux of a given source, and takes no account of any extra absorption experienced by the X-ray radiation. Typically the assumed spectrum is a $\Gamma = 1.5 - 1.7$ power law, typical of the BH hard state spectra and the shape expected of comptonised emission (Shapiro et al., 1976).

2.2.1 Early-type galaxies

Early-type galaxies are made up of older stellar populations with little star formation, and therefore intuitively the X-ray binary population is expected to contain mostly LMXBs. This means that one would expect an early-type galaxy to be a less convoluted population of X-ray binaries than in late-types, where different populations are seen to be associated with the bulge and disc regions (§ 2.2.2). While this makes early-type galaxies an ideal research laboratory for the budding LMXB scientist, such studies are hampered by the lack of sizeable early-types in the Local Group, and those that reside relatively nearby are morphologically unusual - such as Cen A (§2.5, also see review by Israel,

[1]Please note that this thesis exclusively discusses the XLFs of **X-ray binary populations.**

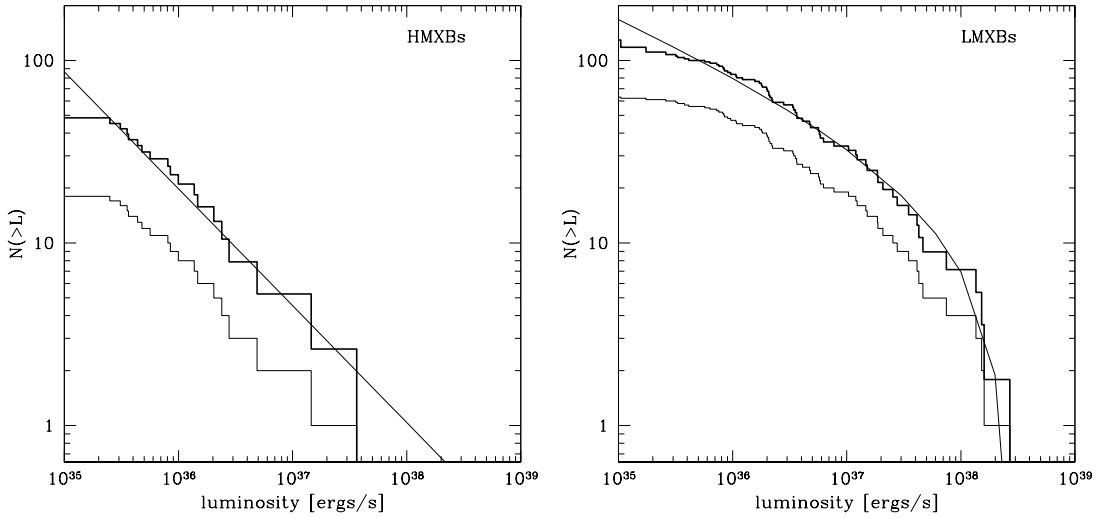

Figure 2.1 X-ray luminosity functions for Galactic HMXBs (*left*) and LMXBs (*right*). Spectra were assumed to be crab like, flux $F = 3.2 \times 10^{-10} \times (\mathrm{countrate})$, based on RXTE ASM data. Thin and thick histograms show the apparent and volume-corrected XLFs. Taken from Grimm et al. (2002).

1998).

The general form of the early-type galaxy XLF is well described by a power law of slope $\gamma = 1.8 \pm 0.2$ up to $\sim 5 \times 10^{38}$ erg s^{-1}, steepening to 2.8 ± 0.6 (Kim & Fabbiano, 2004). There has been evidence of a luminosity break at a few 10^{38} erg s^{-1} in a few early-type galaxies (such as NGC 4697, NGC 1553, NGC 4472 in Sarazin et al., 2000; Blanton et al., 2001; Kundu et al., 2002), although sometimes this break is the result of poorly correcting for source completeness (i.e. NGC 1316, Kim & Fabbiano, 2003). The most natural explanation for this break is a relationship with the Eddington luminosity of NS LMXBs. Kim & Fabbiano (2010) have suggested that the steepness of the luminosity break increases with stellar age, which is illustrated in figure 2.2, which is a schematic summarising early-type galaxy XLFs. XLFs of the 'young' and 'old' early type galaxies are shown in figure 2.2, the other major feature of which is a flattening at a few 10^{37} erg s^{-1}, which is believed to result from a paucity of GC XBs at this luminosity (Discussed further in § 2.2.2). The steepening of the XLF at high luminosity with early-type age could be part of a continual evolution between the XB populations of the old late-types to young early-types. (Zhang et al., 2012) claim that a steepening of the XLF occurs over the broad luminosity range, however, they also report a positive correlation between XLF normalisation and galaxy age that is extremely suspect, the correlation depending on galaxies reportedly older than 14 Gyr[2].

[2]Galaxies are probably younger than the age of the universe.

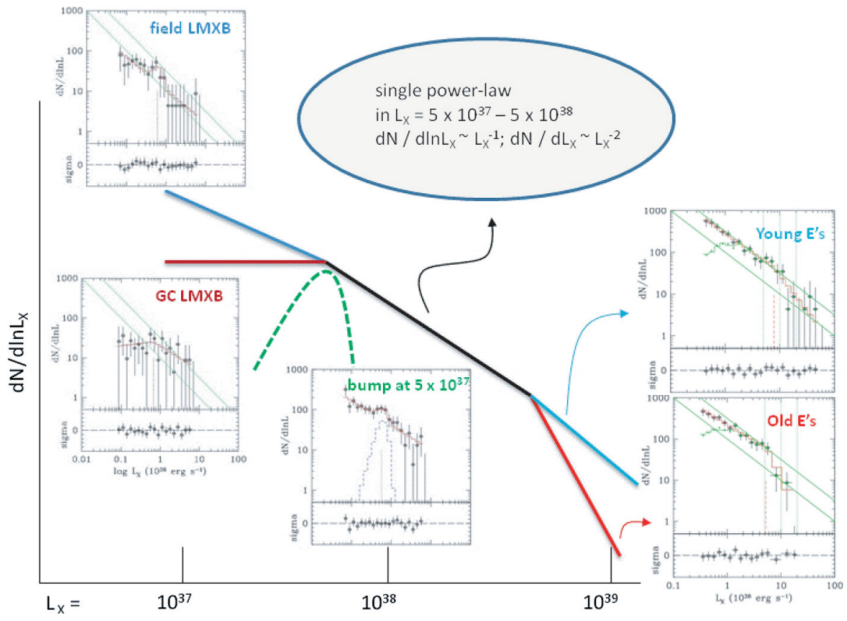

Figure 2.2 Schematic showing evolution of early-type galaxy X-ray binary XLFs with stellar age. In particular, the high-luminosity break is seen to steepen with stellar age. Taken from Kim & Fabbiano (2010).

2.2.2 Late-type galaxies

The proximity of a number of spiral galaxies, and the absence of large early-types inside the Local Group, has allowed them to be the more scrutinised morphology. For example, Andromeda (M31) is slightly larger than the Milky way, and at a distance of only ~ 780 kpc, is an excellent candidate for comparison of the XB population. It is first instructive to familiarise with the XB population of the Milky Way, as though an external observer were monitoring its X-ray binary population. Grimm et al. (2002) attempted to gauge this perspective, and went so far as to construct separate HMXB, LMXB XLFs. The XLFs can be seen in figure 2.1, and it can be seen that LMXBs experience a sharp cut-off at a few 10^{38} erg s^{-1}, which could correspond to the NS Eddington luminosity, while HMXBs follow a power law tightly down to $\sim 10^{37}$ erg s^{-1}.

The population and various sub-populations of M31 were studied by Voss & Gilfanov (2007). In particular, they used *Chandra*'s sub-arcsecond resolution to distinguish the sources in the bulge. As the stellar population in the bulge is older, there is an expectation for the XB population located there to be dominated by LMXBs, and to have a different composition to the disc population. Interestingly, Voss & Gilfanov (2007) found that the LF followed $\propto L^{-1}$ and then flattened at $\sim 2 \times 10^{37}$ erg s^{-1} down to the completeness limit (10^{36} erg s^{-1}), which they ascribed to the sub-population of the

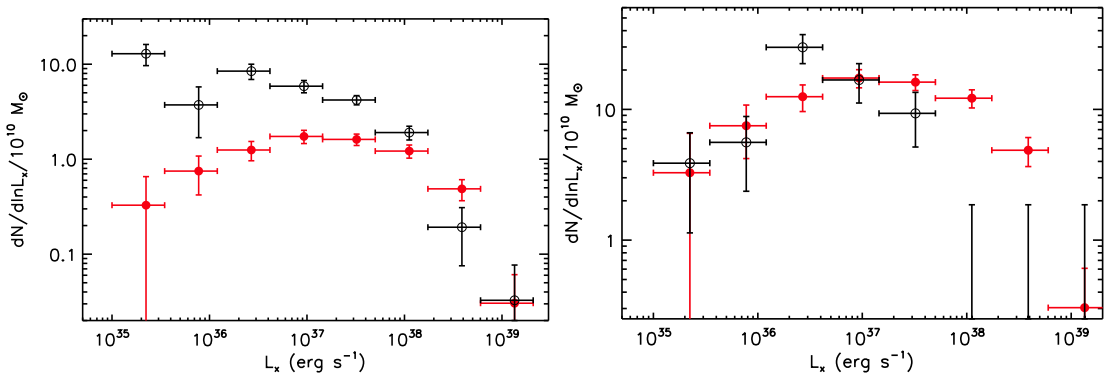

Figure 2.3 Taken from Zhang et al. (2011), showing (*left*) the XLF of GC sources (red) and the field sources (black) across a range of nearby galaxies and (*right*) the XLF of bulge sources in M 31 (black) in contrast to the global GC XLF (red), with arbitrary normalisation.

inner-bulge and GC sources[3], which they showed has a dearth of low luminosity sources. This has recently been confirmed by Zhang et al. (2011), who combined XLFs over a range of galaxies, including M31, and found a statistically significant difference between the GC sources and those in the field across the broad luminosity range of $(0.01-1)\times10^{39}$ erg s^{-1} (figure 2.3). Voss et al. (2009) suggest that this dearth of faint sources in GCs may indicate that GC LMXB companions are He rich, which possess a larger critical mass accretion rate $\dot{M}_{crit}$ above which transient limit-cycle behaviour can take place. Sources approaching the corresponding luminosity to $\dot{M}_{crit}$ become unstable, and are therefore always above or below this luminosity, leaving a gap in the XLF. However, it now appears more likely that the low-luminosity break results from a change in the disk instability criterion at low accretion rates as the disk spectrum peaks at longer wavelengths (van Haaften et al., 2012).

Grouping sources based on their spectral hardness, there is a preference for softer sources to be associated with the star-forming regions in the disc, while harder sources are associated with the bulge (Tennant et al., 2001). Prestwich et al. (2009) found that the soft sources follow a power law of $\gamma = 1.73\pm0.15$, and posit that these must be HMXBs because this is consistent with the XLF of HMXBs ($\gamma = 1.61\pm0.12$, measured by Grimm et al., 2003). However, 1.73 ± 0.15 is also consistent with the XLF of LMXBs, (Early-type galaxy XLF for $L_x \leq 10^{38}$ erg s^{-1} follow $\gamma = 1.8\pm0.2$ Kim & Fabbiano, 2004), so this inference is invalid. Nevertheless, the association with star forming regions suggests that the donors could be young OB stars, and if this is the case, and these soft sources are HMXBs, then it is currently unknown as to why they are more luminous and softer than Galactic HMXBs, and Prestwich et al. (2009) speculate that this could be the result of Roche-lobe powered

[3]i.e. sources formed by dynamical interaction

accretion from a high-mass donor, rather than the wind-fed variety typical of the Galactic sources.

There is a well-established link between the star formation rate of a galaxy and its X-ray binary population. The XLF becomes flatter with more active star formation (e.g. Fabbiano et al., 2001; Matsumoto et al., 2001; Bauer et al., 2001) as more luminous sources contribute to the XB population. Further, use of stellar population synthesis suggests that the XLF slope depends on the time lapsed since the starburst began (STARTRACK project, Belczynski et al., 2004, 2008).

2.3 Globular cluster black holes

As discussed in § 2.2.2, a sizeable number of XBs are associated with globular clusters (GCs). For most galaxies, the fraction of GCs associated with an X-ray source is $\sim 4\%$ (Fabbiano, 2006), but the fraction of XBs associated with GCs can be much larger (70% in the case of NGC 1399, Angelini et al., 2001). The large numbers of XBs found in GCs, particularly those in early-type galaxies, have led to the suggestion that most LMXBs in old stellar populations are formed in GCs, with a high fraction being ejected from their parent cluster (Sarazin et al., 2000).

This link between GCs and LMXBs established, it was noted that no BH LMXBs had been observed associated with a GC (Grindlay et al., 2001). A lack of such a Galactic source was understandable, given the transient nature of most BH XBs and that NS LMXBs naturally occur in greater numbers, but extragalactic studies have achieved superior statistics that show a genuine lack of BH LMXBs in globular clusters. Enhanced formation of binaries in GCs is to be expected as the logical result of a superior rate of dynamical interaction (Hut et al., 1992), so why should this not apply to BHs? It has long been expected that the sub-population of BHs in GCs would undergo the Spitzer mass-segregation instability (Spitzer, 1969); the BH population decoupling from the rest of the cluster and migrating into a dense inner core. Subsequently the BH cluster will evaporate (leaving, perhaps, a solitary BH), or undergo a series of mergers forming an intermediate mass BH (IMBH), the violent formation of which could lead to the BH being ejected from the cluster powered by gravitational radiation recoil (Redmount & Rees, 1989).

The high incidence of X-ray binaries in GCs strongly favours a dynamical formation scenario as opposed to binary systems evolving in situ to the point where mass transfer can take place. Two dynamical formation scenarios exist; exchange interaction, where a stellar mass BH disrupts a pre-existing binary (Heggie et al., 1996), or tidal capture, where a lone main sequence star is directly

captured by a BH's gravity (Fabian et al., 1975). Kalogera et al. (2004b) showed that BH LMXBS formed through exchange interactions would have transient duty cycles $\sim 10^{-3}$, consistent with the lack of observed Galactic GC sources, but binaries formed by tidal capture would have duty cycles ≈ 1.

Practically this amounts to a prediction by Kalogera et al. (2004b) that BH LMXBs detected in GCs will be persistent (observationally biased to be detected) and these are the sources that will have formed by tidal capture. The discovery of the first BH XB associated with a GC (in NGC 4472, Maccarone et al., 2007) is in good agreement with this prediction, a persistent source emitting at $L_x > 4 \times 10^{39}$ erg s^{-1}, while subsequent discoveries of GC transient ULXs in NGC 3379 (Brassington et al., 2010) and NGC 4649 (Roberts et al., 2012) show that this is not exclusively the case. A second GC ULX in NGC 4472, which previously had a nominal luminosity of $L_x \sim 5 \times 10^{38}$ erg s^{-1} also appears to have a duty cycle of unity (Maccarone et al., 2011).

The GC BH XB identified by Maccarone et al. (2007) experienced moderate ($\times 7$) variability on timescales of hours, ruling out explanations involving a superposition of multiple sources. This source has never been observed in quiescence, with $L_{min} \approx 10^{38}$ erg s^{-1} (Maccarone et al., 2010a), and arguably the most interesting research has been carried out by use of optical spectroscopy. Zepf et al. (2007) discovered [O III] emission that is extended over a half-light radius consistent with 3-7 pc (Peacock et al., 2012). Balmer emission associated with the region is comparatively weak (Zepf et al., 2008), suggesting against an origin in interstellar shocks, and a lack of substantial variability favours a bipolar conical outflow from a compact object (Steele et al., 2011). The amount of [O III] observed at high velocities (~ 2000 km s^{-1}) requires the compact object to accrete at or above its Eddington limit, inconsistent with the presence of an accreting IMBH. Further, the high ratio of [O III] to blamer emission is indicative of an evolved companion such as a white dwarf, which combined with a detailed study of the source variability on all timescales, Maccarone et al. (2010a) concludes that the source is a hierarchical triple-system, where the inner binary consists of a stellar mass BH and white dwarf.

There are now 6 BH XB candidates associated with GCs (see table 5 from Zhang et al., 2012). It is noted that XB production is favoured by a factor of 3.4 by red GCs (and at all luminosities, Kim et al., 2013), and there is tentative evidence that BH XB production is also favoured in redder clusters (Maccarone et al., 2011). It is not clear why more metal-rich clusters should favour XB

production, though disentangling the effect of the metallicity from the total stellar mass ($\sim$ stellar light) of the GC is difficult, as it is more intuitive that more populated GCs should facilitate more dynamical interactions.

2.3.1 Further Implications

The discovery of GC BH XBs has some important implications. For example, under the RS2 braneworld model (Randall & Sundrum, 1999) black holes should evaporate by Hawking radiation more quickly than predicted under general relativity, via extra-dimensions (See Maartens & Koyama, 2010, for review). Therefore the older the BH observed, the more the size L of extra-dimensions are constrained. Gnedin et al. (2009) claim that the existence of BHs in ancient GCs 'shrinks the braneworld', placing an upper-limit of $L \lesssim 0.003$ mm (much smaller than current constraints from table-top experiments).

Furthermore, the existence of GC BHs, i.e. proof of BH retention in GCs, affects the predicted detection rates and localisation priors used in gravitational wave astronomy. While some authors predict that the BH-BH merger rate will be comparable between GCs and the field (Morscher et al., 2013), others (Banerjee & Kroupa, 2011) go as far as to predict that core clusters of BHs, stripped of their stars, will gradually migrate towards the Galactic bulge where they will reside as 'dark clusters' that should be detected by *Advanced LIGO* (Harry & LIGO Scientific Collaboration, 2010).

As a final example, the presence of BHs appears to be the best explanation of gas depletion in some GCs (Leigh et al., 2013). Simulations showed that accretion onto stellar mass BHs more readily reproduced observed cluster properties than the effects of supernovae or stellar winds, and on timescales of a few 10^7 yr. If this is the case, then the act of depleting the cluster of gas may actually serve to accelerate the decoupling of the BH population from the rest of the cluster.

2.3.2 Cluster vs Field Sources in NGC 3379 and NGC 4278

In order to judge the relative importance of different XB formation scenarios, dynamical interactions in GCs or evolution of native binary systems, Brassington et al. (2010) and Fabbiano et al. (2010) studied sources in a GC-poor and a GC-rich galaxy (NGC 3379 & NGC 4278), respectively. This saw them develop a robust method for analysing their more high quality spectra, and measuring the hardness ratios of less luminous sources. They found some tentative evidence of differences between

the GC and field sources, with a preference for disc dominated spectra in the field and power law dominated spectra in the GCs for $L_x < 6 \times 10^{38}$ erg s^{-1}.

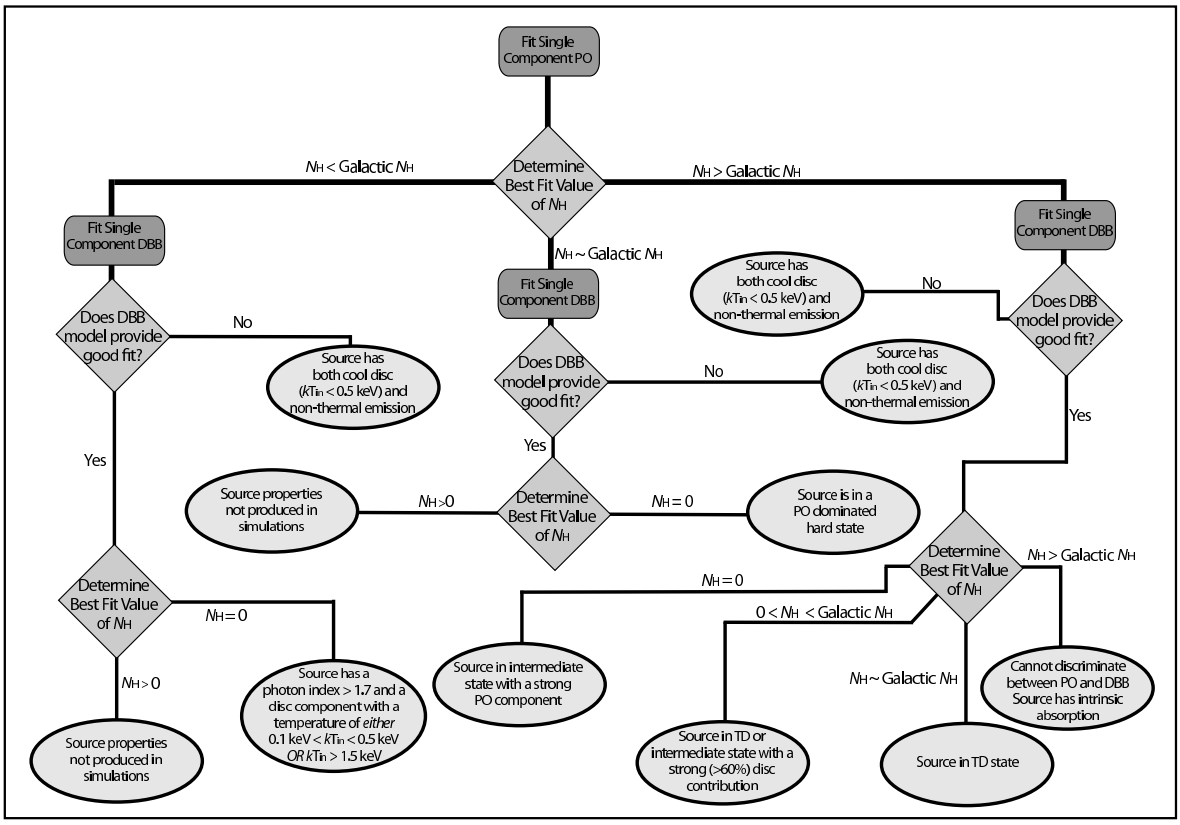

Figure 2.4 Taken from Brassington et al. (2010), this scheme explains the spectral fitting decision-tree, based on the behaviour of the absorption column parameter N_H, which is recovered from fitting simple spectral models. PO denotes an absorbed power law ($phabs \times powerlaw$) while DBB denotes an absorbed disc blackbody model ($phabs \times diskbb$).

The work of Brassington et al. (2010) and Fabbiano et al. (2010) is crucial in the context of this thesis, particularly in terms of their analysis. They were able to perform detailed spectral fitting on the brightest XBs (7 & 8 sources), where they had what might be called 'intermediate' quality data with net counts $\approx 10^2 - 5 \times 10^3$ counts. In this regime, fitting two-component models (as we would expect to find for NS and BH XBs) is difficult, and has a poor record of accurately recovering the spectral parameters. To recover the true properties of the sources, they simulated spectra from the intermediate data regime, using models based around the canonical BH states (§1.2.1, Remillard & McClintock, 2006). Practically, this meant using a combination of disk blackbody and power law models, with varying key parameters (T_{in},Γ) and contribution to the total spectrum, with the absorption used in the simulations was fixed at the Galactic value (Dickey & Lockman, 1990). They then performed spectral fitting, using single models (disk blackbody or power law) and studied their

ability to recover the correct parameter and, more importantly, the behaviour of the parameters when the alternative model dominated the continuum. This gives some measure on what would happen if black hole hard state spectra were fit with an absorbed thermal model, or vice versus. In terms of assessing the dominance of a given component the most important diagnostic parameter proved to be the absorption column N_H. They found that they could identify thermal dominant spectra using this method when disc emission contributed $> 60\%$ of the total flux to the spectrum, and that the inner disc temperature was recoverable to better than ± 0.5 keV at this contribution (which decreased rapidly with larger dominance). The sensitivity of the recovered absorption column to the true spectral state is intuitively explained; a disc blackbody spectrum contains curvature not present in a power law spectrum, and so to allow for this curvature an absorbed power law model fitted to a spectrum that is actually disc blackbody dominated will recover a much larger absorption than is actually present. The full results of spectral fitting these simulated spectra were summarised in a decision tree, figure 2.4, that can be used for the classification of spectra. Note that this decision tree also tests the crucial assumption of the diagnostic, that X-rays from these sources experience no local absorption beyond the Galactic value. The decision tree of Brassington et al. (2010) plays a vital role in diagnosing spectral states of the XBs in Cen A (Chapters 4 & 5).

The bright sources from NGC 3379 and NGC 4472 were of the intermediate count regime ($\sim 200 - 3000$ total counts), corresponding to a limiting luminosity of $L_x \sim 1.8 \times 10^{38}$ erg s^{-1} for spectral fitting, still above the theoretical Eddington luminosity for an accreting NS. The recovered spectral states, luminosities and key parameters are presented in figure 2.5. The thermal state results are clearly consistent with all sources possessing black holes, as indicated by the lines of constant mass (which assume inclination of 60°,see § 1.2.1 and Gierliński & Done, 2004). The power law dominated states are largely consistent with the properties of Galactic LMXBs.

2.4 Ultraluminous X-ray Sources

The mass distribution of galactic black holes in XBs is sharply peaked at $\sim 8 M_\odot$ (Özel et al., 2010; Kreidberg et al., 2012). This being the case, the maximum luminosity we should expect for Galactic sources should be $\sim 10^{39}$ erg s^{-1}, at which point their isotropic luminosity is Eddington-limited. The discovery of bright, non-nuclear X-ray sources in other galaxies with apparent luminosities far in excess of 10^{39} erg s^{-1} (Long & van Speybroeck, 1983; Fabbiano, 1989) heralded the addition of

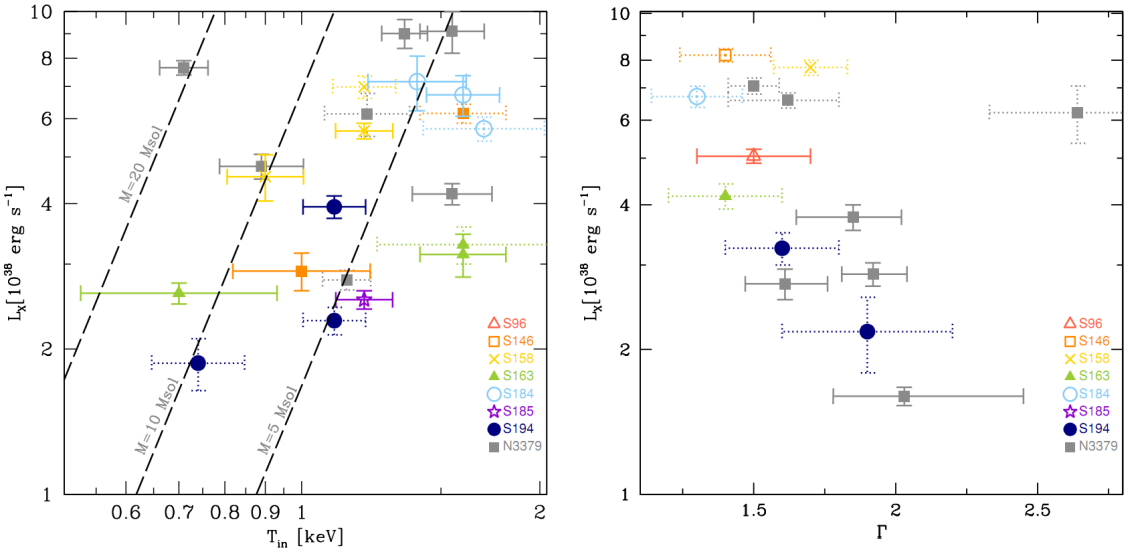

Figure 2.5 Taken from Fabbiano et al. (2010), showing thermal (*left*) and non-thermal (*right*) dominated spectral states from NGC 4278, with NGC 3379 points overlaid in grey. Lines of constant mass, based on $L_x \propto T^4$, based on the work of Gierliński & Done (2004).

a new classification, ultraluminous X-ray source (ULX), to the X-ray point source menagerie. An exciting explanation is that these systems must contain intermediate mass black holes, compact objects in the range $10^2 - 10^4 \mathrm{M}_\odot$, that fill in the gap between the stellar mass and super massive BHs found in the centre of most galaxies (Komossa & Schulz, 1998). Alternatively, ULXs could be stellar mass BH systems with anisotropic emission, viewed from some preferential geometry , or some new accretion scenario (e.g. Okada et al., 1998; King et al., 2001).

Typically ULXs are persistent systems and preferentially found in late-type and starburst galaxies (e.g. Colbert et al., 2004). In Chapter 6, the latest research into two transient ULXs in Cen A is presented, and §6.1 gives a detailed summary of the behaviour of these sources. Studying ULXs at lower luminosities allows for comparison with the well studied behaviour of Galactic BH XBs. Chapter 6 is published as Burke et al. (2013), where only a summary of source properties suffices and so included below is a more in depth discussion of specific transient ULXs (§2.4.2).

2.4.1 An Ultraluminous state?

Some excellent candidate IMBHs exist, most notably HLX-1 in ESO243-49 (Farrell et al., 2009), the first so-called *hyperluminous X-ray source* (HLX), with an apparent luminosity of 1.1×10^{42} erg s^{-1}. However, there is an increasing trend towards models based around stellar mass ($< 100\mathrm{M}_\odot$) BHs

with modified accretion flows as explanation for the majority of ULX systems (For recent review, Feng & Soria, 2011).

ULX spectra show a curvature at low energies, and when fit solely with an absorbed power law, this curvature appears as a soft excess in the fit residuals, which implies the presence of an accretion disc. This excess was successfully fitted using disc blackbody models characterised by a low inner-disc temperature $kT_{in} \sim 0.1 - 0.4$ keV (e.g. Miller et al., 2003, 2004; Feng & Kaaret, 2005), which could indicate the presence of a compact object more massive than a stellar mass BH, and is seen by some as key evidence of IMBHs. However, these excesses can manifest as deficits, depending on the power law (Gonçalves & Soria, 2006), so such an interpretation is not secure. Using high quality spectra, Gladstone et al. (2009) showed that the soft excess is ubiquitous among the 12 nearest ULXs, and also proved the existence of a high energy break in the spectra at energies > 3 keV (but within the *XMM Newton* bandpass). This high energy feature had only been detected in a few sources until this point (e.g. Foschini et al., 2004), and is unfamiliar in the context of Galactic BH XBs. This led to the conclusion that there is an ultraluminous (UL) state; Galactic BH XBs are observed up to their Eddington luminosities only, thus this new state must occur in the regime $> L_{Edd}$, consistent with a stellar mass BH for $L_x > 10^{39}$ erg s^{-1}. Gladstone et al. (2009) tried to interpret this state in terms of slim disc accretion (§1.1.3, Abramowicz et al., 1988) where advection of the photons reduces the luminosity of the inner accretion disc, but found this could not reproduce both the low and high energy features. Instead they used disc plus comptonization (e.g. $diskbb + compTT$) models to simultaneously describe both features, finding evidence of a cool, optically-thick corona. By modelling both components in this way, they could recover the intrinsic kT_{in} of the disc, and found values consistent with those measured in stellar mass BH XBs, and only sometimes slightly cooler. This will only become convincing from further observations that show that follow $L_x \propto T_{in}^4$, as this indicates that the accretion disc actually extends to the ISCO. It is suggested (Roberts, 2007; Gladstone et al., 2009) that the occasionally cooler T_{in} may be result of extreme outflow at larger radii. A softening of the spectra as the luminosity decreases indicates an increasing domination by the disc-like component. The excess cool emission also points to the presence of a wind component that thickens the corona into a photosphere around the inner regions of the disc as the Eddington limit is reached and then exceeded (Poutanen et al., 2007; Roberts et al., 2010).

2.4.2 Specific transient ULXs

There are three ULXs in starburst galaxy M82, two of which are transient. The second brightest ULX, X42.3+59, shows long term flux variability by a factor of > 1000, remaining undetected for many observations and with an inferred $L_x < 10^{37}$ erg s^{-1} to 1.5×10^{40} erg s^{-1} (Feng & Kaaret, 2007), with outbursts lasting for ~ 200 days. Source confusion between the two ULXs in XMM observations and pile-up in Chandra ACIS observations (when the source was ultraluminous) has made studying the spectra of X42.3+59 difficult. The discovery of mHz quasi-periodic oscillations (QPOs) when the source is at its most luminous is reminiscent of the QPOs observed from the Galactic BH LMXB XTE J1550-564, and suggests a BH mass of $\sim 2 \times 10^4$ M$_\odot$ assuming companionless accretion from the interstellar medium. It has been suggested that the third ULX, X37.8+54 undergoes a transition from a hard to soft state at $\sim 1.5 \times 10^{39}$ erg s^{-1} before peaking at $L_x \sim 6 \times 10^{39}$ erg s^{-1}, and when modelled as a disk blackbody, the derived properties of the accretion disk indicate a BH of ~ 36 M$_\odot$ (Jin et al., 2010).

In another starburst galaxy, M83, a recently discovered ULX outburst from $L_x < 10^{36}$ erg s^{-1} to $\sim 5 \times 10^{39}$ erg s^{-1} (Soria et al., 2012), and has remained bright for at least a year. The spectrum during this time was power law dominated, but with a strong thermal component also present. Optical photometry of observations taken before and during outburst, showed a previously undetected blue counterpart that is at least an order-of-magnitude brighter than observed prior to the outburst onset. This is an important result because the presence of a blue counterpart from simultaneous optical observations has been used to argue for young OB star companions in ULX systems, and the lack of optical counterpart during quiescence suggests the optical light is the result of reprocessed emission in the disc.

A recurrent ULX has been studied since the ROSAT era in starburst galaxy NGC 253 (Bauer & Pietsch, 2005), observed with outburst luminosities of 1.4×10^{39} erg s^{-1} and 0.5×10^{39} erg s^{-1} three years later, with a lowest upper limit of 7×10^{36} erg s^{-1}. However, Bauer & Pietsch (2005) assumed a distance of 2.58 Mpc, and subsequent research puts the distance between 3.0 and 4.11 Mpc (e.g. Tully et al., 2008; Crook et al., 2007), so the source may be more luminous than first thought. The spectrum of this ULX was best fit by an absorbed bremsstrahlung model with $kT_{in} \sim 2.24$ keV and no counterpart was detected at other wavelengths.

In the star-forming spiral galaxy M101, a controversial source emits with almost all X-ray flux

beneath 2 keV at peak luminosity. M101 was heavily observed by *Chandra* over the course of 2004, during which time the source underwent two month-long oubursts. Initial studies (Kong et al., 2004; Kong & Di Stefano, 2005) suggested that these outbursts were phenomenally bright, with peak $L_x \sim 10^{40}$ erg s^{-1}, while for the majority of the year $L_x \approx 10^{37}$ erg s^{-1}, with spectral hardness anti-correlated with luminosity. This is reminiscent of the high and low (aka thermal dominant and hard) states of Galactic BH XBs and therefore suggests an accreting IMBH ($M \sim 6000$ M$_\odot$). However, these peak L_x were revised in a subsequent analysis by Mukai et al. (2005) to $(1.0 - 1.5) \times 10^{39}$ erg s^{-1}, indicating a stellar mass BH with $M \sim 30 - 40$ M$_\odot$. Kuntz et al. (2005) suggested a B supergiant counterpart to this source, however it has subsequently been shown that the donor is most-likely a wolf-rayet star based on the spectral energy distributions (SEDs) from many years of HST data, with an estimated orbital period of $1.5 - 4.5$ days (Liu, 2009).

There have been two recent discoveries of transient ULXs in M31 that have subsequently been observed in the $10^{38} - 10^{39}$ erg s^{-1} regime. The first ULX, CXOM31 J004253.1+411422 (Kaur et al., 2012), has been observed as low as 5×10^{38} erg s^{-1}, down from a peak $L_x \sim 3.8 \times 10^{39}$ erg s^{-1} (or 6×10^{38} erg s^{-1}, down from a peak $L_x \sim 5 \times 10^{39}$ erg s^{-1} in Middleton et al., 2012) with a disk-dominated spectrum at sub-ULX luminosities. The source spectrum was described well by a multi-temperature disk blackbody ($kT_{in} \sim 1$ keV) that rapidly decayed with luminosity, and a steep power law ($\Gamma \sim 2.6$), suggesting that the source is powered by a $\sim 10 M_\odot$ BH in the steep power law state. The decline in luminosity of this source was consistent with an exponential decay characterised by an e-fold time of $32 - 40$ days. As was the case with the ULX in M83, a blue companion is reported. The second ULX in M31 is similar, but only grazes 10^{39} erg s^{-1}, and so its status as a 'bona fide' ULX is questionable. The spectrum is disk dominated down to $\sim 10^{38}$ erg s^{-1} (Esposito et al., 2013), the inner disk temperature falling from $kT_{in} \sim 0.9 - 0.4$ keV.

2.5 Centaurus A

For completeness, a short introduction to Centaurus A is in order (For an overview see Israel, 1998). Centaurus A (Cen A) is the name given to the radio source, the largest such object towards the constellation Centaurus. The optical galaxy, NGC 5128 (aka Caldwell 77), has been studied for far longer, but in this thesis the term Cen A is used to refer to the X-ray galaxy. It is the fifth brightest galaxy in the sky, and visible only from the southern hemisphere.

NGC 5128 is the nearest optically luminous early-type galaxy, at a distance of 3.7-3.8 Mpc (Ferrarese et al., 2007; Harris et al., 2012), with $M_B = -21.1$. The main early-type galaxy is experiencing an ongoing merger with a small late-type (Graham, 1979) but evidence from Spitzer observations suggest that these galaxies remain poorly mixed (Quillen et al., 2006). Many active star forming regions exist in the vicinity of vast dust lanes that obscure most of the central regions of the galaxy at many wavelengths. These features can be seen in figure 2.6, the dust lanes as clear, dark streaks running from bottom-left to top-right of the centre of the image, with patches of pink indicating areas of active star formation.

Recently it has been shown that at least 70% of stars in NGC 5128 formed 12 ± 1 Gyr ago, and that a smaller population of more metal rich stars probably formed in the last $2 - 4$ Gyr (Rejkuba et al., 2011). This study is more reliable than most attempts to measure the age of stellar populations in other early-types, the relative proximity of Cen A allowing simulated color-magnitude diagrams to be compared with deep ACS/HST photometry. Therefore we expect the population of XBs in Cen A to be dominated by LMXBs that possess old main sequence companions of $M < 1\mathrm{M}_{\odot}$ with the potential for a small component from XBs with more massive companions.

2.5.1 The X-ray binary population

The early *Chandra* data consists of two ~ 36 ks ACIS-I observations, separated by 5 months between 1999 and 2000, and two ~ 50 ks ACIS-S observations taken a year apart over 2002 and 2003 (see table 4.1).

Six 100 ks *Chandra* observations were taken as part of the Cen A Very Large Project (VLP) spanning the course of 2 months (Jordán et al., 2007). These observations have led to may of the exciting X-ray features of the galaxy to be discussed in detail, such as the jets, (Hardcastle et al., 2007; Worrall et al., 2008; Goodger et al., 2010), radio-lobe shock (Croston et al., 2009) and the extended gaseous emission (Kraft et al., 2008). A substantial portion of analysis presented in this thesis (particularly Chapters 4 & 5) involved the analysis of XBs found in these data.

From the start of 2009, there has been regular monitoring of Cen A with Chandra ACIS-I, with ~ 5 ks observations taken roughly every 6 months. In addition to these observations there is a ~ 50 ks ACIS-S observation from 2009. These observations are the focus of Chapter 6, and are also utilised in Chapter 4.

The first study of the point source population identified 246 sources above $\sim 3 \times 10^{36}$ erg s^{-1}, and was complete for $L_x > 1.3 \times 10^{37}$ erg s^{-1}, and found that the distribution of sources was centrally peaked (Kraft et al., 2001). The VLP data has expanded the known population to over 400 sources, and is complete to 10^{36} erg s^{-1}. The population extends out to $\sim 9'$ from the Cen A nucleus, which is $\approx D_{25}$ but a statistical treatment of the population has shown that the contribution to the point source population from XBs is small beyond the half-light radius ($\sim 5'$ Voss et al., 2009), compared to that of background sources.

The most studied aspect of the point sources to date remains the GC-LMXB relationship. There is a relative lack of GC LMXBs in Cen A compared to other early types, as a fraction of the total population, Kraft et al. (2001) only found 9 associations (for comparison, see §2.3). Voss & Gilfanov (2006) identified 37 GC-LMXB associations out of 266 XB candidates down to a completeness limit of 2×10^{36} erg s^{-1}, and measured the location of the low luminosity break in the XLF to be around $(5 \pm 1) \times 10^{37}$ erg s^{-1}. As discussed in §2.2.2), a lack of faint GC XBs is a ubiquitous feature observed across many galaxies (Kim & Fabbiano, 2010; Zhang et al., 2011). Prior to the Cen A VLP, Woodley et al. (2008) found 67 GC-LMXBs, with redder clusters about three times more likely to host an XB than their bluer counterparts, and also that the number of XBs per unit GC mass was roughly constant. After the VLP data were obtained, Jordán et al. (2007) used the first four observations to identify 45/440 X-ray point sources as coincident with GCs, and found evidence to suggest that the density and size (extent) of the GC are the most important parameters in terms of LMXB production – the implication being that denser systems lead to a higher rate of dynamical interaction. The most substantive study, using all six VLP observations was reported by Voss et al. (2009) and was discussed in §2.3; they confirmed the difference between the XLFs of the GC and field sources, reminiscent of the bulge population in M31.

Two ULXs are known in Cen A, both of which are transients. The first ULX (1RXH J132519.8-430312) was discovered by *ROSAT* (Steinle et al., 2000) and re-detected near the start of the *Chandra* era (Kraft et al., 2001; Ghosh et al., 2006). The *Chandra* detections showed a soft spectrum, well described by a cool multi-temperature disk blackbody or an absorbed steep power law, and from this we infer $L_x \gtrsim 10^{39}$ erg s^{-1}. The luminosity may have been as high as 5×10^{39} erg s^{-1} in the *ROSAT* HRI observations. Claims of identification of the optical counterpart by Ghosh et al. (2006) were later refuted by Sivakoff et al. (2008) using *HST* observations.

A second ULX was discovered in the VLP observations (Sivakoff et al., 2008). These spectra were intermediate quality, and detailed spectral fitting could be carried out. The source appeared to be in the steep power law state, which softened during the course of the outburst as would be expected for a source entering the thermal dominant state. This suggested that the source was similar to Galactic BH LMXBs. No optical counterpart was detected, and a bright OB companion could be ruled out. The integrated optical stellar emission of the region is consistent with K giants, suggesting a low mass companion.

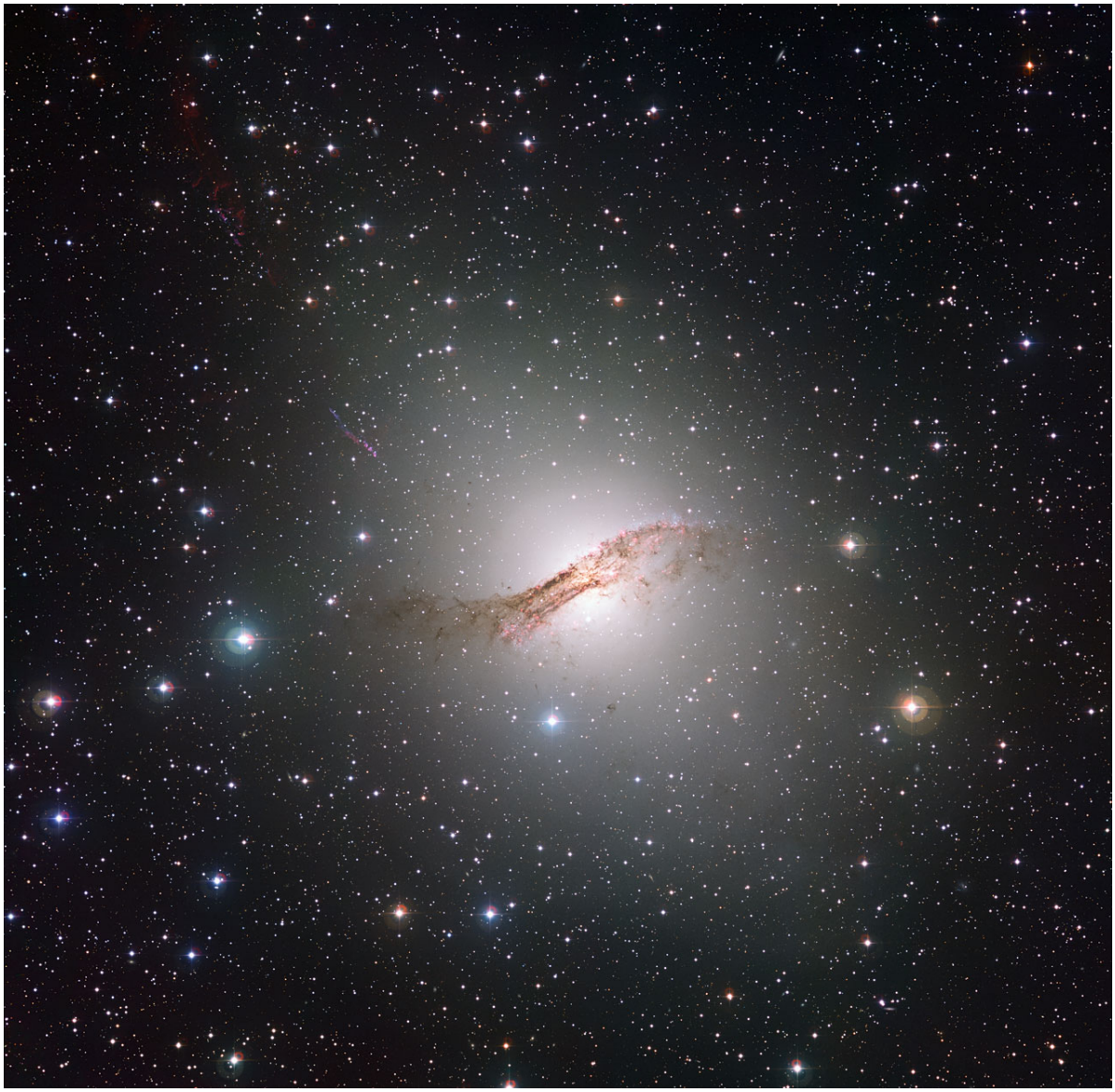

Figure 2.6 European southern observatory (ESO) press release image of NGC 5128 (Cen A), taken with the Wide Field Imager of the MPG/ESO 2.2-metre telescope, these data presented in de Jong et al. (2008).

Chapter 3

Chandra and X-ray Analysis

3.1 Chandra

The *Chandra* X-ray observatory is NASA's flagship X-ray mission, with unprecedented spatial and spectral resolution. Launched in 1999 from the space shuttle Columbia, and with a focal length of ~ 10m, *Chandra* was the largest payload carried into space by the shuttle. A complete mission overview can be found in Weisskopf et al. (2000). The interested reader should also consult the *Chandra* proposers' observatory guide (POG)[1].

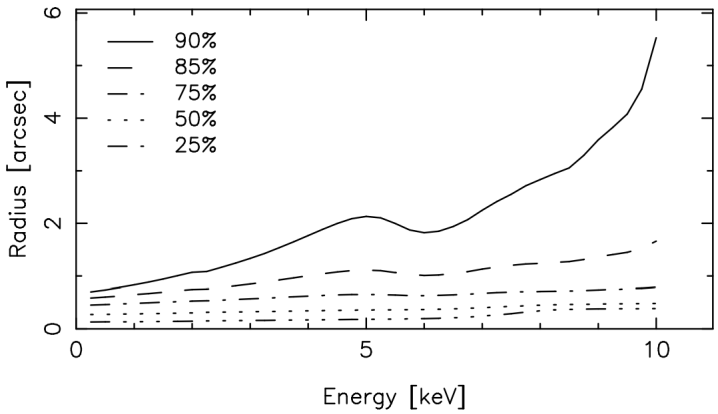

Figure 3.1 Taken from the *Chandra* POG, showing variation of on-axis radial extent for different PSF quantiles with energy, produced using ground-based calibration data.

3.1.1 High-Resolution Mirror Assembly

Chandra contains four concentric thin-walled grazing incidence Wolter type-I mirrors (Wolter 1952), which together constitute the high-resolution mirror assembly (HMRA). Each pair of mirrors is comprised of a paraboloid and a hyperboloid mirror. The large focal length allowed for the greatest

[1] http://cxc.harvard.edu/proposer/POG/html/

spatial resolution of any X-ray telescope to date, as both *Einstein* and *ROSAT* had on-axis point spread functions (PSFs) of $\sim 4''$. For Wolter type-I mirrors, the PSF is a function of energy of the incident photons, with more energetic photons having a wider spatial distribution at the detector. To assess this, a useful quantity is the enclosed energy fraction EEF, which is simply the two-dimensional integral of the PSF for a given chip position. Figure 3.1 shows the on-axis enclosed energy fraction as a function of radius. The PSF size is also a function of position in the focal plane (figure 3.2).

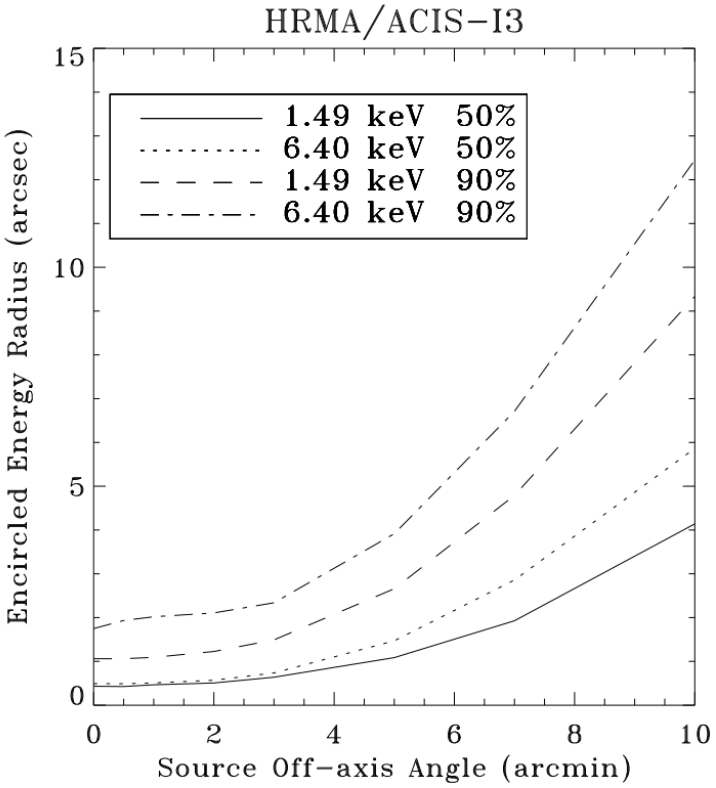

Figure 3.2 Taken from the *Chandra* POG, showing approximate variation of PSF size with off-axis angle for 50% and 90% EEFs with some example energies.

3.1.2 ACIS

There are two primary instruments at the focal point of *Chandra*, the Advanced CCD Imaging Spectrometer (ACIS) and the High Resolution Camera (HRC). This thesis only uses ACIS observations, on account of the HRC having poor spectral resolution.

ACIS consists of 9 CCD chips arranged in two arrays, ACIS-I and ACIS-S, as in figure 3.3. Telemetry issues require that only six of the chips can be used at once, and it is the observers

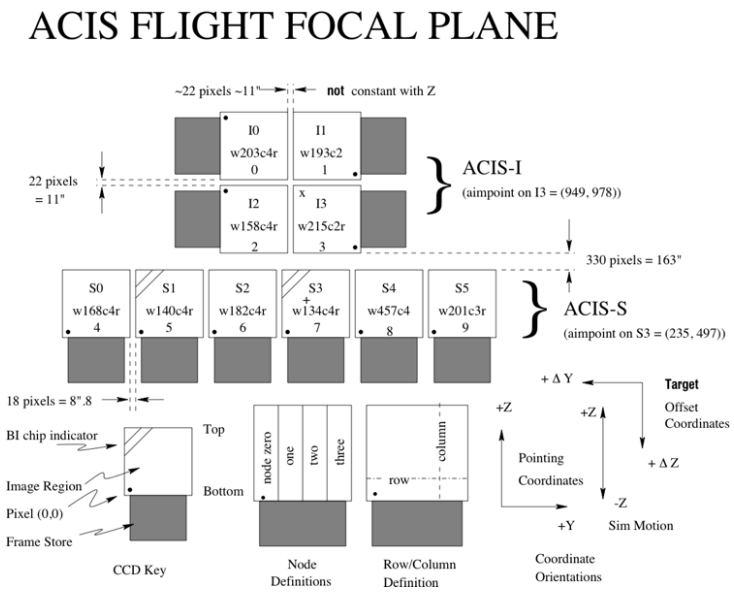

Figure 3.3 Taken from the *Chandra* POG, schematic showing the ACIS chips in the focal plane of the HRMA. ACIS-I and ACIS-S chips are denoted by prefix I and S, respectively. S1 and S3 are the two back-illuminated chips.

prerogative as to which combination of chips suits the science goal of their project. Each chip consists of a silicon CCD, with pixel demarcations defined by a gate structure of electrodes on one side. These gates allow charge to be transferred along the grid to the chip-readout. Each individual pixel has a dispersion corresponding to $0\farcs492$. Two of the chips have this gate structure on the other side of the silicon to the incident light, and these are described as *back-illuminated* chips, while the other chips are *front-illuminated*. In practice it is the case that the back-illuminated chips have better sensitivity at lower energies, but poorer spectral resolution. The ACIS in imaging mode has a moderate spectral resolution, and can distinguish a difference in energy $\Delta E \sim 95$ eV at 1.49 keV, going to 150 eV at 5.90 keV. For higher spectral resolution, ACIS can be used in conjunction with the high energy transmission grating (HETG) or low energy transmission grating (LETG).

Figure 3.4 shows the on-axis quantum efficiency of the ACIS and the resulting effective area of the detector, i.e. the ability to detect a photon of a given energy and chip position based on the effective area of the optics and the quantum efficiency of the detector. Charge-transfer inefficiencies lead to the quantum efficiency varying by as much as 15% at maximum row distance from the read out.

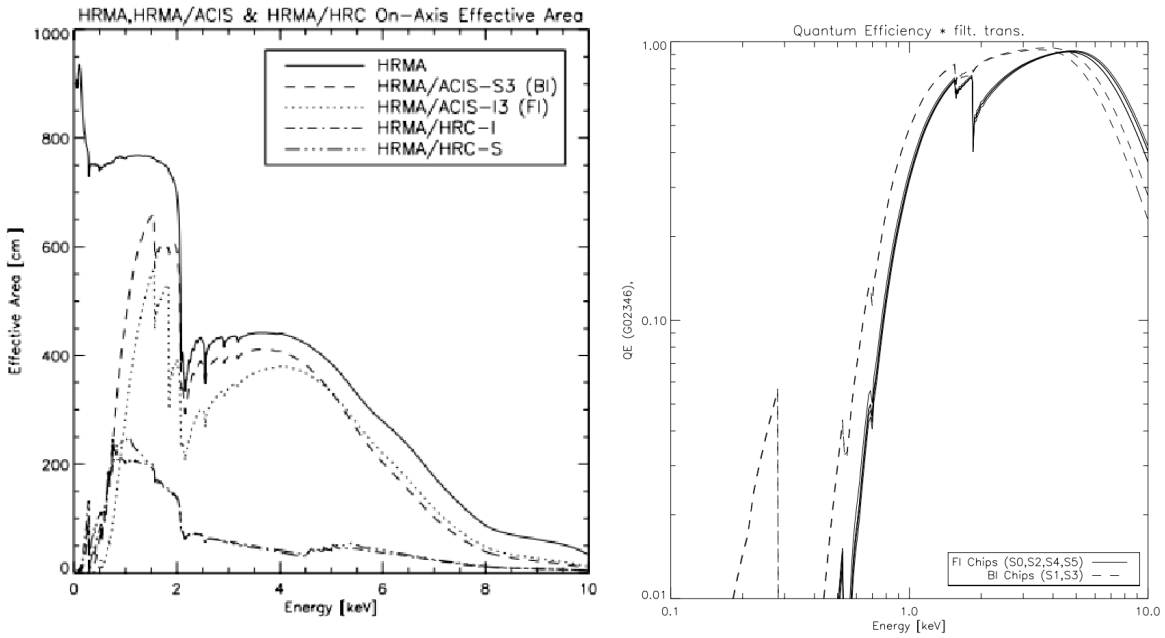

Figure 3.4 Taken from the *Chandra* POG. *Left*, the effective area of the HRMA (solid line). Also shown are the combined effective areas of the HRMA and quantum efficiancy (*right*) of the ACIS and HRC.

3.2 X-ray Analysis

This thesis makes use of standard X-ray analysis software *HEAsoft*[2], particularly the X-ray spectral fitting package *XSPEC* (Arnaud, 1996). *Chandra* specific software, the Chandra Interactive Analysis of Observations (CIAO, Fruscione et al., 2006), was used to reprocess and align observations, perform simple photometry and extract spectra, background spectra and auxiliary files suitable for spectral fitting with *XSPEC*. Other software used include Bayesian estimation of hardness ratios (BEHRs Park et al., 2006) and quantile analysis routines[3] (Hong et al., 2004, 2009). Throughout the thesis the statistical language R[4] is used for plotting, statistical tests and ad-hoc analyses.

3.2.1 Aperture Size

The extraction of spectra in Chapters 4 & 5 uses circular apertures defined at the location of each detected point source. The enclosed energy fraction decreases for a given aperture size with increasing off-axis position, and so the radius r_a of a given aperture used to extract spectra or perform photometry varies with chip position. This section shall briefly outline the steps taken to ensure that

[2] https://heasarc.gsfc.nasa.gov/
[3] http://hea-www.cfa.harvard.edu/ChaMPlane/quantile/pre-release/readme
[4] http://www.r-project.org/

the choice of radius for a given aperture was robust.

For the extraction of point sources, the *ciao* software will attempt to correct for the PSF apertures that are only partially covering the PSF at a given position by adding extra information into the response (arf) file generated. For each channel, the fraction of the PSF (from 0-1) is added to the file. It is necessary for us to assess the point at which this starts to introduce unwanted systematic effects to spectral fitting, as it is often necessary to shrink source regions when source confusion is encountered (i.e. the PSFs are sufficiently large enough to allow meaningful analysis, while small enough that they are not being significantly contaminated by other nearby sources). In our extraction, we define to characteristic radii, r_{p2} and r_{p7} which correspond to the approximate 90% PSF size at a given chip position for 2 keV and 7 keV, respectively. For an ideal source, we choose an extraction radius of r_{p7}, which will yield $> 90\%$ of events for energies < 7 keV, which is sensible with respect to the combined ACIS effective area, which is small above this energy. Shrinking the apertures to r_{p2} in cases of source confusion is logical, as the response peaks between $1-2$ keV. The remaining issue was to ascertain at what level the *ciao* correction starts to affect spectral fitting results. To solve this, an off-axis, isolated, fairly bright source was chosen. Circular regions of different radii were used to extract the source spectra many times, and these spectra were fit with a simple absorbed power law in *XSPEC*. An example of the flux for each spectral fitting versus extraction aperture radius is presented in figure 3.5. While the flux found from using r_{p2} and r_{p7} are consistent, the flux recovered at small r_a shows significant variation, and will bias the measured flux towards higher values in this example. Based on figure 3.5, it would be unwise to shrink extraction radii below $\approx 0.5 r_{p2}$ in the instances of extreme source confusion.

3.2.2 Pile up

Pile up is the apparent detection of a high energy photon that is really the detection of simultaneous lower-energy events; a ubiquitous problem in X-ray astronomy. Pile up is undesireable from any analytical perspective, be it spectral or temporal. Tools are available in *ciao* to assess the degree of pile up for a given source, and models have been developed to parameterise the effect of pile up to allow for accurate spectral fitting (Davis, 2001).

For the *Chandra* ACIS detectors, pile up results from multiple events in the same frame time (3.2s). To assess the amount of pile up in a given dataset, it is recommended to use the *ciao* tool

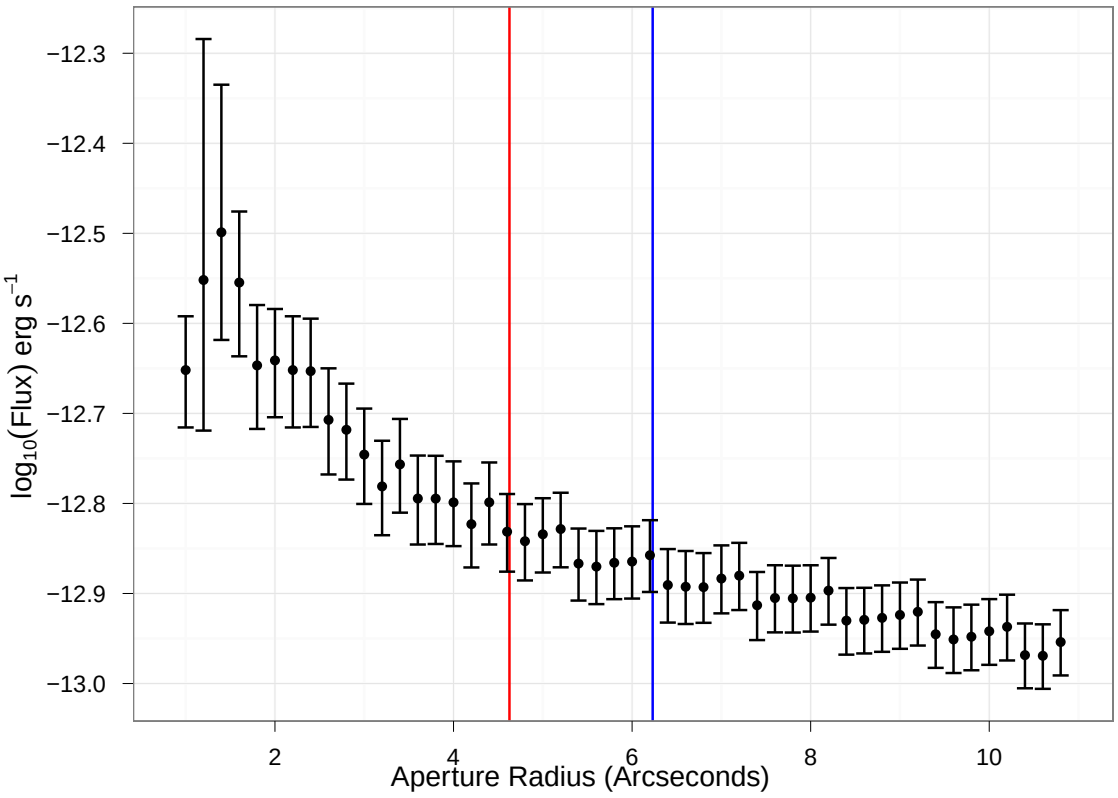

Figure 3.5 Recovered flux from spectral fitting (90% confidence) as a function of aperture region radius applied to a far ($> 3'$) off-axis, bright, isolated source. Vertical lines correspond to r_{p2} (red) and r_{p7} (blue).

pileup_map[5], which outputs an image that is the number of counts per ACIS frame, and a user can convert this image into a pile up fraction [6].

3.2.3 Spectral Fitting - Statistics, damned statistics and lies

A recent change to XSPEC has separated the use of the fitting and test statistics. This is as much a philosophical change as a practical one, and it is in the spirit of this change that this section is written. In the next sub-section, the discussion focusses on using the χ^2, C and W statistics as fitting tools – the act of minimising these statistics through exploration of a parameter space to find a 'best fit'. The subsequent sub-section discusses test statistics, which are tools for gauging how well a model describes the data.

[5] http://cxc.harvard.edu/ciao/ahelp/pileup_map.html
[6] http://cxc.harvard.edu/csc/memos/files/Davis_pileup.pdf

Fitting

Fitting in XSPEC works by finding the least squares value (maximum likelihood) using the Levenberg-Marquardt algorithm (Levenberg, 1944; Marquardt, 1963). This is designed to find the minimum of statistics of the form S, where

$$S = \sum_{i=1}^{N} [O_i - M_i(\theta_\phi)]^2 \tag{3.1}$$

for which N detector channels have an expected number of counts $M_i(\theta_\phi)$ for a given channel and O_i counts were actually observed. Here, θ_ϕ represent the family of parameters peculiar to the model. XSPEC varies θ_ϕ in such a way as to minimise S, such that the first derivative of S with respect to the parameter space of $M_i(\theta_\phi)$ approaches zero. The Levenberg-Marquardt algorithm first calculates the second derivative and the steepness of the second derivative, which is to say how quickly the statistic increases as a given parameter combination moves away from the minimum value of S. Intuitively, one can see that the more sensitive a fit is to a given parameter, the larger the second derivative, and therefore the larger the precision with which θ_ϕ can be constrained. To first-order, the inverse of the second derivative is an estimate of the 1σ uncertainty on the best-fit parameters. In practice the parameters are often inter-dependent, and the inverse of the second derivative would only be meaningful as an uncertainty measure if this were not the case.

In actuality, with XSPEC it is usual to use the χ^2 statistic for spectral fitting,

$$\chi^2 = \sum_{i=1}^{N} \frac{[O_i - M_i(\theta_\phi)]^2}{\sigma^2}, \tag{3.2}$$

which is a statistic in the S form, but weighted by the uncertainties σ_i on the measurement in a given channel, and dependent on each measurement being roughly Gaussian. To this end, it is common to group channels together so that there are enough counts for this to be valid, as in the low count limit the measurements will be poissonian. Equation 3.2 is a prefered variant of the Pearson χ^2_P, which had a denominator of M_i rather than σ_i^2 (Pearson, 1900).

When the channels are poisson-limited, then the Cash statistic C (Cash, 1979) should be used, which is the negative double log-likelihood of the data

$$C = -2\ln\mathcal{L} = \sum_{i}^{N}(O_i \ln M_i - M_i - \ln O_i!)$$
$$= 2\ln\mathcal{L} = \sum_{i}^{N}(M_i - O_i \ln M_i). \tag{3.3}$$

This is particularly useful for poor quality data where there background contribution is negligible. However, there are always background contributions to a particular spectrum, either as a result of distant AGN, or other bright sources in the field of view that will have a non-negligible number of counts in the wings of their PSF. To this end a Cash variant is used[7] known as W,

$$W = 2\sum[t_s m_i + (t_s + t_b)f_i - S_i \log(t_s m_i + t_s f_i) - B_i \log(t_b f_i) - S_i(1 - \log S_i) - B_i(1 - \log B_i)] \tag{3.4}$$

expressed in terms of the count rates m_s, m_b observed in exposure times t_s, t_b for the source and background spectra, with total counts S_i, B_i and $f_i = \hat{b}$.

Testing

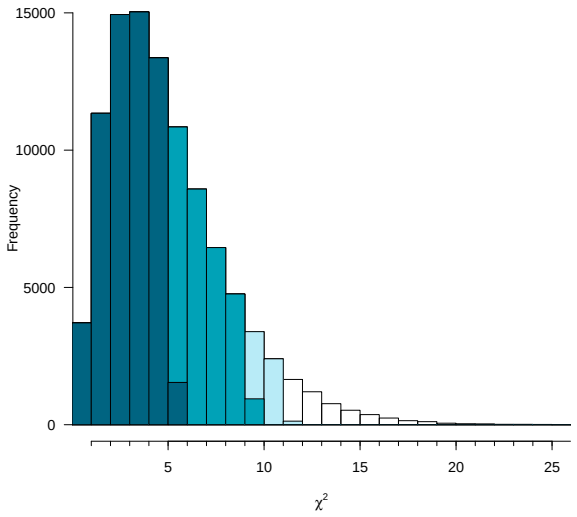

Figure 3.6 χ^2 distribution for 5 degrees of freedom, simulated dataset of 10^5 samples. Shading shows the $95\%, 90\%$ and 60% populations.

[7] heasarc.gsfc.nasa.gov/docs/xanadu/xspec/wstat.ps

Fitting with the χ^2 statistic means that the fit can also be tested with χ^2. Assuming that the model is a good description of the data, the value of χ^2 should be distributed by a χ^2 distribution described by the number of degrees-of-freedom ν in the fit (i.e. the number of channels minus the number of free parameters in the model). This is illustrated in figure 3.6, which simply shows a χ^2 distribution for $\nu = 5$. It is clear that fits that have $\chi^2 \gtrsim 12$ are outside of the main 95% of the distribution, and such a result could be considered a poor description of the data. There is a commonly (mis)used rule-of-thumb that the 'reduced χ^2', $\chi^2_\nu = \frac{\chi^2}{\nu} \approx 1$. This makes sense, as this is simply an expression of the closeness to the peak of the χ^2 distribution of that result. However, this χ^2 test is less useful with with large ν, and potentially can hide the presence of significant features - such as spectral lines and edges - that are thin with respect to the breadth of the continuum. Also, it is worth noting that the distribution of χ^2_ν narrows as ν increases.

To test for the presence of additional features in a spectrum, the most robust method currently available is the likelihood method, rather than the F-test that was used ubiquitously through the early years of high-quality X-ray spectral fitting (Protassov et al., 2002). In summary, this involves simulating the null model (continuum without spectral lines or edges) and then fitting the two alternative models (continuum and then continuum plus feature) to the spectra separately. It can then be shown how often the superior fit statistic from including the feature to the modelling of the source spectra is improved on from statistical variation alone (see also the excellent chapter by Siemiginowska in Arnaud et al., 2011).

Additional well-known test statistics are now available for use in XSPEC. These tests measure the extent to which the fractional cumulative distribution (FCD) of some data matches that of a model or other distribution. The classic example of this is the Kolomogorov-Smirnoff test (K-S test) (Massey, 1951). This test statistic is a measure of the greatest difference between two FCDs. Often, it is desirable to use different versions of this statistic, such as the Anderson-Darling or Cramér–von Mises criterion, which are more adept at examining the extent to which the wings of two distributions are alike.

Exploring Parameter Space

The standard errors on a best-fit are expressed as a surface in the parameter space defined by a constant change in the test statistic, $\Delta\chi^2$. Typically, X-ray astronomers use $\Delta\chi^2 = 2.706$, which

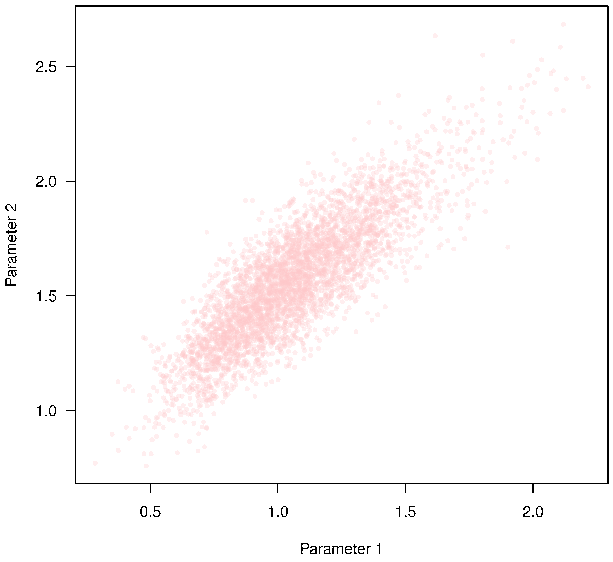

Figure 3.7 MCMC marginalised over two parameters. For clarity, the points are semi-transparent to highlight the high-density regions.

corresponds to a 90% confidence region (Avni, 1976).

The most accurate representation of the parameter space can be achieved by using Markoff chains Monte-Carlo (MCMC) to directly sample the underlying probability distribution. XSPEC uses the Metropolis-Hastings algorithm (Hastings, 1970), which samples the parameter space more numerously in regions of high likelihood. An example of such output, marginalised over two parameters is presented in figure 3.7, which shows more likely regions as higher-shading density (more semi-transparent points overlap). This output has a broad range of useful applications beyond visualising the parameter space, and in Chapter 5 it is used to calculate the approximate probability that two spectra are from the same parent distribution.

Chapter 4

A Transient Sub-Eddington Black Hole X-ray Binary Candidate

4.1 Introduction

The majority of confirmed black hole low-mass X-ray binary (BH LMXB) systems are transient sources that experience outbursts lasting from a few weeks to a matter of years. These outbursts are characterized by an increase in X-ray luminosity by many orders of magnitude from a quiescent state of $L_X \sim 10^{30-34}$ erg s^{-1}, recurring on timescales of months to decades (for a review, see Remillard & McClintock, 2006). The recurrent behavior of the persistent luminosity, characterised by a rapid rise and exponential decay, is thought to be the result of accretion disc instability (Dubus et al., 2001). Research into Galactic BH LMXBs has revealed three common spectral states, between which sources are observed to transit; a thermal state dominated by radiation originating in the inner-regions of a geometrically thin, optically thick accretion disk (Shakura & Sunyaev, 1973), a hard state dominated by a power law with photon index $\Gamma \sim 1.7$, and a steep power law state $\Gamma \sim 2.5$ extending to MeV energies where a significant thermal component is also present. The similarity of these states to the spectra of neutron star (NS) LMXB means that it is often impossible to fully distinguish between bright NS and BH LMXBs on the basis of luminosity and spectra alone. However, a distinction can be drawn between the thermal states, which are typically much harder in NS systems than for BH sources. This is in agreement with the proposal that 'ultrasoft' spectra are a characteristic of BH sources (White & Marshall, 1984). NS systems, as a result of the presence of the physical surface of the compact object, experience behavior in the form of bursting, for lower-luminosity (Atoll) sources such as 4U 1636-536, and flaring, for more luminous ($L_X \sim 10^{38}$ erg s^{-1}, Z-track) systems such as Sco X-1.

Until recently only two transient NS LMXBs with $L_X \sim L_{Edd}$ were known, Cir X-1 and XTE J1806-246. Cir X-1 is a peculiar NS XB with atypical spectral and timing behavior and was once thought to possess a BH primary, an idea which was confounded by the detection of Type-I X-ray bursts (Tennant et al., 1986; Linares et al., 2010). The transient nature of Cir X-1 is also unusual in that it is periodic with a period of 16.6 days and therefore thought to be the result of the eccentric orbit of the donor star (Murdin et al., 1980), rather than accretion disc instability. The peak luminosity of XTE J1806-246, reported as $L_X \sim 1.5 \times 10^{38}$ erg s^{-1} (Wijnands & van der Klis, 1999), is based on a poor distance estimate (8 kpc, based on a sky position coincident with the Galactic bulge). The recent discovery of transient NS LMXB, XTE J1701-462 (Homan et al., 2007), which experienced the full range of spectral and timing behavior observed in all other Galactic NS LMXBs (Lin et al., 2009; Sanna et al., 2010) during a $\sim$ 600 day outburst, demonstrates both that NS transients can be as luminous as some of their BH cousins, and that the short-term variability is fundamentally linked to the accretion rate of the system.

The *Chandra* and *XMM-Newton* X-ray observatories have made possible the detailed study of extragalactic X-ray binary (XB) sources during the last decade. Within the Local Group, Williams et al. (2006) cataloged the properties of 45 transient XBs in M 31, and found that most exist around the central bulge of the galaxy, suggesting that they are part of an older stellar population and therefore more likely to be LMXBs. More detailed studies of brighter transient sources (Trudolyubov et al., 2006) and the overall XB population (Stiele et al., 2011) show many soft sources, with absorbed disc blackbody temperatures $kT_{in} < 1$ keV, and < 0.1 keV in the case of super-soft sources (SSS) that show no emission above 1 keV. Such low values of kT_{in} are inconsistent with spectral fitting results for Galactic NS LMXBs (Revnivtsev & Gilfanov, 2006) and are thus indicative of BH systems in the thermal state, while SSS are thought to be accreting white dwarfs (van den Heuvel et al., 1992; Kahabka & van den Heuvel, 1997). It has been shown that the M 31 X-ray transients are found in three distinct spectral groups at their peak luminosity (Voss et al. 2008), categorized as very soft, soft and hard, half of all the transients being hard. The ChASeM33 project, consisting of 7×200 ks *Chandra* exposures of M 33, allowed source detection to a depth of 5×10^{34} ergs s^{-1}, and 7 transient sources have been discovered, albeit only two with $L_X > 10^{37}$ erg s^{-1} (Williams et al., 2008).

Outside the Local Group, in the elliptical galaxies NGC 3379 and NGC 4278 (Brassington et al.,

2008, 2009), five and three sources respectively have been classified as transient candidates (TCs). Three other sources in each of these galaxies have been identified as possible transient candidates (PTCs). TCs and PTCs correspond to observed changes in luminosity by factors of > 10 and > 5 respectively, and we note that some Galactic sources such as 4U 1705-44 (Homan et al., 2009) and 4U 0513-40 (Maccarone et al., 2010b) are not transients but do show variations significantly greater than a factor of 10. All of these sources have hardness ratios and X-ray colors that are consistent with Galactic LMXBs. Follow-up spectral analysis on the bright, seemingly persistent sources in these galaxies (Brassington et al., 2010; Fabbiano et al., 2010) yielded $L_X \sim 10^{38} - 10^{39}$ erg s^{-1}, with spectral fitting parameters congruent with known BH systems; the strongest BH binary candidate had maximum and minimum unabsorbed luminosities of 1.2×10^{39} erg s^{-1} and 4.1×10^{38} erg s^{-1}.

For observational reasons, the XBs outside the Local Group that have been the most intensely studied are the Ultraluminous X-ray sources (ULXs), which possess outburst luminosities in excess of 10^{39} erg s^{-1}, together with other bright sources with luminosities typically $>$ 2–3L_{Edd} for an accreting NS. These sources represent a comparatively small fraction of XBs in the Local Group, with the solitary ULXs found in M 31 and M 33 being the only constituents of their class (Kaur et al., 2012; Dubus & Rutledge, 2002). Therefore, there exists an asymmetry between the study of XBs inside and outside the Local Group.

4.1.1 NGC 5128

Centaurus A (NGC 5128, Cen A) is the nearest optically luminous large early-type galaxy, situated at a distance of 3.7 Mpc (Ferrarese et al., 2007), with M_B = -21.1. A small late-type galaxy is currently merging with Cen A, however, the galaxies remain poorly mixed (Quillen et al., 2006). The merger has resulted in the presence of vast dust lanes that obscure many of the central regions at optical and soft X-ray wavelengths (Graham, 1979).

Six 100 ks *Chandra* observations were taken as part of the Cen A Very Large Project (VLP) spanning the course of 2 months (Jordán et al., 2007). Other research performed using these observations was outlined in § 2.5.1.

Two transients in the field of Cen A have previously been studied. Sivakoff et al. (2008) discovered a previously undetected transient using VLP observations, CXOU J132518.2-430304. With outburst luminosities in excess of 10^{39} erg s^{-1}, it is by definition an ULX. CXOU J132518.2-430304 underwent

a > 770-fold increase in luminosity between quiescent and active states, with an outburst duration of > 70 days. Spectral analysis coupled with *HST* observations strongly suggest that the source is a BH LMXB that transitions from the steep power law state to the thermally dominant state over the course of the VLP observations. Prior to this, (Kraft et al., 2001) had detected a transient ULX, CXOU J132519.9-43031, ($L_X \sim 10^{39}$ erg s^{-1}) within $\sim 6''$ of a source detected by *ROSAT* over the course of 10 days in 1995. Spectral fitting suggested the source was in a steep power law state (Ghosh et al., 2006).

In this Chapter, we present the first detailed analysis of a sub-Eddington X-ray transient at Mpc distances, CXOU J132527.6-430023, whose flux rose by more than a factor of 100 from quiescence to outburst and reached peak unabsorbed luminosities of $\sim 2 \times 10^{38}$ erg s^{-1} (0.5-7.0 keV) before fading back to a quiescent state by MJD 54250 (Table 4.1). We present evidence that this source is a BH LMXB and compare it to LMXB systems observed both inside and outside the Local Group. This source is clearly a bridge between more typical Galactic and extragalactic XBs. Since Cen A is nearby, this is the only sub- (or $\sim$) Eddington transient where we can perform detailed spectral fitting and attempt to classify the compact object as a BH or NS.

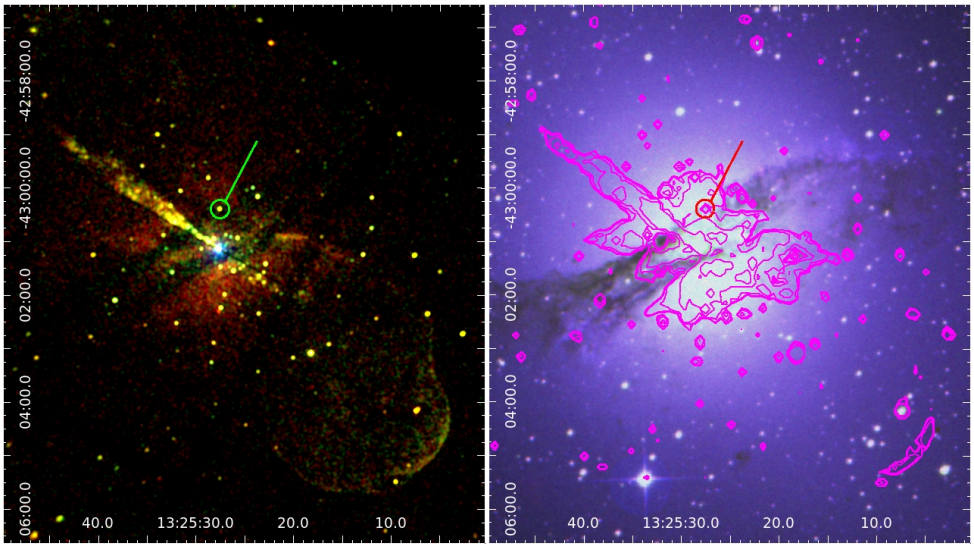

Figure 4.1 Location of CXOU J132527.6-430023 within Cen A. *Left:* A Gaussian-smoothed logarithmic-scale 0.5-1.3 keV (red), 1.3-2 keV (green) 2-7 keV (blue) image of ObsID 7797. *Right:* X-ray 0.5-7 keV contours of the brighter central regions of Cen A (Magenta) overlaid on Deep Sky Survey combined R, I and B band image of Cen A.

Table 4.1. ACIS-I/S Observations of Transient in Cen A

ObsID	Instrument	Exposure (ks)	Date MJD	(y-m-d)	Net Counts[a]
316	ACIS-I	36.18	51517	(1999-12-05)	< 2.7
962	ACIS-I	36.97	51681	(2000-05-17)	< 4.3
2978	ACIS-S	45.18	52520	(2002-09-03)	< 4.3
3965	ACIS-S	50.17	52896	(2003-09-14)	< 4.0
7797	ACIS-I	98.17	54181	(2007-03-22)	$\mathbf{336 \pm 32}$
7798	ACIS-I	92.04	54186	(2007-03-27)	$\mathbf{364 \pm 34}$
7799	ACIS-I	96.04	54189	(2007-03-30)	$\mathbf{375 \pm 35}$
7800	ACIS-I	92.05	54207	(2007-04-17)	$\mathbf{284 \pm 31}$
8489	ACIS-I	95.18	54228	(2007-05-08)	$\mathbf{16^{+9}_{-7}}$
8490	ACIS-I	95.68	54250	(2007-05-30)	< 7.3
10723	ACIS-I	5.15	54835	(2009-01-04)	< 2.6
10724	ACIS-I	5.17	54895	(2009-03-05)	< 2.6
10725	ACIS-I	5.04	54947	(2009-04-26)	< 2.6
10726	ACIS-I	5.15	55003	(2009-06-21)	< 4.0
10722	ACIS-S	50.04	55082	(2009-09-08)	< 2.3
11846	ACIS-I	4.75	55312	(2010-04-26)	< 3.9
11847	ACIS-I	5.05	55455	(2010-09-16)	< 2.6
12155	ACIS-I	5.05	55552	(2010-12-22)	< 2.6
12156	ACIS-I	5.06	55734	(2011-06-22)	-

[a]For observations where the source was not detected, the Net Counts column represents the 90% upper limit placed on the net counts of the source in the 0.5-2.0 keV band. For the **detections**, 90% confidence regions are shown. The position of the source is coincident with the ACIS readout-streak in ObsID 12156 and no upper-limit was calculated in this instance.

4.2 Data Preparation and Analysis

4.2.1 Preliminary Work

An overview of all *Chandra* ACIS observations of Cen A can be found in Table 4.1. All of the 5 ks and 50 ks observations of Cen A were taken with the Advanced CCD Imaging Spectrometer (ACIS) as part of the HRC Guaranteed Observation Time program (PI: Murray).

All the data were reprocessed using CIAO 4.3 and HEASOFT 6.11 with CALDB 4.4.2. All observations were first co-aligned to a precision $< 0\farcs2$ based on the positions of the point sources detected using `wavdetect` and then aligned to the positions of confirmed Cen A globular clusters. This procedure is described in §5.2. CXOU J132527.6-430023 was detected in *Chandra* ObsIDs 7797, 7798, 7799, 7800, and 8489.

We measured the position of CXOU J132527.6-430023 as $\alpha = 13^h25^m27.58^s$, $\delta = -43^\circ00'23\farcs3$

(J2000) with $< 0\farcs2$ uncertainty (Fig. 4.1). The 0.5-2.0 keV lightcurve across the 100 ks observations was generated using the ciao tool `aprates`. The source flux was calculated based on a circular region of radius r_{p2} equal to 90% of the 2 keV PSF centred at the off-axis position of the source, and the background flux from an annulus extending from r_{p2} to $3r_{p2}$. No other sources are seen to overlap these source regions, and no other r_{p2} source regions encroach on the background annuli. In Fig. 4.2, we present lightcurves in the 0.5-2.0 keV band, with the VLP (outburst) lightcurve shown in the bottom panel, while the top panel shows the overall ACIS lightcurve of the source. We restricted ourselves to this low-energy range due to the proximity of the source to the AGN. For the six 100 ks observations, the mean photon energies per effective exposure of each 0.5-2.0 keV event were first calculated using `eff2evt` on both source and background regions and are then used as `aprates` input parameters. For the upper limits, the exposure times of the source and background regions were also used. `aprates` then performs a Bayesian analysis and returns the net 0.5-2.0 keV flux with a 90% confidence interval or count-rate upper limit. A combined upper limit was calculated for the 7×5 ks observations and individual upper limits were obtained for each observation of exposure > 30 ks. The upper limits were then converted to 0.5-2.0 keV fluxes, uncorrected for absorption, using the Chandra X-Ray Center program `PIMMS`, assuming an absorbed power law spectrum with $\Gamma = 2.0$ and $N_H = 0.084 \times 10^{22}$ cm^{-2} (i.e. a relatively steep spectrum for a quiescent LMXB in front of the dust lane). The source position is obscured by the ACIS readout streak in ObsID 12156, no upper limit was obtained in this case. With `aprates`, the combined upper limit on count rate was calculated by inputting the summation of counts, areas and exposure times of the source and background regions. Measured fluxes and upper limits were then converted into luminosity using a distance of 3.7 Mpc. We recognize that a more recent measurement has produced a distance to Cen A of 3.8 ± 0.1 Mpc (Harris et al., 2012), but we have used a distance of 3.7 Mpc in calculations throughout this paper for the sake of consistency with earlier work. This said, the uncertainty of the distance measurement is much less than the uncertainties associated with the calibration and spectral fitting process, which therefore have a greater effect on our luminosity measurement. ObsID 10722 is our lowest luminosity upper limit, $L_X > 3 \times 10^{35}$ erg s^{-1}.

Several factors make CXOU J132527.6-430023 the best transient BH candidate in Cen A to study in the $\sim 10^{38}$ erg s^{-1} regime. It is clear that it is observed in both outburst and quiescent states during the VLP observations. Basic observational criteria regarding the source are satisfied;

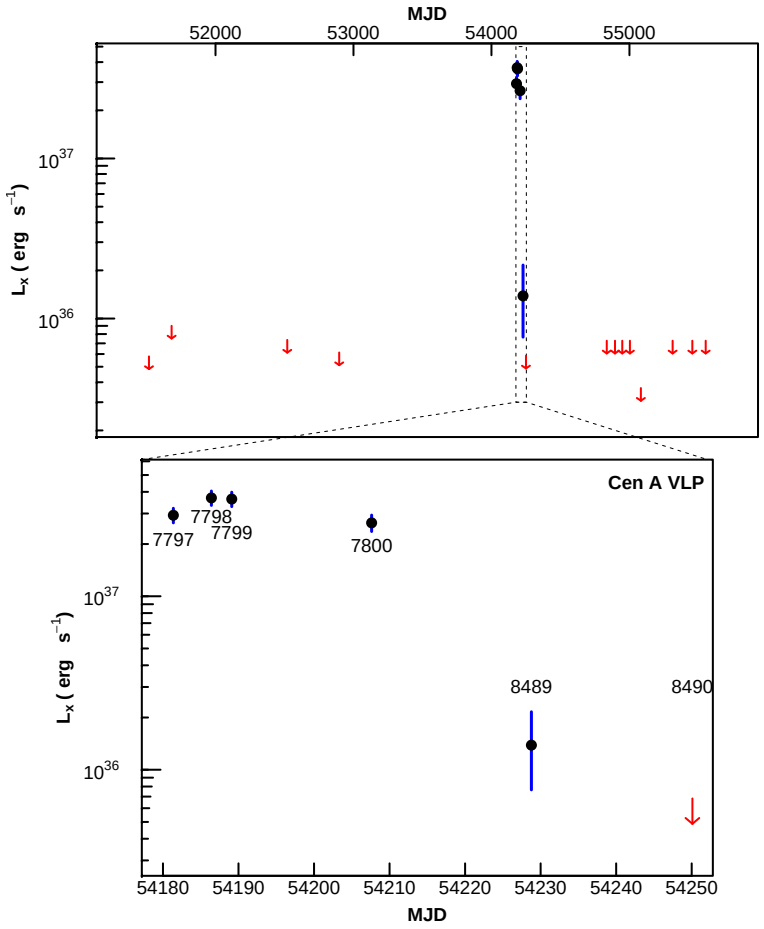

Figure 4.2 X-ray lightcurve (0.5 – 2 keV), uncorrected for absorption. *Top:* Luminosity is displayed with 90% confidence intervals (blue error bars) and with 90% upper limits from other ACIS observations (red arrows). A combined upper limit was obtained from the 5 ks observations (the seven arrows to the right). *Bottom:* Lightcurve of VLP observations.

the source is always in the field of view, far from the ACIS chip edges and has the required counts to perform meaningful spectral analysis. In Chapter 5 we show that no other source observed to be transient in Cen A during the VLP, is as bright in as many observations while also undergoing such a dramatic change in the mean flux (Fig. 4.2), as CXOU J132527.6-430023.

Before the extraction of spectra, we investigated the intra-observation variability, by extracting a count-rate lightcurve of each observation, to test if the source was active throughout a given observation, or was prone to more discrete behavior. In Fig. 4.3 we present the intra-observation 0.5-2.0 keV lightcurve, with count-rate grouped to 10 ks bins. The mean intensity has substantially diminished by the time of ObsID 8489, approximately 20 days after the previous observation. A simple χ^2 test showed no significant variations from the best-fit straight line for any of the 100 ks

Chandra pointings binned to 10 ks.

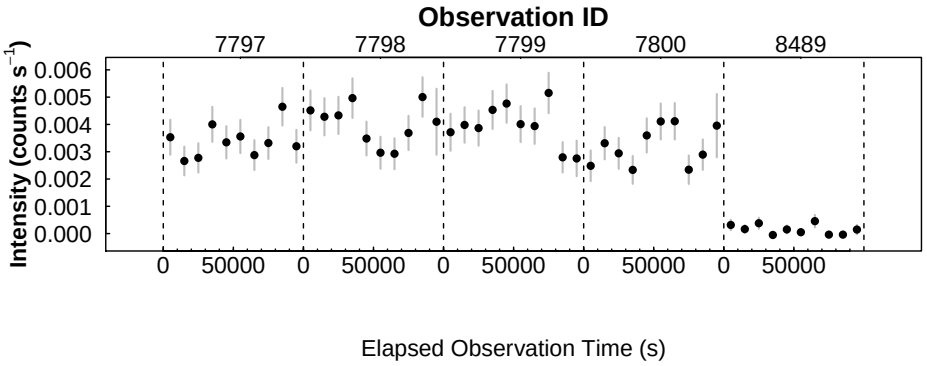

Figure 4.3 Intra-Observation 0.5 – 2.0 keV lightcurves of the net intensity with 10 ks binning within the VLP observations. For the ObsID dates, see Table 4.1.

4.2.2 Possible Counterparts

We investigated the possibility of detecting a counterpart to CXOU J132527.6-430023 at other wavelengths. We examined B and R band images from recent observations (Harris et al., 2012) with the Walter Baade Telescope and the Inamori Magellan Areal Camera (IMACS) and found no point sources coincident with the position of the transient. Further investigation using an *H*ST WFPC2 observation, U4100108M (F814W) showed no optical counterpart. However, the position is coincident with the edge of the dust lane. This being the case, any attempt to perform optical photometry on the source position will be inconclusive. The nearest globular cluster that has been spectroscopically confirmed as belonging to Cen A is $\sim 30''$ away from CXOU J132527.6-430023 (Woodley et al., 2008). However, no clusters have been detected within the radial distance of the transient from the galaxy center, as a result of the high stellar luminosity within $\sim 1.5'$ of the Cen A nucleus, in tandem with the heavy obscuration by the dust lanes.

A 2007 June Very Large Array 8.4 GHz observation using the A configuration, obtained just one week after the final VLP observation, places a 3σ upper limit of 0.13 mJy on the radio emission at this position. Further to this, it has been confirmed that no radio counterpart has been detected in any other VLP observation (Goodger et al., 2010). Galactic transient XBs frequently show evidence of jets during outburst (see Fender, 2006, for review), and have a clear relationship between the strength of the outburst X-ray luminosity and the flux density of the radio emission. Sources typically possess

a flat radio spectrum, with flux densities $\sim 1 - 1000$ mJy when scaled to 1 kpc. Scaling this to the distance to Cen A, suggests that the expected flux density of a typical counterpart would lie in the range $0.07\mathrm{nJy}$ to $0.07\mu\mathrm{Jy}$, far smaller than our upper limit. Cyg X-3 is a high mass X-ray binary (HMXB) where the evidence of a BH is fairly strong (Shrader et al., 2010) and has been seen to emit strong radio flares of up to 20 Jy from an assumed distance of 9 kpc (Corbel et al., 2012); at the distance of Cen A such an outburst would be detected above our upper limit. Therefore a radio detection of an XB counterpart in Cen A would point towards a high mass companion.

4.2.3 Spectral Fitting

Spectra and responses in the 0.5-7.0 keV range for each of the five observations where the source is detected were generated, based on circular apertures of radius r_{p7} equal to 90% of the 7 keV PSF size at the off-axis source position. Background spectra were taken from an annulus $2r_{p7}$ to $4r_{p7}$, minus two overlapping circular r_{p2} source regions corresponding to two faint sources that were only detected in the merged 600 ks dataset. In the four bright observations, 7797 – 7800, the spectra were grouped to a minimum of 20 counts $\mathrm{channel}^{-1}$ to allow use of the χ^2-statistic, whereas the spectrum from observation 8489 contained too few counts for grouping and fitting. All fitting was performed using XSPEC 12.7.0 (Arnaud, 1996).

While the large range in flux from the source negates the possibility of it being a background object, such as an AGN, it is prudent to check that the source is not a foreground flare star. We tested this by attempting to fit an absorbed thermal plasma model ($phabs \times apec$). For the default settings (abundance fixed at 1.0) fit statistics for the spectra from ObsId 7797 to ObsId 7800 were $\chi^2/\mathrm{dof} = 56.52/17, 58.1/20, 102.4/20$ and $44.1/15$ ($\chi^2_\nu > 2$), respectively. Allowing the abundance to vary led to good fits, $\chi^2_\nu \sim 0.8 - 1.4$, but the abundance tended towards zero, approximating a pure bremsstrahlung spectrum. The lack of an optical counterpart in front of the dust lanes strengthens this argument, as no source is detected in HST observations that were used to put a lower limit on m_{F606W} of 24.9 for the ULX positions in Cen A (Sivakoff et al., 2008). M class stars as far away as the diameter of the Milky way (~ 30 kpc) would have an apparent bolometric magnitude of $9.9 - 15.4$ (Kraus & Hillenbrand, 2007). This being the case, if the source has a Galactic origin then it has an unrealistically large X-ray flux to bolometric flux ratio. Brassington et al. (2012a) demonstrated that an X-ray flux of $5 \times 10^{-14}\ \mathrm{erg\ cm^{-2}\ s^{-1}}$ (with a similar optical upper limit) would

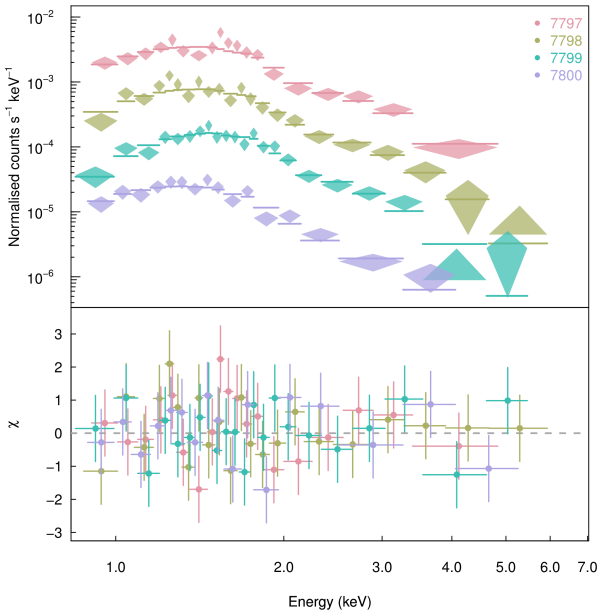

Figure 4.4 Spectra of the four bright VLP observations of CXOU J132527.6-430023. Spectra subsequent to 7797 are offset in y by a factor $\times 5^{-n}$, where n=1 for 7798, n=2 for 7799 etc. Spectra values and associated errors are represented by diamonds while the absorbed disc blackbody model is represented by horizontal lines. Triangles show instances where the uncertainty was greater than the rate in the channel.

be an order of magnitude larger than the most luminous M dwarf flare ever observed (Güdel et al., 2004), and our measured X-ray flux is comparable at $\approx 2 \times 10^{-14}$ erg cm^{-2} s^{-1}. It is reasonable to discount the possibility of CXOU J132527.6-430023 being a foreground object.

We followed the spectral fitting prescription of Brassington et al. (2010), who developed a consistent approach to fitting the spectra of luminous LMXBs in NGC 3379. Absorbed single-component models, starting with a simple power law, are fit first, and the nature of these fits informs a decision on how to proceed to further fitting. Each observation was individually fit in XSPEC with a $phabs \times powerlaw$ model, all parameters of which were left free. Successful fits were achieved for the four observations where the source was bright, with the largest $\chi^2_\nu \sim 1.1$. The fitting yielded quite high values for the photon index, $\Gamma \sim 3.7 - 4.7$, while the absorption column was above the Galactic value of $N_H = 0.084 \times 10^{22}$ cm^{-2} (Dickey & Lockman, 1990), with $N_H \sim 0.9 - 1.7 \times 10^{22}$ cm^{-2}, also larger than the inferred range of N_H the dust lanes and in the $2''$ vicinity of the source (§ 5.4.1). The results of the simulations of Brassington et al. (2010) suggest that XSPEC absorbed power law fits on LMXB will increase the value of N_H as a compensation for instances where there is a lack of a required thermal component. It was therefore appropriate to fit an absorbed multicolored disc blackbody model ($phabs \times diskbb$ in XSPEC) and contrast the two sets of fit results.

f The absorbed disc blackbody was the best-fit model for all four of the bright spectra (Table 4.2), with $\chi^2_\nu < 1$. The addition of a second additive component, such as a power law, cut-off power law or $compTT$ proved unnecessary, as their normalizations tended towards zero. Table 4.2 shows that the N_H in the $phabs \times diskbb$ fits is significantly less than for the $phabs \times powerlaw$ model, above the Galactic value and, for three of the spectra, consistent with the range of $N_H \sim (0.11 - 0.66) \times 10^{22}$ cm^{-2} inferred from (Schreier et al., 1996). However, this is still less than our calculated average value ($N_H \sim 0.6 \times 10^{22}$ cm^{-2}) over a $2''$ region from a K-band optical depth map. These results suggest the source exhibited minor spectral evolution across the four bright observations (Fig. 4.4).

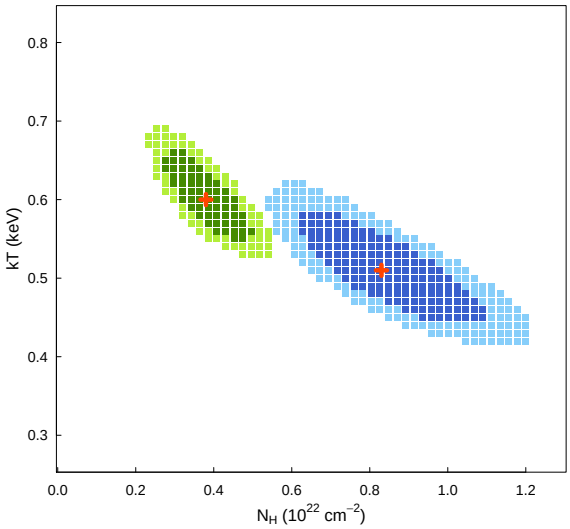

Figure 4.5 90% and 68% confidence regions with best-fit values (red crosses). *Left:* From joint spectral fit to ObsIDs 7797, 7798 & 7800. *Right:* From spectral fit of ObsID 7799.

In order to test whether the apparent difference in absorption between ObsID 7799 and the other spectra was a real effect or the result of stochastic spectral variation, a joint fit using the spectra from ObsIDs 7797, 7798 and 7800 was performed, achieving $\chi^2_\nu \sim 48.5/53$. This produced more constrained parameter values of $N_H = 0.38 \pm 0.12 \times 10^{22}$ cm^{-2} and $kT_{in} = 0.60 \pm 0.05$ keV. The three observations would have luminosities of $(1.28, 1.22 and 0.72) \times 10^{38}$ erg s^{-1}, respectively. We investigated the spectral fitting behavior in the $kT_{in} - N_H$ plane across a 50×50 grid of the parameter space (Fig. 4.5). These results suggest that we can reject consistency of N_H at the 2σ level between the joint fit and the fit to ObsID 7799. This does suggest that there is a genuine

Table 4.2. Best Fit Parameter Values: *phabs* × *diskbb* Model

ObsID	N_H 10^{22} cm^{-2}	Flux[ab] 10^{-14} d	kT_{in} keV	χ^2/dof	L_x[abc] 10^{38} erg s^{-1}
7797	$0.36^{+0.22}_{-0.19}$	$7.69^{+2.04}_{-1.44}$	$0.65^{+0.11}_{-0.10}$	15.85/16	$1.26^{+0.33}_{-0.24}$
7798	$0.43^{+0.22}_{-0.18}$	$7.93^{+2.22}_{-1.49}$	$0.61^{+0.12}_{-0.10}$	15.18/19	$1.30^{+0.36}_{-0.25}$
7799	$0.83^{+0.29}_{-0.23}$	$12.12^{+5.05}_{-2.97}$	$0.51^{+0.09}_{-0.08}$	11.83/19	$1.99^{+0.82}_{-0.49}$
7800	$0.33^{+0.27}_{-0.22}$	$4.30^{+1.92}_{-1.07}$	$0.53^{+0.13}_{-0.11}$	11.75/14	$0.70^{+0.32}_{-0.17}$

[a]Spectral fits to the 0.5 – 7.0 keV band.

[b]Unabsorbed, from the XSPEC $cflux$ parameter.

[c]L_X based on distance of 3.7 Mpc.

[d]ergs cm^{-2} s^{-1}

change in absorption local to the source during ObsID 7799. A change in local absorption has previously been established in other BH systems. Oosterbroek et al. (1997) simulated spectra of various model parameters in an attempt to infer which change in parameter space could reproduce the observed color-color diagrams of GS 2023+338. They concluded that a large increase in the local absorption was the best explanation of the observed color-color tracks, and speculated that the system could be inclined enough for the absorbing material to originate in the edge of the accretion disc. Such a change in absorption has also been reported from an extragalactic BH source, XMMU 122939.7+07533 (Maccarone et al., 2007). This was at first attributed to a warping of the accretion disc (Shih et al., 2010), but the presence of strong, broad OIII lines (Zepf et al., 2008) suggests a strong disc wind varies the amount of absorbing material along the line-of-sight.

4.3 Discussion

In this section we compare the properties of the transient source CXOU J132527.6-430023 to other XBs, both Galactic and extragalactic in origin, in the hope of finding well-studied analogues. The outburst duration is between ∼50 and ∼1500 days. This is consistent with outbursts observed in many Galactic sources, which are active on timescales of months to years – much longer than so-called fast X-ray transients, for which the outburst duration is less than a day (Heise & in't Zand, 2006). The peak unabsorbed luminosity of $\sim 2 \times 10^{38}$ erg s^{-1} is close to the Eddington luminosity of an accreting $1.4\ M_\odot$ NS; however, it is possible that the source reached its peak luminosity prior to

first being detected. The nature of the compact object is ambiguous based solely on the luminosity.

Samples of luminous LMXBs from NGC 3379 and NGC 4278 have been used to give an indication of BH mass (Brassington et al., 2010; Fabbiano et al., 2010) based on the $L_X - kT_{in}$ relation of Gierliński & Done (2004). In agreement with the broad trend shown by these more luminous sources, the spectral fitting results for three of the CXOU J132527.6-430023 spectra are compatible with a $\sim 10\ M_\odot$ BH (Fig. 4.6). The best-fit to ObsID 7799 yields a value of N_H that is double that obtained from the other spectra (albeit they are constrained to 90% uncertainties of $\pm 50\%$). If this is not a real effect, then it could result in an artificial increase in the unabsorbed flux found from fitting. We find a 2σ difference between the fits for this ObsID 7799 and a joint fit of the three other bright spectra (Fig. 4.5), indicating that a physical change near the source has occurred. The fitting parameters from ObsID 7799 would be consistent with an $\sim 18\ M_\odot$ BH; however, it seems very improbable that the compact object gained, and then lost, so much mass during this time.

The spectral fitting process resulted in a best-fit model of an absorbed multicolor disc blackbody (Table 4.2); the fits to the power law model lead to extremely steep spectra with $\Gamma > 3.7$ and can be ruled out. The absorption column parameter is still above the Galactic value ($0.084 \times 10^{22}\ \mathrm{cm}^{-2}$); however, judging from the position of the source within Cen A ($\alpha = 13^h25^m27.58^s$, $\delta = -43^\circ00'23\farcs3$, Fig. 4.1), this is not unexpected. The structure of the dust lane is complex, with the source residing in an $\sim 2''$ radius quasi-circular region of lower density dust bordered by regions of higher density, which complicates accurately computing the amount of absorption at the source location. All values of N_H from the spectral fitting are consistent with studies of the extinction in the Cen A dust lanes (Schreier et al., 1996), with $0.5 < A_V < 3.0$ indicating an N_H of $(0.11 - 0.66) \times 10^{22}\ \mathrm{cm}^{-2}$ (Güver & Özel, 2009). Analysis of the K-band optical depth map (Figure 5.10) presented in Kainulainen et al. (2009) yielded a mean $A_K = 0.325$, indicating $N_H \sim 0.6 \times 10^{22}\ \mathrm{cm}^{-2}$, this would be almost double the absorption column found from three of the spectral fits. The Cen A ULX found by Sivakoff et al. (2008) - outside of the dust lanes - was found to have a similar absorption column to CXOU J132527.6-430023 but only when the source was in the steep power law state, the column apparently decreasing to consistency with the Galactic value as the thermal component began to dominate the spectrum.

The inner-disc temperatures, $kT_{in} \sim 0.6\ \pm 0.1$ keV, are softer than the spectra of NS LMXBs, which typically vary between 1-2 keV. This temperature is also below that of the ULX, which had

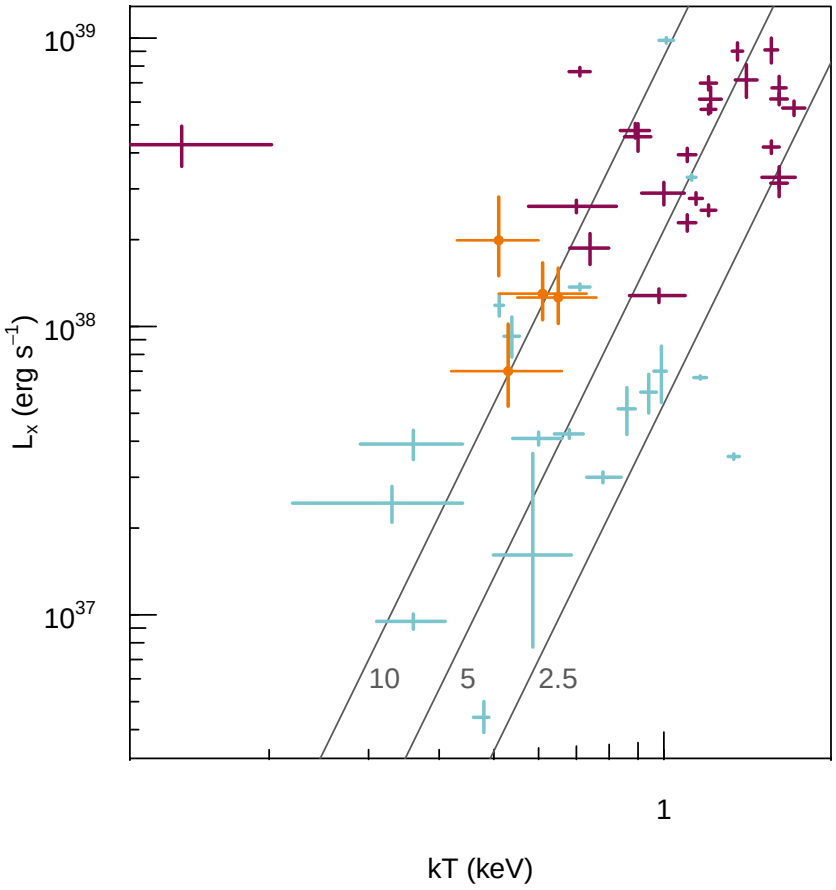

Figure 4.6 Comparison of $L_X - kT_{in}$ for CXOU J132527.6-430023 (orange with points) with other sources in the thermally dominant state both outside (magenta) and inside (light blue) the Local Group. We make use of the spectral fitting results from sources in NGC 3379 (Brassington et al., 2010) and NGC 4278 (Fabbiano et al., 2010). The Local Group sample is based on spectral fits to Galactic (McClintock & Remillard, 2006; Soria et al., 2011) and M 31 (Trudolyubov et al., 2006; Stiele et al., 2011) sources with L_X adjusted to the 0.5-7.0 keV band using Xspec. Lines of constant BH mass with increasing kT_{in} for 10 $M_\odot$, 5 $M_\odot$ and 2.5 $M_\odot$ BH are based on the prescription of Gierliński & Done (2004) and assumptions of Brassington et al. (2010).

$kT_{in} \sim 1$ keV. Such soft spectra are reminiscent of Galactic BH transients in the thermal state (McClintock & Remillard, 2006), and are not seen in NS LMXBs of comparable luminosity. The corresponding bolometric luminosities found from the spectral model are $\sim 1.4 \times 10^{38}$erg s^{-1}, which equates to $\sim 10\%$ Eddington for a 10 $M_\odot$ BH; consistent with known BH systems in the thermal state. A NS primary emitting at L_{Edd} seems unlikely based on comparison with Galactic analogues. None of the brighter persistent (Z-track) sources exhibit spectral states as soft, and the only bright NS LMXB transient, XTE J1701-462, exhibited 'Atoll-like' behavior (harder spectra) in the 60 days prior to its return to quiescence. Spectral fits of absorbed disc blackbodies to M 31 XBs have also produced kT_{in} of 0.3-0.6 keV, such as XMMU J004144.7+411110 (Trudolyubov et al., 2006). This

source has an estimated unabsorbed luminosity of $3-4\times10^{37}$ erg s^{-1} for the best-fit spectral model of an absorbed disc blackbody with $kT_{in}\sim0.6-0.8$ keV. Power law fits resulted in $\Gamma\sim2.8-3.3$ and a column density far in excess of Galactic absorption, while the disc blackbody fits resulted in N_H only double that of the Galactic value, very similar behavior to our transient. XMMU J004144.7+411110 also lacks an optical counterpart ($m_v>21$).

CXOU J132527.6-430023 shows that our study of XB outside the Local Group is starting to probe lower-luminosity BH LMXB with properties more typical of Galactic sources (Fig. 4.6). For the time being, Cen A contains the only population of such objects ($10^{37}-10^{38}$ erg s^{-1}, non-Local Group) that can be subjected to meaningful spectral fitting. In Chapter 5 we will report on detailed spectral analysis of the Cen A XB population of sources with $L_X>10^{37}$ erg s^{-1} which will, for the first time, allow contrast between the nature of typical LMXBs in our galaxy with analogs from beyond the Local Group.

4.4 Conclusion

We believe that the following evidence makes a strong case for CXOU J132527.6-430023 being a transient BH LMXB candidate.

(i) Long-term Variability. The absorbed flux varies by a factor >100 between quiescent and active states on timescales of months. This behavior favors a low mass companion, as all dynamically confirmed BH HMXB systems (Cyg X-1 in the Milky Way, LMC X-1 & LMC X-3 in the Large Magellanic Cloud) show persistent X-ray emission (McClintock & Remillard 2005). This stated, there is now a very strong case for a BH in HMXBs Cyg X-3 (Shrader et al., 2010) and SS433 (e.g. Blundell et al., 2008), both of which show considerable long-term variability. To date, such variability has been observed in very few NS LMXB systems, while all confirmed BH LMXB, confirmed by direct measurement of the radial velocity and spectral type of the companion, are transients.

(ii) Spectral fitting results. The best-fit model of an absorbed disc blackbody with a measured inner disc temperature of ~0.6 keV is softer than is typical of NS LMXBs emitting at similar luminosities, and is characteristic of several observed BH systems in the thermal state. The values of N_H retrieved from fitting are consistent with those derived from source position in K-band optical depth maps that were presented in Kainulainen et al. (2009). This is not the case for the absorbed power law model, which required an extremely steep spectral slope, a much larger value of absorption

column and achieved a less likely best-fit.

The parameter values of the best-fit absorbed disc blackbody model are typical of an accreting $10M_{\odot}$ black hole in the thermally dominant state. If indeed this source is an accreting BH, it is the first confirmed transient non-ULX black hole system in outburst to be identified outside the Local Group.

Chapter 5

Spectral Properties of X-ray Binaries in Cen A

5.1 Introduction

Population studies of extragalactic X-ray binaries (XBs) located beyond the Local Group have been made possible thanks to the excellent sensitivity and spatial resolution of the *Chandra* X-ray observatory (Weisskopf et al., 2000). For over a decade, astronomers have resolved the hard X-ray spectral component of galaxies at sub-arcsecond precision into predominantly non-nuclear point sources (Sarazin et al., 2000). Much research has focused on associations with globular clusters, which contain the majority of X-ray point sources in some elliptical galaxies (e.g. Angelini et al., 2001). It has been observed that metal rich clusters are clearly favored as the hosts of X-ray sources (Kundu et al., 2002) and that the densest clusters preferentially host X-ray sources (Jordán et al., 2007). Ultraluminous X-ray sources, which display isotropic luminosities $L_x > 10^{39}$ erg s^{-1} (Fabbiano, 1989), have been studied in great detail by both *Chandra* and *XMM-Newton*. Optical observations have been used to detect counterparts for these sources in star-forming galaxies (Roberts et al., 2008), and to demonstrate association with globular clusters in a few early-type galaxies (e.g. Maccarone et al., 2007; Brassington et al., 2012b).

The X-ray luminosity function (XLF) is a well-studied statistical characteristic of the X-ray source population for a given galaxy. Grimm et al. (2002) conducted a study of Galactic XBs and found that the XLF of high-mass X-ray binaries (HMXBs) tightly follows a power law above 10^{37} erg s^{-1}, while that of low-mass X-ray binaries (LMXBs) experiences a sharp cut-off above a few 10^{38} erg s^{-1}. Usually there are too few counts to derive the source spectra directly and XLFs are produced using an assumed spectrum, typically a power law with $\Gamma \sim 1.5 - 1.7$, which approximates the emission from Galactic XBs. An LMXB population dominates the XLF of discrete sources in early-type galaxies (see Fabbiano, 2006, for review), due to their older stellar population; early-type galaxies contain

relatively few high luminosity($> 10^{38}\,\mathrm{erg\,s^{-1}}$) sources compared to late-type star-forming galaxies.

The tendancy of LMXBs to dominate the discrete source XLFs in early-type galaxies can be linked to the study of XB populations in late-type galaxies, where two distinct populations have been observed (Prestwich et al., 2009). One population, associated primarily with the bulge, follows an XLF that steepens after a few $\times 10^{38}$ erg s^{-1}, while the other population is associated with the spiral arms and has an XLF consistent with that of HMXBs. The latter population has both softer colours and higher luminosities than Galactic, wind-driven HMXBs, most of which are accretion-powered pulsars with high magnetic fields, and the spectra are well-described by relatively cool disk blackbodies (0.1-1.1 keV), suggesting that they too are Roche-lobe-filling accretion driven systems.

A luminosity break at $L_x \sim 2.5 - 5.0 \times 10^{38}$ erg s^{-1} has been seen in the discrete source population of numerous early-type galaxies (e.g., Sarazin et al., 2001) and is potentially the Eddington-limited extent of the brightest neutron star (NS) LMXBs. The brightest sources are super-Eddington for a 1.4 $\mathrm{M}_\odot$ NS and are probably BH XRBs or the more massive extreme of the NS LMXB population. The luminosity break was examined in detail over a sample of nearby elliptical galaxies by Kim & Fabbiano (2010), who found that the lack of sources with $L_x > 5 \times 10^{38}$ erg s^{-1} was more pronounced for older (> 5 Gyr) galaxies. The observed steepening of the break in the XLF suggests that young early-type XB populations are intermediate in nature between those of star-forming galaxies and old early-types.

A small late-type galaxy is currently merging with Cen A (Graham, 1979); however, the galaxies remain poorly mixed (Quillen et al., 2006). The central regions of the galaxy are notable for the presence of vast dust lanes that contain many active star forming regions. Rejkuba et al. (2011) compared simulated color-magnitude diagrams with deep ACS/HST photometry and concluded that *at least* 70% of stars in NGC 5128 formed 12 ± 1 Gyr ago and a smaller population of more metal rich stars formed in the last 2-4 Gyr. Therefore we expect the population of XBs to be dominated by LMXBs that possess old main sequence companions of $M < 1\mathrm{M}_\odot$ with the potential for a small component from LMXBs with more massive companions.

Six 100 ks *Chandra* observations of NGC 5128 were taken as part of the Cen A Very Large Project (VLP) spanning the course of 2 months in 2007 (§2.5.1 Jordán et al., 2007). The relationship between XBs and globular clusters was investigated by Voss et al. (2009), who confirmed the presence of a low-luminosity break in the XLF at $L_x \sim 1.5 - 4 \times 10^{37}$ erg s^{-1} and a lack of GC sources with

$L_x < 3 \times 10^{36}$ erg s^{-1}. Voss et al. (2009) suggested that this dearth of faint sources may indicate that GC LMXB companions are He rich, which possess a larger critical mass accretion rate $\dot{M}_{crit}$ to become transients. Sources approaching the corresponding luminosity to $\dot{M}_{crit}$ become unstable, and are therefore always above or below this luminosity, leaving a gap in the XLF (§2.3). However, it now appears more likely that the low-luminosity break results from a change in the disk instability criterion at low accretion rates as the disk spectrum peaks at longer wavelengths (van Haaften et al., 2012). These Cen A data were also used by Zhang et al. (2011) as part of a large sample of GC-LMXBs from many elliptical galaxies, and discrepancies between the GC and field XLFs were found across $L_x \sim 10^{36} - 10^{39}$erg s^{-1}.

The current era of deep X-ray observations has enabled more detailed study of individual XBs beyond the Local Group. Brassington et al. (2010) and Fabbiano et al. (2010) present the results of spectral fitting the brightest sources in the early-type galaxies NGC 3379 and NGC 4278, down to a limiting unabsorbed luminosity of $\sim 1.2 \times 10^{38}$ erg s^{-1}. These samples contained 8 and 7 XBs, respectively, of which 7 were coincident with globular clusters (GCs). These works adopted a diagnostic approach to spectral fitting, inferring the state of a source based on fitting simple spectral models, a multi-colored disk blackbody and power law. The true state of the source can be inferred from the behavior of the absorption parameter N_H, which simulations showed to behave in a characteristic way depending on the true state of the source. This method essentially assesses the relative contribution of thermal and non-thermal emission to the spectrum, and is fully described by Brassington et al. (2010) (see section 5.3.2). A further study of 18 transient-type sources from galaxies NGC 3379, NGC 4278 and NGC 4697 by Brassington et al. (2012b) found a host of exotic sources, including a GC ULX in outflow and an unusually luminous bursting source. They distinguished spectral states down to $\sim 10^{38}$ erg s^{-1}.

In Cen A we expect to detect both neutron star (NS) and black hole (BH) XBs, both of which can be transients. It is generally thought that the transient behavior occurs due to the disk ionization instability mechanism (DIM), which was first developed for explaining the dwarf nova outbursts of cataclysmic variables (§1.1.3, Smak, 1984). The essential feature of this model is that the viscosity of ionized gas is larger than that of neutral gas. Its application to X-ray binaries is complicated by irradiation of the outer accretion disk, which is a considerably more important factor (Dubus et al., 2001). Recently, Coriat et al. (2012) tested the DIM with a population of Galactic sources, finding

that the critical mass accretion rate above which sources are persistent is lower than that predicted when irradiation is not taken into account. Black holes are more massive than neutron stars, but have similar radiative efficiencies, and a consequence is that the outer disk temperatures for black hole X-ray binaries at a given orbital period will be smaller than those for neutron star X-ray binaries; thus black hole systems are far more likely to be transient than are neutron star systems (King et al., 1996).

An empirical understanding of the properties of transient X-ray binaries has started to develop. The size of the accretion disk should determine the peak outburst luminosity (e.g. Shahbaz et al., 1998), and this has been borne out as large samples of such transient outbursts have developed (Portegies Zwart et al. (2004); Wu et al. (2010)). As sources change in luminosity, they follow loops in a hardness-intensity diagram (Maccarone & Coppi, 2003), indicating that they are changing spectral shapes hysteretically. In general, the spectral changes occur rapidly, with X-ray binaries in outburst spending most of their time in just a few spectral states (§1.1.3). Remillard & McClintock (2006) posit that BH LMXBs possess spectra characterized by three key spectral states. The thermal-dominant state, where the emission appears to be dominated by a ~ 1 keV multicolor disk blackbody, is essentially the same as the standard geometrically thin, optically thick accretion disk of Shakura & Sunyaev (1973) (§1.1.1). During the ingress and egress of outburst, the source experiences a hard power-law state of $\Gamma \sim 1.7$, the emission likely due to inverse Compton scattering in an optically thin, geometrically thick region (Thorne & Price, 1975). Near the peak of outburst, some sources also exhibit a steep power law state $\Gamma \sim 2.5$ extending to MeV energies with a significant thermal component also present. These spectral states are also associated with the rapid variability of the sources (Homan et al., 2001) and changes in the radio jet properties (Fender et al., 2004).

NS LMXBs generally show similar spectral state phenomenology to BH systems (van der Klis, 1994), but have some differences since the NS surface provides a boundary layer. Nonetheless, in both cases, low/hard type spectra are typically seen below $\sim 2\%$ of the Eddington luminosity, except during the hysteretic intervals near the beginning of outbursts (Maccarone, 2003), and steep power law states are generally seen only at very high luminosities, near the Eddington limit (Remillard & McClintock, 2006). This spectral state phenomenology allows, with high quality spectra, a source to be classified as a candidate BH XB on the basis of its having a cool accretion disk at 10^{38} erg s^{-1}, as discussed by White & Marshall (1984). Burke et al. (2012) used the Cen A VLP data to show

that such distinctions are now possible for sources outside the Local Group, presenting evidence that CXOU J132527.6-430023 (S14, Table 1) is a BH LMXB.

The relative proximity of Cen A, coupled with the superb quality of these data, allows us unrivaled insight into the XBs of an early-type galaxy. In this work we divide sources into thermal and non-thermally dominant states, where appropriate, down to a luminosity of 2×10^{37} erg s^{-1} – reliably measuring the spectral properties of XBs at similar luminosities to those found in the Local Group.

5.2 Data Preparation

5.2.1 Source Detection and Alignment

Each of the six 100 ks observations was analysed using CIAO 4.3, and was reprocessed using the *chandra_repro* script. The *destreak* tool was used to remove the ACIS readout streak, caused by the bright Cen A nucleus. Light curves of each event file were produced using *dmextract* to check for background flares, which were not present. To search for point sources, we used a 0.5-2.0 keV event file for each observation. We used this band because the central AGN is so bright (6-10 count s^{-1} in ACIS-I) that the wings of the PSF contain a significant number of counts, the PSF being broader at higher energies for *Chandra*. An exposure map was created for each file, weighted by the typical power law spectrum of an LMXB, with a photon index of $\Gamma = 1.7$ and absorption column at the Galactic value of $N_H = 8.4 \times 10^{20}$ cm^{-2} (Dickey & Lockman, 1990). Inside a 5′ region centered on the Cen A nucleus, we located point sources using the CIAO tool *wavdetect* using the spectrally weighted exposure map, wavelet scales of 1.0 to 16.0 in steps of $\sqrt{2}$, a threshold significance of 10^{-6} and a maximum of ~ 1 false source per ACIS chip. All subsequent work is within 5′ of the Cen A nucleus, which corresponds to $\sim$ the half-light radius of Cen A (Graham, 1979).

The six observations were aligned by applying an appropriate x-y shift to five of the aspect solution files using the CIAO tool *reproject_events*. All observations were aligned to the point source positions from obsID 8490, chosen because of the proximity of the Cen A nucleus to the ACIS-I focus. Each shift was calculated from the mean offset in α and δ obtained performing $2''$ matching between point source lists from the two observations. To reduce the effect of false matches on our offset correction, we found the mean offset in α and δ and then calculated the mean offset within $\pm 0.5''$ of this mean. By applying $5''$ shifts in α and δ, subsequent $2''$ matching found ~ 6 false matches between source

lists.

To allow for accurate analysis of globular cluster (GC) sources in our subsequent work, we utilized the well known LMXB-GC connection to align our observations to GC positions (Harris et al., 2012), again using $2''$ matching (we estimate an approximate GC size of $\sim 2''$), we calculated the mean x-y shift between LMXB positions in obsID 8490 and the globular clusters, and applied this shift to all obsID, maintaining the initial alignment of the X-ray data.

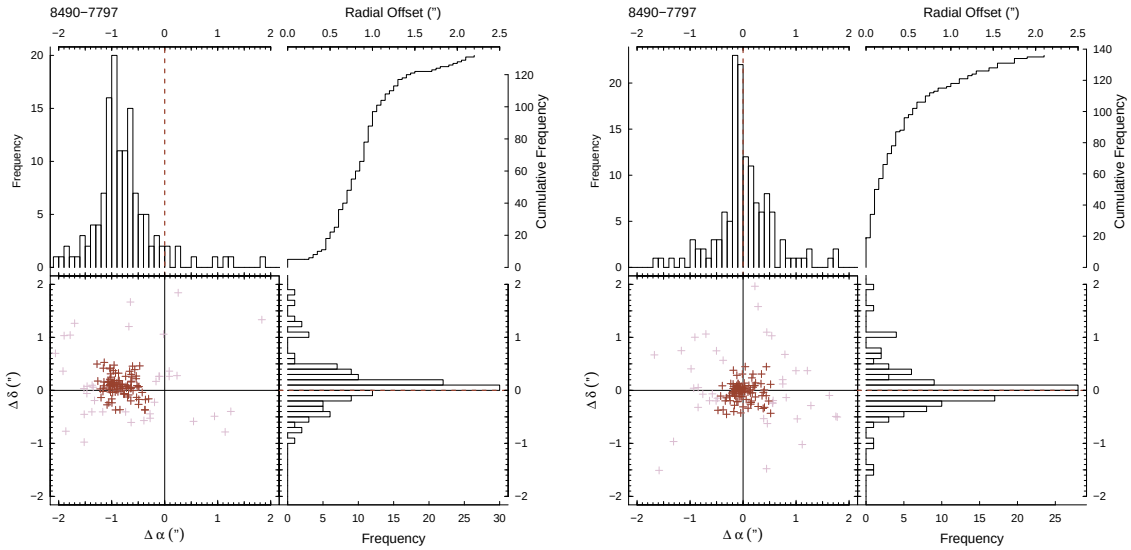

Figure 5.1 Alignment between XPS locations in obsID 7797 and 8490 before and after application of X-Y shift.

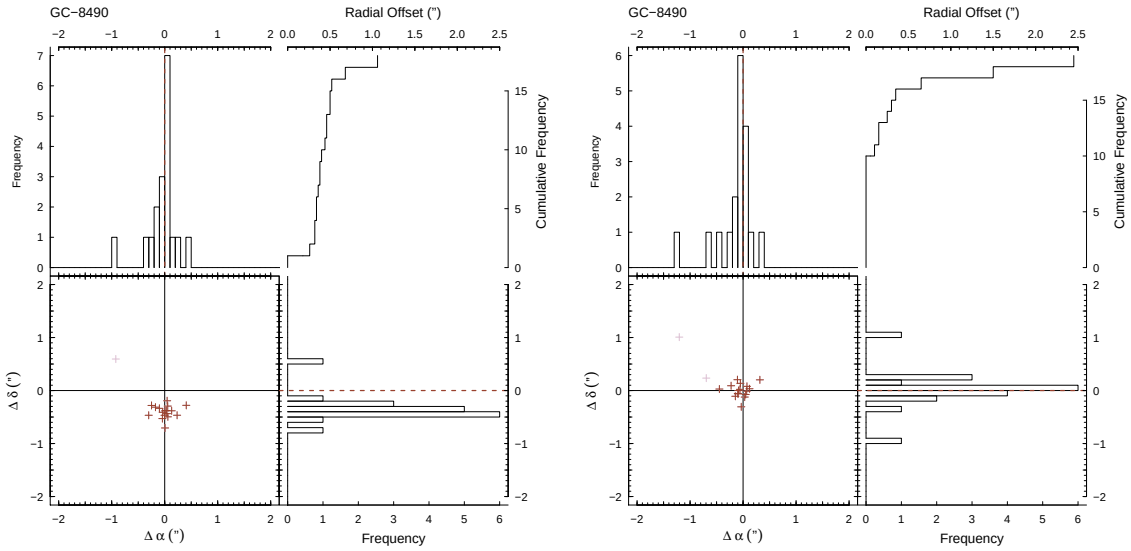

Figure 5.2 Alignment between GC and XPSs, before and after application of X-Y shift.

We created a merged event file using the CIAO script *merge_all* and a corresponding exposure map, as before. The point source list produced by a subsequent run of *wavdetect* was used as a master list of source positions that was consistent with the positions of the individual runs on each obsID, for each observation in which the source was detected. Circular extraction regions were produced, centered on the chip position of each source, whether it is detected in an observation or not. As was the case for the work of Burke et al. (2012), these regions had radius r_{p7}, equal to 90% of the 7 keV extraction radius at that chip position. We then excluded regions in the jet, radio lobe and nucleus from our source list. Additional region files were produced, covering the removed read-out streak of the bright central AGN. Background region files were then created based on annuli from $2r_{p7}$ to $4r_{p7}$, with all source regions and the read-out region excluded. Subsequently we tested for source confusion, which was a significant problem in observations 7798 and 7799, where the point source population is further off-axis and the point-spread function is much wider. Sources found to have a neighbor at angular half-distance $d/2$ inside r_{p7} were given a new extraction region radius of $d/2$ provided that $d/2 \geq r_{p2}$ (where r_{p2} is 90% PSF radius at 2keV), while sources with $d/2 < r_{p2}$ were declared confused (Table 5.1). Spectral fitting using various sized extraction regions for isolated, off-axis sources determined that the normalisation found from fitting was consistent between r_{p2} and r_{p7}, but increased systematically as the extraction radius decreased further.

The net counts inside each extraction region were estimated using *dmextract* to the requisite properties of the source and background region, followed by using *aprates* to calculate a 90% confidence bound for each value or, where appropriate, a 90% confidence upper-limit. Sources were then sorted, based on their highest count-flux observed in any individual observation and names assigned based on this ranking. We present these results in Table 5.1, and emphasize that these are *not* the estimated source counts, but the net source counts present in a given extraction region. This indicates the quality of the resulting spectra we extracted for a given source. The 61 sources presented in table 5.1 are shown overlaid on the merged X-ray image of the Cen A VLP (0.5-8.0 keV) in figure 5.3

Table 5.1. Basic Source Properties

Source	α	δ	Net Counts (0.5 – 8.0 keV) 7797	7798	7799	7800	8489	8490	G − L_{max}	Type	Notes
S1	$13^h25^m18.25^s$	$-43°03'04.''9$	7183^{279}_{139}	8366^{302}_{151}	7372^{284}_{142}	6623^{270}_{134}	9624^{323}_{161}	8454^{303}_{151}	5		Sivakoff et al. (2008)
S2	$13^h25^m38.29^s$	$-43°02'05.''6$	1685^{136}_{68}	1364^{122}_{61}	1429^{125}_{62}	1062^{108}_{54}	1858^{142}_{71}	1366^{122}_{61}	9		
S3	$13^h25^m02.70^s$	$-43°02'43.''3$	1120^{110}_{55}	FoV	FoV	917^{103}_{51}	1575^{132}_{66}	981^{103}_{52}	1	NSC	
S4	$13^h25^m26.16^s$	$-43°01'32.''6$	1101^{114}_{57}	929^{107}_{53}	897^{105}_{52}	555^{87}_{43}	197^{56}_{28}	29^{35}_{17}	0	TBHC	D
S5	$13^h25^m07.64^s$	$-43°01'15.''3$	880^{98}_{49}	174^{46}_{23} C	176^{46}_{23} C	726^{93}_{46}	1009^{105}_{53}	1040^{106}_{53}	5	NSC	GC0129
S6	$13^h25^m06.30^s$	$-43°02'21.''1$	741^{90}_{45}	FoV	FoV	614^{86}_{43}	1024^{106}_{53}	613^{82}_{41}	6		
S7	$13^h25^m23.69^s$	$-43°00'09.''5$	756^{91}_{46}	787^{96}_{48}	871^{101}_{50}	655^{87}_{44}	608^{82}_{41}	603^{82}_{41}	0	NSC	D
S8	$13^h25^m22.88^s$	$-43°01'24.''9$	818^{96}_{48}	703^{94}_{47}	557^{83}_{41}	829^{100}_{50}	618^{85}_{42}	651^{86}_{43}	0	NSC	
S9	$13^h25^m28.19^s$	$-43°00'56.''5$	539^{97}_{48}	684^{102}_{51}	701^{103}_{51}	747^{104}_{52}	431^{91}_{45}	368^{95}_{47}	0		N
S10	$13^h25^m27.45^s$	$-43°02'14.''1$	600^{83}_{41}	SC	SC	SC	537^{78}_{39}	451^{72}_{36}	8		
S11	$13^h25^m54.57^s$	$-42°59'25.''4$	408^{69}_{35}	278^{55}_{28} C	313^{58}_{29} C	353^{62}_{31}	402^{67}_{33}	533^{80}_{40}	0	NSC	GC0330
S12	$13^h25^m32.45^s$	$-43°01'34.''2$	483^{75}_{37}	496^{78}_{39}	440^{74}_{37}	289^{62}_{31}	448^{72}_{36}	291^{59}_{30}	1	PBHC	D
S13	$13^h25^m25.76^s$	$-43°00'55.''8$	451^{76}_{38}	445^{85}_{42}	419^{83}_{41}	208^{68}_{34}	159^{53}_{27}	418^{75}_{37}	0	TBHC	D
S14	$13^h25^m27.58^s$	$-43°00'23.''3$	407^{69}_{34}	409^{74}_{37}	421^{75}_{37}	292^{66}_{33}	19^{25}_{12}	1^{14}_{1}	0	TBHC	D, Burke et al. (2012)
S15	$13^h25^m26.43^s$	$-43°00'54.''2$	309^{68}_{34}	271^{66}_{33}	322^{70}_{35}	225^{64}_{32}	147^{55}_{28} R	417^{78}_{39}	0		N
S16	$13^h25^m31.59^s$	$-43°00'03.''0$	303^{59}_{29}	327^{63}_{31}	338^{64}_{32}	400^{68}_{34}	353^{63}_{31}	409^{70}_{35}	1	NSC	GC0225
S17	$13^h25^m12.89^s$	$-43°01'14.''6$	405^{67}_{33}	311^{63}_{31}	288^{61}_{30}	323^{64}_{32}	349^{63}_{31}	84^{31}_{15}	0	NSC	
S18	$13^h25^m27.50^s$	$-43°01'28.''1$	368^{76}_{38}	323^{81}_{40}	370^{83}_{42}	345^{83}_{41}	355^{74}_{37}	364^{75}_{37}	0		N
S19	$13^h25^m27.08^s$	$-43°01'59.''2$	335^{64}_{32}	274^{71}_{35}	317^{75}_{37}	194^{64}_{32}	363^{66}_{33}	280^{59}_{29}	0	NSC	
S20	$13^h25^m28.75^s$	$-42°59'48.''3$	287^{58}_{29}	301^{62}_{31}	341^{65}_{32}	332^{63}_{31}	329^{61}_{30}	256^{56}_{28}	0	NSC	

Table 5.1 (cont'd)

Source	α	δ	Net Counts (0.5 – 8.0 keV) 7797	7798	7799	7800	8489	8490	$G - L_{max}$	Type	Notes
S21	$13^h25^m22.32^s$	$-42°57'17.''3$	282^{57}_{28}	172^{48}_{24}	330^{63}_{31}	244^{53}_{26}	286^{57}_{29}	312^{62}_{31}	10		
S22	$13^h25^m40.54^s$	$-43°01'14.''9$	265^{55}_{28}	258^{54}_{27}	312^{59}_{29}	217^{50}_{25}	112^{35}_{18}	307^{59}_{30}	1	NSC	
S23	$13^h25^m35.50^s$	$-42°59'35.''2$	186^{47}_{23}	271^{55}_{28}	280^{56}_{28}	308^{59}_{29}	295^{57}_{29}	256^{56}_{28}	6		GC0249
S24	$13^h25^m11.99^s$	$-43°00'10.''7$	288^{56}_{28}	270^{61}_{30}	256^{60}_{30}	256^{58}_{29}	259^{54}_{27}	129^{38}_{19}	1		D
S25	$13^h25^m09.56^s$	$-43°05'29.''2$	286^{57}_{29}	FoV	FoV	SC	65^{32}_{16}	53^{26}_{13}	1	NSC	
S26	$13^h25^m46.58^s$	$-42°57'03.''1$	264^{57}_{28}	247^{52}_{26}	284^{56}_{28}	272^{55}_{27}	92^{34}_{17}	226^{53}_{26}	2	NSC	GC0295
S27	$13^h25^m43.97^s$	$-43°06'06.''8$	273^{56}_{28}	211^{51}_{25}	248^{55}_{27}	70^{37}_{19}	202^{48}_{24}	206^{49}_{24}	6		
S28	$13^h25^m24.19^s$	$-42°59'59.''4$	269^{56}_{28}	SC	SC	226^{52}_{26}	271^{56}_{28}	213^{51}_{25}	0	PBHC	D
S29	$13^h25^m33.93^s$	$-42°58'59.''7$	217^{50}_{25}	217^{50}_{25}	232^{52}_{26}	215^{49}_{24}	257^{54}_{27}	224^{52}_{26}	0	NSC	
S30	$13^h25^m12.03^s$	$-43°00'44.''7$	254^{53}_{26}	SC	SC	R	228^{51}_{25}	81^{30}_{15}	6		
S31	$13^h25^m23.57^s$	$-43°02'20.''5$	246^{53}_{26}	209^{58}_{29}	161^{54}_{27}	219^{58}_{29}	215^{50}_{25}	242^{52}_{26}	0	NSC	
S32	$13^h25^m09.18^s$	$-42°58'59.''3$	249^{53}_{26}	214^{53}_{26}	177^{48}_{24}	209^{52}_{26}	207^{50}_{25}	123^{38}_{19}	0	NSC	GC0134
S33	$13^h25^m23.52^s$	$-43°01'38.''4$	227^{52}_{26}	SC	SC	SC	236^{52}_{26}	243^{53}_{26}	7		
S34	$13^h25^m33.34^s$	$-43°00'52.''7$	208^{51}_{26}	208^{54}_{27}	192^{52}_{26}	193^{52}_{26}	224^{51}_{26}	219^{53}_{27}	0	NSC	D
S35	$13^h25^m18.50^s$	$-43°01'16.''1$	4^{9}_{4}	SC	SC	SC	9^{18}_{8}	218^{50}_{25}	1	T-	GC0182
S36	$13^h25^m32.01^s$	$-43°02'31.''3$	217^{50}_{25}	207^{52}_{26}	212^{52}_{26}	188^{51}_{25}	84^{31}_{16}	153^{42}_{21}	2	NSC	
S37	$13^h25^m29.45^s$	$-43°01'08.''1$	162^{60}_{30}	90^{74}_{37}	146^{77}_{38}	19^{50}_{19}	213^{60}_{30}	153^{60}_{30}	0		N
S38	$13^h25^m22.85^s$	$-43°00'17.''4$	2^{10}_{2}	9^{24}_{9}	3^{19}_{3}	0^{15}_{0}	1^{9}_{1} R	194^{48}_{24}	0	BHC	D
S39	$13^h25^m28.42^s$	$-43°03'15.''2$	162^{43}_{21}	187^{50}_{25}	163^{47}_{24}	171^{49}_{25}	58^{26}_{13}	110^{35}_{18}	1	AGN	
S40	$13^h25^m26.95^s$	$-43°01'04.''8$	171^{66}_{33}	SC	SC	SC	13^{38}_{13} R	186^{65}_{32}	0		N

Table 5.1 (cont'd)

Source	α	δ	Net Counts (0.5 – 8.0 keV) 7797	7798	7799	7800	8489	8490	$G - L_{max}$	Type	Notes
S41	$13^h25^m26.94^s$	$-43°00'52.''5$	136^{56}_{28}	162^{57}_{29}	135^{55}_{27}	164^{60}_{30}	120^{54}_{27}	182^{62}_{31}	1		N
S42	$13^h25^m16.40^s$	$-43°02'55.''1$	190^{46}_{23}	133^{48}_{24}	137^{48}_{24}	137^{49}_{24}	163^{44}_{22}	103^{34}_{17}	0	NSC	
S43	$13^h25^m28.20^s$	$-43°02'53.''4$	156^{43}_{21}	108^{40}_{20}	112^{41}_{20}	98^{39}_{19}	179^{45}_{22}	170^{44}_{22}	6		
S44	$13^h25^m20.06^s$	$-43°03'10.''1$	166^{43}_{22}	94^{43}_{21}	134^{47}_{23}	124^{46}_{23}	146^{41}_{21}	136^{39}_{20}	2	NSC	GC0587
S45	$13^h25^m39.06^s$	$-42°56'53.''7$	78^{36}_{18}	104^{35}_{17}	51^{26}_{13}	158^{42}_{21}	87^{33}_{17}	125^{45}_{23}	2	NSC	
S46	$13^h25^m25.15^s$	$-43°01'26.''9$	146^{49}_{24}	SC	SC	SC	125^{46}_{23}	88^{41}_{21}	0	NSC	D
S47	$13^h25^m23.07^s$	$-43°01'45.''6$	139^{43}_{21}	SC	SC	SC	128^{42}_{21}	147^{44}_{22}	2	NSC	
S48	$13^h25^m32.42^s$	$-42°58'50.''2$	87^{34}_{17}	143^{42}_{21}	104^{36}_{18}	133^{39}_{19}	87^{32}_{16}	121^{41}_{20}	1	β NSC	GC0230
S49	$13^h25^m52.72^s$	$-43°05'46.''4$	72^{33}_{17}	61^{30}_{15}	108^{37}_{19}	108^{40}_{20}	71^{31}_{15}	138^{42}_{21}	9		GC0320
S50	$13^h25^m10.09^s$	$-42°56'08.''3$	FoV	FoV	FoV	138^{45}_{22}	124^{43}_{21}	75^{37}_{18}	0	FG	
S51	$13^h25^m45.47^s$	$-42°58'15.''8$	117^{40}_{20}	114^{36}_{18}	118^{36}_{18}	123^{37}_{19}	133^{40}_{20}	95^{40}_{20}	6		
S52	$13^h25^m25.50^s$	$-43°01'29.''9$	127^{48}_{24}	SC	SC	SC	0^{NA}_{NA}	8^{22}_{8}	0		N
S53	$13^h25^m23.50^s$	$-42°56'51.''7$	111^{37}_{18}	119^{41}_{20}	131^{42}_{21}	113^{37}_{18}	95^{36}_{18}	129^{44}_{22}	1	NSC	
S54	$13^h25^m23.63^s$	$-43°03'25.''7$	58^{26}_{13}	58^{35}_{18}	66^{37}_{18}	82^{40}_{20}	117^{37}_{18}	25^{17}_{8}	1		
S55	$13^h25^m39.87^s$	$-43°05'01.''8$	110^{36}_{18}	111^{38}_{19}	103^{37}_{18}	97^{39}_{19}	92^{32}_{16}	87^{32}_{16}	0	NSC	GC0266
S56	$13^h25^m38.10^s$	$-43°05'13.''7$	62^{27}_{14}	71^{32}_{16}	80^{33}_{16}	74^{36}_{18}	81^{31}_{15}	112^{36}_{18}	0		
S57	$13^h25^m55.11^s$	$-43°01'18.''3$	96^{37}_{18}	96^{33}_{16}	77^{30}_{15}	84^{31}_{16}	91^{33}_{16}	112^{41}_{20}	0		
S58	$13^h25^m24.76^s$	$-43°01'24.''6$	22^{31}_{15} R	R	R	SC	77^{39}_{20}	112^{43}_{22}	0		
S59	$13^h25^m07.71^s$	$-42°56'29.''8$	FoV	FoV	FoV	66^{35}_{18}	103^{41}_{20}	109^{40}_{20}	2	NSC	
S60	$13^h25^m23.07^s$	$-43°01'34.''3$	103^{39}_{19} R	SC	SC	SC	100^{39}_{19}	80^{36}_{18}	0		

Table 5.1 (cont'd)

Source	α	δ	Net Counts (0.5 – 8.0 keV) 7797	7798	7799	7800	8489	8490	G − L_{max}	Type	Notes
S61	$13^h25^m11.55^s$	$-43°02'26.''3$	103^{34}_{17}	SC	SC	SC	78^{31}_{15}	109^{35}_{17}	6		

Note. — Type column is explained in section 5.2.2, see also the extended discussion in section 4.3.

[N]Within 20″ of the Cen A nucleus

[R]Source is coincident with read-out streak

[C]Source is coincident with chip-edge

[FoV]Source is outside of the field-of-view

[SC]Source confused

[GC]Coincident with globular cluster

[D]Coincident with dust lane

5.2.2 Source Selection

The presence of short-term variability may indicate important spectral changes within an X-ray source, and so we choose to exclude sources that vary during an observation from our sample. To assess the variability we made use of the Gregory-Loredo algorithm (Gregory & Loredo, 1992), implemented as the CIAO tool *glvary*[1]. This produces an optimally-binned lightcurve for each source in each observation, and calculates an odds ratio of each lightcurve against a constant count-rate, with a ratio of 10 indicating the highest probability of variation and 0 being consistent with a constant count rate. A source is defined as showing definite variability when this index is ≥ 6. The maximum ratio for each source is reported in Table 5.1. Given the potential for rapidly changing spectra within an observation, sources with a maximum score of 6 or higher were removed from our sample for spectral analysis.

At this point we also flagged sources within $20''$ of the Cen A nucleus, which require more careful extraction to deal with the significant flux contribution present from the nucleus. This contribution likely exceeds the source counts in some observations for any sources with fewer than ~ 300 counts, depending on how far off-axis the nucleus is in the observation. Analysis of the sources that showed definite intra-observation variability and the sources within $20''$ of the nucleus will be reported in a future work.

Table 5.1 summarises some basic source data; the celestial position, net counts in each source region for each observation and the intra-observational variability ($\mathrm{G} - \mathrm{L}_{\max}$). We also include our eventual source classification of persistent (P) or transient (T) black hole candidates (BHC), neutron star candidates (NSC), foreground stars (FG), active galactic nuclei (AGN) and also denote S48 as a highly-magnetised NSC (β).

The distribution of hardness ratios showed that source S50 was far softer than the rest of the population, with S/H~ 9 where S is the counts from 0.5–2.0 keV and H is the counts from 2.0–8.0 keV. The spectrum of this source was well fit with an absorbed apec model (Raymond & Smith, 1977), peaking at 0.9 keV, across all observations, consistent with expectations from a foreground star. Inspection of the data taken with the Inamori Magellan Areal Camera and Spectrograph (IMACS) camera on the Magellan Observatory Baade telescope (Harris et al., 2012), showed that S50 is coincident with an object consistent with being stellar. We used ishape, which determines

[1] *http://cxc.harvard.edu/ciao/ahelp/glvary.html*

an object's shape parameters by analytically convolving a *King62* (King, 1962) model with the PSF of the image, which is then subtracted from the input image of the object itself. From the residual image, the pixels are assigned a weighting based on their deviation from other pixels at the same distance from the center of the object, and then a reduced χ^2 is calculated. The initial parameters of the model are adjusted and the process is repeated with the new model until a minimation of the χ^2 is obtained and convergence is reached. Our best fit with *ishape* indicates that our object has a FWHM of 0.02 pc, consistent with a star, and very different from the typical globular cluster which are generally 2-4 pc in size (Harris et al., 2010), and we do not consider it further.

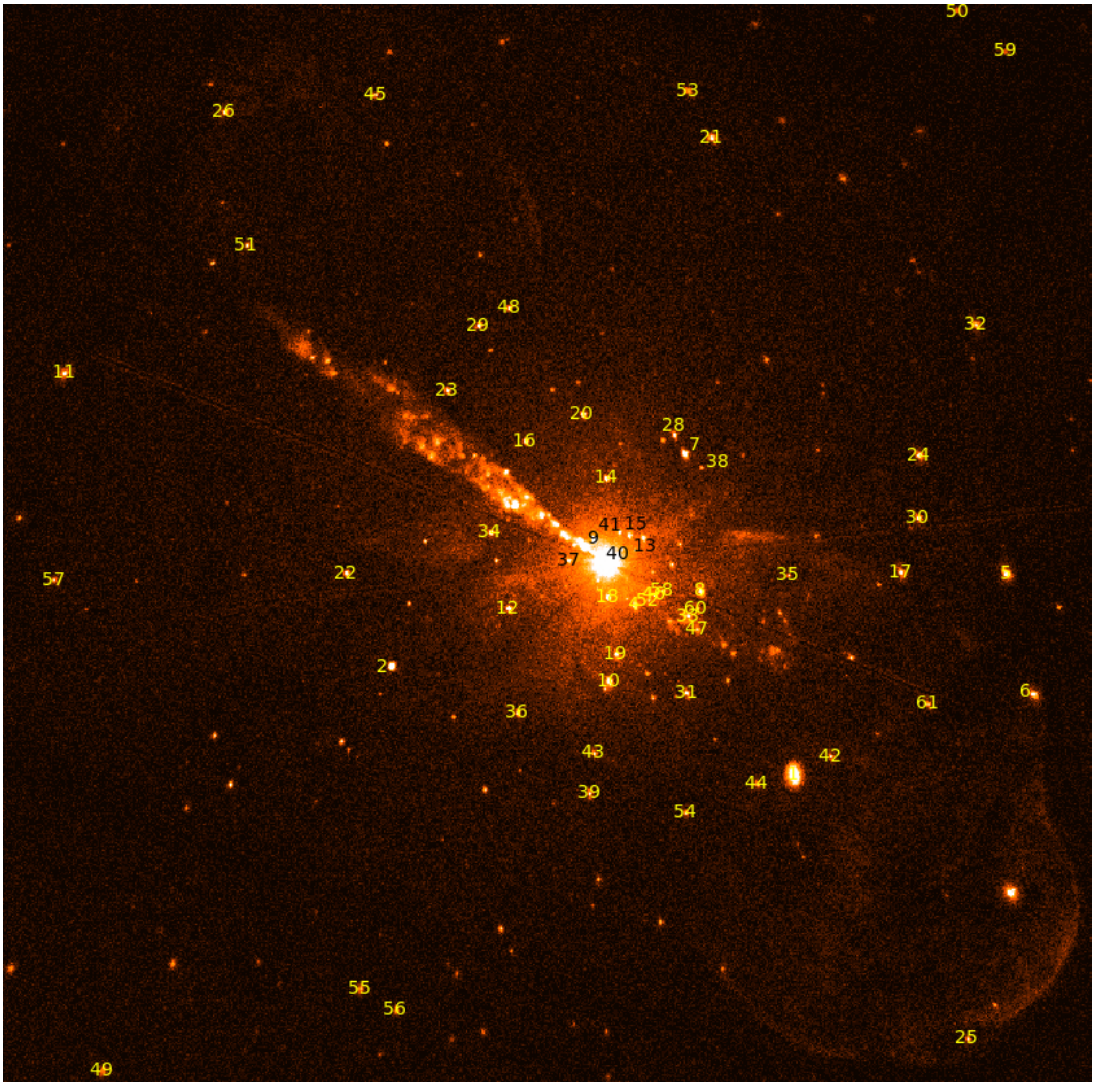

Figure 5.3 Labels show sources $1-61$ overlaid on merged 0.5-8.0 keV VLP (600 ks) image of Cen A.

In our spectral fitting sample we estimate that there are at most $4-5$ sources from the cosmic

X-ray background (CXB) present. We arrived at this figure using the results of Voss & Gilfanov (2006); Voss et al. (2009), who state that there are $34 - 47$ sources inside the central $10'$ of Cen A above 10^{37} erg s^{-1}. Correcting for the fact that our sample includes only $34/60$ sources at or above this luminosity, and only examines a region of radius $5'$, this leaves $\approx 4 - 5$. We believe this number to be a secure maximum, as our selection criteria will give some preference in the sample towards brighter sources, i.e. flux regimes where there are fewer CXB sources per square degree, and note that the numbers estimated by Voss & Gilfanov (2006) are still 50% larger than predicted by using the results of Moretti et al. (2003) alone.

5.3 Spectral Analysis

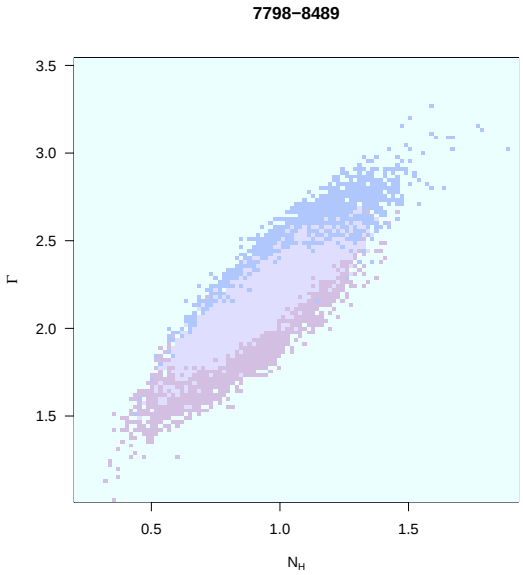

Figure 5.4 Example MCMC output binned over N_H and Γ for two spectra of S24. We show 90% confidence regions, with the overlap indicated by the lighter region. There is an $\sim 75\%$ probability that true combinations of N_H and Γ are shared between the two MCMCs.

Our primary objective is using spectral fitting of sample models to infer the spectral state of each source. Ideally, this would involve fitting all observations of a given source together, taking advantage of more bins to reduce the high-likelihood region of the parameter space. A more constrained absorption parameter, N_H provides a stronger argument for a given spectral state (see section 5.3.2). However, it is often the case with joint fitting that spectra from different states of a source will produce a best fit that, while well constrained and even statistically 'acceptable', may poorly represent the

true spectra individually. To address this issue, we designed a comparative test between the spectra to allow us to judge the extent of spectral changes for each source, and thus the appropriateness of joint fits. Since we allow for changes in luminosity for a given spectral state, and only sought to determine a difference in the spectral shape of a source, the normalization of each spectrum is kept free in the joint fits.

Spectra were extracted using the CIAO script *specextract* for each observation that had > 100 net counts. We chose to fit only the spectra of sources where we measured > 150 counts in one observation, or more than two observations with > 100 counts. This is motivated by the Brassington et al. (2010) simulations, which indicate the method is sound to use in the $\sim 100 - 200$ count regime, but the results become less statistically robust below this number.

5.3.1 Spectral Variation

Using the spectral fitting package *XSPEC* (Arnaud, 1996), we performed spectral fits using an absorbed power law to the ungrouped spectrum, then used the covariance matrix of each fit in a subsequent Markov chain Monte Carlo (MCMC) exploration of the parameter space for each spectrum of each source in the sample. We then tried to compare each spectrum with the (up to) five other spectra for a given source. For the MCMC results of a particular spectrum, we binned the parameter values of N_H and Γ, which describe the spectrum, into a 100×100 grid; the resulting bin widths were used to extend the grid, if necessary, to cover the other set of parameter co-ordinates. This approach was intended to prevent the binning being too coarse or fine, the extent of the MCMC-explored region of the parameter space increasing as the number of counts in a given spectrum decreased. The number of counts in each bin, normalized by the total number of samples, gives the approximate 2D posterior probability density for the N_H – Γ space. The probability that the true coordinate is in an overlapping bin is the product of the sum of the probabilities for all the overlapping bins from both distributions. We adopted an *a priori* threshold of $< 5\%$ for determining if two spectra were too dissimilar to use in a joint fit, and the resulting spectral groups can be seen in our preliminary spectral fitting results (Table 5.3). We show typical 90% confidence interval contours (fewest bins to contain 90% of all samples) of two similar spectra from S24 in figure 5.4. For a handful (~ 3) of instances when the behaviour of a source was not clear cut, i.e. spectrum A and spectrum B were different, while both were consistent ($> 5\%$) with spectrum C we took the more consistent of the

two groupings, guided by the 90% confidence contours (i.e. a noticeable difference in shape inside the parameter space between two groups).

5.3.2 Spectral Fitting

After identifying sets of spectra for each source, we proceeded to fit absorbed single-component models to the 0.5-8.0 keV spectra, following the prescription of Brassington et al. (2010), who showed that the results from such fits – particularly the behavior of absorption parameter N_H – can give a strong indication of the actual spectral state of a given source. These results are summarised as a scheme for spectral fitting by means of a flow-chart (Figure 2.4) and we direct the interested reader to inspect this chart in tandem with our results. Thermally dominant spectra, where a disk blackbody component accounts for $> 60\%$ of the source flux, show a level of absorption significantly above the Galactic value N_H^{Gal} (Dickey & Lockman, 1990) when fit with an absorbed power law, while a power law dominated spectrum will have an absorption less than the Galactic value when fit with an absorbed disk blackbody. If N_H is significantly above the Galactic value for both fits, then the source was deemed to have intrinsic absorption. If N_H was above N_H^{Gal} for the power law fit but significantly below N_H^{Gal} for the $diskbb$ model, then this indicates a thermal dominant spectrum with some power law component also present. Conversely, if N_H from fitting was zero for both models, then this was indicative of the source spectrum being dominated by a steep ($\Gamma > 1.7$) power law component with a cool ($kT_{in} < 0.5$ keV) disc component also present. More specific effects are discussed in section 5.4.

We present results of fitting $phabs \times powerlaw$ and $phabs \times diskbb$ in Table 5.3, and indicate in the last column the spectral state(s) suggested by the Brassington et al. (2010) systematic scheme. We emphasize that the results in this table demonstrate a phenomenological test. Sources judged to be in a thermal dominant or power law dominant state were subsequently re-fit, imposing a lower limit on N_H at N_H^{Gal}, and we refer the reader to Table 5.2 for the realistic source properties. The tendency for so many of the sources coincident with the dust lane to have an inferred 'intrinsic' absorption (i.e., N_H from both absorbed power law and disk blackbody models was significantly above N_H^{Gal}), meant that we tried to determine the 'true' absorbing column along those lines-of-sight, for a more realistic and useful comparison.

5.3.3 Dust lane sources

There is clearly a strong correlation between sources that possess intrinsic absorption, according to our method, and coincidence with the dust lane, as expected if the sources lie behind or within the dust. To define the spectral states for these sources, we obtain a value of N_H independently from the X-ray spectral fitting, and consider the extra absorbing column in Cen A as well as the Galactic contribution. We converted a K-band optical depth map of the dust lane (Kainulainen et al., 2009) to N_H assuming $A_K \sim 0.09 A_v$ (Whittet, 1992) and $N_H \sim A_v \times 2.1 \times 10^{21}$ cm^{-2} (Güver & Özel, 2009). The mean N_H was then calculated using the IRAF tool *imexam*[2] for each source coincident with the dust lanes, using circular apertures of radius $2''$, centered on the source position (Figure 5.10). The N_H^{DBB} and N_H^{PO} from spectral fitting were compared to the mean N_H inferred from the optical depth map at each source position, to infer the true spectral state, if possible. Dust lane sources that we determined to be dominated by disk blackbody or power law spectra are included in Table 5.2, and in Figures 5.6 & 5.7 when the parameters could be constrained. A full discussion of these sources can be found in Section 5.4.1.

5.3.4 Inter-Observation Variability

We can further our knowledge of these sources by taking the degree of inter-observational variability into account over the course of our 2 month snapshot. We calculated the net photon flux[3] for each source region using the ciao tool *aprates*[4], after calculating the average effective exposure in the region using a 0.5-8.0 keV exposure map. To assess the variability, we calculate the fractional variability of the source, which we define for a set of fluxes F_i as $(F_{max} - F_{min})/F_{max}$. For sources that are below the detection threshold in some observations, the 90% upper-limit was used for F_{min}. We present these results in Figure 5.5, where we show the fractional variability against spectral parameter (kT_{in} & Γ) for a given spectral state. The majority of sources display $10 - 40\%$ variability over the time period spanned by the VLP.

[2] http://stsdas.stsci.edu/cgi-bin/gethelp.cgi?imexamine
[3] We emphasise that this does not involve assuming a spectral model
[4] http://cxc.harvard.edu/ciao4.2/ahelp/aprates.html

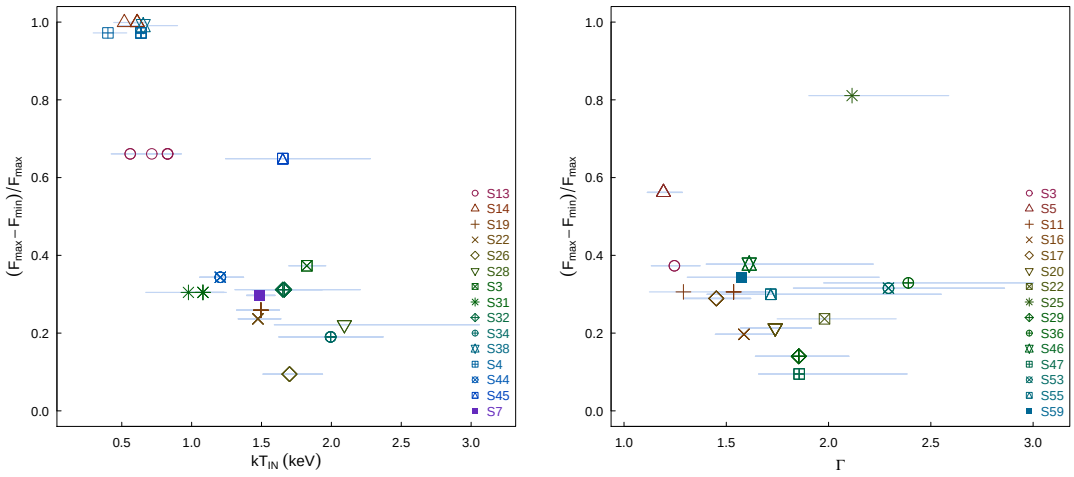

Figure 5.5 Inter-observation fractional variability against *(Left)* thermal state inner-disk temperatures and *(Right)* Power law state photon indices.

5.4 Discussion

In this section we first discuss each source coincident with the dust lane in turn, identifying the spectral state our method favors where possible. We then present the unabsorbed luminosities as a function of key parameters of thermal and power law dominated states, and discuss the implications and source classification based on these results. We discuss possible transient NS LMXBs in outburst and also those states for which we are not able to make an adequate diagnosis using simple models. Finally, we offer an explanation for an apparent enhancement in the number of accreting BHCs found beyond the vicinity of the merged late-type galaxy.

5.4.1 Dust lane sources

For those sources that are coincident with the dust lane and where spectral fitting suggests a high N_H we infer the spectral state of a given source based on the mean absorption calculated from a K-band optical depth map. We discuss each source in turn below, and where a particular state is suggested we present it in Table 5.2. Our spectral diagnostic, inferring the spectral state from fitting simple spectral models, is outlined in section 5.3.2.

S4

The brightest dust lane source, S4, is $\sim 30''$ from the Cen A nucleus, coincident with a southern filament of the dust. From the optical depth map we calculate $N_H = (3.64 \pm 0.07) \times 10^{21}$ cm^{-2}, which, while above the Galactic value, is still below $N_H^{DBB} (= 6.5 \times 10^{21}$ cm$^{-2})$. It seems likely that the spectrum is dominated by a thermal component; the discrepancy in absorption is either a consequence of additional intrinsic absorption from material local to the source, or the result of some significant non-thermal component contributing to the spectrum. The true kT_{in} may be somewhat cooler than that found from just fitting $phabs(diskbb)$, as suggested by the simulations of Brassington et al. (2010), an effect we discuss in more detail for S12. Fixing N_H at the value obtained from the optical depth map preserves the cool disk temperature in spectral fitting. There is a large fall in flux from this source, the spectral counts falling to 29 in the final observation from over 1100 in the first; however, it is still above our detection limit. The low inner-disk temperature in the thermal state, combined with the high inter-observation variability, strongly suggests that this is a BH LMXB transient candidate, similar to S14 (Burke et al., 2012). NS LMXBs at this luminosity, $L_x > 10^{38}$ erg s^{-1}, typically have a much flatter spectral shape over the *Chandra* band.

S7

For S7 the absorption map gave $N_H = (6.52 \pm 0.08) \times 10^{21}$ cm^{-2}, which is below N_H^{PO} but above N_H^{DBB}. This suggests that the source is behind the dust lane in a thermal dominant state, but with some power law component present. We are not able to determine the flux contribution of the power law component. Based on the simulations of Brassington et al. (2010) we estimate the absolute systematic error to be ± 0.5 keV on the temperature of the disk component.

S12

In the case of S12, the inferred $N_H = (16.5 \pm 0.2) \times 10^{21}$ cm^{-2}. This is significantly above the values found from spectral fitting, and allows for the source to be located within the dust lane, rather than behind it. If we assume that the source is behind the dust lane, i.e. has a line-of-sight absorption column of $N_H = (16.5 \pm 0.2) \times 10^{21}$ cm^{-2}, then we have fitting results that were not produced by the simulation work of Brassington et al. (2010), where N_H^{DBB} went to zero and N_H^{PO} was less than the Galactic value, which was the result obtained when the simulated spectrum was a dominant,

steep power law component with a cool disk also present. Those simulations were based on a fairly low value of N_H, less than 1×10^{21} cm^{-2}, and so the tendency for N_H^{DBB} to go to zero for instances where $N_H^{PO} < N_H^{Galactic}$ is not surprising, as N_H^{DBB} will nearly always be less than N_H^{PO} and so the size of the high-likelihood region of the parameter space is small.

To investigate our ability to recover the parameters of a heavily absorbed cool disk plus steep power law spectrum, we carried out simulations in XSPEC. We assumed a heavily absorbed ($N_H \sim 1.6 \times 10^{22}$ cm^{-2}) cool disk ($kT_{in} \sim 0.4$ keV) and a steep power law ($\Gamma \sim 2.6$). Sets of 200 simulated spectra were produced, varying the $diskbb$ fraction of the total flux from 0.1 to 0.9. We then fitted $phabs \times diskbb$ to these spectra to look at the effect of varying the initial spectral parameters on those recovered by fitting a simple, single component spectrum. We found that the fits recovered the initial properties of the disk when the simulated spectrum was thermally dominated, but as the fraction of flux taken by the power law component increased in significance, so the recovered value of N_H decreased, eventually reaching N_H^{DBB} comparable with that found from fitting the spectra of S12. A consequence of lower N_H^{DBB} as the power law contribution increased was that the recovered inner-disk temperature rose to beyond 1.5 keV. This fits neatly with the $phabs \times diskbb$ fit to S12, which has a high value of kT_{in} ($=3.96^{-1.73}_{+0.87}$ keV), implying an unphysically warm accretion disc around a stellar BH. We take this result as an indication that our assumption about S12 is correct; that it is obscured fully behind the dust lane, with a line-of-sight $N_H > 10^{22}$ cm^{-2}, and has a spectrum dominated by a power law with some small disk contribution. Further simulations suggest that high inner-disk temperatures (> 3 keV) are also recovered with a less steep power law component ($\Gamma < 1.5$). This is clearly a complicated parameter space, the full properties of which are beyond the scope of this work to investigate. It is worth noting that these results indicate a significant under-estimation in the flux of the source by just fitting simple models; the actual L_x is probably $> 6 \times 10^{38}$ erg s^{-1}, and could conceivably be $> 10^{39}$ erg s^{-1}, based on our simulations. Fitting more complex (two component) models failed to give acceptable fits or successfully accommodate both components, with poorly constrained parameters.

S12 is analogous to S102 in NGC 3379 (Brassington et al., 2010), for which simulations indicated that the spectra were dominated by a steep power law with some contribution from a cool disk, while a successful fit was achieved using a combined $diskbb + powerlaw$ model yielding $kT_{in} \sim 0.14$ keV and $\Gamma \sim 1.6$ and $L_x = 1.1 \times 10^{39}$erg s^{-1}.

S13

We calculate $N_H = (7.95 \pm 0.13) \times 10^{21}$ cm^{-2} in the vicinity of S13, which is below or consistent with the N_H^{PO} values obtained, but these are poorly constrained and the fits are statistically poor with $\chi^2_\nu > 1.3$. Conversely, N_H is above N_H^{DBB}, which is significantly larger than N_H^{Gal}. As was the case with S7, such results are indicative of a thermally dominant state with some non-thermal emission also present, by which we mean that the thermal state contributes $> 60\%$ of the total flux. The inner temperature in the disk of this source is less than that typically seen for NS systems at equivalent luminosities. This source displays high inter-observation variability, but remains in outburst throughout the length of our observations. This variability coupled with the low inner-disk temperature suggests that this system is a BHC LMXB, though examination of further observations will be required to show more substantive evidence of the transient nature of this source.

S14

S14 is a transient source, analysis of which has previously been reported in Burke et al. (2012). N_H^{PO} was larger than the value inferred from the dust lane, N_H^{DBB} was found to be consistent with this value, which led us to conclude the source was in a thermally dominant state. The cool disk at high luminosity, coupled with its transient nature, led us to conclude that the source is a BH LMXB candidate. Our fitting results for the first group suggests the presence of a power law component in the more luminous state.

S24

While S24 is coincident with the dust lanes, its position is not covered by our optical depth map. This being the case we cannot feasibly proceed further with our inference of spectral states based on the behavior of N_H, given that our first stage of spectral fitting is highly suggestive of increased line-of-sight absorption, above the Galactic value.

S28

For S28, we find $N_H = (7.63 \pm 0.12) \times 10^{21}$ cm^{-2} from the K-band optical depth map. We fit two groups of spectra for this source. For the first group, consisting of spectra from obsIDs 7797 and 8490, we find a large uncertainty on N_H for both models, which is consistent with any location

relative to the dust lanes at the 2σ level. The second group, using spectra from obsIDs 7800 and 8489, have N_H significantly above $N_H^{Galactic}$, which indicates that there is significant absorption along the line-of-sight to the source, which we attribute to the dust lane. For this group, N_H^{PO} is above the value obtained from the optical depth maps, while N_H^{DBB} is consistent with this value, suggesting that the source is in a thermally dominant state. Assuming that the source is behind the dust lane, as the second set of spectral fitting results suggests, and assuming a 1σ knowledge of $N_H^{PO} = 0.51^{0.26}_{0.24} \times 10^{22}$ cm^{-2} and $N_H^{DBB} = 0.44^{0.18}_{0.15} \times 10^{22}$ cm^{-2}, then, for the first group, the situation is similar to that seen in S12, where N_H^{PO} is consistent with the line-of-sight value while N_H^{DBB} is lower but non-zero. The higher, unrealistic (and poorly constrained), inner-disk temperature of 5.97 keV is consistent with this result, suggesting that the source is in a power law state during these epochs, with a minor contribution from a cool ($kT_{in} < 0.5$ keV) disk component.

S34

S34 is close to the edge of the dust lane but is not coincident with the lane itself. The high N_H in one of the spectral fitting groups, of which obsID 8490 provided the only spectrum, prompted us to investigate the line-of-sight absorption using the optical depth map; we found $N_H = (1.10 \pm 0.08) \times 10^{21}$ cm^{-2}, consistent with the Galactic value. We are not able to deduce more about the state from this information; the source could have some intrinsic absorption not present in the other obsIDs. This behavior is reminiscent of the black hole in globular cluster RZ 2109 from NGC 4472, where the variation in N_H is believed to be the result of a photoionizing, high-velocity wind (Shih et al., 2010). However, S34 is much fainter than this class of system, and the apparent increase in absorption could be an effect of incorrectly modelling the boundary layer emission, or the absorption may be a real effect and the system is at a high inclination, undergoing a long period of dipping.

S38

S38 is only detected in obsID 8490. From the optical depth map, we infer $N_H = (4.54 \pm 0.07) \times 10^{21}$ cm^{-2} for this source. This is consistent with N_H^{DBB} and significantly less than N_H^{PO}, suggesting a source in the thermally dominant state with an inner disk temperature ~ 0.65 keV, similar to S14, albeit at a lower luminosity of $L_x \sim 5.5 \times 10^{37}$ erg s^{-1}, which points to it being a transient BH LMXB candidate.

S46

The X-rays from S46 would only experience an absorption column of $N_H = (2.81 \pm 0.08) \times 10^{21}$ cm^{-2} if the source is behind the dust lane. N_H^{PO} is less than this line-of-sight value, and consistent with $N_H^{Galactic}$ while N_H^{DBB} tends to zero, suggesting a source in front of the dust lane, in a power law dominated hard state.

Table 5.2. Spectral fits using inferred dominant model (0.5-8.0 keV)

Source	N_H 10^{22} cm^{-2}	kT_{in} keV	L_x $(0.5-10.0$ keV) 10^{37} erg s^{-1}	χ^2/dof	Inferred N_H 10^{22} cm^{-2}	Note
DBB						
S3	$0.08^{0.02}_{0.08}$	$1.82^{0.14}_{0.13}$	$24.58^{1.75}_{1.72}, 39.27^{2.41}_{2.36}$	120.7/140		
S4	$0.65^{0.07}_{0.06}$	$0.64^{0.03}_{0.03}$	$21.06^{2.23}_{2.04}, 37.49^{3.41}_{3.09}$	206.9/203	0.364 ± 0.007	D
S4	$0.59^{0.48}_{0.35}$	$0.40^{0.13}_{0.11}$	$6.15^{7.79}_{2.57}$	10.0/14		D
S7	$0.51^{0.07}_{0.06}$	$1.49^{0.11}_{0.1}$	$18.6^{1.5}_{1.4}, 27.2^{1.8}_{1.8}$	271.5/256	0.652 ± 0.008	D
S8	$0.08^{0.05}_{0.05}$	$1.93^{0.25}_{0.17}$	$15.71^{1.41}_{1.34}, 21.91^{1.85}_{1.76}$	135.7/132		
S8	$0.08^{0.03}_{0.08}$	$1.1.74^{0.3}_{0.23}$	$14.19^{1.37}_{1.29}, 21.07^{2.12}_{1.96}$	87.8/87		
S13	$0.40^{0.13}_{0.12}$	$0.83^{0.1}_{0.09}$	$10.57^{1.53}_{1.33}, 14.41^{1.93}_{1.69}$	110.7/89	0.75 ± 0.13	D
S13	$0.39^{0.37}_{0.29}$	$0.56^{0.17}_{0.14}$	$4.34^{2.55}_{1.26}, 6.33^{3.72}_{1.77}$	37.5/30		D
S13	$0.35^{0.21}_{0.17}$	$0.71^{0.13}_{0.11}$	$11.65^{2.68}_{1.97}$	44.9/33		D
S14	$0.37^{0.12}_{0.11}$	$0.61^{0.07}_{0.06}$	$7.00^{1.24}_{1.03}, 12.33^{2.07}_{1.68}$	72.0/71	0.60 ± 0.1	D
S14	$0.81^{0.28}_{0.23}$	$0.52^{0.08}_{0.08}$	$18.8^{7.4}_{4.4}$	14.6/27		D
S19	$0.09^{0.08}_{0.09}$	$1.50^{0.13}_{0.17}$	$5.45^{0.92}_{0.89}, 7.59^{0.85}_{0.8}$	119.3/135		
S22	$0.08^{0.03}_{0.08}$	$1.47^{0.16}_{0.14}$	$4.93^{0.71}_{0.68}, 6.49^{0.76}_{0.73}$	63.6/67		
S26	$0.08^{0.05}_{0.08}$	$1.70^{0.24}_{0.19}$	$6.13^{0.83}_{0.77}, 7.02^{0.97}_{0.89}$	51.6/60		GC
S28	$1.10^{0.45}_{0.4}$	$2.09^{0.97}_{0.5}$	$11.62^{1.76}_{1.66}, 11.9^{1.7}_{1.1}$	34.8/28	0.76 ± 0.12	D
S31	$0.08^{0.05}_{0.08}$	$1.08^{0.15}_{0.13}$	$4.01^{0.57}_{0.53}, 4.2^{0.55}_{0.53}$	39.7/43		
S31	$0.12^{0.38}_{0.12}$	$0.98^{0.27}_{0.31}$	$3.1^{0.94}_{0.64}$	13.3/12		
S32	$0.08^{0.07}_{0.08}$	$1.66^{0.27}_{0.23}$	$5.26^{0.9}_{0.82}, 6.56^{1.08}_{0.98}$	28.2/50		GC
S32	$0.08^{0.13}_{0.08}$	$1.65^{0.55}_{0.34}$	$5.46^{1.19}_{0.97}, 7.67^{2.04}_{1.62}$	16.0/16		GC
S34	$0.08^{0.12}_{0.08}$	$1.99^{0.37}_{0.37}$	$4.71^{0.82}_{0.76}, 6.19^{1.01}_{0.92}$	52.6/67	0.11 ± 0.08	
S38	$0.60^{0.52}_{0.43}$	$0.65^{0.25}_{0.17}$	$5.48^{3.68}_{1.70}$	7.8/9	0.45 ± 0.07	D
S44	$0.08^{0.08}_{0.08}$	$1.21^{0.17}_{0.15}$	$2.41^{0.42}_{0.4}, 2.93^{0.48}_{0.45}$	29.3/42		GC
S45	$0.18^{0.26}_{0.18}$	$1.65^{0.63}_{0.41}$	$2.86^{0.65}_{0.6}, 3.65^{0.78}_{0.7}$	28.5/21		
PO		Γ				
S3	$0.13^{0.08}_{0.13}$	$1.25^{0.13}_{0.11}$	$36.29^{2.35}_{2.3}, 38.22^{2.74}_{2.65}$	109.6/117		

Table 5.2 (cont'd)

Source	N_H 10^{22} cm^{-2}	kT_{in} keV	L_x $(0.5-10.0$ keV) 10^{37} erg s^{-1}	χ^2/dof	Inferred N_H 10^{22} cm^{-2}	Note
S5	$0.11^{0.05}_{0.11}$	$1.19^{0.09}_{0.08}$	$29.37^{1.91}_{1.87}, 36.56^{2.3}_{2.25}$	180/214		GC
S8	$0.08^{0.16}_{0.06}$	$1.31^{0.28}_{0.2}$	$21.11^{2.52}_{2.37}$	23.2/34		
S11	$0.08^{0.17}_{0.08}$	$1.29^{0.29}_{0.17}$	$13.52^{1.87}_{1.75}$	17.3/23		GC
S11	$0.09^{0.11}_{0.09}$	$1.54^{0.19}_{0.08}$	$12.44^{1.37}_{1.17}, 16.6^{1.54}_{1.36}$	72.3/73		GC
S16	$0.14^{0.08}_{0.14}$	$1.59^{0.15}_{0.14}$	$10.05^{1.09}_{1.06}, 14.26^{1.62}_{1.58}$	126.5/129		GC
S17	$0.16^{0.11}_{0.16}$	$1.45^{0.17}_{0.16}$	$10.77^{1.16}_{1.13}, 13.39^{3.07}_{3}$	93.1/105		
S20	$0.17^{0.10}_{0.17}$	$1.74^{0.18}_{0.17}$	$8.43^{0.98}_{0.95}, 11.25^{1.3}_{1.24}$	83.5/113		
S22	$0.08^{0.14}_{0.08}$	$1.98^{0.35}_{0.23}$	$5.85^{0.86}_{0.75}$	13.4/14		
S25	$0.11^{0.21}_{0.11}$	$2.11^{0.47}_{0.21}$	$6.24^{1.66}_{0.73}$	14/15		
S29	$0.16^{0.12}_{0.16}$	$1.85^{0.24}_{0.21}$	$5.86^{0.81}_{0.76}, 6.65^{0.87}_{0.82}$	65.1/64		
S36	$0.20^{0.23}_{0.2}$	$2.39^{0.61}_{0.41}$	$4.96^{2.11}_{1.03}, 5.08^{2.11}_{1.03}$	23.8/23		
S42	$0.13^{0.22}_{0.13}$	$1.69^{0.36}_{0.30}$	$3.97^{0.87}_{0.79}, 5.06^{1.06}_{0.99}$	46.5/44		
S46	$0.11^{0.45}_{0.11}$	$1.61^{0.61}_{0.21}$	$3.00^{0.99}_{0.77}, 4.28^{1.25}_{0.83}$	28.2/27	0.281 ± 0.08	D
S47	$0.11^{0.26}_{0.11}$	$1.86^{0.53}_{0.2}$	$3.26^{0.82}_{0.6}, 3.52^{0.79}_{0.65}$	14.7/23		
S53	$0.30^{0.32}_{0.30}$	$2.29^{0.57}_{0.46}$	$3.25^{1.66}_{0.86}, 3.91^{1.81}_{0.93}$	16/19		
S55	$0.19^{0.59}_{0.19}$	$1.72^{0.83}_{0.31}$	$3.34^{1.56}_{0.73}, 4.36^{2.05}_{0.99}$	15.1/14		GC
S59	$0.11^{0.42}_{0.11}$	$1.57^{0.67}_{0.26}$	$2.91^{0.74}_{0.67}, 3.14^{0.91}_{0.67}$	9.8/12		

Note. — Spectral fitting results with the appropriate simple model for thermally dominant (**DBB**) and power law dominant (**PO**) states, with N_H forced to be above the Galactic value to reach a better estimate of the source luminosity. GC denotes that the source is coincident with globular cluster while D indicates that a source is in the vicinity of the dust lane. Where possible, we include the N_H values inferred from the optical depth map, for the first spectrum from each source.

5.4.2 BH & NS LMXBs

None of the sources in our sample is confirmed to have $L_x > 4 \times 10^{38}$ erg s^{-1}, compared to 3 sources apiece in NGC 3379 and NGC 4278 in the sample of Fabbiano et al. (2010). We caution that our sample is drawn from within the half-light radius, as opposed to D_{25}, on account of the relative proximity of Cen A. In addition, Cen A is a slightly smaller galaxy with $M_B = -21.1$ (Ferrarese et al., 2007) compared to -22.28 and -22.02 for NGC 3379 and NGC 4278 (Cappellari et al., 2006), and the LMXB population scales with galaxy mass to first order. While we also exclude the sources that vary during the course of an observation or are close to the Cen A nucleus for a later study, it is unlikely that these sources have $L_x > 5 \times 10^{38}$ erg s^{-1} (Table 5.1) unless the intra-observation variability is extreme. Assuming the XLF follows an unbroken power law, with $dN/dL \sim KL^{\alpha}$ and $\alpha = -2$

(Kim & Fabbiano, 2004), and assuming there are ~ 40 sources between $\sim 2 \times 10^{37}$ erg s^{-1} and $\sim 10^{38}$ erg s^{-1} (Table 5.1), then $K \sim 10^{39}$ and there would be ~ 8 sources between 10^{38} erg s^{-1} and 5×10^{38} erg s^{-1} and we would expect a single source in the range 5×10^{38} erg s^{-1} to 10^{39} erg s^{-1}. These values are consistent with our results.

We present the thermally dominant and power law dominant spectral properties in Figures 5.6 & 5.7, respectively. In Figure 5.6, we plot the unabsorbed disk luminosity against inner-disk temperature for the thermally dominant states (note that one point is representative of one ACIS spectrum, as we allowed for normalization, i.e. the flux, to be a free parameter during fitting). We show illustrative bands of constant mass for $10M_{\odot}$, $5M_{\odot}$ and $2M_{\odot}$ assuming a non-rotating compact object (Gierliński & Done, 2004), where the width of the bands shows the variation with inclination θ, from $\cos\theta = 0.25$ to $\cos\theta = 0.75$ (for which we use correction factors presented in Zhang et al., 1997), and we assume $f_{col} = 1.8$. What is most striking is the apparent bimodal nature of the thermal state sources, between those that are consistent with, or to the right of our $2M_{\odot}$ band, and those to the left of the $5M_{\odot}$ band. In Figure 6 of Burke et al. (2012), we presented a population of Local Group thermal states, all of which lie to the left of our supposed $2M_{\odot}$ line. The fact that the bulk of our sources lie to the right of this line, with $kT_{in} > 1$ keV in the range of $L_x \sim 10^{37} - 10^{38}$ erg s^{-1}, is very suggestive that our thermal state sample is dominated by NS LMXBs.

We suggest tentatively that this result is reminiscent of the well-known 'mass gap' problem (Bailyn et al., 1998). The mass distribution of compact objects in transient systems strongly deviates from theoretical predictions, with a characteristic paucity between the most massive NSs ($\sim 3M_{\odot}$) and the least massive BHs, while the mass distribution of BHs is seen to peak at $\sim 8M_{\odot}$. If not a systematic effect (e.g. Farr et al., 2011; Kreidberg et al., 2012), then this feature in the mass distribution favours 'rapid' initial stellar collapse models of supernovae, where initial instabilities grow on timescales of 10-20 ms (Belczynski et al., 2012), over models that require more prolonged instability growth (> 200 ms). To quantitatively test if these data are distributed bimodally in this plane, we first calculate a 'mass' for each source based on the observed peak luminosity, assuming $\cos\theta = 0.5$. We then fitted[5] both a single Gaussian, and then dual Gaussians to the observed mass distribution and from these fits calculate the Akaike's Information Criterion (AIC) (Akaike, 1974) for both models. The

[5]Using the function *fitdistr*, part of the MASS package in R

dual Gaussian fit had means (standard deviations) of 1.93 (0.76) $M_\odot$ and 15.74 (8.46) $M_\odot$ while the single Gaussian was centred on 5.6 (7.55) $M_\odot$. The AIC for the single Gaussian fit (=114.11) was larger than that of the dual Gaussian fit (=83.66), such that the latter was strongly favoured, with the single Gaussian 2.44×10^{-7} times as probable as the double Gaussian. These results are the first hint that the mass gap exists outside the Local Group.

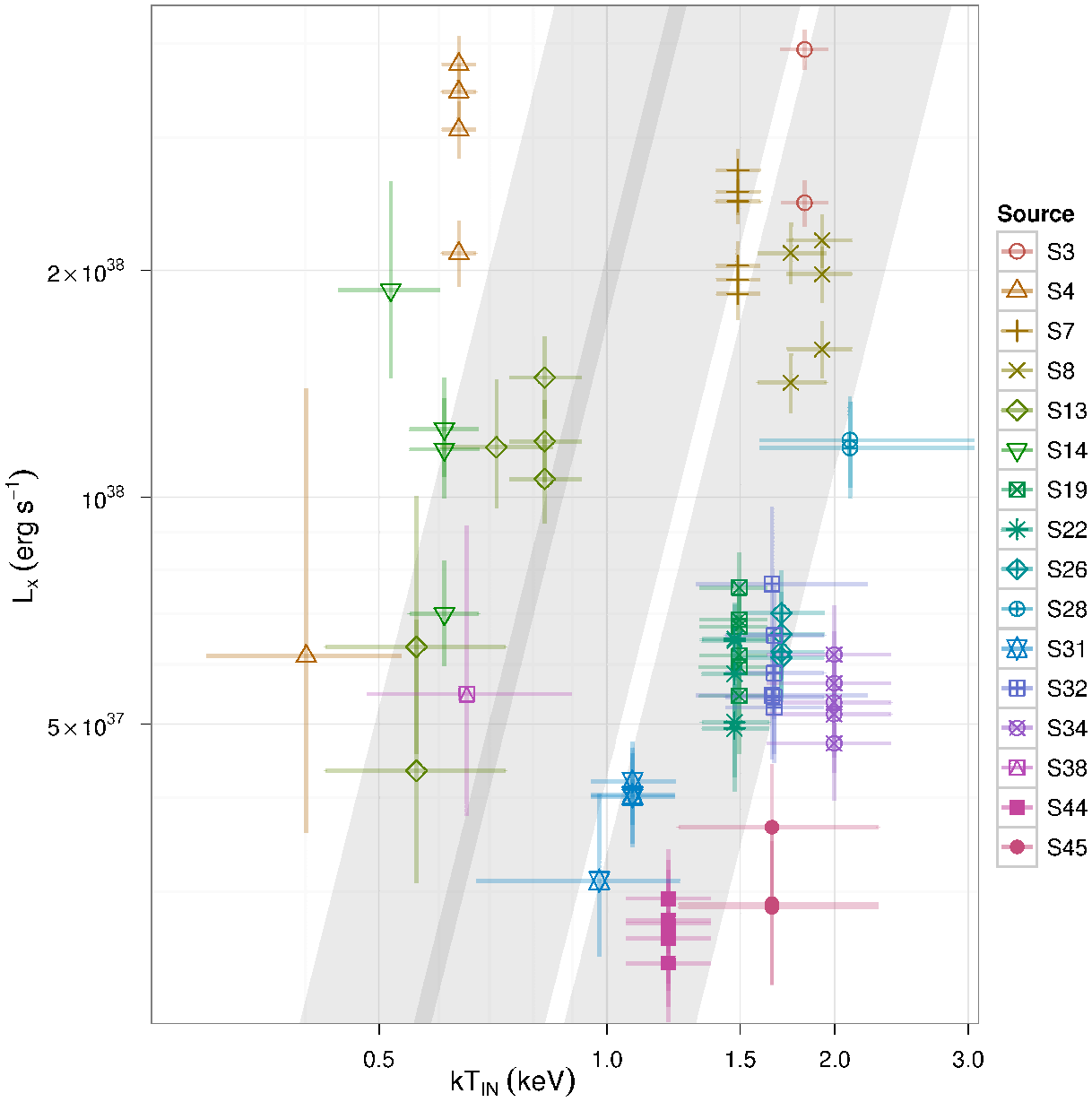

Figure 5.6 X-ray luminosity against inner-disk temperature for states deemed to be in the thermal state. Diagonal bands represent constant mass for (*left* to *right*) 10 $\mathrm{M}_\odot$, 5 $\mathrm{M}_\odot$ and 2 $\mathrm{M}_\odot$ non-rotating compact objects. The width of the bands shows an assumed inclination θ of $\cos\theta = 0.25$ to $\cos\theta = 0.75$.

BH systems do not have thermal emission from a boundary layer, as one would expect from

the NS LMXBs. The flatness of the S3 and S5 spectra, which our method suggests are power law dominated with $\Gamma \sim 1.2$, is more consistent with the spectra of LMXB NS Z-track sources than those of BH sources in the hard state at $L_x > 10^{38}$ erg s^{-1}. We know this based on simulating the spectra of NS LMXBs using the model and parameters reported by Lin et al. (2012), who modeled the spectra of a bright NS LMXB, GX17+2, using a combination of disk blackbody, blackbody, and a power law component that is significant only on the Z-track horizontal branch. Regardless of whether this is a physically correct description or not, it is clearly a good phenomenological description of the spectral shape. At similar count rates to S3 and S5, we find that the parameters of this multi-component model are poorly recovered by a two-component $phabs(diskbb + bbody)$ fit, but that the shape of the spectrum is typically well-described by a shallow power law of $\Gamma \sim 1.0 - 1.4$, which does not vary substantially between Z-track states over the *Chandra* bandpass. For what is judged to be the thermally dominant state of S3, kT_{in} is higher than for the BH candidate systems. We therefore conclude that S3 and S5 are candidate Z-track sources.

The power law states do not show a bimodality as we see for the thermal states, but they are consistent with Galactic NS and BH XBs, and there appears some slight favoring of steeper Γ at lower luminosities. However, such an effect was also seen by Fabbiano et al. (2010), whose limiting luminosity for spectral fitting was much higher. In Figure 9 of Brassington et al. (2010) it is shown using 1000 count simulated spectra that the change in Γ with flux contribution favoured larger values from spectral fitting, particularly for cooler disks. It is conceivable that this effect becomes more pronounced when there are fewer counts.

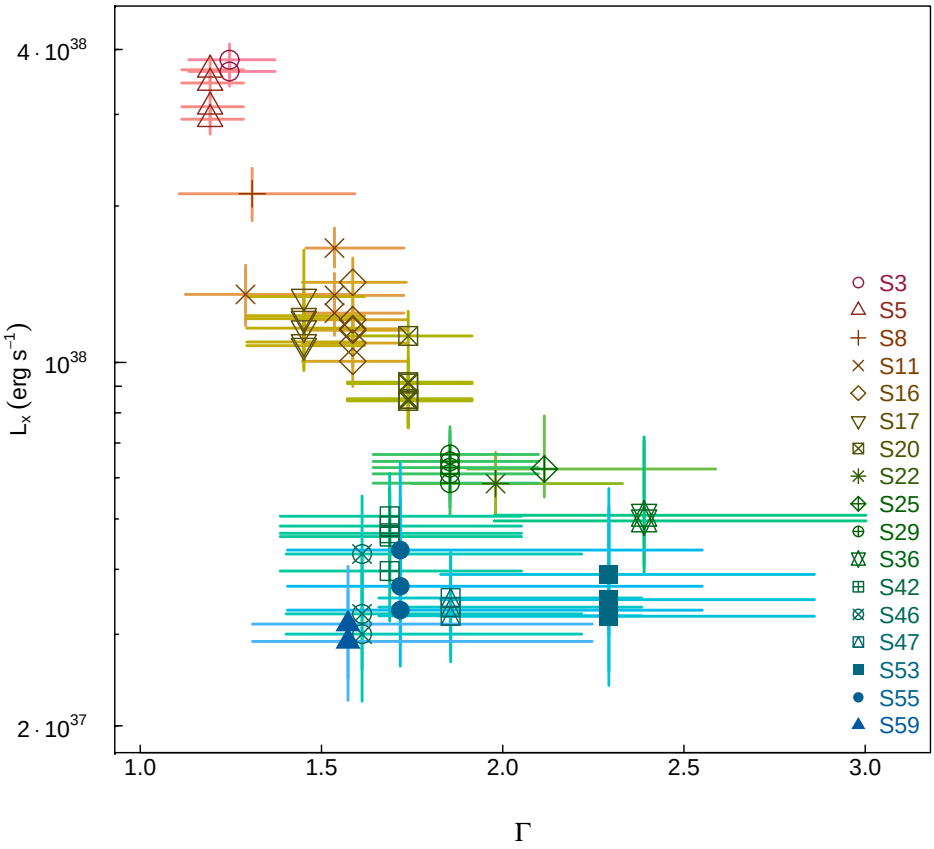

Figure 5.7 X-ray luminosity against photon index for those states determined to be power law dominated.

Table 5.3. Cen A Sources: Spectral fitting and State Identification

Source	ObsIDs	$N_H^{\rm PO}$ 10^{22} cm^{-2}	$\Gamma^{\rm PO}$	L_x $(0.5-10.0$ keV$)^{\rm PO}$ 10^{37} erg s^{-1}	χ^2/dof	$N_H^{\rm DBB}$ 10^{22} cm^{-2}	$kT_{in}^{\rm DBB}$ keV	L_x $(0.5-10.0$ keV$)^{\rm DBB}$ 10^{37} erg s^{-1}	χ^2/dof	State
S3	7797, 7800	$0.13^{0.08}_{0.07}$	$1.25^{0.13}_{0.12}$	$36.2^{2.4}_{2.3}, 38.2^{2.7}_{2.6}$	109.6/117	$0.00^{0.05}_{0.00}$	$2.61^{0.32}_{0.35}$	$30.3^{2.5}_{2.3}, 31.7^{2.9}_{2.7}$	106.7/117	P1
S3	8489, 8490	$0.21^{0.07}_{0.06}$	$1.50^{0.11}_{0.11}$	$31.7^{2.1}_{2.0}, 50.7^{2.8}_{2.7}$	131/140	$0.04^{0.05}_{0.04}$	$1.92^{0.21}_{0.17}$	$24.5^{1.8}_{1.7}, 39.2^{2.5}_{2.4}$	118.6/140	T1
S4	7797, 7798, 7799, 7800	$1.25^{0.11}_{0.1}$	$3.76^{0.19}_{0.18}$	$93.77^{24.83}_{18.44}, 166.21^{42.48}_{31.51}$	241.2/203	$0.65^{0.07}_{0.06}$	$0.64^{0.03}_{0.03}$	$21.06^{2.23}_{2.04}, 37.49^{3.41}_{3.09}$	206.9/203	I
S4	8489	$1.22^{0.7}_{0.51}$	$5.07^{1.69}_{1.22}$	62^{447}_{46}	10.5/14	$0.59^{0.48}_{0.35}$	$0.40^{0.13}_{0.11}$	$6.15^{7.79}_{2.57}$	10.0/14	I
S5	7797, 7800, 8489, 8490	$0.11^{0.05}_{0.05}$	$1.19^{0.09}_{0.09}$	$29.4^{1.9}_{1.9}, 36.6^{2.3}_{2.2}$	180/214	$0.00^{0.00}_{-0.82}$	$2.83^{0.31}_{0.25}$	$24.9^{1.9}_{1.8}, 31.1^{2.4}_{2.2}$	185.7/214	P1,N
S7	7797, 7798, 7799, 8490, 7800, 8489	$0.89^{0.1}_{0.1}$	$1.99^{0.12}_{0.11}$	$28.8^{2.8}_{2.6}, 42.0^{3.8}_{3.4}$	275.7/256	$0.51^{0.07}_{0.06}$	$1.49^{0.11}_{0.1}$	$18.6^{1.5}_{1.4}, 27.2^{1.8}_{1.8}$	271.5/256	I
S8	7797, 7798, 8490	$0.29^{0.08}_{0.08}$	$1.58^{0.14}_{0.13}$	$20.6^{1.66}_{1.62}, 28.44^{2.14}_{2.07}$	128/132	$0.08^{0.05}_{0.05}$	$1.93^{0.25}_{0.21}$	$15.71^{1.41}_{1.34}, 21.91^{1.85}_{1.76}$	135.7/132	T1
S8	7799	$0.06^{0.16}_{0.06}$	$1.31^{0.28}_{0.2}$	$21.11^{2.52}_{2.37}$	23.2/34	$0.00^{0}_{-0.82}$	$2.07^{0.57}_{0.38}$	$16.8^{2.8}_{2.4}$	27.6/34	P1,N
S8	7800, 8489	$0.23^{0.10}_{0.09}$	$1.57^{0.17}_{0.16}$	$18.6^{1.56}_{1.51}, 27.58^{2.26}_{2.20}$	87.6/87	$0.04^{0.06}_{0.04}$	$1.87^{0.3}_{0.23}$	$14.19^{1.37}_{1.29}, 21.07^{2.12}_{1.96}$	87.8/87	T1
S11	7797	$0.07^{0.18}_{0.07}$	$1.26^{0.32}_{0.23}$	$13.5^{1.9}_{1.8}$	17.3/23	$0.00^{0.00}_{-0.82}$	$2.19^{0.74}_{0.45}$	$10.8^{2.1}_{1.7}$	17.8/23	P1,N
S11	7800, 8489, 8490	$0.09^{0.11}_{0.09}$	$1.54^{0.19}_{0.18}$	$12.4^{1.4}_{1.3}, 16.6^{1.5}_{1.5}$	72.3/73	$0.00^{0.00}_{-0.82}$	$1.66^{0.20}_{0.17}$	$9.52^{1.15}_{1.07}, 12.5^{1.4}_{1.2}$	83/73	P1,N
S12	7797, 7798, 7799, 7800, 8489, 8490	$0.72^{0.21}_{0.19}$	$1.12^{0.18}_{0.17}$	$16.35^{1.88}_{1.85}, 26.54^{2.34}_{2.29}$	150.8/157	$0.49^{0.13}_{0.12}$	$3.96^{1.73}_{0.87}$	$14.49^{1.91}_{1.79}, 23.5^{2.5}_{2.3}$	153.6/157	I
S13	S7797, 7798, 8490	$0.9^{0.2}_{0.18}$	$2.97^{0.31}_{0.29}$	$27.05^{10.35}_{6.46}, 36.85^{13.55}_{8.44}$	122/89	$0.4^{0.13}_{0.12}$	$0.83^{0.1}_{0.09}$	$10.57^{1.53}_{1.33}, 14.41^{1.93}_{1.69}$	110.7/89	I
S13	7800, 8489	$1.02^{0.57}_{0.44}$	$3.99^{1.16}_{0.89}$	$22.53^{67.86}_{13.54}, 33^{100.31}_{19.79}$	41.3/30	$0.39^{0.37}_{0.29}$	$0.56^{0.17}_{0.14}$	$4.34^{2.55}_{1.26}, 6.33^{3.72}_{1.77}$	37.5/30	I
S13	7799	$0.85^{0.34}_{0.27}$	$3.33^{0.61}_{0.51}$	$35.79^{33.25}_{13.48}$	58.2/33	$0.35^{0.21}_{0.17}$	$0.71^{0.13}_{0.11}$	$11.65^{2.68}_{1.97}$	44.9/33	I
S14	7797, 7798, 7800	$0.95^{0.19}_{0.17}$	$3.81^{0.39}_{0.35}$	$31.4^{17.7}_{10.0}, 55.4^{30.7}_{17.4}$	78.1/71	$0.37^{0.12}_{0.11}$	$0.61^{0.07}_{0.06}$	$7.00^{1.24}_{1.03}, 12.33^{2.07}_{1.68}$	72/71	I
S14	7799	$1.65^{0.46}_{0.37}$	$4.66^{0.78}_{0.64}$	192^{356}_{108}	19.9/27	$0.81^{0.28}_{0.23}$	$0.52^{0.08}_{0.08}$	$18.8^{7.4}_{4.4}$	14.6/27	I
S16	7797, 7798, 7799, 7800, 8489, 8490	$0.14^{0.08}_{0.08}$	$1.59^{0.15}_{0.14}$	$10.0^{1.1}_{1.1}, 14.3^{1.6}_{1.6}$	126.5/129	$0.00^{0.00}_{-0.82}$	$1.67^{0.16}_{0.14}$	$7.50^{0.86}_{0.83}, 10.5^{1.3}_{1.2}$	133.7/129	P1,N
S17	7797, 7798, 7799, 7800, 8489, 8490	$0.16^{0.11}_{0.10}$	$1.45^{0.17}_{0.16}$	$10.77^{1.16}_{1.13}, 13.4^{3.1}_{3.0}$	93.1/105	$0.00^{0.06}_{0.00}$	$1.98^{0.24}_{0.17}$	$8.21^{0.8}_{0.94}, 10.28^{2.26}_{2.25}$	92.5/105	P1
S19	7797, 7798, 7799, 7800, 8489, 8490	$0.35^{0.13}_{0.11}$	$1.84^{0.2}_{0.19}$	$7.91^{1.37}_{1.31}, 11.08^{1.36}_{1.23}$	121/135	$0.09^{0.08}_{0.07}$	$1.5^{0.21}_{0.17}$	$5.45^{0.92}_{0.89}, 7.59^{0.85}_{0.82}$	119.3/135	T1
S20	7797, 7798, 7799, 8489, 8490, 7800	$0.17^{0.1}_{0.09}$	$1.74^{0.18}_{0.17}$	$8.43^{0.98}_{0.95}, 11.25^{1.30}_{1.24}$	83.5/113	$0.00^{0.00}_{-0.82}$	$1.45^{0.14}_{0.12}$	$5.98^{0.72}_{0.69}, 7.94^{0.94}_{0.89}$	90.2/113	P1,N
S22	7797	$0.0^{0.2}_{0.0}$	$1.82^{0.46}_{0.21}$	$5.61^{1.00}_{0.78}$	12.9/14	$0.00^{0.00}_{-0.82}$	$1.16^{0.28}_{0.23}$	$4.21^{0.74}_{0.66}$	20.9/14	P1,N

Table 5.3 (cont'd)

Source	ObsIDs	$N_H^{\rm PO}$ 10^{22} cm^{-2}	$\Gamma^{\rm PO}$	L_x $(0.5-10.0$ keV$)^{\rm PO}$ 10^{37} erg s^{-1}	χ^2/dof	$N_H^{\rm DBB}$ 10^{22} cm^{-2}	$kT_{in}^{\rm DBB}$ keV	L_x $(0.5-10.0$ keV$)^{\rm DBB}$ 10^{37} erg s^{-1}	χ^2/dof	State
S22	7798, 7799, 7800, 8489, 8490	$0.21^{0.13}_{0.12}$	$1.7^{0.22}_{0.21}$	$6.90^{0.93}_{0.90}, 8.83^{1.07}_{1}$	60.1/67	$0.00^{0.00}_{-0.82}$	$1.62^{0.19}_{0.16}$	$4.94^{0.74}_{0.69}, 6.40^{0.78}_{0.74}$	60/67	T2,M3,I
S24	7797	$0.36^{0.4}_{0.33}$	$1.54^{0.52}_{0.47}$	$10.68^{2.11}_{1.62}$	9.4/14	$0.13^{0.26}_{0.13}$	$1.85^{1.12}_{0.52}$	$7.80^{1.75}_{1.34}$	8.6/14	NA
S24	7798, 7799, 7800, 8489	$0.64^{0.28}_{0.25}$	$1.72^{0.3}_{0.27}$	$10.4^{1.9}_{1.5}, 12.8^{2.4}_{1.8}$	74.8/67	$0.33^{0.18}_{0.16}$	$1.68^{0.38}_{0.27}$	$7.31^{0.96}_{0.92}, 9.03^{1.21}_{1.15}$	67.2/67	I
S25	7797	$0.11^{0.21}_{0.11}$	$2.11^{0.47}_{0.36}$	$6.24^{1.66}_{1.08}$	14/15	$0.00^{0.00}_{-0.82}$	$1^{0.18}_{0.15}$	$4.28^{0.59}_{0.56}$	14.1/15	P1,N
S26	7797, 7798, 7799, 7800	$0.22^{0.13}_{0.12}$	$1.57^{0.21}_{0.20}$	$8.29^{1}_{0.98}, 9.38^{1.17}_{1.13}$	49.1/60	$0.02^{0.09}_{0.02}$	$1.84^{0.32}_{0.28}$	$6.14^{0.92}_{0.85}, 7.03^{1}_{0.92}$	50.3/60	T1
S28	7797, 8490	$0.51^{0.53}_{0.48}$	$0.87^{0.41}_{0.39}$	$1.20^{1.78}_{1.67}, 17.07^{2.54}_{2.38}$	17.5/27	$0.44^{0.36}_{0.30}$	$5.60^{NA}_{2.72}$	$11.1^{2.43}_{1.94}, 15.74^{3.54}_{2.80}$	17.0/31	I
S28	7800, 8489	$1.66^{0.72}_{0.64}$	$1.71^{0.49}_{0.45}$	$16.58^{6.19}_{3.21}, 16.95^{6.58}_{3.3}$	36.7/28	$1.10^{0.45}_{0.4}$	$2.09^{0.97}_{0.5}$	$11.62^{1.76}_{1.66}, 11.9^{1.7}_{1.1}$	34.8/28	I
S29	7797, 7799, 7800, 8489, 8490	$0.16^{0.12}_{0.11}$	$1.85^{0.24}_{0.23}$	$5.86^{0.81}_{0.76}, 6.65^{0.87}_{0.82}$	65.1/64	$0.00^{0.00}_{-0.82}$	$1.28^{0.15}_{0.13}$	$4.00^{0.55}_{0.53}, 4.45^{0.62}_{0.58}$	80.2/64	P1,N
S29	7798	$0.83^{0.50}_{0.39}$	$2.55^{0.65}_{0.55}$	$10.30^{8.80}_{3.30}$	9/10	$0.38^{0.32}_{0.26}$	$1.04^{0.32}_{0.22}$	$5.14^{1.24}_{0.96}$	8/10	I
S31	7797, 7800, 8490	$0.26^{0.17}_{0.15}$	$2.08^{0.34}_{0.31}$	$6.23^{1.19}_{0.93}, 6.51^{1.25}_{0.95}$	30/43	$0.00^{0.09}_{0.00}$	$1.20^{0.11}_{0.18}$	$3.91^{0.59}_{0.45}, 4.09^{0.56}_{0.47}$	37.4/43	T1
S31	7798, 8489	$0.00^{0.82}_{0.00}$	$1.29^{0.20}_{0.19}$	$6.31^{1.80}_{1.37}, 6.69^{1.00}_{1.11}$	21.3/27	$0.00^{0.82}_{0.00}$	$1.85^{0.66}_{0.40}$	$4.72^{1.10}_{0.86}, 5.17^{1.35}_{1.00}$	24.5/27	NA
S31	7799	$0.53^{0.60}_{0.43}$	$2.58^{1.06}_{0.77}$	$6.24^{9.34}_{2.22}$	13.7/12	$0.12^{0.38}_{0.12}$	$0.98^{0.58}_{0.31}$	$3.10^{0.94}_{0.74}$	13.3/12	T1
S32	7797, 7798, 7799, 7800	$0.26^{0.18}_{0.16}$	$1.61^{0.28}_{0.26}$	$7.22^{1.16}_{1.09}, 8.98^{1.32}_{1.25}$	26.5/50	$0.03^{0.12}_{0.03}$	$1.79^{0.36}_{0.32}$	$5.27^{0.94}_{0.85}, 6.58^{1.13}_{1.01}$	27.5/50	T1
S32	8489, 8490	$0.00^{0.00}_{-0.82}$	$1.32^{0.23}_{0.22}$	$7.18^{1.35}_{1.21}, 10.61^{2.39}_{2.1}$	13/16	$0.00^{0.00}_{-0.82}$	$1.8^{0.69}_{0.40}$	$5.45^{1.30}_{1.03}, 7.75^{2.21}_{1.71}$	14.3/16	T2,M3,I,N,M2
S34	7797, 7798, 7799, 7800, 8489	$0.32^{0.18}_{0.16}$	$1.55^{0.26}_{0.24}$	$6.23^{0.96}_{0.93}, 8.14^{1.13}_{1.08}$	48.2/67	$0.08^{0.12}_{0.08}$	$2.00^{0.58}_{0.37}$	$4.72^{0.84}_{0.76}, 6.19^{1.03}_{0.92}$	52.6/67	T1
S34	8490	$0.97^{0.55}_{0.43}$	$2.26^{0.62}_{0.52}$	$11.34^{7.61}_{3.03}$	8.5/13	$0.49^{0.34}_{0.27}$	$1.32^{0.46}_{0.3}$	$6.46^{1.23}_{1.11}$	7.3/13	I
S35	8490	$0.51^{0.6}_{0.49}$	$1.81^{0.74}_{0.66}$	$8.02^{4.0}_{1.54}$	7.1/10	$0.20^{0.40}_{0.20}$	$1.49^{1.05}_{0.47}$	$5.28^{1.28}_{0.98}$	6.9/10	NA
S36	7797, 7798, 8490	$0.20^{0.21}_{0.18}$	$1.54^{0.36}_{0.34}$	$4.5^{0.94}_{0.86}, 7.31^{1.14}_{1.06}$	30.5/31	$0.02^{0.14}_{0.02}$	$1.71^{0.46}_{0.38}$	$3.20^{0.82}_{0.66}, 5.17^{1.09}_{0.87}$	29.7/31	NA
S36	7799, 7800	$0.20^{0.23}_{0.20}$	$2.39^{0.61}_{0.50}$	$4.96^{2.11}_{1.04}, 5.08^{2.11}_{1.04}$	23.8/23	$0.00^{0.00}_{-0.82}$	$0.87^{0.19}_{0.15}$	$2.85^{0.49}_{0.45}, 2.92^{0.50}_{0.45}$	33.4/23	P1,N
S38	8490	$1.41^{0.76}_{0.64}$	$3.87^{1.25}_{1.00}$	$31.34^{126.4}_{20.9}$	6.1/9	$0.60^{0.52}_{0.43}$	$0.65^{0.25}_{0.17}$	$5.48^{3.68}_{1.70}$	7.8/9	I
S39	7797, 7798, 7799	$0.93^{0.43}_{0.38}$	$1.98^{0.48}_{0.44}$	$7.05^{2.65}_{1.44}, 9.28^{3.42}_{1.9}$	37.2/30	$0.41^{0.27}_{0.24}$	$1.65^{0.65}_{0.38}$	$4.45^{0.79}_{0.73}, 5.80^{1.06}_{0.96}$	41.3/30	I
S39	7799, 7800, 8490	$0.92^{0.45}_{0.37}$	$2.34^{0.53}_{0.47}$	$8.11^{4.8}_{2.22}, 10.08^{5.64}_{2.71}$	19.6/26	$0.43^{0.29}_{0.24}$	$1.2^{0.36}_{0.24}$	$4.28^{0.90}_{0.79}, 5.46^{1.16}_{1.07}$	21.3/26	I

Table 5.3 (cont'd)

Source	ObsIDs	$N_H^{\rm PO}$ 10^{22} cm^{-2}	$\Gamma^{\rm PO}$	L_x $(0.5-10.0$ keV$)^{\rm PO}$ 10^{37} erg s^{-1}	χ^2/dof	$N_H^{\rm DBB}$ 10^{22} cm^{-2}	$kT_{in}^{\rm DBB}$ keV	L_x $(0.5-10.0$ keV$)^{\rm DBB}$ 10^{37} erg s^{-1}	χ^2/dof	State
S42	7797, 7799, 7800, 8489, 8490	$0.13^{0.22}_{0.13}$	$1.69^{0.36}_{0.30}$	$3.97^{0.87}_{0.79}, 5.06^{1.06}_{0.99}$	46.5/44	$0.00^{0.00}_{-0.82}$	$1.38^{0.25}_{0.19}$	$2.78^{0.58}_{0.54}, 3.54^{0.78}_{0.71}$	44.7/44	P1,N
S44	7797, 7799, 7800, 8489, 8490	$0.30^{0.20}_{0.18}$	$2.03^{0.34}_{0.31}$	$3.71^{0.84}_{0.67}, 4.37^{1.05}_{0.81}$	30.2/42	$0.01^{0.13}_{0.01}$	$1.30^{0.22}_{0.21}$	$2.37^{0.42}_{0.40}, 2.83^{0.50}_{0.42}$	28.4/42	T1
S45	7798, 7800, 8490	$0.48^{0.39}_{0.32}$	$1.76^{0.49}_{0.44}$	$4.07^{1.37}_{0.91}, 5.19^{1.51}_{1.02}$	27.7/21	$0.18^{0.26}_{0.18}$	$1.65^{0.77}_{0.41}$	$2.86^{0.65}_{0.60}, 3.65^{0.78}_{0.70}$	28.5/21	T1
S46	7797, 8489, 8490	$0.11^{0.45}_{0.11}$	$1.61^{0.61}_{0.32}$	$3.00^{0.99}_{0.81}, 4.28^{1.25}_{0.95}$	28.2/27	$0.00^{0.21}_{0.00}$	$1.51^{0.48}_{0.36}$	$2.16^{0.70}_{0.57}, 3.13^{0.84}_{0.70}$	26.3/27	P1
S47	7797, 8489, 8490	$0.11^{0.26}_{0.11}$	$1.86^{0.53}_{0.35}$	$3.26^{0.82}_{0.63}, 3.52^{0.79}_{0.68}$	14.7/23	$0.00^{0.00}_{-0.82}$	$1.13^{0.26}_{0.19}$	$2.16^{0.45}_{0.40}, 2.32^{0.53}_{0.45}$	17.3/23	P1,N
S48	7798, 8490, 7799	$0.00^{0.00}_{-0.82}$	$0.75^{0.22}_{0.22}$	$5.17^{1.49}_{1.24}, 6.97^{1.45}_{1.31}$	12.8/18	NA^{NA}_{NA}	NA^{NA}_{NA}	NA, NA	NA/NA	M2
S53	7797, 7800, 8490	$0.30^{0.32}_{0.28}$	$2.29^{0.57}_{0.49}$	$3.25^{1.66}_{0.86}, 3.91^{1.81}_{0.93}$	16/19	$0.00^{0.00}_{-0.82}$	$1.07^{0.21}_{0.17}$	$1.93^{0.37}_{0.35}, 2.28^{0.45}_{0.43}$	17.8/19	P1,N
S55	7797, 7798, 7799	$0.19^{0.59}_{0.19}$	$1.72^{0.83}_{0.45}$	$3.34^{1.55}_{0.75}, 4.36^{2.05}_{1.01}$	15.1/14	$0.00^{0.00}_{-0.82}$	$1.42^{0.53}_{0.32}$	$2.27^{0.65}_{0.52}, 2.94^{0.9}_{0.68}$	17/14	P1,N
S59	8489, 8490	$0.11^{0.42}_{0.11}$	$1.57^{0.67}_{0.39}$	$2.91^{0.74}_{0.68}, 3.14^{0.92}_{0.81}$	9.8/12	$0.00^{0.00}_{-0.82}$	$1.55^{0.74}_{0.41}$	$2.07^{0.67}_{0.52}, 2.3^{0.83}_{0.62}$	10.6/12	P1,N

Note. — Results from fitting absorbed power law (PO) and disk blackbody (DBB) models with all parameters free to vary and 95% confidence intervals. The state column denotes the spectral states that a given set of spectra are consistent with, based on the classification scheme proposed by Brassington et al. (2010). T indicates a thermally dominant state, P indicates power law dominant state, M suggests that there is significant, unmodelled emission from another component ($> 30-40\%$), N suggests a result was not-produced by the Brassington et al. (2010) simulations and I indicates there is additional line-of-sight absorption, when both simple models have N_H significantly above the Galactic value. The extent to which a component dominates is indicated by the associated number, i.e. 1 implies the state is almost completely dominated by that component, while 2 indicates that there is some unmodelled component also present. Instances of $N_H^{DBB} = 0.00^{0.00}_{-0.82}$ for some fits are the result of not being able to constrain an upper-limit in Xspec. We believe the source to be in the power law state at these times, with N_H^{PO} consistent with the Galactic value. In the state column, 'NA' denotes where no inference can be made regarding the state (see section 5.4.4) and for S48 shows where no fit could be achieved (i.e. $\chi/dof > 2$), which is discussed in section 5.4.3.

[a]Minimal and maximal values of L_x are shown for absorbed power law (PO) and disk blackbody (DBB) models

NS Transient Candidates

Of the less luminous sources that do not appear to be BHCs we find that S25, S35 and S45 display extreme variability. S25 is only bright enough for spectral fitting in one observation, where we determine the source to be in a power law dominant state. While the source is always above our detection limit, the flux falls to $\sim 20\%$ of the initial value after obsID 7797, and the spectrum becomes dramatically softer by obsID 8490, with $log_{10}(S/H) \sim 1.1$ and a 90% confidence lower-limit of ~ 0.6 in obsID 8490. That a source displays quasi-super-soft behavior (Di Stefano & Kong, 2003) at low luminosity but $\Gamma \sim 2$ may indicate that S25 is a classical nova.

S35 is only detected in obsID 8490, but in fitting simple models we are not able to constrain N_H such as to show that it is above, below or consistent with N_H^{Gal}. All the parameters are poorly constrained, but taken at face value the Γ or kT_{in} are not inconsistent with NS LXMBs. The variability demonstrated by the source would be consistent with a transient atoll-type NS LMXB towards the peak of outburst.

We believe that S45 may also be a transient NS LMXB in outburst. It displays significant temporal variability over the course of the six observations, and appears to be in a thermally dominant state with an inner-disc temperature $kT_{in} \sim 1.3 - 2.3$ keV, consistent with disc temperatures obtained from Aql X-1 (e.g. Lin et al., 2007), which we suggest is an analogue to this source.

5.4.3 S48: A high magnetic field NS in a GC?

S48 is a peculiar source. Coincidence with a spectroscopically-confirmed GC means that it is highly unlikely to be a background AGN or foreground star. The spectrum is well-fit by a power law model of $\Gamma \sim 0.7$ experiencing negligible absorption, and a good fit cannot be achieved for the thermal model (Table 5.2). The luminosity of S48 makes it unlikely to be a cataclysmic variable, but it is similar to IGR J17361-4441, a hard X-ray transient detected by INTEGRAL in the Galactic globular cluster NGC 6388 (Ferrigno et al., 2011), which is possibly a high-magnetic field binary such as GX 1+4 (Paul et al., 2005), and has a similar power law slope. The spectra of these sources are well described by a cut-off power law of $\Gamma \sim 0.7 - 1.0$ with a high energy cut-off at 25 keV (Bozzo et al., 2011). The spectral shape is consistent with the compact object being a highly magnetized NS, the emission emanating from accretion columns that impact the NS surface. Young, highly magnetized radio pulsars have been observed in GCs by Boyles et al. (2011), so this is a plausible explanation.

However, such sources typically show short-term modulation on a scale of a few hours (Corbet et al., 2008); while we do not detect any variability inside of any observation (Table 5.1), such modulation might be too small to be detected.

5.4.4 Uncharacterised Spectral States

There are a handful of examples of spectra that could not be formally distinguished by our method (Section 5.3.2). In the case of S29, S32, S34 and S36, we are able to determine the spectral state for a subset of the observations but not for others that we had previously shown to have a different spectral shape. In the case of S29, obsID 7798, the source may be experiencing an increase in absorption or some intermediate stage as it moves away from the hard state, as is the case with S34 obsID 8490. In obsIDs 7797, 7798 and 8490 of S36, we find N_H consistent with the N_H^{Gal} for both models. With the point estimate of N_H^{DBB} much closer to zero, we could tentatively suggest that this source remains in a power law dominated state throughout, the spectra becoming harder at certain times. We note that the softer state of this source coincides with its most luminous epoch, reminiscent of Galactic NS LMXBs such as 4U 1635-536, the spectra of which tend to harden as the source reaches its lowest outburst luminosities. In S31, there are two clear examples that seem to favor a thermal shape, but there is also clear evidence of a much harder state in 0bsIDs 7798 & 8489 where it becomes more difficult for the fit to constrain the absorption column. For S32 obsID 8490, N_H could not be constrained for either simple model.

5.4.5 A different population?

Spectral fitting of simple models indicates that 6 of the 8 sources we highlight as being coincident with the dust lane (Table 5.1) experience a greater line-of-sight absorption than that provided by Galactic column alone. The two sources that were consistent with N_H^{Gal}, S34 and S46, are on the edge of the dust lane, they are thus the worst candidates for coincidence and were labeled as such out of caution. Of sources not coincident with the dust lane, only one source, S39, appears to experience excess absorption by our diagnostic. Inspection of the spectra of this source in more detail has led us to conclude that it is a background AGN, with a redshifted Fe line at ~ 4 keV present in the spectrum.

The good agreement between sources coincident with the dust lane and those that possess

absorption surplus to the Galactic column strongly suggests that these sources experience additional absorption from the dust lane, and validates our previous analysis in section 5.4 using a K-band optical depth map to estimate the average N_H in the vicinity of each source (with the exception of S24, which is not within the FoV of the map), and then infer the dominant component in each of the spectra. This technique assumes that the sources are completely behind the dust lane, and that the N_H does not vary substantially over a $2''$ radius region, while in reality the material is likely to be clumpy and non-uniformly distributed.

Our four transient BH LMXB candidates are all dust lane sources, and are observed with $kT_{in} < 0.9$ keV. Two further dust lane systems, S12 & S28, possess very cool (< 0.4 keV) disks with a strong power law component, mildly suggesting that they also possess BHs. This result indicates an enhancement of classic BHC transients inside of the merged late-type galaxy relative to the halo.We note that previous studies identified the two known ULXs in the south-west quadrant of Cen A as transient X-ray binaries that are strong BHCs (e.g., Ghosh et al., 2006; Sivakoff et al., 2008). Although their presence strongly suggests that there is a population of transient BHCs outside of the merger region, neither source would have been identified as a transient based on the observations we consider in this paper. As such, we exclude them from our analysis.

Previously, hardness-intensity or color-color diagrams have been used to indicate which sources in a sample are heavily absorbed or not, but these were not ideal for giving an indication as to whether the sources themselves were similar, as any further difference in hardness or color could be ascribed to the additional (unknown and unconstrained) absorption. These results from detailed spectral fitting clearly point to particular types of source being present in the late-type galaxy that are absent from the rest of Cen A.

We propose a straightforward explanation of the lack of BHC transients outside of the late-type remnant. An empirical relation exists between orbital period and peak outburst luminosity (Wu et al., 2010), with larger luminosities produced by the systems with longer orbital periods. For transients that contain BHs, this luminosity exceeds 10^{38} erg s^{-1}, which corresponds to an orbital period of ~ 10 hours, based on the Wu et al. (2010) relation. For a main sequence companion filling its Roche lobe, the mass m in $M_\odot$ will be related to the orbital period P in hours by $m \sim 0.11P$ (Frank et al., 2002), which means that the companion star must be be at *least* 1 $M_\odot$. It is likely that the donor is more evolved, particularly in a BH LMXB transient ($< 0.75M_{MS}$, King et al., 1996), and

therefore the actual main sequence lifetime of the $\sim 1M_{\odot}$ donors is shorter. The majority (70-80%) of stars in the halo of Cen A were formed 12 ± 1 Gyr ago, with the rest formed from some event 8-10 Gyr later (Rejkuba et al., 2011). Therefore the majority of stars in the halo have $m < 1\mathrm{M}_{\odot}$, which accounts for the relative absence of bright BH LMXB transients. Inside the late-type galaxy the star formation rate is at least 0.1 $\mathrm{M}_{\odot}\ \mathrm{yr}^{-1}$, though could be as high as 1 $\mathrm{M}_{\odot}\ \mathrm{yr}^{-1}$ (Marconi et al., 2000); therefore there is a population of $\geq 1\mathrm{M}_{\odot}$ donors to feed the accreting BHs by Roche lobe overflow.

It has been proposed that the two ULXs in Cen A are BH LMXBs observed in the so-called *ultraluminous* state (e.g., Gladstone et al., 2009) at $L_x > 10^{39}\mathrm{erg\ s}^{-1}$ and in quiescence with $L_x < 10^{36}\ \mathrm{erg\ s}^{-1}$. These sources have not been observed in the 'classic' BH LMXB states (Remillard & McClintock, 2006) with $L_x \sim 10^{37}$ – $10^{39}\ \mathrm{erg\ s}^{-1}$; the non-UL outburst luminosity of these sources is unknown and therefore they should not be compared directly with the dust lane BHCs until they have been observed below $10^{39}\ \mathrm{erg\ s}^{-1}$ but above the detectability threshold. In these relatively atypical sources, it is not yet clear how the orbital period and peak outburst luminosity are related, which complicates direct comparison with the dust lane sources.

If confirmed, the above explanation for the lack of BHC transients outside of the late-type remnant also accounts for the results of Kim & Fabbiano (2010) for a sample of other nearby early-type galaxies, who found the population of sources with $L_x > 4\times10^{38}\mathrm{erg\ s}^{-1}$ diminished significantly with early-type age, a steepening of the discrete source XLF. We recommend population synthesis work be carried out to investigate the effects of a declining population of transient BH LMXBs with stellar age. We also suggest a deep monitoring campaign of other early-type galaxies with Chandra, to further investigate occurences of transient BHC XBs.

5.5 Conclusions

Our investigation into the X-ray binaries of Cen A has found:

i) The population is mostly NS LMXBs, with 6 BH candidates, four of which are inferred as such from the inner-disk temperature in the thermal state and inter-observational variability, and two from the inferred presence of a cool disk at a high luminosity. The proximity of Cen A, coupled with the depth of the VLP data, means that this is the only early-type galaxy where it is possible to perform detailed spectral fitting to sources in the classic XB luminosity range of $10^{37} - 10^{38}\ \mathrm{erg\ s}^{-1}$,

similar to those sources we observe in the Milky Way. As a population of NS LMXBs outside of the Local Group, these are older analogues of sources that have been studied since the dawn of X-ray astronomy. We identify two sources that we suggest are Z track systems, based on their spectral shape, unabsorbed luminosity and persistent nature.

ii) There is some evidence that the mass distribution of compact objects is bimodal, and there is tentative evidence of the so-called 'mass gap' between $\sim 2.5 - 5 M_{\odot}$ that has been observed in the population of Galactic transient LMXBs. This is the first time that the mass gap has been hinted at outside the Local Group.

iii) Besides the two known ULXs in Cen A, the only black hole candidate transient systems we can identify are found coincident with the dust lanes that arise from the merged late-type galaxy. These are four transient BH LMXB candidates observed in the thermal-dominant state. We propose that this is simply the result of stellar age; the older population of stars in the halo is unable to supply Roche lobe-filling companions that are required for the transient BHCs to have outburst peak $L_x > 10^{38} \mathrm{erg\ s^{-1}}$. This also explains other recent results that show a steepening of the XLF of early-type galaxies with stellar age for $L_x > 4 - 5 \times 10^{38} \mathrm{erg\ s^{-1}}$(Kim & Fabbiano, 2010), as such sources would require more massive companions that have long since evolved off the main sequence. Similar analysis applied to other early-type galaxies where the ages of the stellar populations are known, coupled with stellar population synthesis work, is required to investigate the robustness of this explanation.

5.6 Appendix of Chapter

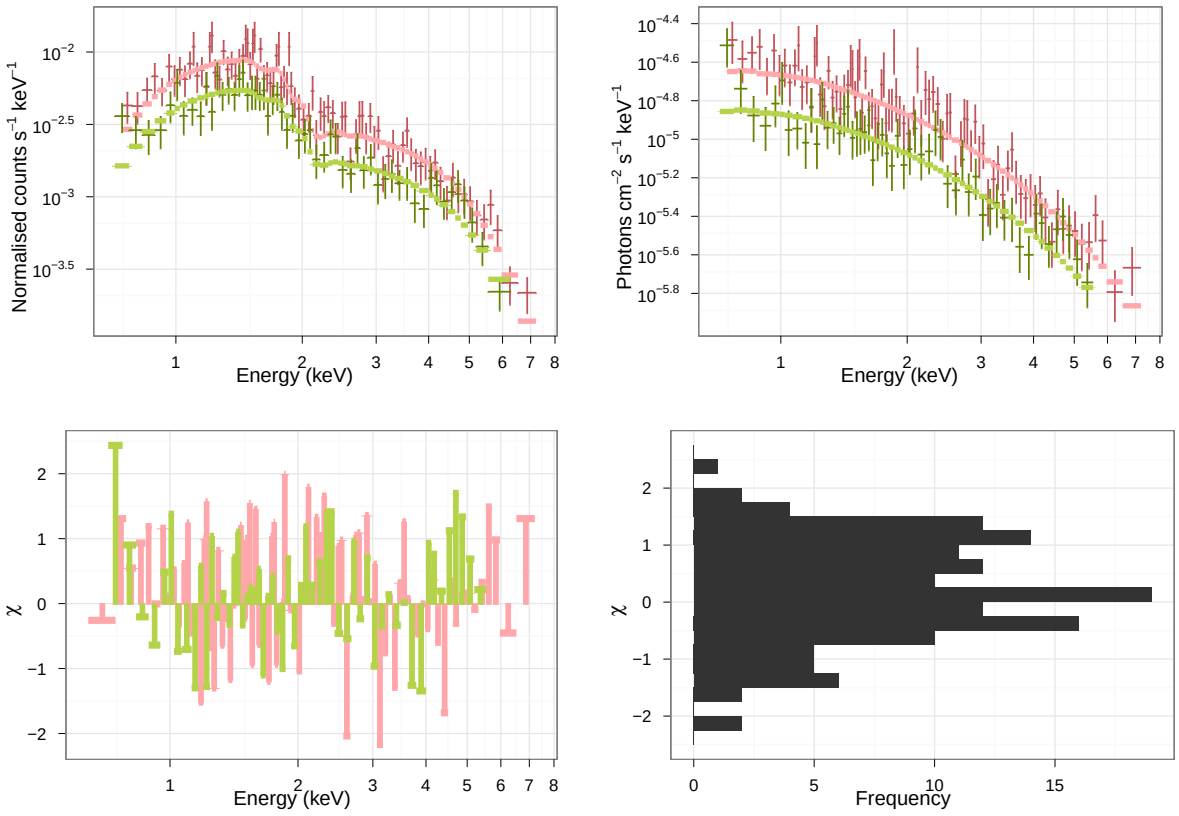

Figure 5.8 Example spectral fit of S3 in the instances when the thermal state was prefered. This shows the *diskbb* fit, with fixed Galactic absorption, to the spectra from obsIDs 8489 and 8490. Top-left shows the spectral fit, with fit residuals bottom-left which are histogrammed in the bottom-right. In the top-right panel is the unfolded spectrum, i.e. the model shape independent of the ACIS response.

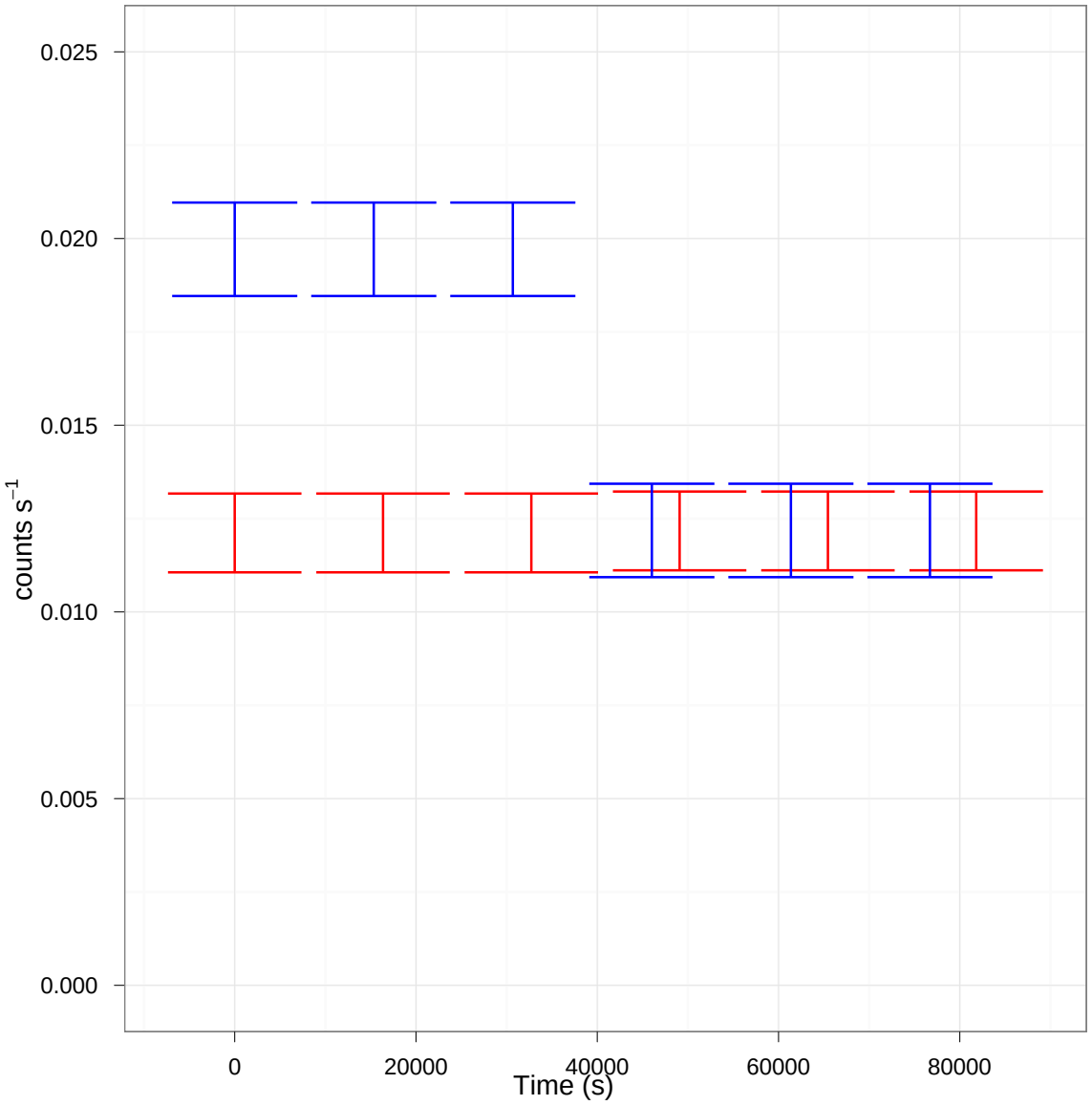

Figure 5.9 Example of optimum lightcurves output by Gregory-Loredo algorithm *glvary*. Instances where a source was seen to be highliy variable (index $= 9$) and constant. These lightcurves are S2 (red) in obsID 7798 and S4 (blue) in obsID 7797. Error bars represent 3σ confidence regions.

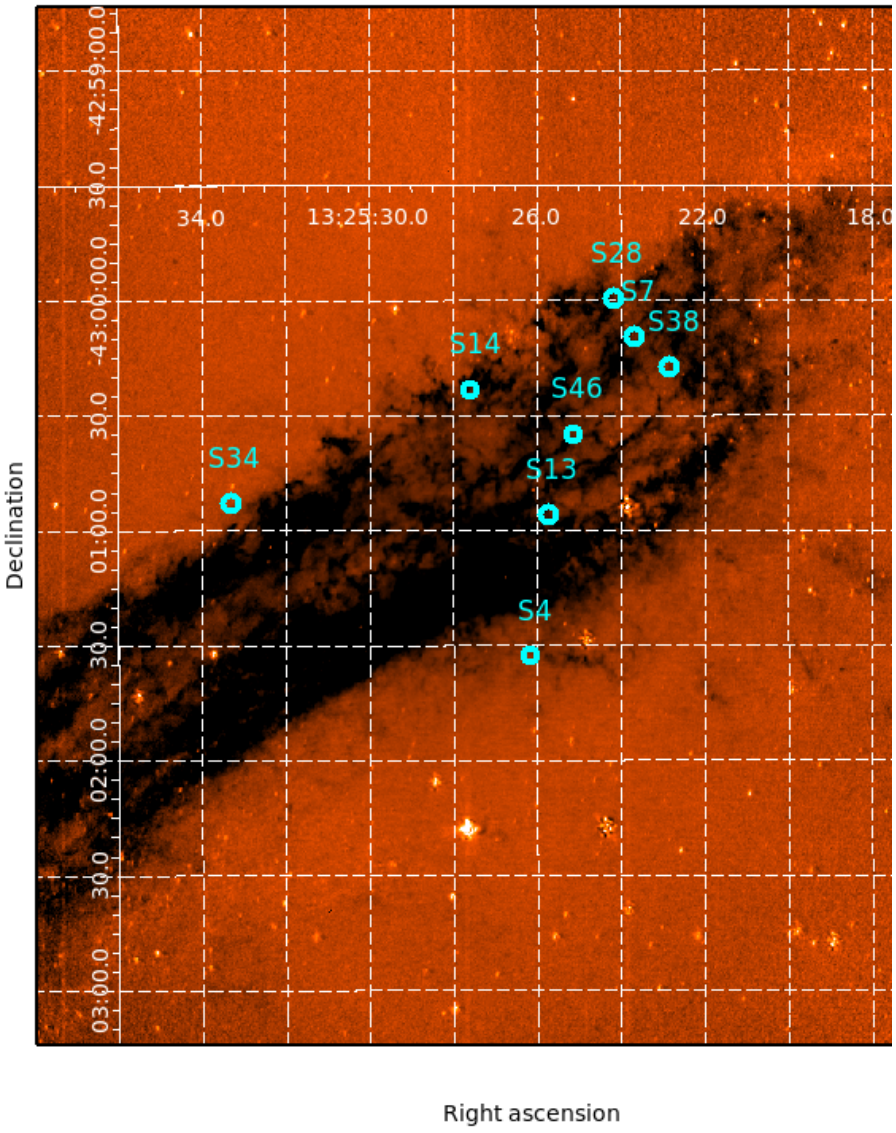

Figure 5.10 K-band optical depth map showing the prominant Cen A dust lanes. Positions of the dustlane sources are marked as circular regions of radius $2''$.

Chapter 6

The fading of two transient ULXs

6.1 Introduction

Ultraluminous X-ray sources (ULXs) are X-ray point sources with isotropic luminosities $> 10^{39}\ \mathrm{erg\ s^{-1}}$, displaced from the nucleus of their parent galaxy. Our knowledge of such systems has increased dramatically in the *Chandra* and *XMM-Newton* eras, where high spatial resolution coupled with large variability has supplied strong evidence against the high luminosities resulting from source superposition. These luminosities are an order of magnitude above the Eddington limit L_{Edd} of accreting neutron stars (NSs) and therefore it seems likely that ULXs possess black hole (BH) primaries.

The key debate in ULX research concerns the mass of the compact object. Stellar mass black holes, which have an empirical mass distribution peaked at $\sim 8\mathrm{M}_{\odot}$ (Özel et al., 2010; Kreidberg et al., 2012), would have to be emitting $\gtrsim L_{Edd}$, while some analyses favour an explanation involving intermediate mass black holes (IMBHs) of $M \gtrsim 10^{3}\mathrm{M}_{\odot}$ accreting at a fraction of their Eddington rate. The existence of IMBHs has implications across a broad range of astrophysics including the studies of stellar populations, gravitational wave astronomy and the origins of super massive black holes.

6.1.1 Transient ULXs

Most ULXs are observed to be persistent over multi-epoch observations, and consistently at luminosities above $10^{39}\ \mathrm{erg\ s^{-1}}$ (Colbert, 2004; Liu et al., 2006). However, we are now aware of a handful of transient ULXs that experience large long-term variability over many orders of magnitude, rising to $L_x > 10^{39}\ \mathrm{erg\ s^{-1}}$ from below the typical detection limits of extragalactic X-ray binaries (XBs). The study of such transient sources is important because they must cross the luminosity range typical of Galactic BH XBs during their rise and decay. If a ULX can be observed during such a transition

we can attempt to determine whether it behaves like an ordinary stellar-mass BH, in terms of its spectral transitions and timing properties, or whether it is a fundamentally different type of accretion phenomenon in the ordinary BH luminosity regime.

Few transient ULXs are known due to the lack of regular deep X-ray monitoring for every galaxy over a prolonged period. It may prove to be the case that outburst durations are $\sim 10 - 100$ years, particularly for sources associated with old stellar populations (Piro & Bildsten, 2002), which is longer than the *Chandra* and *XMM* eras. A handful of sources have now shown variability and outburst timescales comparable to Galactic BH LMXBs, with luminosities on occasion $\gtrsim 10^{39}$ erg s^{-1} and $\lesssim 10^{38}$ erg s^{-1} at other times. These ULXs have been detected in both starburst (e.g. Feng & Kaaret, 2007; Soria et al., 2012; Bauer & Pietsch, 2005) and early-type (e.g. Kraft et al., 2001; Roberts et al., 2012) galaxies. Outburst durations and recurrence times remain largely unconstrained, but some outbursts have remained bright ($> 10^{39}$ erg s^{-1}) for over a year (Soria et al., 2012). Seemingly persistent behaviour is a common feature of bright ($> 8 \times 10^{38}$ erg s^{-1}) sources in early-type galaxies (e.g. Irwin, 2006), and outside of globular clusters the high accretion rates implied by such luminosities suggests that the sources may have started to accrete comparatively recently. An empirical, scattered correlation between outburst duration and orbital period has been demonstrated for Galactic XBs (Portegies Zwart et al., 2004) and a stronger correlation found between the peak L_x and orbital period by (Wu et al., 2010). This leads us to predict that the population of bright low mass X-ray binaries is dominated by large period (> 30d) systems with an evolved companion, experiencing large outbursts with larger recurrence times.

The physical origin of the distinction between the transient ULXs and the persistent sources remains unknown. The majority of Galactic BH low mass X-ray binaries (LMXBs) are transient, experiencing outbursts on timescales of weeks to months, recurring on months to years (for review see Remillard & McClintock, 2006). It is thought that transient behaviour is the result of the disk instability mechanism (DIM) (§1.1.3 Lasota, 2001) which has been successful in explaining the limit-cycle behaviour observed from the lightcurves of short-period cataclysmic variables (Smak, 1984). Transient behaviour should occur from below a critical accretion rate, above which the entire disk is always warmer than the ionisation temperature of hydrogen ($\approx 6,500$ K) and emission is persistent. In LMXB, irradiation of the outer disk by the central X-ray source should mean that this threshold is at a lower accretion rate than for CVs (Dubus et al., 2001) and less than a few percent Eddington, a

prediction that was recently found to be in good agreement with the accretion of Galactic sources (Coriat et al., 2012). A question that remains regarding transient ULXs is whether they are IMBHs that outburst via the DIM and observed at a fraction of their $\dot{M}_{Edd}$, or ordinary stellar BHs accreting $> \dot{M}_{Edd}$. Maccarone (2003) showed that the transition from the soft to the hard state before quiescence occurs at a few percent Eddington for Galactic BH XBs, and Maccarone et al. (2003) showed that this is also the case for super massive BH accretion in AGNs, and also that the low/hard and quiescence are indistinguishable (albeit softening slightly with decreasing L_x, Constantin et al., 2009). This similar behaviour observed at the extremes of the BH mass spectrum suggests a common accretion behaviour that should be applicable to the complete range of BH masses. An IMBH of $1000\mathrm{M}_{\odot}$ would have $L_{Edd} \sim 1.5 \times 10^{41}$ erg s^{-1}, and therefore for $L_x \lesssim 10^{39}$ erg s^{-1} the accretion rate is much less than 1% Eddington, and the source spectra should be hard. In contrast, BH XBs at peak L_x are usually in the so called steep power law (aka very-high) state, before dimming into the canonical thermal dominant state, when the thermal emission from the disk dominates the spectrum. Therefore evidence of a soft or disc-dominated spectrum at sub-UL luminosities argues against accreting IMBHs. It is for this reason that Hyper-luminous X-ray source HLX-1 has been dubbed the 'best' IMBH candidate to date as the spectra are consistent with canonical thermal dominant and hard states at 10^{42} erg s^{-1} and 10^{40} erg s^{-1}, respectively (Servillat et al., 2011).

The identification and classification of ULX optical counterparts are problematic, as observations of the host galaxies are often unable to resolve the dense stellar fields, nor deep enough to place meaningful constraints on the color via a significant non-detection. The greater abundance of ULXs in late-type galaxies, particularly star-forming regions (Swartz et al., 2009), suggests young donors may reside in the majority of systems. Those companions that are identified are often blue, which may indicate an OB donor (e.g. Liu et al., 2004). However, for some sources it has been shown that the blue light is only present during the X-ray outburst, which suggests that the optical light is mostly reprocessed emission in the disk (e.g. Soria et al., 2012). Recently, an *HST* census of optical counterparts in nearby (≤ 5 Mpc) galaxies (Gladstone et al., 2013) reported upper limits of $M_v = -4$ to -9 for 9/33 systems, ruling out O type companions for 4, and used SED fitting to rule out a further 20 O-types and an OB donor completely for one ULX in NGC 253. The nature of the counterpart is important in the context of the IMBH debate, as massive donors should produce persistent X-ray sources unless the compact object is very massive (King et al., 2001), which is the dichotomy

between BH HMXB and BH LMXB donors observed in the Milky Way (Remillard & McClintock, 2006). For transient behaviour to occur for $M \approx 5-20$ $\mathrm{M}_{\odot}$ donors from a young stellar population, the compact object must be > 50 $\mathrm{M}_{\odot}$ (Kalogera et al., 2004a). A ULX with a B9 supergiant donor in spiral galaxy NGC 7793 that was recently observed to vary between $L_x \sim (5-400) \times 10^{37}$ erg s^{-1} (Motch et al., in prep.) would have violated this hypothesis, as the BH mass is constrained ≤ 15 $\mathrm{M}_{\odot}$. However, the authors argue that this is not a true transient, but rather that it is a high inclination source where the fainter state results from obscuration by the precessing disk rim.

6.1.2 NGC 5128 ULXs

NGC 5128 (Centaurus A) is the nearest optically luminous early-type galaxy, situated at a distance of 3.7 Mpc (Ferrarese et al., 2007), with $M_B = -21.1$. Two ULXs are known in Cen A, both of which are transients. The first ULX (1RXH J132519.8-430312, herein ULX1) was discovered by *ROSAT* (Steinle et al., 2000) and re-detected near the start of the *Chandra* era (Kraft et al., 2001; Ghosh et al., 2006). The Chandra detections showed a soft spectrum, well described by a cool multi-temperature disk blackbody or a steep power law, and from this we infer $L_x \gtrsim 10^{39}$ erg s^{-1}. The luminosity may have been as high as 5×10^{39} erg s^{-1} in the ROSAT HRI observations.

Six 100 ks *Chandra* observations of NGC 5128 were taken in 2007 as part of the Cen A Very Large Project (VLP), spanning the course of 2 months (Jordán et al., 2007). Over the course of these observations a second ULX was discovered (CXOU J132518.2-430304, herein ULX2, Sivakoff et al., 2008). Its spectra were reminiscent of the steep power law state at a luminosity of $\sim (2-3) \times 10^{39}$ erg s^{-1}; it softened during the course of the outburst, as would be expected for a BH LMXB entering the thermal dominant state. The spectra were modelled using thermal disk blackbody and power law components. Returning to study these spectra, we note that the inner-temperature of the disk is cool ($0.6-1.0$ keV) for a stellar mass BH at such a high luminosity, and the normalisation of the component requires an inner disk radius of ≈ 19 km for a face-on disk, much smaller than the innermost stable circular orbit for a ~ 10 $\mathrm{M}_{\odot}$ BH. Therefore the disk component is unlikely to be a physical description of the actual disk, and the source has spectra consistent with either the steep-power law or the so-called 'Ultraluminous state' (Gladstone et al., 2009). Unambiguously distinguishing the ultraluminous state relies on high quality data with enough sensitivity above 5 keV to detect the high-energy rollover with simultaneous low temperature disk blackbody in the spectrum.

This feature is hard to detect with *Chandra*, which has a smaller collecting area than *XMM-Newton*.

In Chapters 4 & 5, we have shown that the transient BH LMXB candidates of Cen A, analogous to the BH systems of the Milky Way in terms of transient behaviour and thermal state spectra, are only associated with a merged late-type remnant (Burke et al., 2013). We suggested that the merged late-type was a more favourable environment for such systems to exist owing to the ancient stellar population of the halo (~ 12 Gyrs, Rejkuba et al., 2011) resulting in a relative paucity of massive enough donors for the longer orbital periods required to achieve the observed luminosities. ULX1 and ULX2 are in the halo of Cen A, to the south-west of the nucleus, and are therefore associated with an older stellar population than the more typical (in Milky Way terms) BHC LMXBs that are associated with the late-type galaxy remnant.

In this paper we report on a series of Chandra observations since the 2007 VLP. We use the VLP observations to show the lowest upper limit for the quiescent state of ULX1, and report on subsequent detections of both ULXs. Both sources are detected at luminosities substantially sub-Eddington for a 10 $\mathrm{M}_{\odot}$ BH LMXB, and we take advantage of a rare opportunity to study the spectra of ULXs during their decline from outburst. We discuss spectra, recurrence times and duty cycles and show that these are further evidence of the connection between ordinary stellar mass BH LMXBs and ULXs, and argue against the need for IMBH primaries in these systems. Finally, we discuss the lack of transient ULX discoveries in early-type galaxies.

6.2 Data Preparation and Analysis

Since 2007, Chandra observations have been made as part of the HRC Guaranteed Observation Time program (PI: Murray), amounting to a series of regular 5 ks 'snapshots' and a single 50 ks observation (ObsID 10722). We previously presented data from some of these observations in table 4.1 (table 1 from Burke et al., 2012), and in addition to these we now include three further datasets, obsIDs 13303, 13304 and 15294 made on MJD 56031, MJD 56168 and MJD 56387. These data were reduced and aligned to the other Cen A *Chandra* ACIS observations in the manner detailed in chapter 5 (Burke et al., 2013). We make use of the VLP data to obtain deep upper limits on the emission from ULX1 during 2007.

Table 6.1. Net Counts (0.5-8.0 keV)

ULX	10723	10724	10725	10726	10722	11846	11847	12155	12156	13303	13304	15294
1	< 5.9	< 2.6	< 2.6	< 5.9	< 4.3	< 3.2	< 3.2	< 3.2	$\mathbf{24.2^{+9.7}_{-7.6}}$	< 2.6	< 2.6	< 2.6
2	$\mathbf{20.1^{+9.6}_{-8.1}}$	$\mathbf{9.9^{+6.6}_{-4.6}}$	$\mathbf{6.5^{+5.6}_{-3.6}}$	< 4.9	$\mathbf{45.5^{+13.5}_{-11.5}}$	< 3.8	$\mathbf{4.3^{+4.8}_{-2.8}}$	< 3.2	$\mathbf{8.6^{+6.3}_{-4.3}}$	< 3.5	< 3.2	< 2.6

Note. — **Net counts** and 90% upper limits for each new observation of ULX1 and ULX2.

6.2.1 Observed Count Rates

With the objective of securing count rates for the ULXs in the post-VLP observations, and upper limits for ULX1 in the 100 ks observations we used *MARX*[1] to define ellipses around the positions of both sources describing the 90% PSF at 8 keV. This was adequate to avoid source confusion in the snapshot observations, but in some of the 100 ks observations the positions are so much further off-axis that the position of ULX1 overlaps with a bright neighbour, so that source regions could only be defined for three of the VLP observations. For background, we defined a source-free rectangular region based on the merged observation file, to the north of the ULXs. We used the *ciao* tool *aprates* to estimate 90% confidence count rates and upper limits, which we present as a lightcurve for both ULXs in Fig. 6.1. The detection count rates are substantially smaller than when the sources were observed in the UL regime; $\approx (1-5) \times 10^{-3}$ s^{-1} down from $\approx 8 \times 10^{-2}$ s^{-1} in the UL regime. From the VLP observations, the lowest upper limit for ULX1 is 5×10^{-5} s^{-1}, which assuming a power law described by photon index $\Gamma = 1.7$ experiencing Galactic absorption, is an upper limit of $L_x \approx 10^{36}$ erg s^{-1} over $0.5 - 8.0$ keV.

We combine three of the ~ 100 ks observations (obsIDs 7797, 8489, 8490) to obtain the deepest upper limit to ULX1. We obtain a count rate limit of 5.34×10^{-5} s^{-1}, corresponding to a luminosity of $L_x \sim 1.2 \times 10^{36}$ erg s^{-1}. Similarly we measure a combined upper limit of 1.6×10^{-4}s^{-1} over obsIDs 13303, 13304 and 15294 subsequent to the latest detection, which means that $L_x < 10^{37}$ erg s^{-1}.

We combined obsIDs 11846, 11847 and 12155 to calculate the average count rate for ULX2. Running *wavdetect*, as before, identified the source in the combined image (there was no detection by wavdetect in obsID 11847 alone) and measure a count rate of $3.21^{+3.93}_{-2.81} \times 10^{-4}$ s^{-1} (90% confidence). This would correspond to a ($0.5 - 8.0$ keV) luminosity of 5.8×10^{36} erg s^{-1}, with an upper limit of

[1] http://space.mit.edu/cxc/marx/

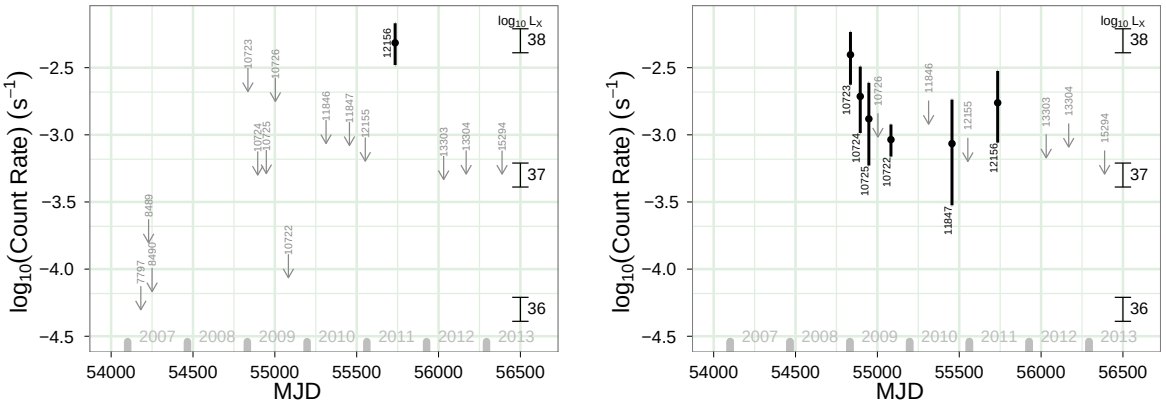

Figure 6.1 X-ray lightcurves (0.5-8.0 keV) since 2007 for (*left*) ULX1, including the VLP observations, and (*right*) ULX2. Arrows denote 90% confidence upper limits and obsIDs are labelled. We obtained a detection for ULX2 using obsIDs 11846, 11847 & 12155 (Section 6.2.1). On the right of each lightcurve we show $\log_{10}(L_x)$, for a range of power law spectra with $\Gamma = 1.5 - 2.5$. Note that obsID 10722 is an ACIS-S observation and the $\log_{10}(L_x)$ were calculated using webPIMMs for ACIS-I observations.

1.2×10^{37} erg s^{-1}. Given the subsequent detection in obsID 12156, this suggests that the source remained in outburst after obsID 10722, lingering at $L_x \approx 10^{37}$ erg s^{-1}. A combined measurement including obsID 12156 has a count rate of $6.6^{+4.2}_{-3.2} \times 10^{-4}$ s^{-1}. We measure an average upper limit of 3.0×10^{-4} s^{-1} ($L_x < 10^{37}$ erg s^{-1}) over obsIDs 13303, 13304 and 15294.

Finally, we tested the intra-observational variability of the sources, for each individual detection, using the *ciao* tool *glvary*[2] (Gregory & Loredo, 1992). No variability was detected, and the variability indices were ≤ 1. Significant variability is defined as variability index of at least 6.

6.2.2 Spectral fitting

We attempted fitting simple spectral models to the more count-rich spectra. ULX2 in obsID 10722 has ~ 45 counts, and in obsID 10723 has ~ 22 counts. Using the modified Cash statistic (Cash, 1979; Arnaud et al., 2011) (aka 'W' statistic) in XSPEC we fit the ungrouped spectra using simple power law and disk blackbody models (*powerlaw* & *diskbb*, respectively). In fitting the low count spectra in various joint fits we could not achieve a good fit, with $95 - 100\%$ of Monte-Carlo goodness-of-fit simulations possessing a lower test statistic than that achieved in fitting. For obsID 10722, we found converging fits with an absorbed power law model (*phabs* $\times$ *powerlaw*) and an absorbed disk-blackbody model (*phabs*$\times$*diskbb*). We initially left the absorption parameter N_H free, to make use of the diagnostics of Brassington et al. (2010) which we applied successfully in chapter 5 to infer the spectral states of many X-ray binaries in Cen

[2] http://cxc.harvard.edu/ciao/ahelp/glvary.html

A. However, the N_H recovered from fitting had large uncertainties that rendered such inference impossible, and the point estimates tended towards zero. When N_H was fixed to the Galactic value (8.4×10^{20} cm^{-2}) the *diskbb* fit yields $kT_{in} = 0.74^{+0.45}_{-0.33}$ keV with $L_x \approx (0.7 - 1.6) \times 10^{37}$ erg s^{-1}. The fit is acceptable, as Kolmogorov-Smirnov & Anderson-Darling tests[3] produce values that are consistent with simulations, i.e. 'goodness test' of 2000 samples shows that $\approx 40\%$ of realisations produce smaller test statistics. We present the integrated counts of ULX2 during obsIDs 10722, 10723 and 10724 in figure 6.2, together with the best fitting *diskbb* model and confidence region for obsID 10722. For an absorbed power law, $\Gamma = 2.2^{+0.7}_{-0.6}$ and $L_x \approx (1.1 - 2.2) \times 10^{37}$ erg s^{-1}, with $\sim 20\%$ realisations producing better values of the test statistic.

6.2.3 Quantile Analysis

We have a very rare opportunity to try to infer the spectral state of ULXs in the non-UL regime. However, in our observations there are often too few counts to perform reliable spectral fitting (see section 6.2.2 for discussion). Hardness ratios, the traditional workhorse of X-ray astronomy, are dependent on the subjective choice of energy bands. For reference, we present hardness ratios for these detections in table 6.2, calculated using the BEHRs software[4]. The spectra with the most counts, obsIDs 10722, 10723 are the softest, and while the lower-quality spectra appear harder, they are not significantly so. Quantile analysis maximises the use of all the photons detected. Using the source and background regions described in section 6.2.1, we extracted the spectra from the observations where a given ULX was detected. We employ techniques and software described by Hong et al. (2004, 2009), who showed that the median energy E_m is a superior tool to hardness ratios for inferring spectral states. Our 5 detections of ULX2 and new detection of ULX1 all have < 50 counts per observation. We present the median energies and 1σ uncertainties from the individual detections in table 6.3.

Hong et al. (2009) define what they call a 'quantile color-color diagram' (QCCD) to separate sources into spectral groups. The axes of these plots are an expression of E_m (in terms of the bounds of the energy band, x-axis) and the ratio of the energy of the 25% to the 75% quantiles ($\times 3$, y-axis). For our purposes this was not an informative diagram for comparing the spectra, as the uncertainties in the y coordinate were too large to determine if any spectral changes had occured. We therefore focus on the behaviour of the median energy.

A key issue that we wish to address is whether ULXs experience canonical BH LMXB spectral states in the classic luminosity regime. As discussed in § 6.1.1, opinions on this are divided into whether ULXs transition to a hard state (power law dominated) as they leave the UL regime (as would be expected for an IMBH, which would be at a few percent Eddington), where they remain in quiescence, or whether they enter a thermal dominant state first, as is seen for the majority of stellar mass BH systems. To this end we include a small grid of parameters for absorbed power law spectra in Fig. 6.3. We present this next to the QCCD datum of

[3] Available in XSPEC 12.8.0

[4] http://hea-www.harvard.edu/AstroStat/BEHR/#refs

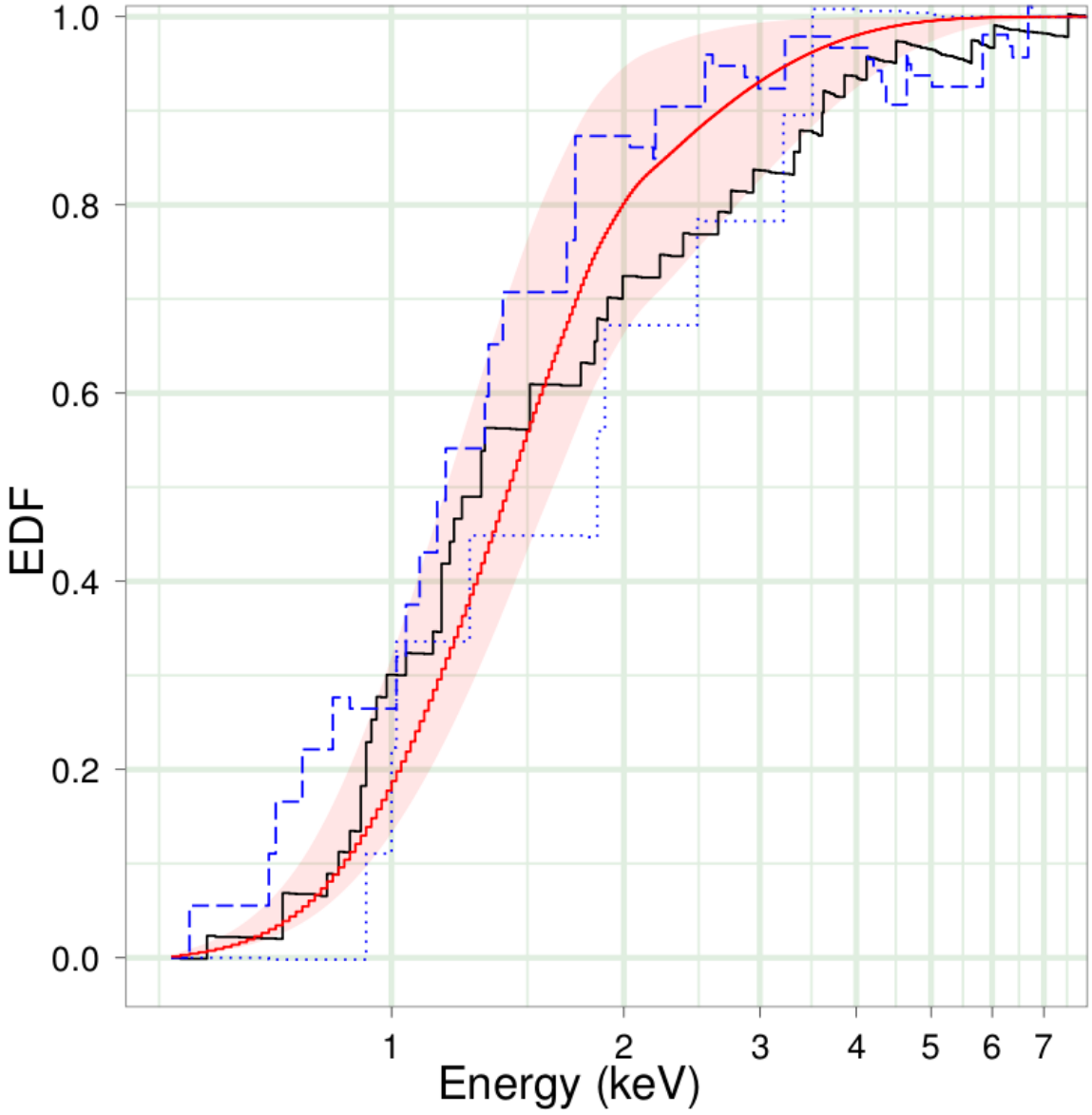

Figure 6.2 Integrated counts (Empirical Distribution Function) from ULX2 in obsIDs 10722 (solid), 10723 (dashed) and 10724 (dotted), overlaid on the best fit $diskbb$ ($kT_{in} = 0.74^{+0.45}_{-0.33}$ keV, see section 6.2.2) from obsID 10722 (red line) with 90% confidence region (shaded) .

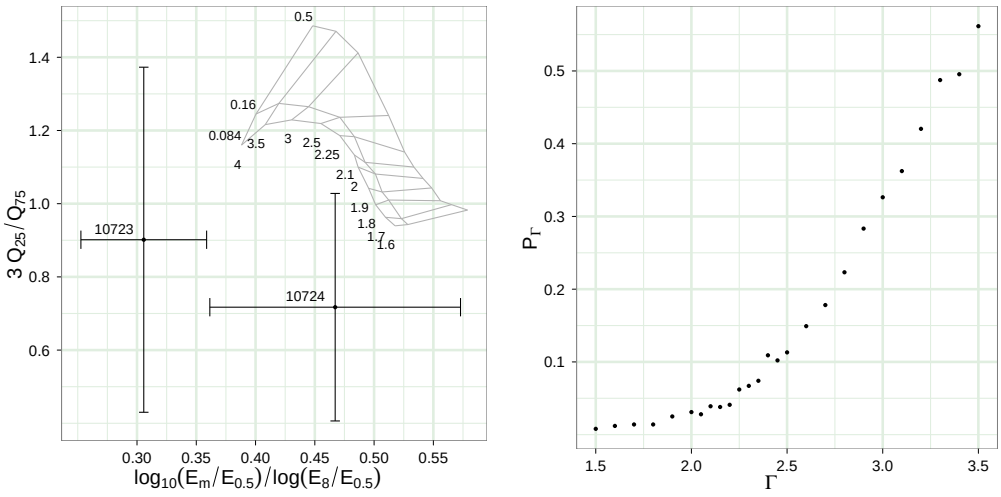

Figure 6.3 *Left*, QCCD for ULX2 with parameter grid corresponding to an absorbed power law for $N_H = (0.084, 0.16, 0.5) \times 10^{22}$ cm^{-2} and $\Gamma = 1.6 - 4.0$, with quantiles from obsIDs 10723 and 10724. *Right*, proportion of simulated spectra that possess median energies as extreme as that measured for ULX2 in obsID 10723 for a range of Γ, with $N_H = 0.084 \times 10^{22}$ cm^{-2}. Each point represents a sample of 1000 simulated spectra.

Table 6.2. Hardness Ratios (0.5-1.5 keV)/(1.5-8.0 keV)

ULX	10723	10724	10725	10722	12156
1	-	-	-	-	$1.20^{+0.75}_{-0.45}$
2	$1.62^{+2.11}_{-0.82}$	$0.54^{+0.66}_{-0.30}$	$0.55^{+1.01}_{-0.38}$	$1.14^{+0.50}_{-0.34}$	$0.63^{+0.89}_{-0.38}$

Note. — Hardness ratios calculated using BEHRs (Park et al., 2006). Confidence intervals are 68.5%

Table 6.3. Median Energies (keV)

ULX	10723	10724	10725	10722	12156
1	-	-	-	-	$1.44^{+0.21}_{-0.21}$
2	$1.17^{+0.17}_{-0.17}$	$1.83^{+0.54}_{-0.54}$	$1.39^{+0.28}_{-0.28}$	$1.30^{+0.19}_{-0.19}$	$1.56^{+0.23}_{-0.23}$

Note. — Median energies of ULX1 and ULX2, with 1σ uncertainties as calculated by Hong et al. (2004).

ULX2 from obsID 10723, as this E_m is at the most extreme position from the grid (see below). Hong et al. (2004) state that the estimated uncertainties are possibly over-estimated by as much as $20-30\%$ in the <30 count regime, where most of our detections lie. To determine how extreme this E_m would be for a source in the hard state, we simulated many spectra described by a power law of $\Gamma = 1.5$–2.1 with the same number of counts (≈ 22) as obsID 10723, calculated E_m for each spectrum, and then found the proportion P_Γ of simulated spectra for each Γ that had E_m smaller than that measured from obsID 10723 (Fig. 6.3).

Fig. 6.3 shows that for obsID 10723 we can exclude an absorbed power law of $\Gamma \leq 2.2$ at 95% confidence. A source in the canonical hard state would be well described by a power law of $\Gamma \sim 1.7$, with $\Gamma = 2.1$ at the most extreme for GRS 1915+105 (based on values quoted in Remillard & McClintock, 2006). However, some authors suggest that GRS 1915+105 does not experience the canonical hard state (Reig et al., 2003), and the hardest spectra for the canonical hard state have $\Gamma \sim 1.9$, and tend to be for the sources that peak at lower luminosities. therefore it seems unlikely that the source is in the BH LMXB low/hard state during this observation. We find that $\Gamma = 1.5$ is still allowed at the 20%, 10%, and 30% levels for obsIDs 10722, 10725, and 12156 respectively, and $\sim 10\%$ for ULX1 in obsID 10726, so for these detections, this method is inconclusive. Therefore it seems that the source is not in the canonical hard state in at least one of the snapshot observations. That the spectra appear to harden during the decline in luminosity is consistent with the transition from the thermal dominant to low/hard state, a fortiori because the hardest BH XB spectra are associated with this transition (Wu & Gu, 2008).

It is suggestive that the subsequent observation, obsID 10724, is the furthest median energy from obsID 10723 (table 6.3), and has a median energy consistent with a grid of power law states (Fig. 6.3). Tentatively, this is indicative of the source moving from a soft, higher luminosity state, to a harder, lower luminosity state, as observed for the Galactic binaries as they return to quiescence. Spectral fitting to obsID 10722, for which we have the most counts from a single observation, showed no preference between power law or thermal dominant states. However, fitting both spectral models recovered parameters consistent with those of the Galactic BH XBs.

6.3 Discussion

This chapter focuses on a series of regular *Chandra* observations of Cen A to search for recurrence of the two known ULXs. These sources are transient in nature, and only a handful of similar sources (observed $Lx > 10^{39}$ erg s^{-1} and $L_x < 10^{38}$ erg s^{-1} in separate epochs) have been reported.

The Cen A ULXs have been documented at $L_x > 10^{39}$ erg s^{-1}, with count rates of $(7-8) \times 10^{-2}$ s^{-1} (Ghosh et al., 2006; Sivakoff et al., 2008). By contrast, we present new detections in the $(0.5-5.0) \times 10^{-3}$ s^{-1} range. If one assumes a canonical hard state for all detections, i.e. a power law of $\Gamma \sim 1.7$ experiencing Galactic absorption, this equates to luminosities $\approx 10^{37} - 10^{38}$ erg s^{-1}. For the low counts regime, estimating the exact luminosity will of course vary by a factor of a few depending on the assumed spectral model. This is an opportunity to examine ULXs at substantially sub-Eddington luminosities, and compare them to Galactic BH XBs.

6.3.1 Spectral States

Galactic BH XBs typically emit the most energy as X-rays in the thermal state, where the contribution of comptonized emission to the spectrum is low. Physically, it is thought that the softer state results from the exposed optically thick, geometrically thin accretion disk, which is well-described by a disk blackbody. In this model, the temperature T_{in} of the innermost part of the accretion disk is recoverable by performing detailed spectral fitting, and for stellar mass BHs $kT_{in} \sim 1.0$ keV (but can reach 1.5 keV, e.g. Sobczak et al., 2000). The temperature of the disk scales inversely with radius from the center of the compact object, and as more mass leads to a larger ISCO, therefore more massive objects have cooler inner disks. In terms of accretion rate $\dot{m}$ ($= \dot{M}/\dot{M}_{Edd}$), thermal states are observed between $0.03 - 0.50$ Eddington for stellar mass BHs; however, it was noted by Soria et al. (2009) that ULXs are not in the thermal state at peak luminosity, remaining hard during any variability. A possible explanation is that such hard-state ULXs are IMBHs (Winter et al., 2006), that never reach accretion rates $\dot{m} \approx 0.03$, high enough to make them switch to the thermal state, even at their peak luminosities. Alternatively, if ULXs contain BHs of stellar origin ($M < 100 M_{\odot}$), their broad power law-like X-ray spectrum at peak luminosity may be the result of Comptonization in an optically thick medium (Roberts, 2007; Gladstone et al., 2009); they would not be in the thermal dominant state because $\dot{m} > 1$. In the latter scenario, we predict that the thermal state may be seen in transient sources during their decline, when $0.03 < \dot{m} < 0.5$, before they switch back to a hard state for $\dot{m} < 0.03$. Failure to see transient ULXs passing through the thermal dominant state is either due to the very small number of such sources observed so far in the right accretion regime, or suggests that not all BHs necessarily switch to the thermal state during their outburst evolution.

The results from quantile analysis for the two transient ULXs in Cen A support the possibility that ULXs enter the canonical thermal state when they decline to lower luminosities. Both sources have spectra consistent

with those of XBs at 10^{38} erg s^{-1}, and in one observation of ULX2, obsID 10723, we can exclude the hard state with $> 95\%$ confidence based on the median energy of the spectrum, while analysis of the other spectra were inconclusive. At even lower luminosities, $L_x \sim 2\times10^{37}$ erg s^{-1}, there is tentative evidence of a hardening of the ULX2 spectra, consistent with the behaviour of the canonical low/hard state. No intra-observational variability was detected from these sources using the *ciao* tool *glvary*, as would be characteristic behaviour in the hard state; however, we are skeptical as to whether such variability would be detected, and note that it has previously not been detected using higher-quality data from hard state sources in Cen A (Burke et al., 2013). These spectral results broadly support the argument that these ULXs contain stellar mass BHs.

The detection of ULX2 in a thermal state at $\sim 10^{38}$ erg s^{-1} is consistent with other work on transient ULXs. A transient source in M31 that peaked at between $(2-5)\times10^{39}$ erg s^{-1} ULXs using *XMM Newton*, had spectra that were described well by a disk blackbody model down to $L_x \approx 6\times10^{38}$ erg s^{-1} (e.g. Middleton et al., 2012; Kaur et al., 2012; Esposito et al., 2012). Steep power law spectra (interpreted as near-Eddington states) and soft states have been inferred for the globular cluster transient ULXs in NGC 4649 ($\sim (2-5)\times10^{38}$ erg s^{-1}, Roberts et al., 2012) and NGC 1399 (5×10^{38} erg s^{-1} Shih et al., 2010), respectively. As a possible exception to this trend, a transient ULX in NGC 3379 (Brassington et al., 2008) has been inferred progressing to a hard state at $\sim 1\times10^{39}$ erg s^{-1} (Brassington et al., 2012b), and while the source was later detected at $\approx 2\times10^{37}$ erg s^{-1}, there were too few counts to determine if the spectra remained hard.

Based on our inferred spectral properties, we estimate the source luminosity based on the appropriate model. Assuming that ULX2 is in a soft state in obsID 10723, we take the spectrum of the source to be dominated by a $kT_{in} = 1.0$ keV disk blackbody experiencing Galactic absorption ($N_H = 8.4\times10^{20}$ cm^{-2}), then the observed 90% confidence count rate corresponds to $L_x \sim (0.5-1.3)\times10^{38}$ erg s^{-1} in the $0.5-8.0$ keV band. In terms of systematic differences in the parameters of this model, changing kT_{in} to 0.5 keV only reduces the maximum luminosity by $\sim 10\%$. ObsID 10723 has the highest count rate observed in the post-VLP observations, and therefore it is secure to state that our subsequent detections of both ULXs are below $L_x \sim 10^{38}$ erg s^{-1}. Similarly we estimate the luminosity in obsID 10722 to be $\approx 2\times10^{37}$ erg s^{-1}.

6.3.2 Outburst Duration

It is clear that both ULXs spend an appreciable amount of time in outburst. ULX1 has now been detected in three separate epochs (1995 with *ROSAT*, 1999 and 2011 with *Chandra*) with secure non-detections between them down to an interesting luminosity ($< 10^{37}$ erg s^{-1}). In contrast, ULX2 remained undetected until 2007, and the number of outbursts that we have witnessed is less clear-cut. There are two reasonable scenarios; the first is that we have witnessed a single outburst that was at UL luminosities in 2007, decayed from 10^{38} erg s^{-1} down to $\approx 10^{37}$ erg s^{-1} between MJD 54835 and MJD 55082 (April-September 2009), and then, because

this is approximately the detection limit for a 5 ks observation, remains on the cusp of being detected. The second possibility is that there have been two outbursts, one in 2007 and another in 2009, of which we only witness the egress, and then the luminosity stays at $\approx 10^{37}$ erg s^{-1} for hundreds of days.

The overall behaviour of ULX2, while similar to other transient ULXs, is not directly analogous to any of the Galactic BH LMXBs. In terms of the shape of the lightcurve, very few are seen to outburst longer than a few hundred days, and certainly not as long as a thousand (Remillard & McClintock, 2006). However, some show signs of slow decays the end-points of which are unknown owing to the end of observations, such as V404 Cyg, which was probably still active after cessation of observations 150 days into its 1989 outburst (e.g., Chen et al., 1997). The long period spent at lower luminosities for ULX2 is reminiscent of Swift J1753.5-0127 which has been seen to linger at lower luminosities an order of magnitude or more below the peak luminosity for > 1500 days as of May 2010 (RXTE, Soleri et al., 2012), displaying both hard and soft spectral states during the lingering stage. However, the peak luminosity of J1753.5-0127 is probably not much more than 10^{36} erg s^{-1}, and therefore the low/hard state is close to what would be considered quiescence for many sources. The comparably low luminosity may be a consequence of the tightness of this particular system ($P_{orb} \sim 3.2$ hr).

Alternatively, it is perhaps only the persistent systems with higher mass companions that would potentially give similar lightcurves if sampled with *Chandra* from Cen A, such as Cyg X-1, LMC X-1 and LMC X-3. The transient source GRS 1915+105, which has been in outburst since 1992, could be a more pertinent comparison, depending on whether ULX2 has now returned to quiescence or is still in outburst, below 10^{37} erg s^{-1}.

6.3.3 Duty Cycle

The duty cycle d is defined as the ratio of the time spent in outburst to the total time spent in outburst and quiescence.

For ULX1, let us assume that an outburst lasts a maximum of ≈ 500 days (Fig. 6.1), which is consistent with the ≈ 800 day upper limit of Steinle et al. (2000), and also assume that we have observed every possible outburst (3) since 1990. Then it would seem that a reasonable upper limit for $d_{ULX1} \approx 1500/8000 \sim 0.19$, as the outbursts will probably be shorter than 500 days, which compensates for the possibility of there having been unobserved outbursts.

ULX2 was first detected at the start of the VLP (MJD 54181) and the outburst lasts at least until the end of obsID 12156 (MJD 55552), assuming a single outburst. This places a secure upper limit on the time spent in outburst of at least 1553 days (Fig. 6.1). Under the two-outburst scenario, the shortest possible outburst durations are 69 days (MJD 54228 from MJD 54181) plus 899 days (MJD 55734 from MJD 54835) in the second outburst, giving 968 days in outburst over the 20 years of observations. For ULX2, the longest reasonable $\tau_{out} \approx 1600$ days, yielding $d_{ULX2} \sim 0.2$, similar to ULX1, while a lower limit based on ~ 970 days

observed in outburst gives $d_{ULX2} \approx 0.12$.

To emit persistently at UL luminosities, a low-mass donor would be exhausted on timescales of 10^6 years after the initial mass transfer is triggered, assuming radiative efficiency $\eta = 0.1$. However, the Cen A sources reach the ULX threshold only for a fraction of the time, their luminosity averaged over the outburst phases is only $\sim 10^{37}$ erg s^{-1}, corresponding to $\dot{M} \sim 10^{-9}\ M_\odot\ \mathrm{yr}^{-1}$. If they do have duty cycles as high as 20%, this implies that their donor stars can sustain them for a characteristic timescale of 1 Gyr after the onset of mass transfer. Based on this characteristic behaviour, we speculate that ULX behaviour is associated with an evolved donor star (subgiant and red giant phases).

6.3.4 Other Early-type Galaxies

We investigate an apparent paucity of ULX transient candidates in other early-type galaxies compared to Cen A. Only two other such sources are known, which are globular cluster ULXs in NGC 3379 and NGC 4649 (Brassington et al., 2012b; Roberts et al., 2012). Zhang et al. (2012) showed there are approximately $12-13$ ULXs in a sample of 20 large early-type galaxies that included NGC 4649 and NGC 3379 but excluded Cen A, suggesting that transient candidates typically make up only $\sim 15\%$ of the ULXs in early-type galaxies. To evaluate the rarity of the lack of discoveries we examine the large ellipticals NGC 4472 and NGC 4649, which have 171 and 168 XBs above a limiting luminosity of $L_x \sim 6 \times 10^{37}$ erg s^{-1} (completeness corrected, see Zhang et al., 2012). By contrast, in chapter 5 we showed that Cen A has ~ 35 sources above this luminosity, two of which are ULX transients[5]. Scaling the number of ULX per number of LMXBs leads to an expectation of ≈ 10 transient ULXs per galaxy. To date, only one confirmed ULX with transient-like behaviour has been observed in either (in NGC 4649, Roberts et al., 2012).

Is it strange that only one such source has been detected given that we expect each galaxy to possess ~ 10? To answer this we have to consider the respective observing campaigns for NGC 4472 and NGC 4649. We simulated 10^5 on-off lightcurves for a range of duty cycles, where we define an 'ultraluminous' duty cycle d_{UL}, which only considers the period of time spent with $L_x > 10^{39}$ erg s^{-1} (i.e. where 'on' corresponds to $L_x > 10^{39}$ erg s^{-1} and 'off' represents some less luminous epoch) and folded these through the respective *Chandra* observing campaigns. To register as a transient ULX, a source had to be observed in both regimes by the sequence of observations. In Fig. 6.4 we present the proportion p of simulated lightcurves that registered as transient ULXs against d_{UL}. To judge how unusual a detection of one source in a given galaxy is, we take an expectation value $E_{ulx}(=10)$ modified by p such that $E'_{ulx} = pE_{ulx}$ (e.g. in Fig. 6.4, for NGC 4649 where $E_{ulx} = 10$, $E' < 6$ for all d_{UL}). For an observed number of transient ULXs O_{ulx} given an expectation

[5]Burke et al. (2013) studied sources inside the half-light radius of Cen A, whereas Zhang et al. looked at sources within the D_{25} ellipses; however, Voss & Gilfanov (2006) showed that the background sources became the major contributor to the point source population of Cen A at the half-light radius, with only ≈ 10 LMXBs beyond this point. Zhang et al. (2012) corrected for background sources in their population study, so it is valid to compare these numbers.

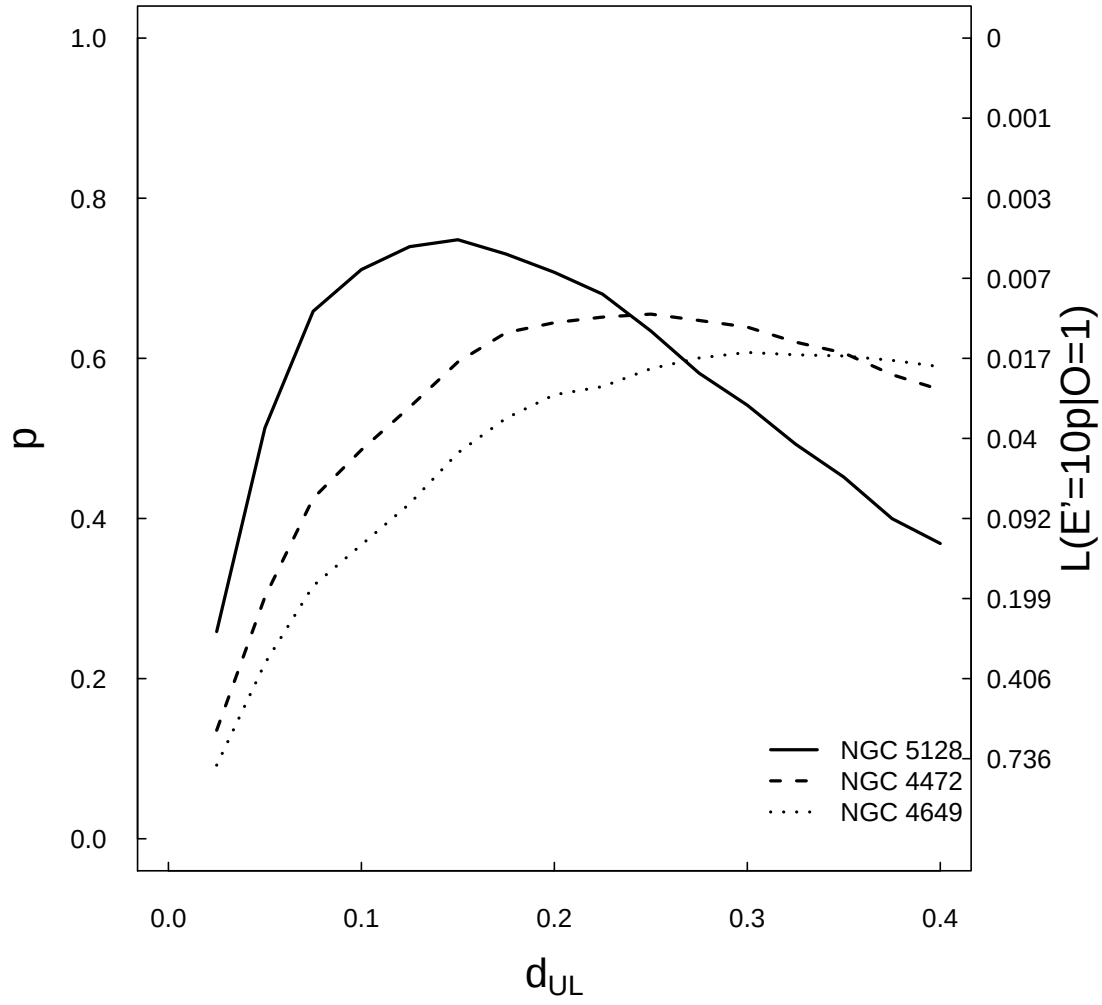

Figure 6.4 Proportion of simulated transient ULX detections for different UL duty cycles given the *Chandra* observing campaign for galaxies NGC 4472 and NGC 4649 and NGC 5128 (Cen A). Secondary y-axis shows probability of observing one or fewer such sources, when there are ten per galaxy, using expectation value $10p$ (see §6.3.4).

number E'_{ulx} we assessed the likelihood function $\mathcal{L}(E'_{ulx}|O_{ulx}) \equiv P(O_{ulx}|E'_{ulx})$ for $O_{ulx} = 1$. This is simply the poisson probability where $\lambda = E'_{ulx}$, which we plot as a secondary y-axis in Fig. 6.4, taking $E_{ulx} = 10$.

For NGC 4472, Fig. 6.4 shows that a detection of 1 or fewer sources is indeed unusual at 95% confidence for $d_{UL} \gtrsim 0.1$, and for NGC 4649, this is closer to 0.2. These values are consistent with the outburst duty cycle d discussed in §6.3.3, and by definition $d_{ul} \leq d$. Therefore, at least two possibilities exist to account for the scarcity of similar sources identified in NGC 4472 and NGC 4649. Firstly, the duty cycle of the UL regime may be small, $\lesssim 10\%$, which would be consistent with our results, and detections unlikely from the current set of observations. Secondly, it may be wrong to assume that the number of transient ULXs scales with the total number of LMXBs. There may be other properties of the stellar populations that are enhancing the creation of transient ULXs in Cen A compared with those other two galaxies. In particular, the evolutionary stage of the donor star may be a key factor. It has been tentatively suggested that ULX2 has a K giant companion (Sivakoff et al., 2008); more generally, we speculate that transient ULXs in an old population are mostly associated with low-mass donors in the subgiant or giant stage, because those evolved donors are more likely to provide the mass transfer rate required to achieve ULX luminosity. If so, the number of ULX transients in a galaxy may be proportional to the number of evolved stars, which is a function of both age and total stellar mass. The stellar mass of Cen A ($M_* \approx (1-2) \times 10^{11} M_\odot$) is almost three times lower than the stellar masses of NGC 4472 and NGC 4649 ($M_* \approx 3.2 \times 10^{11} M_\odot$), based on their K-band brightnesses (Ellis & O'Sullivan, 2006) and stellar mass-to-light ratios (Humphrey et al., 2006), and assuming a Kroupa IMF (Kroupa, 2001). However, $\approx 20 - 30\%$ of the stars in the Cen A halo are ≈ 4 Gyr old (Rejkuba et al., 2011) by virtue of its more recent merger, while the characteristic age of the stellar population in the other two galaxies is ~ 10 Gyr. Using Starburst99 (Leitherer et al., 1999; Vázquez & Leitherer, 2005; Leitherer et al., 2010), we estimate that NGC 4472 and NGC 4649 currently contain $\approx 1.2 \times 10^9$ subgiants and giants each, while Cen A contains $\approx (0.6 - 1.2) \times 10^9$ evolved stars. Therefore, in this scenario E_{ulx} is similar in all three galaxies and a non-discovery is consistent with the small-number statistics.

Regular, short observations of all three galaxies over an extended period of time would allow for a better determination of d_{UL} and distinction between the effects of observational bias and host galaxy in the detection of transient ULX sources.

6.4 Conclusion

We report on the latest detections of the two known ULXs in Cen A and present the count rate lightcurves in Fig.6.1. These sources are at substantially sub-Eddington luminosities. We place the duty cycles in the range $12 - 20\%$ and it seems likely that much of the time in outburst is spent at luminosities of a few 10^{37} erg s^{-1}. Both sources are currently at luminosities below 10^{37} erg s^{-1}, based on combined limits from the three most recent observations, and may have gone into a quiescent state.

The available evidence from studying the spectra of these sources at lower luminosity favours stellar mass BH primaries that occasionally emit at Eddington/super-Eddington isotropic luminosities, rather than IMBH accretors. This is consistent with other recent studies of transient ULXs at sub-Eddington luminosities.

We attempt to account for an apparent lack of transient ULXs in other, much larger early-type galaxies. While this could be accounted for by the majority of such sources spending only a small amount of their outbursts in the UL regime, our total knowledge of transient ULXs suggests that it is not uncommon for them to spend over a year at such luminosities. It seems likely that the number of transient ULXs scales not with the XB population, but with the size of the subgiant and giant populations, which are comparable between Cen A and the larger galaxies. This is consistent with the tentative suggestion that ULX2 has a K giant companion.

Chapter 7

Conclusion

7.1 Summary

This thesis details research into X-ray binaries in Centaurus A, the nearest large early-type galaxy. The narrative establishes that we are now able to identify BH LMXB candidates that are direct analogues to population accreting stellar mass BHs of the Milky Way. This is a foundation to the further work, which identifies more BH LMXB candidates. Interestingly, it appears that these sources more readily exist in the prominent dust lane of Cen A rather than the halo. The dust lane arose from a merging late type galaxy with the centre of Cen A, and is rife with star formation, possessing a far younger stellar population than that which dominates the Cen A halo. We propose that for the transient BH candidates to reach the peak luminosities observed, they need the more massive, younger stars found toward the dust lane, which makes use of an empirical result that brighter BH transients in the Milky way have larger periods. This may explain a well known feature of early-type galaxies, where the X-ray luminosity function is found to cut off at high luminosities; an effect that is known to steepen for older the stellar populations.

A tangential result is the tentative detection of the 'mass gap' in the distribution of compact object masses. This is the first time the existence of the mass gap has been hinted at beyond the Local group. The gap has wide-reaching implications across astrophysics and only by studying the X-ray transient population of other galaxies can we hope to demonstrate its existence – as a ubiquitous feature of the universe – with any certainty.

Cen A possesses two transient ULXs. Our analysis of a series of regular short observations taken since 2007 has shown evidence that favours a stellar, rather than intermediate, black hole powering the accretion in these systems. This is in good agreement with other studies of such sources in M31 and elsewhere. Further observations with longer exposures, or with X-ray telescopes that have a larger collecting area, would provide better statistics and allow for conventional spectral fitting. This would be possible with ULX2, which is more spatially isolated than ULX1, which would be source confused by the resolution of other telescopes.

There are several avenues of investigation and loose ends that should be followed up in the future, both with respect to Cen A, and in other areas of X-ray astronomy. In the next few sections I outline a few of these areas.

7.2 Cen A Variable Sources

In Chapter 5 the brighter sources in Cen A that exhibit intra-observational variability were omitted, to be presented in a future publication. A lot of preliminary work on these sources exists, and some of the more exciting results shall be discussed here. We have yet to develop a systematic approach for the spectral analysis of these sources. Do we fit different flux epochs within a single lightcurve separately or with the same shape and a different normalisation? Would our MCMC method of determining spectral similarity really be the best tool for making that same assessment here? Do we need to utilise more sophisticated analysis for investigating these sources over one observation? All questions that require serious thought and testing before the results are satisfactory for publication.

7.2.1 Unusual Quasi-soft Sources

Brassington et al. (2012a) report an unusual flaring quasi-soft source in NGC 3379. This source was well-described by a low-temperature disc blackbody model ($kT_{in} \sim 220$ eV) and varies in luminosity during a flare from a quiescent level of 2×10^{38} erg s^{-1} to 9×10^{38} erg s^{-1}. The possibility of this object being a foreground flare star can be ruled out by luminosity arguments, and remaining, feasible explanations of this behaviour are that the flares are NS superbursts (Cornelisse et al., 2000), however, the best-fit temperature is inconsistent with such sources, and perhaps indicates a white dwarf accretor with a helium-rich companion (Kato et al., 1989, 2000) or a double white dwarf binary. It is clear that we do not have a conclusive explanation for these rapid, repeated bursting behaviour with very cool temperature spectra.

I believe that there are two analogues to this source in Cen A, S21 and S49 , both of which exhibit intense intra-observational variability (Table 5.1). The spectra are equally soft, when the whole observation is examined, with negligible emission above 2 keV. An investigation of these sources would likely warrant a separate publication. One of the lightcurves from S49 is shown in figure 7.1, and the luminosity range spanned from non-flare to the peak luminosity is $\sim 10^{37}$ erg s^{-1} to $\sim 4 \times 10^{38}$ erg s^{-1}. Two such flares are present in the VLP observations from S49, and a similar event is observed in S21.

7.3 Model Selection

It is often the case that researchers do not know the correct model to fit to the spectra of a given source, particularly with newly discovered X-ray point sources, or where the data are of very low quality. Frequently models with very different physical interpretations are found to describe the available data equally well, e.g. have similar values of χ^2_ν. A given researcher's choice of the preferred model is more often dictated by physical or phenomenological constraints, rather than any statistical superiority of one model over another other. It should be remembered, and often repeated, that χ^2 style tests will only ever give some indication of how

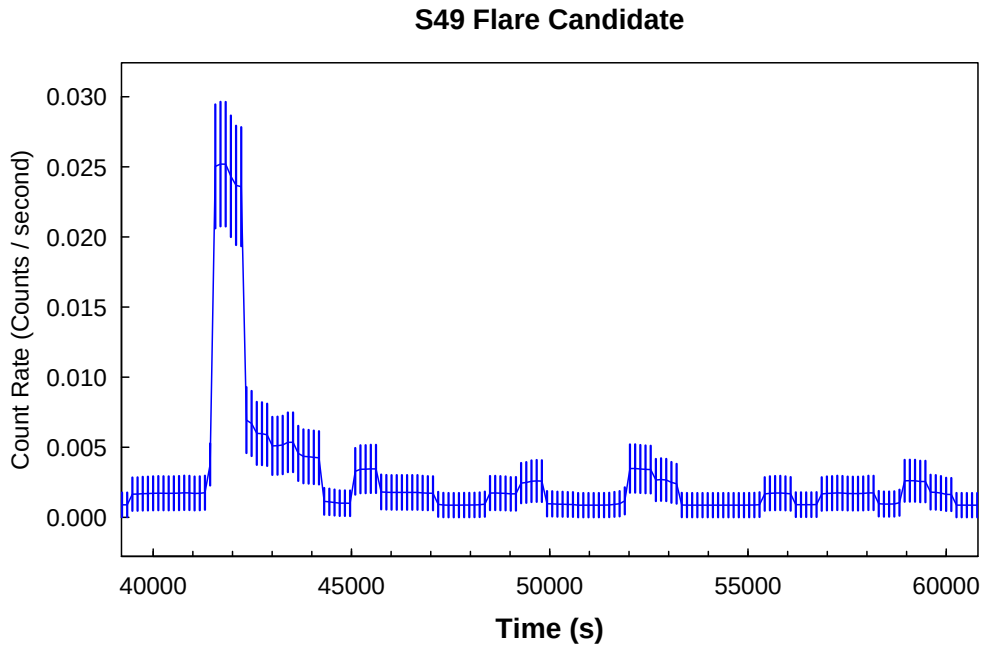

Figure 7.1 Quasi-soft source candidate S49 lightcurve, output from *glvary*.

well a model describes a dataset, and never the preference of one family of parameters over another. Rather, preference is something that is often inferred by a superior best-fit, but may not be true.

In this thesis there is an obvious example of where determining the preference of a model to a dataset would be desirable; between power law states that are very steep ($\Gamma \sim 2.5$) and disk blackbodies with reasonably cool innermost temperatures ($kT_{in} \sim 0.5$ keV) in the intermediate count regime ($10^2 - 10^4$ counts). While we were able to assess the spectral states of sources using the behaviour of the absorption parameter N_H in spectral fitting, this is subject to uncertainties, and a more robust, statistical measure to compare the two possible models (or, rather, the contribution of the two components to the overall spectrum) is desirable. As mentioned in Chapter 3, recent upgrades to *XSPEC* include implementations of K-S style statistics that test the consistency of the cumulative distribution function of the data to that of the model. However, these still only assess how well a given model will describe the data, not the preference of one model over another.

Hypothesis testing must therefore be able to test one model against another, rather than a comparisson of how well the data is described by the individual models. To compare two models with respect of data D, one must contrast the marginal likelihood $P(D)$ of both to give the so-called *evidence* ratio E,

$$E = \frac{P(D_1)}{P(D_2)}. \tag{7.1}$$

This comes from Bayes theorem, where the probability of model M given dataset D can be expressed as

$$P(M|D) = \frac{P(D|M)P(M)}{P(D)} \tag{7.2}$$

Where $P(D|M)$ is the likelihood and $P(M)$ represents the prior belief that the model is the correct one. The marginal likelihood $P(D)$, represents the integrated probability of the model over its own parameter space. The so-called Jeffreys scale judges whether a value of E shows signifcant favourability for one model over another, with $E > 3$ considered the minimum for one model to be 'substantially' favoured over another (Jeffreys, 1998).

It has been shown by Weinberg (2009) that P(D) can be estimated accurately from Markov Chains Monte Carlo (MCsMC) exploration of parameter space. Such chains sample directly from the posterior distribution of the parameter space in a manor that is proportional to the probability of a given parametric region (i.e. will draw more samples from regions of high probability). Weinberg (2009) show that the parameter space likelihoods can be integrated by use of KD trees to find the marginal likelihood for a given model and data. Further, he developed a method that ignored the lowest-likelihood regions of the parameter space to increase the accuracy of the calculation. By utilising this method, using Python code developed at Birmingham (Sidery et al., in prep.) we hope to use the MCMC capabilities of XSPEC to calculate marginal likelihoods and, from that, the evidence. This code has now been adjusted to accommodate XSPEC output, and is in a testing-and-development stage, which requires the use of computing clusters to perform MCMCs over many simulated spectra of a known model. The development of such a technique for X-ray spectral analysis would be a major boon, as it potentially will provide a direct measure of the preference of one model over another. This could have profound implications for the analysis of data of 'intermediate' quality, as well as high quality data that can be modelled by a multiple components.

Appendix A

Source List

Here I include, without further refinement, an early source list I made for Cen A from the VLP, ordered by the highest count rate per detection for a given source. From this list we chose which sources to study in Chapter 5. It should be noted that sources labelled as 'NUC' are within $30''$ of the Cen A nucleus, and in Chapter 5 we excluded sources within $20''$. We remind the reader that this list is a subset of the full point source list, as we excluded sources that are probably the X-ray jet, interstellar shock or the AGN itself.

Table A.1. Cen A Sources: Net Counts inside aperture (0.5-7.0 keV)

Index	RA	Dec.	7797	7798	7799	7800	8489	8490
S1	201.326037	-43.051364	$7228.4^{141.2}_{140.2}$	8430.6^{153}_{152}	$7431.6^{143.8}_{142.9}$	$6674^{136.3}_{135.5}$	$9697.4^{163.4}_{162.5}$	$8508.4^{153.1}_{152.2}$
S2	201.409548	-43.034897	$1692.8^{68.5}_{68.1}$	$1370.7^{61.7}_{61.3}$	$1430.9^{63}_{62.6}$	$1064.4^{54.6}_{54.3}$	$1864.8^{71.8}_{71.3}$	$1366.1^{61.5}_{61.2}$
S3	201.261258	-43.045352	$1125.3^{55.8}_{55.4}$	NA^{FOV}	NA^{FOV}	$918.6^{51.7}_{51.4}$	$1585.2^{66.5}_{66.2}$	$985.9^{52.3}_{51.9}$
S4	201.358992[NUC]	-43.025732	$1112.0^{57.7}_{57.3}$	$938.8^{54.1SN}_{53.8}$	$908.4^{53.2SN}_{53.0}$	$565.9^{44.2SN}_{44.0}$	$196.6^{28.2}_{28}$	$27^{18}_{16.3}$
S5	201.281825	-43.020913	$876.7^{49.2}_{49}$	$176.4^{23.1SN}_{23.0}$	$175.9^{23.1SN}_{23.0}$	$703.7^{45.1W}_{44.9}$	$1006.8^{53}_{52.7}$	$1042.1^{53.6}_{53.3}$
S6	201.276253	-43.039184	$745.9^{45.6}_{45.2}$	NA^{FOV}	NA^{FOV}	$617.8^{43.1}_{42.9}$	$1031.7^{53.8}_{53.5}$	$618.4^{41.5}_{41.3}$
S7	201.348688	-43.002649	$759.8^{46.2}_{45.9}$	$791.5^{48.7}_{48.4}$	$875.9^{51.1}_{50.7}$	$657.6^{44.1}_{43.8}$	$614.3^{41.7}_{41.4}$	$605.8^{41.5}_{41.4}$
S8	201.345341	-43.023579	$819.3^{48.3}_{48.1}$	$638.1^{43.18W}_{42.9}$	$508.0^{38.8W}_{38.6}$	$749.0^{46.5W}_{46.7}$	$621.4^{42.6}_{42.4}$	$650.9^{43.4}_{43.2}$
S9	201.367447[NUC]	-43.015688	$534^{48.6}_{48.4}$	$673.6^{51.1SN}_{50.8}$	$682.3^{51.1SN}_{50.8}$	$664.5^{52.1}_{51.8}$	$432.3^{45.6}_{45.4}$	$398.6^{47.2}_{47}$
S10	201.364375	-43.037242	$602.3^{41.6}_{41.4}$	NA^{SC}	NA^{SC}	NA^{SC}	$541.4^{39.3}_{39.1}$	$451^{36.1}_{36}$
S11	201.47737	-42.990391	$407.8^{34.9}_{34.6}$	$277.3^{27.7C}_{27.6}$	$316.7^{29.6C}_{29.4}$	$354.8^{31.4}_{31.2}$	$400.6^{33.6}_{33.4}$	$536.6^{40.1}_{39.8}$
S12	201.385188	-43.026168	$475.1^{37.5}_{37.3}$	$491.3^{39}_{38.8}$	$436.3^{37}_{36.9}$	$291.7^{31.3}_{31.2}$	$448.4^{36.2}_{36}$	$289.8^{29.8}_{29.7}$
S13	201.357318[NUC]	-43.015502	$451.7^{38.1}_{37.8}$	$443.7^{42.727SN}_{42.468}$	$419.4^{41.868SN}_{41.614}$	$199.2^{33.8}_{33.7}$	$172.8^{26.7}_{26.6}$	$417.9^{37.8}_{37.5}$
S14	201.364934	-43.006459	$412.7^{34.8}_{34.6}$	$413.1^{37.4}_{37.2}$	$427^{37.7}_{37.6}$	$294.7^{33.4}_{33.2}$	$20.9^{13.3}_{11.7}$	< 17.3
S15	201.360144[NUC]	-43.015054	$304.2^{34}_{33.8}$	$250.3^{32.5SN}_{32.3}$	$318.4^{35.2SN}_{35.0}$	$211.7^{31.8SN}_{31.6}$	$157.1^{27.5R}_{27.3}$	$417.1^{38.5}_{38.3}$
S16	201.38164	-43.000841	$304.8^{29.8}_{29.6}$	$327.9^{31.7}_{31.4}$	$336.9^{32.1}_{31.8}$	$401.3^{34.5}_{34.2}$	$355.8^{31.9}_{31.7}$	$413.7^{35.4}_{35.1}$
S17	201.303725	-43.02071	$409.5^{33.8}_{33.6}$	$313.2^{31.3SN}_{31.1}$	$289.8^{30.2SN}_{30.1}$	$313.8^{31.7}_{31.5}$	$349.4^{31.9}_{31.6}$	$83.2^{15.4C}_{15.4}$
S18	201.364583[NUC]	-43.024467	$366.1^{38.1}_{37.9}$	$311.6^{40.1SN}_{39.9}$	$365.0^{41.8SN}_{41.5}$	$289.2^{41.2SN}_{41.5}$	$350.1^{37}_{36.8}$	$372.4^{37.4}_{37.1}$
S19	201.362821	-43.033125	$336.2^{32.2}_{32.1}$	$277.6^{35.7}_{35.5}$	$320.6^{37.7}_{37.5}$	$198.8^{32.3}_{32.2}$	$364.9^{33.5}_{33.2}$	$283.2^{30}_{29.7}$
S20	201.369801	-42.996758	$288.9^{29.2}_{29}$	$303.7^{31.1}_{30.9}$	$342.1^{32.6}_{32.5}$	$329.8^{31.7}_{31.5}$	$333^{30.9}_{30.7}$	$255.2^{28.4}_{28.1}$
S21	201.343004	-42.954802	$286.4^{28.8}_{28.7}$	$174.8^{24.1}_{24}$	$330.6^{31.5}_{31.4}$	$245^{26.7}_{26.5}$	$288.5^{28.9}_{28.8}$	$315.3^{31.1}_{30.9}$
S22	201.41892	-43.020805	$266.3^{27.9}_{27.7}$	$260.6^{27.2}_{27}$	$314.2^{29.8}_{29.6}$	$216.6^{25.3}_{25.2}$	$113.8^{18}_{17.9}$	$309.8^{30}_{29.9}$
S23	201.397918	-42.993107	$187^{23.6}_{23.5}$	$269.2^{27.8}_{27.6}$	$282.1^{28.4}_{28.3}$	$307.4^{29.5}_{29.3}$	$294.4^{28.8}_{28.7}$	$254.9^{28}_{27.9}$
S24	201.299974	-43.002971	$287.9^{28.4}_{28.3}$	$269^{30.2}_{30}$	$254^{29.9}_{29.7}$	$261.4^{29.4}_{29.2}$	$261.7^{27.5}_{27.3}$	$128.8^{19.2}_{19.1}$
S25	201.289814	-43.091457	$287.8^{28.9}_{28.7}$	NA^{FOV}	NA^{FOV}	NA^{SC}	$64.1^{16.2}_{16.1}$	$53.5^{13.1}_{13.1}$
S26	201.444072	-42.950855	$264.2^{28.6}_{28.4}$	$247.5^{26.4}_{26.3}$	$285.4^{28.3}_{28.1}$	$273.7^{27.6}_{27.4}$	$93^{16.9C}_{16.8}$	$227.9^{26.5SN}_{26.4}$
S27	201.433207	-43.101889	$275.9^{28.5}_{28.3}$	$213.5^{25.6}_{25.5}$	$250^{27.5}_{27.4}$	$76.5^{18.7}_{18.6}$	$200.8^{24}_{23.9}$	$207.5^{24.5}_{24.4}$
S28	201.35081	-42.999845	$269.4^{28}_{27.9}$	NA^{SC}	NA^{SC}	$225^{26.2}_{26}$	$270.3^{27.9}_{27.8}$	$208.7^{25.3}_{25.2}$
S29	201.391383	-42.983262	$218.1^{25.4}_{25.3}$	$216.2^{25.1}_{24.9}$	$234.6^{26.1}_{26}$	$216^{24.7}_{24.6}$	$255^{26.9}_{26.8}$	$225.8^{26.2}_{26.1}$
S30	201.300126	-43.012426	$254.5^{26.7}_{26.6}$	NA^{SC}	NA^{SC}	NA^{R}	$229.2^{25.7}_{25.5}$	$79.7^{15.1}_{15}$

Table A.1 (cont'd)

Index	RA	Dec.	7797	7798	7799	7800	8489	8490
S31	201.348202	-43.039032	$248.6^{26.7}_{26.7}$	$184.2^{23.5SN}_{23.4}$	$176.9^{23.2SN}_{23.0}$	$170.1^{22.7SN}_{22.6}$	$217.8^{25.3}_{25.1}$	$242.1^{26.3}_{26.2}$
S32	201.288259	-42.983126	$248.5^{26.6}_{26.5}$	$217.4^{26.5}_{26.4}$	$174.5^{24}_{23.8}$	$210.5^{26}_{25.8}$	$208.8^{25}_{24.7}$	$125.8^{19.1C}_{19}$
S33	201.348002	-43.027328	$230.2^{26}_{25.9}$	NA^{SC}	NA^{SC}	NA^{SC}	$237.1^{26.4}_{26.2}$	$245.5^{26.7}_{26.6}$
S34	201.38892	-43.01465	$208.3^{25.8}_{25.6}$	$207.5^{27}_{26.9}$	$192.1^{26.3}_{26.1}$	$196.1^{26.4}_{26.4}$	$226.2^{25.9}_{25.8}$	$221.3^{27}_{26.8}$
S35	201.327098	-43.02114	$3.9^{5.3C}_{3.8}$	NA^{SC}	NA^{SC}	NA^{SC}	$9.2^{9.4}_{8}$	$219.3^{25.4}_{25.2}$
S36	201.383378	-43.04203	$218.6^{25.3}_{25.1}$	$206.9^{26.1}_{25.8}$	$213^{26.2}_{26.1}$	$187.5^{25.6}_{25.5}$	$85.4^{15.9}_{15.7}$	$153.6^{21.3}_{21.1}$
S37	201.372708^{NUC}	-43.018917	$161.8^{30}_{29.8}$	$73.9^{36.3}_{36.3}$	$143.7^{38.6}_{38.3}$	< 17.9	$214.9^{30}_{29.8}$	$156.5^{30.1}_{29.9}$
S38	201.345225	-43.004842	< 10.6	< 23.6	< 19.3	< 14.4	$< 10.3^{R}$	$196.9^{24.4}_{24.2}$
S39	201.368428	-43.054212	$161.8^{21.6}_{21.5}$	$191.8^{25.2}_{25}$	$165.3^{23.8}_{23.6}$	$174.4^{24.9}_{24.7}$	$56.9^{12.9}_{12.9}$	$111.8^{17.8}_{17.7}$
S40	201.36229^{NUC}	-43.017998	$168.1^{32.6}_{32.4}$	NA^{SC}	NA^{SC}	NA^{SC}	$< 38.6^{R}$	$190.9^{31.9}_{31.7}$
S41	201.362238^{NUC}	-43.014577	$134.7^{27.8}_{27.7}$	$145.59^{28.6SN}_{28.4}$	$121.4^{27.2SN}_{27.0}$	$158.0^{30.1SN}_{30.0}$	$131.3^{27}_{26.9}$	$190.9^{30.9}_{30.8}$
S42	201.318346	-43.048629	$190.7^{23.4}_{23.2}$	$133.8^{23.9}_{23.7}$	$137^{24.3}_{24.1}$	$138.7^{24.3}_{24.1}$	$164.5^{22.4}_{22.3}$	$102.7^{17.2}_{17.1}$
S43	201.367501	-43.048168	$156.8^{21.4}_{21.4}$	$110.3^{20.4}_{20.2}$	$113.6^{20.5}_{20.4}$	$100.9^{19.6}_{19.5}$	$181.1^{22.9}_{22.7}$	$168.9^{22}_{21.9}$
S44	201.333575	-43.052806	$166.9^{21.8}_{21.7}$	$92.4^{21.1}_{21.1}$	$135^{23.5}_{23.3}$	$126.9^{23.3}_{23.1}$	$147.6^{21}_{20.8}$	$136.8^{19.8}_{19.7}$
S45	201.412738	-42.948246	$76.4^{17.7}_{17.6}$	$104.5^{17.7}_{17.5}$	$51.5^{13}_{12.9}$	$160^{21.2}_{21.1}$	$88.4^{16.8}_{16.8}$	$123.3^{22.5}_{22.4}$
S46	201.354779	-43.024139	$154.3^{24.5}_{24.3}$	NA^{SC}	NA^{SC}	NA^{SC}	$124.8^{23.1}_{23}$	$89.1^{20.7}_{20.5}$
S47	201.346115	-43.029344	$142.8^{21.7}_{21.6}$	NA^{SC}	NA^{SC}	NA^{SC}	$128.4^{21.2}_{21}$	$149.9^{22.2}_{22.1}$
S48	201.385077	-42.980621	$86^{16.7}_{16.7}$	$142.4^{20.8}_{20.7}$	$105.4^{18.1}_{18}$	$132.5^{19.6}_{19.5}$	$88.4^{16.3}_{16.2}$	$119.6^{20.2}_{20.1}$
S49	201.469668	-43.096231	$70^{16.3}_{16.1}$	$56.1^{14.3}_{14.3}$	$105.8^{18.4}_{18.3}$	$108.1^{20}_{19.9}$	$71.4^{15.3}_{15.2}$	$138.7^{21.2}_{21.1}$
S50	201.292042	-42.935652	NA^{FOV}	NA^{FOV}	NA^{FOV}	$137.8^{22.1}_{22}$	$126.2^{21.4}_{21.2}$	$78.6^{18.4}_{18.3}$
S51	201.439457	-42.971058	$118.6^{19.9}_{19.7}$	$115.1^{18.1}_{18.1}$	$119.1^{18.4}_{18.3}$	$124.3^{18.8}_{18.6}$	$134.6^{20.1}_{19.9}$	$99^{20.3}_{20.2}$
S52	201.356245^{NUC}	-43.024977	$133.8^{24}_{23.8}$	NA^{SC}	NA^{SC}	NA^{SC}	< 14.8	< 23.3
S53	201.347925	-42.947695	$110.6^{18.4}_{18.3}$	$117.6^{20.2}_{20}$	$133.7^{21.3}_{21.1}$	$115.3^{18.8}_{18.7}$	$95.2^{17.8}_{17.7}$	$127.2^{21.7}_{21.5}$
S54	201.348454	-43.057146	$57.7^{13.2}_{13}$	$54.4^{17.4}_{17.2}$	$68.4^{18.3}_{18.2}$	$81.8^{19.7}_{19.5}$	$118^{18.6}_{18.5}$	$25.4^{9.5}_{7.9}$
S55	201.41611	-43.083826	112.4^{18}_{18}	$114.9^{19}_{18.9}$	$101.4^{18.2}_{18}$	$98.8^{19.4}_{19.2}$	$93.9^{16.5}_{16.3}$	86.9^{16}_{16}
S56	201.408744	-43.087126	$62.5^{13.8}_{13.7}$	$73.3^{16.1}_{16}$	$82.2^{16.6}_{16.6}$	$70.3^{17.6}_{17.5}$	$81.4^{15.5}_{15.4}$	$113.7^{18.2}_{18}$
S57	201.479619	-43.021758	$100.3^{18.5}_{18.4}$	$96.2^{16.6}_{16.5}$	$78.8^{15}_{14.9}$	$85.9^{15.9SC}_{15.9}$	$91.9^{16.5SC}_{16.3}$	$113.1^{20.2SC}_{20.1}$
S58	201.353175	-43.023504	$27.9^{16.1R}_{14.5}$	NA^{R}	NA^{R}	NA^{SC}	$73.6^{19.3}_{19.2}$	$110.9^{21.6}_{21.5}$
S59	201.282105	-42.9416	NA^{FOV}	NA^{FOV}	NA^{FOV}	$68^{17.6}_{17.4}$	$105.6^{20.4}_{20.4}$	$109.8^{19.9}_{19.7}$
S60	201.346123	-43.026191	$109.2^{19.7R}_{19.5}$	NA^{SC}	NA^{SC}	NA^{SC}	$101.5^{19.6}_{19.6}$	$79.1^{17.8}_{17.8}$

Table A.1 (cont'd)

Index	RA	Dec.	7797	7798	7799	7800	8489	8490
S61	201.298138	-43.04065	$102.5^{17.1}_{17}$	NA^{SC}	NA^{SC}	NA^{SC}	$77.4^{15.3}_{15.2}$	$109.1^{17.7}_{17.6}$
S62	201.386949	-43.074719	$34.6^{11.5}_{9.7}$	$70.1^{15.8}_{15.8}$	$88.4^{17.3}_{17.2}$	$45.1^{15.3}_{13.6}$	$88.7^{16.1}_{16}$	$108.5^{17.7}_{17.6}$
S63	201.387788	-43.018892	$77.5^{17.4}_{17.4}$	$57.1^{18.1}_{17.9}$	$72^{19.2}_{19.1}$	$53.3^{18.4}_{18.3}$	$107.6^{18.9}_{18.8}$	$82.6^{18.3}_{18.1}$
S64	201.271006	-43.025951	$107.1^{17.5}_{17.4}$	< 2.3	< 2.3	$87^{20.7}_{20.5}$	$23.3^{10.5}_{8.9}$	$75.4^{15}_{14.8}$
S65	201.284299	-43.0863	$79.9^{17.3}_{17.2}$	NA^{FOV}	NA^{FOV}	NA^{SC}	$97.3^{18.7}_{18.6}$	$105.4^{18.8}_{18.7}$
S66	201.455114	-43.080038	$72.8^{15.6}_{15.4}$	$60.2^{14}_{13.8}$	$67.9^{14.8}_{14.7}$	$65^{15.9}_{15.8}$	$79^{15.4}_{15.4}$	$101.3^{17.9}_{17.8}$
S67	201.419989	-43.046296	$72.3^{14.8}_{14.7}$	$99.1^{17}_{16.9}$	$90^{16.3}_{16.2}$	NA	$100.7^{16.9}_{16.8}$	$82.3^{15.4}_{15.3}$
S68	201.351774	-43.028102	$96.7^{20.2}_{20}$	NA^{SC}	NA^{SC}	NA^{SC}	$72.2^{18.3}_{18.1}$	$90^{18.9}_{18.8}$
S69	201.446409	-43.045364	$77.7^{15.4}_{15.4}$	$88^{16.1}_{15.9}$	$95.5^{16.7}_{16.5}$	$48.5^{13}_{11.4}$	$52.2^{12.3}_{12.2}$	$48.3^{13.7}_{12.1}$
S70	201.3398	-43.037079	$17.3^{8.8}_{7.1}$	$47^{20.1}_{18.5}$	$58.4^{20.1}_{20}$	$95.4^{21.9}_{21.7}$	$67^{14.9}_{14.8}$	$54.6^{13.3}_{13.2}$
S71	201.321421	-43.015123	$48.1^{12.9}_{11.3}$	$91.4^{21.5}_{21.3}$	$86.7^{21.4}_{21.3}$	$95.3^{22.8}_{22.6}$	$17.9^{11.2}_{9.6}$	< 10.4
S72	201.314152	-43.033539	$94.2^{16.6}_{16.6}$	NA^{R}	NA^{R}	NA^{SC}	NA^{SC}	$51.5^{12.4}_{12.4}$
S73	201.353702	-43.073731	$48.1^{13}_{11.3}$	NA^{SC}	NA^{SC}	NA^{SC}	$72.6^{14.7}_{14.7}$	$92^{16.2}_{16.1}$
S74	201.315778	-42.96097	$89^{16.4}_{16.4}$	$72.8^{18.2}_{18.1}$	$87.8^{19.3}_{19.3}$	$61.4^{15.3}_{15.1}$	$46.8^{14.2}_{12.5}$	$81.4^{16.9}_{16.8}$
S75	201.410579	-42.955612	$37^{14}_{12.4}$	$59.1^{13.7}_{13.6}$	$86.4^{16.2}_{16}$	$51.9^{12.6}_{12.4}$	$34.4^{12.2}_{10.4}$	$16.7^{14.1}_{12.6}$
S76	201.33415	-42.937525	NA^{FOV}	NA^{FOV}	NA^{FOV}	$50.5^{13.9}_{13.8}$	$86.3^{17.8}_{17.7}$	$67.7^{17.9}_{17.9}$
S77	201.359182[NUC]	-43.017304	< 24.4	NA	NA	NA	$86^{26.1}_{26}$	$74.4^{26.4}_{26.3}$
S78	201.360721[NUC]	-43.021679	< 19	< 31	< 23.9	$82.8^{53.9}_{53.6}$	< 13.3	< 23.6
S79	201.351399	-43.019571	$81.4^{18}_{17.8}$	NA^{SC}	NA^{SC}	NA^{SC}	$76.4^{18}_{17.8}$	$75.5^{17.6}_{17.4}$
S80	201.340562	-43.031675	$59^{14.3}_{14.2}$	NA^{SC}	NA^{SC}	NA^{SC}	$81.2^{16.7}_{16.5}$	$69.5^{15.7}_{15.5}$
S81	201.349736	-43.016378	$31.9^{14.1}_{12.5}$	$73.6^{23.4}_{23.3}$	$76.9^{23.8}_{23.7}$	$41.3^{23.9}_{22.1}$	$69.8^{18.6}_{18.5}$	$79.7^{18.8}_{18.7}$
S82	201.366623	-43.067246	$33.6^{11}_{9.4}$	$36.8^{15.2}_{13.5}$	$62.8^{16.4}_{16.3}$	$59.3^{16.5}_{16.4}$	$48.5^{13}_{11.2}$	$79.5^{15.2}_{15.2}$
S83	201.402537	-43.015961	$41.2^{15.2}_{13.4}$	$77.7^{17.1}_{17}$	$39^{14.7}_{12.9}$	$55.6^{15.8}_{15.7}$	77.2^{16}_{16}	$50.9^{15.5}_{15.5}$
S84	201.328941	-43.026879	< 8.6	NA	NA	NA	$21.8^{11.3}_{9.6}$	$77^{16.1}_{16}$
S85	201.351949	-43.014405	< 14	$75.6^{23.1}_{23}$	$63.1^{22.8}_{22.8}$	$57.5^{24.4}_{24.3}$	< 23.6	$47.8^{18.1}_{16.5}$
S86	201.331753	-42.988439	$47.9^{13.3}_{11.6}$	$51.6^{15.9}_{15.9}$	$61.9^{17.2}_{17.2}$	$75.4^{17.1}_{16.9}$	$65.5^{14.7}_{14.6}$	$42.5^{13.5}_{11.9}$
S87	201.390172	-43.053636	$50.4^{12.5}_{12.4}$	$65.5^{15.6}_{15.5}$	$69.4^{15.4}_{15.3}$	$65.7^{16.1}_{16}$	$62.6^{13.7}_{13.6}$	$74.7^{14.9}_{14.9}$
S88	201.446662	-42.973735	$63.5^{15.8}_{15.6}$	$57.7^{12.9}_{12.9}$	$73^{14.4}_{14.4}$	$71.7^{14.5}_{14.4}$	$72.9^{15.1}_{15}$	$65.3^{18}_{17.9}$
S89	201.285783	-43.012732	< 5.7	NA	NA	$72.9^{17.9}_{17.7}$	< 7.1	< 3.7
S90	201.355271	-43.039711	$69.7^{15.2}_{15.1}$	$40.9^{20.7}_{19.1}$	61.6^{21}_{21}	$63.5^{20.6}_{20.5}$	$69.6^{15.3}_{15.2}$	$61.6^{14.3}_{14.2}$

Table A.1 (cont'd)

Index	RA	Dec.	7797	7798	7799	7800	8489	8490
S91	201.338621	-43.032934	$31.9^{11.8}_{10.1}$	NA	NA	NA	$68.4^{15.8}_{15.8}$	$61.1^{14.5}_{14.4}$
S92	201.360837^{NUC}	-43.024673	$39.3^{22.4}_{20.7}$	NA	NA	NA	$66^{22.9}_{23}$	$44.3^{22}_{20.5}$
S93	201.356757^{NUC}	-43.02332	$57.7^{20.6}_{20.7}$	NA	NA	NA	$46.5^{21.9}_{20.3}$	$61.9^{21.2}_{21.3}$
S94	201.396689	-43.042627	$30.5^{11.6}_{9.8}$	$61.4^{15}_{14.8}$	$37^{13.4}_{11.7}$	$48.7^{15.2}_{13.4}$	$43.3^{12.7}_{11}$	$26.5^{11}_{9.3}$
S95	201.36522	-43.038337	60.9^{15}_{15}	NA	NA	NA	$58.2^{14.5}_{14.5}$	$60.2^{14.7}_{14.7}$
S96	201.340804	-43.080829	$49.1^{13.4}_{11.7}$	$54.3^{17.9}_{17.8}$	$60.1^{18.6}_{18.5}$	$47.3^{19.8}_{18.2}$	$34.3^{11.5}_{9.7}$	$44.5^{12.9}_{11.1}$
S97	201.384284	-43.024109	< 8.5	< 16.3	< 23.3	$59.7^{19.3}_{19.3}$	$13.4^{12.3}_{10.8}$	< 6.2
S98	201.376157	-42.992997	$26.7^{12.2}_{10.6}$	$37^{14.3}_{12.5}$	$31.4^{13.9}_{12.2}$	$42.6^{14.2}_{12.4}$	$57.2^{13.9}_{13.7}$	$47.9^{15.5}_{13.9}$
S99	201.385224	-43.021784	$33.2^{15.8}_{14.1}$	$38.8^{18}_{16.3}$	$39.1^{18.1}_{16.3}$	$57^{18.9}_{18.9}$	$27^{14.2}_{12.5}$	$23.7^{14.8}_{13.2}$
S100	201.362006	-43.001226	$10^{10.2}_{8.9}$	$37^{17.9}_{16.2}$	$56.7^{18.5}_{18.4}$	$37.1^{17.3}_{15.5}$	$21^{12.3}_{10.7}$	$12.1^{11.9}_{10.5}$
S101	201.347222	-43.012072	$25.6^{13.4}_{11.8}$	NA	NA	$56^{19.9}_{19.7}$	$34.9^{15}_{13.3}$	$27.1^{14.2}_{12.7}$
S102	201.361681^{NUC}	-43.017083	< 19.1	NA	NA	NA	< 5	$55.8^{25.4}_{25.2}$
S103	201.386392	-42.940063	$41.8^{14.8}_{13.2}$	$54.9^{13.8}_{13.8}$	$51.6^{13.4}_{13.4}$	$46.4^{12.7}_{11.1}$	$29.9^{12.3}_{10.7}$	$40.2^{16}_{14.3}$
S104	201.405982	-43.025381	$47.5^{13.8}_{12}$	$47.7^{13.9}_{12.4}$	$38.6^{12.8}_{11.2}$	$27.8^{13.3}_{11.6}$	$12.4^{7.7}_{5.9}$	$53.6^{13.6}_{13.5}$
S105	201.299887	-42.953707	< 0	$15.1^{11.1}_{9.3}$	$20.6^{12}_{10.4}$	$38.2^{14.9}_{13.3}$	$51.9^{14.8}_{14.6}$	$47.7^{15.4}_{13.7}$
S106	201.349092	-43.027011	$40.4^{13.5}_{11.8}$	NA	NA	NA	$51.6^{14}_{13.8}$	$32.1^{12.6}_{10.8}$
S107	201.348901	-43.02832	$51.3^{15.6}_{15.5}$	NA	NA	NA	$49.5^{16}_{14.3}$	$42.5^{15.5}_{13.9}$
S108	201.277908	-43.080667	$20.1^{12.1}_{10.4}$	NA	NA	NA	$51.1^{18.1}_{18.1}$	< 11.1
S109	201.446993	-42.946512	$41.2^{14.9}_{13.3}$	$15.2^{8.2}_{6.5}$	$27.2^{10.4}_{8.7}$	$49.8^{13}_{11.3}$	< 2.3	NA
S110	201.310485	-42.93664	< 0	< 2.3	< 2.3	$49.5^{15.5}_{13.9}$	< 15.9	< 8.6
S111	201.444568	-42.964648	< 18.2	$18.2^{8.9}_{7.3}$	$28.8^{10.3}_{8.7}$	$19.8^{8.9}_{7.3}$	$19.1^{10.8}_{9.1}$	$49.2^{17.7}_{16.1}$
S112	201.391205	-42.972582	$44.4^{13.9}_{12.4}$	$28.9^{11.3}_{9.8}$	$35.6^{12.7}_{11}$	$26.3^{10}_{8.4}$	$49.1^{13.6}_{12}$	$34.1^{14.5}_{12.9}$
S113	201.308395	-43.022543	$48.5^{13.6}_{12}$	NA	NA	$47.1^{17.5}_{15.9}$	$47.6^{14.6}_{12.9}$	$14^{8.4}_{6.8}$
S114	201.353229	-43.000645	$36.5^{12.9}_{11.3}$	NA	NA	$41.5^{14.7}_{13}$	$48.1^{14.2}_{12.5}$	$42.4^{14.5}_{12.8}$
S115	201.396083	-43.081511	$47.5^{12.9}_{11.3}$	NA	NA	NA	$10.8^{7.5}_{5.7}$	< 3.6
S116	201.289966	-43.031467	$4.8^{6}_{4.6}$	< 12.2	$12.6^{13}_{11.8}$	$47.2^{18.5}_{17}$	$27.4^{11.4}_{9.8}$	$7.7^{7}_{5.3}$
S117	201.319486	-43.019016	$8.9^{8.2}_{6.5}$	$38.6^{17.6}_{15.8}$	$30.7^{17.4}_{15.7}$	$46.5^{19.3}_{17.6}$	$11^{10.5}_{9}$	< 12.3
S118	201.356356	-43.036017	$46.1^{14.8}_{13.2}$	$35.5^{19.6}_{18}$	$45.8^{20}_{18.2}$	$30^{18.3}_{16.7}$	$7.3^{8.6}_{7.2}$	$19.7^{11.1}_{9.4}$
S119	201.362968	-43.029739	$15.8^{14.3}_{12.7}$	$44.4^{27.6}_{25.9}$	$44.8^{27.5}_{26.1}$	$30.5^{26}_{24.5}$	$18.9^{14.7}_{12.9}$	< 12.3
S120	201.389051	-42.986986	$43.1^{13.6}_{11.9}$	$31.9^{12.2}_{10.6}$	$32.6^{12.6}_{10.9}$	$21.4^{9.8}_{8.1}$	$24.6^{10.2}_{8.6}$	$23.4^{12.3}_{10.6}$

Table A.1 (cont'd)

Index	RA	Dec.	7797	7798	7799	7800	8489	8490
S121	201.31785	-43.069384	< 9.8	$42.3^{15.8}_{14}$	$42.8^{15.9}_{14.2}$	< 19.9	$8.9^{8.8}_{7.3}$	< 6.8
S122	201.355314^{NUC}	-43.020687	$37.7^{17.7}_{16}$	< 18.1	< 14.7	< 10.9	$42.3^{20.3}_{18.7}$	$18.9^{16.8}_{15.4}$
S123	201.410058	-42.941791	$38.9^{15.1}_{13.5}$	$32.7^{11.6}_{10}$	$30.9^{11.9}_{10.3}$	$25.3^{10.1}_{8.4}$	$41.1^{13.7}_{12}$	$38.5^{17.1}_{15.4}$
S124	201.308625	-43.045213	$26.6^{10.4}_{8.7}$	$23.3^{16.8}_{15.2}$	$40.1^{19}_{17.4}$	< 20.7	$19.6^{10.6}_{9}$	$10.5^{7.4}_{5.7}$
S125	201.315376	-43.021222	$8^{8}_{6.5}$	$17.5^{14.7}_{13.2}$	$29.1^{16.3}_{14.6}$	$39.2^{17.9}_{16.4}$	$18.5^{11.9}_{10.3}$	$10.7^{9.1}_{7.5}$
S126	201.452119	-43.056347	$39^{12.5}_{10.8}$	$36.4^{11.4}_{9.8}$	$20.5^{9.1}_{7.4}$	$30.2^{11.9}_{10.3}$	$27.5^{10}_{8.3}$	$29.6^{11.8}_{10.1}$
S127	201.303521	-43.101916	$8^{7.4}_{5.8}$	< 2.3	< 2.3	$37.9^{17.1}_{15.5}$	< 4.3	$10^{7.3}_{5.5}$
S128	201.44015	-43.020995	$20.7^{11.3}_{9.5}$	$26.7^{10.4}_{8.7}$	$23.1^{9.8}_{8.1}$	$15.6^{8.8}_{7.1}$	$31.5^{10.8}_{9}$	$37.8^{13.8}_{12}$
S129	201.390392	-43.008038	NA	NA	NA	NA	$37.5^{12.8}_{11}$	NA
S130	201.311152	-43.070087	< 9.9	$27.1^{13.3}_{11.7}$	$37.3^{14.5}_{12.8}$	NA	$11.7^{10.2}_{8.5}$	$7.4^{7}_{5.3}$
S131	201.380501	-43.022212	$20.3^{15.4}_{13.7}$	NA	NA	NA	$21.9^{14.4}_{12.7}$	$36.9^{16.3}_{14.8}$
S132	201.336704	-43.002965	$6.6^{7.3}_{5.9}$	< 14.2	$20.1^{16.4}_{14.8}$	$36.8^{16.1}_{14.5}$	$8.5^{8.4}_{6.8}$	$15.6^{10.3}_{8.7}$
S133	201.384729	-43.078158	$33.7^{11.2}_{9.5}$	$12.8^{10.4}_{8.8}$	$19^{11.3}_{9.5}$	$36.3^{14.2}_{12.4}$	$34.8^{11.3}_{9.7}$	$33.2^{11.1}_{9.3}$
S134	201.389489	-43.007628	NA	NA	NA	NA	$36.1^{13.1}_{11.3}$	NA
S135	201.328669	-42.95214	$13.5^{8.8}_{7.2}$	$21.3^{13.5}_{11.8}$	$28.3^{13.8}_{12.3}$	$35.8^{13.3}_{11.6}$	$35.9^{13.1}_{11.3}$	$30^{13.9}_{12.3}$
S136	201.302956	-42.958751	< 2.3	$27.1^{13.9}_{12.3}$	$13^{12}_{10.5}$	$35.3^{13.9}_{12.1}$	$17.1^{11.8}_{10.1}$	$17.1^{11.4}_{9.8}$
S137	201.264381	-42.991576	$34.7^{11.4}_{9.6}$	NA	NA	NA	NA	NA
S138	201.44152	-42.947474	$34.6^{14.2}_{12.4}$	$8.4^{7.6}_{6}$	< 9.9	$9.3^{7}_{5.4}$	< 5.8	NA
S139	201.350303	-43.029354	$32.8^{14.8}_{13.2}$	NA	NA	NA	$34.6^{14.8}_{13.3}$	$34^{14.1}_{12.4}$
S140	201.288954	-42.98827	$12.1^{8.7}_{7}$	$9.5^{10.5}_{9.3}$	$34.4^{14.9}_{13.3}$	$19.1^{13.5}_{12}$	$22.9^{11.2}_{9.5}$	$10.7^{7.9}_{6.2}$
S141	201.327841	-43.028071	$20.1^{9.4}_{7.9}$	NA	NA	NA	$14.4^{10.2}_{8.5}$	$33.9^{12.7}_{11}$
S142	201.378457	-43.024259	$29.1^{15.6}_{13.8}$	$20.7^{19.3}_{18}$	$33.8^{21.2}_{19.7}$	$23.4^{20.8}_{19.5}$	$15.3^{12.9}_{11.2}$	< 8.1
S143	201.365013	-43.090308	$33.5^{11.1}_{9.4}$	$33.7^{13.9}_{12.2}$	$28.5^{13.2}_{11.7}$	$20.9^{14}_{12.2}$	$9.4^{7}_{5.3}$	$19.1^{8.8}_{7}$
S144	201.342429	-43.046017	$8.6^{7}_{5.3}$	< 13	< 22.4	$27.1^{17}_{15.2}$	$33.1^{11.8}_{10.1}$	$32.7^{11}_{9.4}$
S145	201.330237	-43.032895	$26.4^{10.1}_{8.3}$	NA	NA	NA	NA	$32.8^{11.3}_{9.4}$
S146	201.329374	-43.032566	$19.1^{9}_{7.2}$	NA	NA	NA	NA	$32.5^{11.2}_{9.5}$
S147	201.466931	-42.953213	$31.8^{15.2}_{13.6}$	$9.2^{7}_{5.3}$	< 8.9	$11.8^{7.4}_{5.8}$	< 0	$21^{16}_{14.4}$
S148	201.329322	-42.966323	$31.7^{11.8}_{10.1}$	$12.6^{11.9}_{10.5}$	$10.8^{11.1}_{9.7}$	$16.4^{9.9}_{8.2}$	$18.3^{10.2}_{8.7}$	$12.3^{10.2}_{8.6}$
S149	201.31192	-43.049592	$16.7^{9.1}_{7.5}$	$27.7^{16.5}_{14.9}$	$31.6^{17.4}_{15.7}$	$26.4^{17.6}_{16}$	$9.4^{8.8}_{7.2}$	< 7.1
S150	201.268139	-43.002187	$31.5^{11.1}_{9.4}$	NA	NA	$14.1^{11.7}_{10.1}$	$22.1^{12}_{10.4}$	$25.6^{10.5}_{8.9}$

Table A.1 (cont'd)

Index	RA	Dec.	7797	7798	7799	7800	8489	8490
S151	201.382372	-43.0218	$20.2^{14.9}_{13.3}$	NA	NA	NA	$14^{12.8}_{11.2}$	$31.5^{15.3}_{13.7}$
S152	201.36683^{NUC}	-43.023284	< 18.9	NA	NA	NA	$31.2^{23.7}_{22.1}$	< 5.7
S153	201.393213	-43.017599	$20.9^{12.5}_{11}$	$24.8^{14.5}_{12.9}$	$17.9^{13.8}_{12.1}$	$17.1^{13.8}_{12.2}$	$9.6^{9.2}_{7.6}$	$31.2^{14.7}_{13}$
S154	201.434816	-42.942637	$15.2^{13.7}_{12.3}$	$9.3^{8.4}_{6.7}$	$11.8^{8.5}_{6.8}$	< 7.8	< 3.6	$30.9^{17.9}_{16.2}$
S155	201.268472	-42.997372	$30.6^{11.1}_{9.4}$	NA	NA	< 16.7	$16.1^{10.7}_{9}$	$20^{9.8}_{8.1}$
S156	201.294286	-43.069679	$30.5^{11}_{9.4}$	NA	NA	NA	$23.5^{12.3}_{10.6}$	< 6.7
S157	201.277794	-43.045406	< 8.4	NA	NA	NA	$30.1^{12.7}_{11.1}$	$6.3^{6.9}_{5.4}$
S158	201.364624	-43.097166	$8.8^{6.8}_{5}$	$19.8^{13.1}_{11.5}$	$24.8^{13.9}_{12.3}$	$30^{15.8}_{14}$	$14.1^{8.1}_{6.3}$	$20.2^{8.9}_{7.2}$
S159	201.278389	-43.065545	$11.7^{9.4}_{7.7}$	NA	NA	NA	$29.7^{13.5}_{11.8}$	$9.7^{8.2}_{6.6}$
S160	201.340192	-43.0087	< 12.7	$16.2^{16.1}_{14.8}$	$29.6^{19.8}_{18.1}$	$21.9^{16.9}_{15.4}$	$9.4^{9.4}_{7.9}$	$10.3^{9.8}_{8.3}$
S161	201.370802	-42.991867	$23^{11.7}_{10.1}$	$14.9^{12.1}_{10.6}$	$18.3^{12.6}_{10.9}$	$19.2^{11.8}_{10.1}$	$23.9^{10.9}_{9.2}$	$29.3^{13.5}_{11.9}$
S162	201.321058	-43.002138	$28.1^{10.8}_{9.1}$	$29.3^{16.9}_{15.3}$	$17.5^{15.3}_{13.8}$	$19.4^{14.2}_{12.5}$	$9.3^{8.6}_{7.1}$	$14.9^{9.4}_{7.7}$
S163	201.462443	-43.021915	< 11.1	$12.5^{7.6}_{6}$	$18.3^{8.7}_{7.1}$	$29.1^{11}_{9.2}$	< 5	< 11.9
S164	201.272051	-42.952857	< 0	< 2.3	< 2.3	$10^{10.4}_{9.1}$	$14.7^{13.1}_{11.5}$	$28.2^{12.5}_{10.8}$
S165	201.373426^{NUC}	-43.022757	$14.2^{15.2}_{14.1}$	< 11.9	< 16.3	< 26.6	$27.8^{16}_{14.4}$	< 14.4
S166	201.366112^{NUC}	-43.012663	< 12.1	< 13.8	< 12.2	< 12.6	< 26.9	$27.6^{20.3}_{18.7}$
S167	201.36877^{NUC}	-43.025379	< 23.5	< 13.5	< 20.4	< 32.3	< 16.8	$27.5^{18.9}_{17.2}$
S168	201.418502	-43.04761	$13.9^{8.4}_{6.7}$	$15.4^{8.8}_{7.1}$	$26.7^{10.4}_{8.6}$	NA	$23.4^{9.6}_{8}$	$14.6^{8.2}_{6.5}$
S169	201.322919	-43.024166	$9^{8.2}_{6.6}$	< 29	$26.6^{20}_{18.5}$	$16.3^{16.8}_{15.7}$	$17.3^{11.3}_{9.5}$	$21.7^{10.8}_{9}$
S170	201.373031	-43.03397	$15.2^{12.8}_{11.2}$	$16.6^{15.8}_{14.4}$	$26.3^{18.5}_{17}$	$12.6^{13.5}_{12.2}$	$13.1^{11.7}_{10.1}$	< 17.4
S171	201.315066	-43.036298	< 5.1	NA	NA	NA	< 6.6	$26^{10}_{8.4}$
S172	201.324045	-43.063883	$25.1^{10}_{8.4}$	NA	NA	NA	$10.8^{7.9}_{6.2}$	$12.8^{7.1}_{5.5}$
S173	201.396641	-43.017057	$11.7^{11.4}_{10}$	$20.9^{14.1}_{12.4}$	$25^{14.6}_{12.8}$	$20.9^{14.3}_{12.6}$	< 10	$23.2^{14.7}_{13}$
S174	201.371748	-42.962961	< 12.8	< 14.2	< 12.5	$6.4^{7}_{5.4}$	$6.7^{7.3}_{5.8}$	$24.6^{13.4}_{11.8}$
S175	201.254331	-43.054165	< 5.4	< 0	< 0	$24.4^{15.3}_{13.6}$	< 16.5	< 3.2
S176	201.369941	-43.034234	$9.4^{10.6}_{9.3}$	< 15.7	< 15	< 14.1	$24.4^{13.7}_{12.1}$	< 10.7
S177	201.341429	-43.030427	$24.2^{11.7}_{9.9}$	NA	NA	NA	< 10.1	$10.1^{9.7}_{8.3}$
S178	201.411995	-43.09373	$7.6^{7.5}_{5.9}$	$12.4^{9.4}_{7.6}$	$24.1^{11}_{9.2}$	NA	$13.8^{8.2}_{6.6}$	$15.2^{9}_{7.3}$
S179	201.332474	-43.028103	$11.7^{7.6}_{6}$	NA	NA	NA	$7.7^{8.7}_{7.3}$	$24^{11.5}_{9.7}$
S180	201.332762	-43.032646	< 5.3	NA	NA	NA	$23.9^{11.9}_{10.2}$	$15.9^{10.5}_{8.9}$

Table A.1 (cont'd)

Index	RA	Dec.	7797	7798	7799	7800	8489	8490
S181	201.300165	-42.975095	$23.4_{8}^{9.8}$	NA	NA	NA	NA	NA
S182	201.397242	-43.091627	$17.9_{7.3}^{9}$	$13.4_{9.6}^{11.3}$	$10.2_{8.6}^{10.1}$	$22.6_{12.2}^{13.9}$	$18.5_{7.5}^{9.1}$	$17_{7.1}^{8.8}$
S183	201.411974	-43.039181	$21.3_{8.8}^{10.4}$	$21.9_{9}^{10.7}$	$18.2_{8.5}^{10.1}$	< 11.6	< 6	$5.4_{5.2}^{6.5}$
S184	201.473027	-43.026236	$10.8_{8.5}^{10}$	$7.2_{5}^{6.8}$	$7.2_{4.6}^{6.2}$	$16.4_{7.1}^{8.8}$	$8.5_{5.5}^{7.2}$	$21.7_{11.3}^{13}$
S185	201.357552	-42.992576	< 7.3	$21.7_{12.6}^{14.3}$	< 20.3	$10.8_{9.5}^{10.9}$	< 7.3	< 11.9
S186	201.371863	-43.089229	$13.7_{6.1}^{7.9}$	NA	NA	NA	$21.5_{8}^{9.6}$	$14.9_{6.3}^{8.1}$
S187	201.363733	-42.974599	$21.4_{9.3}^{10.9}$	< 14.9	< 10.7	$8.9_{5.8}^{7.5}$	$7.7_{6.3}^{7.7}$	< 14.1
S188	201.354771	-43.009683	$21.1_{11.2}^{12.9}$	$18.5_{18.1}^{19.3}$	< 17.2	< 11.4	$13.1_{9.8}^{11.4}$	$10.5_{10.1}^{11.3}$
S189	201.346196	-42.969597	< 5	< 16.9	< 10.7	< 7.7	$21_{8.6}^{10.3}$	< 15.8
S190	201.370292	-43.039289	$9.5_{8}^{9.5}$	$14_{13.5}^{14.8}$	$20.9_{16}^{17.5}$	$17.3_{14.8}^{16.2}$	$14.2_{8.8}^{10.5}$	< 10.6
S191	201.304682	-42.97781	$14.6_{7.6}^{9.2}$	< 6.2	$20.8_{10.8}^{12.6}$	$10.7_{8.9}^{10.3}$	$12.3_{8}^{9.5}$	< 8.6
S192	201.448304	-42.984093	NA	$12.6_{5.7}^{7.4}$	$9.5_{5.3}^{7}$	$8_{4.6}^{6.2}$	$20.6_{8}^{9.6}$	NA
S193	201.301249	-42.973383	$20.4_{7.7}^{9.5}$	NA	NA	NA	NA	NA
S194	201.341883	-42.991814	$11.9_{7}^{8.7}$	< 19.6	$12_{11.1}^{12.3}$	< 12.6	$13_{7.4}^{9}$	$20.2_{9.6}^{11.2}$
S195	201.382932	-43.050749	$20.1_{7.9}^{9.7}$	$12.8_{9.5}^{11.2}$	$15.1_{9.5}^{11}$	< 12.9	$14.1_{6.8}^{8.4}$	$11.6_{5.7}^{7.4}$
S196	201.342724	-43.031521	$12.6_{8.8}^{10.4}$	NA	NA	NA	$19.9_{10.5}^{12.3}$	< 8.9
S197	201.315609	-43.032862	$6.7_{5.1}^{6.7}$	NA	NA	NA	$10.1_{5.7}^{7.4}$	$19.7_{7.6}^{9.3}$
S198	201.350497	-43.03944	$10.3_{7.2}^{8.8}$	NA	NA	NA	$19.2_{8.8}^{10.5}$	< 9.4
S199	201.328577	-43.02387	$7_{4.8}^{6.5}$	NA	NA	NA	$18.9_{9.4}^{11.1}$	< 9.6
S200	201.34463	-43.010535	$12.6_{9.1}^{10.9}$	NA	NA	$18.8_{14.6}^{16.1}$	< 11	< 12.4
S201	201.32786	-43.034948	$18.7_{8.6}^{10.3}$	NA	NA	NA	$13.6_{8.5}^{10.2}$	$15.2_{8.4}^{10}$
S202	201.311168	-43.0646	< 9.6	NA	NA	NA	$18.6_{9.7}^{11.4}$	$5.1_{4.2}^{5.9}$
S203	201.391279	-43.007297	NA	NA	NA	NA	$18.5_{9}^{10.8}$	NA
S204	201.405389	-42.980022	$6.9_{6.7}^{8}$	$11.9_{6.5}^{8.3}$	$11.7_{6.4}^{8.1}$	< 8.7	< 7.7	$18.5_{11}^{12.6}$
S205	201.292523	-42.966975	< 5.8	$10.7_{9.8}^{11.2}$	< 16.9	< 4.2	$11.4_{8.9}^{10.5}$	$18.5_{9}^{10.6}$
S206	201.43737	-43.079836	$17_{7.8}^{9.5}$	$14.6_{7.9}^{9.5}$	$18.4_{8.2}^{9.8}$	< 10.3	$15.4_{6.7}^{8.4}$	$7_{5.7}^{7.2}$
S207	201.349106	-43.024167	$18.3_{10.4}^{12.1}$	NA	NA	NA	$12.3_{9.6}^{11.3}$	$9.6_{8.7}^{10.2}$
S208	201.395719	-42.960167	< 14.8	< 11.1	$13.6_{7.5}^{9.2}$	$14.6_{6.5}^{8.3}$	$11.3_{7.3}^{9}$	$18.1_{11.9}^{13.5}$
S209	201.363311	-43.004349	$12.2_{9.7}^{11.3}$	< 14.2	$18.1_{14.4}^{15.7}$	< 13	$12.8_{9.7}^{11.2}$	< 19.6
S210	201.287079	-43.006799	$4.9_{4.2}^{5.8}$	$17.8_{13.3}^{14.6}$	< 11.3	< 8.5	< 10	$7.5_{5.3}^{7}$

Table A.1 (cont'd)

Index	RA	Dec.	7797	7798	7799	7800	8489	8490
S211	201.459628	-42.981311	$17.3^{12.4}_{10.8}$	$8.5^{6.5}_{4.8}$	$3.5^{4.9}_{3.2}$	$4.2^{4.7}_{3}$	$8.9^{7.5}_{5.8}$	< 18.7
S212	201.352105	-43.018518	$17.2^{12.9}_{11.3}$	NA	NA	NA	< 10.8	< 14.9
S213	201.390938	-43.006371	NA	NA	NA	NA	$16.8^{11.2}_{9.5}$	NA
S214	201.392603	-42.952771	NA	$13.2^{9.7}_{8.1}$	< 10.7	$4^{5.3}_{3.8}$	$16.7^{9.7}_{8}$	NA
S215	201.37989	-42.967456	$7.3^{8.4}_{7}$	$16.6^{10.4}_{8.7}$	$12.6^{10.1}_{8.4}$	$6.3^{6.6}_{5.1}$	< 9	NA
S216	201.284636	-43.080066	$8.5^{8.3}_{6.6}$	NA	NA	NA	$15.7^{12.8}_{11.2}$	$16.5^{9.3}_{7.7}$
S217	201.425853	-42.943072	$11.6^{11.9}_{10.5}$	< 6.3	$7.7^{8.1}_{6.5}$	< 6.9	$16.5^{10.8}_{9.1}$	< 21
S218	201.425216	-43.072179	< 9.2	$10^{8}_{6.4}$	< 10.9	$9.8^{9.9}_{8.5}$	$16.3^{8.4}_{6.7}$	$7.8^{7.3}_{5.5}$
S219	201.294729	-43.065511	$16.2^{9.3}_{7.7}$	NA	NA	NA	$7.6^{8.4}_{7.2}$	< 6.5
S220	201.423861	-42.949876	< 5.5	< 6.4	$6.2^{7}_{5.5}$	$15.7^{8.6}_{6.9}$	$10^{9.5}_{8}$	NA
S221	201.365784	-42.984373	$10.3^{9.2}_{7.7}$	$9.9^{10}_{8.5}$	$9.8^{10}_{8.6}$	< 13.3	$15.5^{9.2}_{7.5}$	< 12.2
S222	201.413654	-43.01617	$15.4^{10.8}_{9.1}$	< 10.3	$6.3^{7.2}_{5.8}$	$8.4^{8.5}_{6.9}$	$7.6^{7.2}_{5.5}$	$13.3^{11}_{9.3}$
S223	201.477669	-42.955665	$14.2^{13.1}_{11.7}$	$15.3^{8}_{6.3}$	$15^{8}_{6.4}$	$11.4^{7}_{5.2}$	< 0	< 11.6
S224	201.384013	-42.961113	$9.5^{9.5}_{7.9}$	$15.2^{10.2}_{8.5}$	< 12.5	$6.2^{6.6}_{5}$	$7.9^{8.2}_{6.7}$	NA
S225	201.432982	-43.083091	< 10.4	$7.4^{8}_{6.5}$	< 6.9	< 6.3	$15.1^{8.6}_{7}$	$6.7^{7.2}_{5.6}$
S226	201.347838	-42.976397	< 5.9	$10^{10.5}_{9.1}$	$15.1^{12}_{10.5}$	$6.2^{7.3}_{6.1}$	$9.8^{8.4}_{6.8}$	< 12.5
S227	201.392088	-43.006651	NA	NA	NA	NA	$14.8^{9.6}_{8}$	NA
S228	201.310291	-42.982885	< 9.7	$10.6^{11.5}_{10.2}$	< 8.4	< 7.3	$14.7^{9.7}_{8.1}$	< 7.8
S229	201.367875	-43.071267	$12.2^{7.6}_{6}$	< 15.8	$13.4^{11.1}_{9.6}$	$14.7^{12.1}_{10.6}$	$12.6^{7.9}_{6.2}$	$12.4^{7.6}_{6}$
S230	201.443636	-43.019067	$14.4^{10.1}_{8.3}$	< 6.6	< 6.8	< 3.3	< 2.8	< 4.2
S231	201.470361	-43.036927	< 10.1	$4.5^{5.5}_{3.9}$	< 8.4	< 7.1	< 5.4	$14.2^{11.4}_{9.7}$
S232	201.411991	-43.075689	< 5.9	< 8.2	< 11.2	< 9	$8.5^{7}_{5.3}$	$14.1^{8.4}_{6.8}$
S233	201.332984	-43.034078	$13.7^{8.6}_{7}$	NA	NA	NA	$11.8^{10}_{8.5}$	$14.1^{10.5}_{8.9}$
S234	201.420739	-43.010632	$13.5^{10.5}_{8.8}$	$11.3^{8.1}_{6.4}$	$8.5^{7.6}_{5.9}$	$14^{9.2}_{7.6}$	$7.2^{6.7}_{5.1}$	$11.5^{10.7}_{9.3}$
S235	201.319266	-43.081968	< 7.9	NA	NA	NA	$13.9^{10.3}_{8.7}$	< 7.6
S236	201.280198	-43.076352	$13.8^{9.5}_{7.9}$	NA	NA	NA	< 18.4	$11.4^{8.9}_{7.4}$
S237	201.301843	-43.013883	$12.8^{8.1}_{6.3}$	NA	NA	NA	$13.8^{9.1}_{7.5}$	< 7.1
S238	201.371113	-43.100757	$6.5^{6.7}_{5}$	$13.7^{12.3}_{10.7}$	< 16.8	< 12.3	< 5.5	$6.7^{6.5}_{4.8}$
S239	201.45424	-42.961026	< 15.8	< 2.3	$13.7^{7.6}_{5.9}$	< 5.4	< 8.2	< 10.1
S240	201.278544	-43.062926	$13.7^{9.5}_{7.9}$	NA	NA	NA	$12.5^{11.1}_{9.6}$	$6.1^{7.4}_{6}$

Table A.1 (cont'd)

Index	RA	Dec.	7797	7798	7799	7800	8489	8490
S241	201.427998	-42.995275	< 9.1	$7.7^{6.7}_{5.1}$	< 6.9	$4.5^{5.7}_{4.1}$	$12.9^{7.8}_{6.2}$	$13.5^{11.7}_{10.1}$
S242	201.366481	-42.964764	$13.4^{9.9}_{8.2}$	< 11.3	< 9.1	< 11.1	$10.3^{8.7}_{6.9}$	< 15.4
S243	201.4277	-42.948214	NA	< 11	< 10.6	$4.3^{5.6}_{4.3}$	$13.3^{10.3}_{8.7}$	NA
S244	201.457612	-43.075048	< 12.1	< 10.6	$8.7^{7.8}_{6.2}$	< 7.7	$13.1^{8.1}_{6.3}$	$13.2^{9.9}_{8.2}$
S245	201.380162	-42.964873	NA	NA	NA	$5.8^{6.7}_{5.1}$	$13.1^{8.7}_{6.9}$	NA
S246	201.402122	-43.027479	< 12.8	$12.5^{10}_{8.4}$	$8.5^{9}_{7.4}$	$12.7^{10.8}_{9.2}$	< 4.1	$9.8^{9.1}_{7.6}$
S247	201.443839	-43.010057	< 6.4	$10.7^{7.4}_{5.8}$	$12.6^{7.9}_{6.2}$	$6.1^{6.2}_{4.5}$	$7.7^{6.7}_{5.1}$	< 9.6
S248	201.335974	-42.994965	$7.8^{7.6}_{5.9}$	$12.5^{12.7}_{11.4}$	$11.1^{12.2}_{10.9}$	< 12.5	$7.2^{7.7}_{6.1}$	< 9.6
S249	201.321986	-43.0972	$11.5^{7.9}_{6.2}$	NA	NA	NA	$12.4^{9.2}_{7.5}$	$6.1^{6}_{4.2}$
S250	201.325247	-43.06186	$12.3^{7.9}_{6.2}$	NA	NA	NA	< 5.6	< 5.2
S251	201.440434	-43.093298	< 12.5	< 8.2	$10^{9.5}_{7.8}$	NA	$12.2^{8.3}_{6.6}$	< 8.4
S252	201.277702	-43.015454	< 7.8	NA	NA	NA	$12.2^{9.4}_{7.8}$	< 7.4
S253	201.286498	-43.082774	$12^{9.3}_{7.5}$	NA	NA	NA	< 10.2	$9.6^{8.2}_{6.6}$
S254	201.362547	-43.008545	< 13.9	< 11	< 20.7	< 24.7	< 10.6	$12^{12.9}_{11.7}$
S255	201.390065	-43.031061	$12^{9.8}_{8.2}$	< 11.1	< 17.9	< 14.1	$7.3^{7.7}_{6.2}$	< 10.1
S256	201.325884	-43.031237	$10.7^{8.5}_{6.8}$	NA	NA	NA	$12^{10}_{8.5}$	$9.4^{8.8}_{7.2}$
S257	201.411595	-43.044677	$11.9^{8.3}_{6.5}$	< 4.8	< 7.6	< 9.7	< 6	< 3.1
S258	201.397939	-43.080105	$11.5^{7.6}_{6}$	NA	NA	NA	$5.8^{6.3}_{4.8}$	$11.8^{8.1}_{6.4}$
S259	201.424703	-43.046651	$7.3^{7.3}_{5.7}$	< 9.1	$11.8^{8.1}_{6.4}$	$9.4^{8.8}_{7.3}$	< 7.3	< 9
S260	201.282519	-43.016626	$6.9^{6.5}_{4.8}$	NA	NA	NA	$11.7^{9.1}_{7.4}$	< 7.2
S261	201.320078	-42.993542	$11.7^{7.6}_{6}$	NA	NA	NA	NA	NA
S262	201.437722	-43.090194	$10.7^{9}_{7.4}$	< 7.2	$10.9^{9.5}_{8}$	< 6.4	$8.1^{7.4}_{5.8}$	$11.6^{8.3}_{6.6}$
S263	201.347071	-43.066754	< 8.2	$11.5^{12.3}_{11}$	< 10.2	< 7	< 2.8	< 4.3
S264	201.379229	-42.970562	< 10.5	$11.5^{9.5}_{7.9}$	$6.9^{8.1}_{6.8}$	$10.2^{7.9}_{6.2}$	< 9.6	< 17
S265	201.329811	-43.099828	< 5.9	$7.7^{8.8}_{7.4}$	$9^{9.3}_{7.8}$	$11.5^{11.8}_{10.5}$	< 4.6	< 4.3
S266	201.389474	-42.951716	NA	< 7.1	$11.4^{8}_{6.3}$	< 4.2	< 7.9	NA
S267	201.336787	-43.031646	< 10.3	NA	NA	NA	$11.4^{10.2}_{8.7}$	$9.2^{9}_{7.7}$
S268	201.39898	-43.061188	< 6.9	< 12.7	$11^{9.3}_{7.7}$	$9.5^{10}_{8.5}$	$11.4^{7.6}_{6}$	$7.4^{6.8}_{5.1}$
S269	201.372702	-43.069672	< 5.5	< 5.5	$11.1^{10.8}_{9.1}$	< 15.8	$8.9^{6.8}_{5}$	$7.8^{6.5}_{4.8}$
S270	201.425403	-43.05542	$11.1^{8.1}_{6.4}$	$9.8^{8.1}_{6.4}$	$10.9^{8.1}_{6.4}$	< 8.1	$10.9^{7.3}_{5.5}$	$11^{7.9}_{6.2}$

Table A.1 (cont'd)

Index	RA	Dec.	7797	7798	7799	7800	8489	8490
S271	201.290092	-43.045255	< 5	NA	NA	NA	$11.1^{9.1}_{7.5}$	$7.5^{7.2}_{5.5}$
S272	201.390108	-43.028686	< 10.7	< 9.7	$11.1^{10.4}_{8.9}$	< 8.2	$8.2^{8.6}_{7.2}$	< 10.9
S273	201.399893	-43.086074	< 2.9	$11^{10}_{8.7}$	< 11.7	< 6.3	< 3.8	< 5.8
S274	201.375951	-43.055836	$9.7^{7.4}_{5.8}$	< 16.8	$10.9^{10.7}_{9.4}$	< 12	$8.5^{7}_{5.3}$	$7.7^{7.2}_{5.5}$
S275	201.363675	-43.04923	$10.8^{8.7}_{7}$	$10.1^{11}_{9.7}$	< 9.5	< 6.6	$8.8^{7.9}_{6.2}$	$6^{6.3}_{4.8}$
S276	201.463458	-43.071443	< 7.7	$10.6^{7.9}_{6.2}$	< 6.6	< 7.2	$5.8^{6.5}_{4.9}$	< 12
S277	201.381607	-42.963485	NA	NA	NA	$10.6^{8.1}_{6.4}$	$6.8^{7.2}_{5.6}$	NA
S278	201.383999	-42.96712	$8.1^{8.8}_{7.4}$	< 11.1	< 12.1	$9.4^{7.8}_{6.2}$	$10.5^{9}_{7.4}$	< 13.9
S279	201.297178	-42.976365	$4.3^{5.7}_{4.2}$	NA	NA	NA	$10.5^{8.8}_{7.1}$	$10.1^{8.1}_{6.4}$
S280	201.27244	-43.033477	< 3.3	< 2.3	< 2.3	< 22.9	< 11	< 5
S281	201.314816	-43.061691	< 7.3	NA	NA	NA	$10.4^{9.2}_{7.5}$	< 3.5
S282	201.416828	-42.978377	< 11	< 9.3	$10.4^{7.7}_{6}$	< 3	$8.5^{7.5}_{5.7}$	NA
S283	201.311765	-43.013711	< 9.2	NA	NA	NA	< 9.7	$10.4^{8.1}_{6.4}$
S284	201.342915	-42.98123	< 9.4	$10.4^{10.8}_{9.5}$	< 14.8	< 10.2	< 9.6	< 13.8
S285	201.311553	-42.977816	< 11.4	$10.3^{11.2}_{10}$	< 13.3	< 6.7	$6.9^{7.9}_{6.6}$	$6.2^{7.4}_{6}$
S286	201.317507	-42.947029	< 2.3	< 5.9	< 5	$9.9^{10}_{8.5}$	$8.9^{9.6}_{8.2}$	< 14.1
S287	201.358951	-42.943426	NA	NA	NA	$9.5^{7.9}_{6.2}$	NA	NA
S288	201.320083	-42.992238	$9.4^{7}_{5.3}$	NA	NA	NA	NA	NA
S289	201.406373	-43.028281	< 8	$6.8^{7.8}_{6.3}$	$9.3^{8.6}_{6.9}$	< 12.5	< 3.4	< 8.9
S290	201.427275	-42.99077	< 11	< 10.6	< 7.3	$9.3^{7.9}_{6.2}$	< 5	< 14.2
S291	201.301077	-42.988573	< 4.2	< 17.1	< 18.4	< 18.8	$9.3^{8.9}_{7.4}$	$5.8^{6.9}_{5.4}$
S292	201.321778	-42.980695	$9.3^{7.8}_{6.2}$	< 8.6	< 10.6	< 7.9	$6.2^{7.3}_{5.9}$	< 9.4
S293	201.326884	-43.08584	$9.2^{7.8}_{6.2}$	NA	NA	NA	< 11.8	< 3.6
S294	201.261321	-43.083464	$9.2^{8}_{6.4}$	NA	NA	NA	< 8.2	$8.2^{7.2}_{5.6}$
S295	201.323205	-42.974561	$6.7^{7.2}_{5.6}$	< 19.8	< 10.4	< 7.4	$7.5^{7.9}_{6.4}$	$7.3^{8}_{6.6}$
S296	201.394024	-43.065228	< 5.2	< 7.2	$7^{8.2}_{6.9}$	< 9.8	$9^{6.8}_{5}$	$3.8^{5.1}_{3.8}$
S297	201.352674	-43.036037	< 13.7	NA	NA	NA	< 8.9	$8.9^{8.4}_{6.9}$
S298	201.296186	-43.025626	$8.4^{6.8}_{5.1}$	< 7.6	< 20.5	< 9.1	$8.4^{8.5}_{6.9}$	$4.5^{5.8}_{4.3}$
S299	201.424702	-43.028199	< 6.5	$7.5^{7.1}_{5.5}$	< 9.2	$8.2^{8.6}_{7.2}$	< 6.9	$7.6^{8.1}_{6.7}$
S300	201.399699	-43.035979	< 6.9	< 9.2	$8.1^{8.6}_{7.1}$	< 8.7	< 7.8	< 11.7

Table A.1 (cont'd)

Index	RA	Dec.	7797	7798	7799	7800	8489	8490
S301	201.431988	-43.092623	< 6.6	$8^{8.7}_{7.2}$	< 10	< 8.7	< 8	< 6.8
S302	201.393975	-42.944387	< 6.7	< 10.5	< 6.5	< 6.9	< 7.5	< 19.4
S303	201.266922	-43.01117	< 3.6	NA	NA	NA	$8^{8.5}_{7.2}$	< 2.9
S304	201.35707	-43.0735	$7.9^{6.7}_{5.1}$	NA	NA	NA	< 4.2	< 3.5
S305	201.291191	-43.078833	$7.4^{7.5}_{5.9}$	NA	NA	NA	< 13.8	$6.8^{6.9}_{5.2}$
S306	201.272973	-43.014771	$7.4^{6.9}_{5.3}$	NA	NA	NA	< 8.3	< 3.5
S307	201.327005	-43.064738	< 3.2	NA	NA	NA	< 4.4	$7.1^{6.5}_{4.8}$
S308	201.370781	-42.948828	< 14.3	< 10.6	< 7.2	$7^{7.1}_{5.5}$	< 10.2	< 13.7
S309	201.455307	-43.068698	< 7.4	< 5.1	< 10.2	< 11.7	< 9	$6.9^{7.8}_{6.5}$
S310	201.416687	-43.048719	$6.4^{6.7}_{5}$	$6.8^{6.9}_{5.2}$	< 9.5	NA	$4.6^{5.7}_{4.1}$	< 8.7
S311	201.441351	-43.050285	< 7.6	$6.6^{6.5}_{4.8}$	< 9.4	< 4.7	$6.7^{6.3}_{4.5}$	< 9.3
S312	201.3486	-43.030196	< 12.8	NA	NA	NA	< 4.4	< 16
S313	201.427897	-43.037121	< 8.9	< 7	< 9.2	$6.4^{7.2}_{5.7}$	< 3	< 7
S314	201.293627	-42.995273	$4.3^{5.6}_{4.3}$	< 12.8	< 13	< 17.5	< 8.9	< 4.7
S315	201.353589	-43.06128	$6.3^{6}_{4.3}$	< 5.5	< 12.3	< 15.1	< 2.9	$4.7^{5.7}_{4.1}$
S316	201.380299	-43.046135	$6.3^{7.2}_{5.7}$	< 10.3	< 8.4	< 8.3	< 5.4	< 8.7
S317	201.452981	-43.01246	< 14.4	< 6.5	< 4.9	< 4.2	< 6.5	< 8.9
S318	201.343647	-42.987166	< 4	< 17	< 10.6	< 10.4	< 8.1	< 8.9
S319	201.294508	-42.972272	< 5.5	NA	NA	< 14.3	< 12.5	< 7.2
S320	201.351851	-42.959955	< 9.7	< 14.6	< 14.7	< 9.8	< 5.2	< 7.5
S321	201.452078	-43.049443	< 9.1	$4.7^{5.7}_{4.1}$	$4.5^{5.7}_{4.1}$	< 5.7	$5.8^{5.4}_{3.7}$	< 8.9
S322	201.390157	-42.949776	NA	< 4.8	< 5.6	< 5.8	$5.7^{6.5}_{5.1}$	NA
S323	201.381064	-43.015788	< 15	< 22.6	< 19.2	< 13.8	< 13.8	< 8.9
S324	201.291524	-43.048481	$5.5^{6.4}_{4.9}$	NA	NA	NA	< 6	< 4.9
S325	201.29119	-43.053395	$5.5^{6.3}_{4.9}$	NA	NA	NA	< 9.5	< 6.3
S326	201.319526	-43.078383	< 8.2	NA	NA	NA	< 10.5	$5.4^{6.2}_{4.7}$
S327	201.419724	-42.978337	< 10.5	< 6.9	< 9.4	< 3.1	$5.2^{6.2}_{4.6}$	NA
S328	201.375654	-43.091132	< 2.3	NA	NA	NA	$5.2^{6.2}_{4.6}$	< 5.6
S329	201.427313	-43.048973	< 2.9	< 7.2	< 6.5	< 6.1	$5.2^{5.9}_{4.2}$	< 3.8
S330	201.449689	-42.981838	NA	$3.9^{5.1}_{3.6}$	< 4.7	$4.9^{5.1}_{3.4}$	< 9.9	NA

Table A.1 (cont'd)

Index	RA	Dec.	7797	7798	7799	7800	8489	8490
S331	201.264971	-42.993352	$4.5^{5.7}_{4.1}$	NA	NA	NA	NA	NA
S332	201.279238	-43.011954	< 8	NA	NA	NA	< 11.7	< 7.8
S333	201.296573	-43.047985	$4.4^{5.6}_{4.3}$	NA	NA	NA	< 7	< 7.1
S334	201.293737	-43.051851	< 9.7	NA	NA	NA	NA	< 9
S335	201.347627	-43.023892	< 13.1	NA	NA	NA	< 12.6	< 8.7
S336	201.271954	-43.01077	< 4.6	NA	NA	NA	< 8.6	< 9.8
S337	201.350109	-43.037306	< 6	NA	NA	NA	< 11.1	< 9.8
S338	201.279647	-43.049983	< 9.2	NA	NA	NA	< 5.7	< 6.5
S339	201.283578	-42.997195	< 8.8	< 11	< 7.6	< 9.7	< 5.8	< 6.1
S340	201.284031	-43.037713	< 6.1	< 2.3	< 2.3	< 13.1	< 5	< 8.3
S341	201.361579	-42.944167	NA	NA	NA	< 8.9	NA	NA
S342	201.321624	-43.090448	< 9.6	NA	NA	NA	< 5.5	< 6.9
S343	201.316164	-43.03426	< 2.7	NA	NA	NA	< 8.5	< 4.8
S344	201.304084	-43.027389	< 4.9	< 12.1	< 9.1	< 17.5	< 9.4	< 6.2
S345	201.293099	-43.050303	< 8.2	NA	NA	NA	NA	< 7.1
S346	201.29567	-43.0139	< 6.9	NA	NA	NA	< 8.5	< 3.8
S347	201.416858	-43.073515	< 2.7	< 6.3	< 4.5	< 11.6	< 3.9	< 5.9
S348	201.305066	-43.036666	< 6.8	NA	NA	NA	< 7.4	< 2.9
S349	201.317574	-43.058604	< 7.3	NA	NA	NA	< 5.5	< 6
S350	201.32183	-43.031669	< 5.8	NA	NA	NA	< 7	< 7.4
S351	201.414491	-43.096333	< 3.5	< 7	< 8.2	NA	< 6.3	< 2.9
S352	201.307809	-43.012392	< 5.8	NA	NA	NA	< 4.7	< 6.6
S353	201.297292	-43.038775	< 3.3	NA	NA	NA	< 6.5	< 2.7
S354	201.259865	-43.091797	< 6.8	NA	NA	NA	NA	< 5.1
S355	201.329008	-43.000047	< 3.7	< 12	< 12.9	< 12.4	< 5.6	< 4.1
S356	201.257061	-43.089859	< 3.7	NA	NA	NA	NA	< 5.5
S357	201.261859	-43.010635	< 3.7	NA	NA	NA	< 5.8	< 6.3
S358	201.286464	-43.061136	< 4.4	< 2.3	< 2.3	< 8.7	< 5.4	< 3
S359	201.308173	-43.035788	< 3.5	NA	NA	NA	< 7.3	< 3.6
S360	201.366686^{NUC}	-43.02191	< 28.2	NA	NA	NA	< 17.5	< 7.1

Table A.1 (cont'd)

Index	RA	Dec.	7797	7798	7799	7800	8489	8490

[C] Overlaps with a chip edge

[R] Overlaps with a readout streak

[FOV] Outside the FOV

[S] Might Worth trying a smaller aperture, e.g. if a source appears bright in DS9 but has been excluded through Nearest Neighbour criteria (ONLY worth doing for the very brightest

[SC] Source Confusion

References

Abramowicz, M. A., Czerny, B., Lasota, J. P., & Szuszkiewicz, E. 1988, ApJ, 332, 646

Akaike, H. 1974, IEEE Transactions on Automatic Control, 19, 716

Angelini, L., Loewenstein, M., & Mushotzky, R. F. 2001, ApJL, 557, L35

Arnaud, K., Smith, R., & Siemiginowska, A. 2011, Handbook of X-ray Astronomy, ed. R. Ellis, J. Huchra, S. Kahn, G. Rieke, & P. B. Stetson

Arnaud, K. A. 1996, in Astronomical Society of the Pacific Conference Series, Vol. 101, Astronomical Data Analysis Software and Systems V, ed. G. H. Jacoby & J. Barnes, 17

Avni, Y. 1976, ApJ, 210, 642

Bailyn, C. D., Jain, R. K., Coppi, P., & Orosz, J. A. 1998, ApJ, 499, 367

Banerjee, S. & Kroupa, P. 2011, ApJL, 741, L12

Bauer, F. E., Brandt, W. N., Sambruna, R. M., Chartas, G., Garmire, G. P., Kaspi, S., & Netzer, H. 2001, AJ, 122, 182

Bauer, M. & Pietsch, W. 2005, A&A, 442, 925

Belczynski, K., Kalogera, V., Rasio, F. A., Taam, R. E., Zezas, A., Bulik, T., Maccarone, T. J., & Ivanova, N. 2008, ApJS, 174, 223

Belczynski, K., Kalogera, V., Zezas, A., & Fabbiano, G. 2004, ApJL, 601, L147

Belczynski, K., Wiktorowicz, G., Fryer, C. L., Holz, D. E., & Kalogera, V. 2012, ApJ, 757, 91

Blanton, E. L., Sarazin, C. L., & Irwin, J. A. 2001, ApJ, 552, 106

Blundell, K. M., Bowler, M. G., & Schmidtobreick, L. 2008, ApJL, 678, L47

Boyles, J., Lorimer, D. R., Turk, P. J., Mnatsakanov, R., Lynch, R. S., Ransom, S. M., Freire, P. C., & Belczynski, K. 2011, ApJ, 742, 51

Bozzo, E., Ferrigno, C., Stevens, J., Belloni, T. M., Rodriguez, J., den Hartog, P. R., Papitto, A., Kreykenbohm, I., Fontani, F., & Gibaud, L. 2011, A&A, 535, L1

Brassington, N. J., Fabbiano, G., Blake, S., Zezas, A., Angelini, L., Davies, R. L., Gallagher, J., Kalogera, V., Kim, D.-W., King, A. R., Kundu, A., Trinchieri, G., & Zepf, S. 2010, ApJ, 725, 1805

Brassington, N. J., Fabbiano, G., Kim, D.-W., Zezas, A., Zepf, S., Kundu, A., Angelini, L., Davies, R. L., Gallagher, J., Kalogera, V., Fragos, T., King, A. R., Pellegrini, S., & Trinchieri, G. 2008, ApJS, 179, 142

—. 2009, ApJS, 181, 605

Brassington, N. J., Fabbiano, G., Zezas, A., Kundu, A., Kim, D.-W., Fragos, T., King, A. R., Pellegrini, S., Trinchieri, G., Zepf, S., & Wright, N. J. 2012a, ApJ, 755, 162

—. 2012b, ArXiv e-prints

Burke, M. J., Raychaudhury, S., Kraft, R. P., Brassington, N. J., Hardcastle, M. J., Goodger, J. L., Sivakoff, G. R., Forman, W. R., Jones, C., Woodley, K. A., Murray, S. S., Kainulainen, J., Birkinshaw, M., Croston, J. H., Evans, D. A., Gilfanov, M., Jordán, A., Sarazin, C. L., Voss, R., Worrall, D. M., & Zhang, Z. 2012, ApJ, 749, 112

Burke, M. J., Raychaudhury, S., Kraft, R. P., Maccarone, T. J., Brassington, N. J., Hardcastle, M. J., Kainulainen, J., Woodley, K. A., Goodger, J. L., Sivakoff, G. R., Forman, W. R., Jones, C., Murray, S. S., Birkinshaw, M., Croston, J. H., Evans, D. A., Gilfanov, M., Jordán, A., Sarazin, C. L., Voss, R., Worrall, D. M., & Zhang, Z. 2013, ApJ, 766, 88

Cappellari, M., Bacon, R., Bureau, M., Damen, M. C., Davies, R. L., de Zeeuw, P. T., Emsellem, E., Falcón-Barroso, J., Krajnović, D., Kuntschner, H., McDermid, R. M., Peletier, R. F., Sarzi, M., van den Bosch, R. C. E., & van de Ven, G. 2006, MNRAS, 366, 1126

Cash, W. 1979, ApJ, 228, 939

Chandrasekhar, S. 1931, ApJ, 74, 81

Chen, W., Shrader, C. R., & Livio, M. 1997, ApJ, 491, 312

Colbert, E. J. M. 2004, in Bulletin of the American Astronomical Society, Vol. 36, American Astronomical Society Meeting Abstracts #204, 749

Colbert, E. J. M., Heckman, T. M., Ptak, A. F., Strickland, D. K., & Weaver, K. A. 2004, ApJ, 602, 231

Constantin, A., Green, P., Aldcroft, T., Kim, D.-W., Haggard, D., Barkhouse, W., & Anderson, S. F. 2009, ApJ, 705, 1336

Corbel, S., Dubus, G., Tomsick, J. A., Szostek, A., Corbet, R. H. D., Miller-Jones, J. C. A., Richards, J. L., Pooley, G., Trushkin, S., Dubois, R., Hill, A. B., Kerr, M., Max-Moerbeck, W., Readhead, A. C. S., Bodaghee, A., Tudose, V., Parent, D., Wilms, J., & Pottschmidt, K. 2012, MNRAS, 421, 2947

Corbet, R. H. D., Sokoloski, J. L., Mukai, K., Markwardt, C. B., & Tueller, J. 2008, ApJ, 675, 1424

Coriat, M., Fender, R. P., & Dubus, G. 2012, MNRAS, 424, 1991

Cornelisse, R., Heise, J., Kuulkers, E., Verbunt, F., & in't Zand, J. J. M. 2000, A&A, 357, L21

Crook, A. C., Huchra, J. P., Martimbeau, N., Masters, K. L., Jarrett, T., & Macri, L. M. 2007, ApJ, 655, 790

Croston, J. H., Kraft, R. P., Hardcastle, M. J., Birkinshaw, M., Worrall, D. M., Nulsen, P. E. J., Penna, R. F., Sivakoff, G. R., Jordán, A., Brassington, N. J., Evans, D. A., Forman, W. R., Gilfanov, M., Goodger, J. L., Harris, W. E., Jones, C., Juett, A. M., Murray, S. S., Raychaudhury, S., Sarazin, C. L., Voss, R., & Woodley, K. A. 2009, MNRAS, 395, 1999

Davis, J. E. 2001, ApJ, 562, 575

Davis, S. W., Done, C., & Blaes, O. M. 2006, ApJ, 647, 525

de Jong, J. T. A., Kuijken, K. H., & Héraudeau, P. 2008, A&A, 478, 755

Di Stefano, R. & Kong, A. K. H. 2003, ApJ, 592, 884

Dickey, J. M. & Lockman, F. J. 1990, ARA&A, 28, 215

Done, C., Gierliński, M., & Kubota, A. 2007, A&AR, 15, 1

Dubus, G., Hameury, J.-M., & Lasota, J.-P. 2001, A&A, 373, 251

Dubus, G. & Rutledge, R. E. 2002, MNRAS, 336, 901

Ellis, S. C. & O'Sullivan, E. 2006, MNRAS, 367, 627

Esin, A. A., McClintock, J. E., & Narayan, R. 1997, ApJ, 489, 865

Esposito, P., Motta, S. E., Pintore, F., Zampieri, L., & Tomasella, L. 2012, MNRAS, 186

—. 2013, MNRAS, 428, 2480

Fabbiano, G. 1989, ARA&A, 27, 87

—. 2006, ARA&A, 44, 323

Fabbiano, G., Brassington, N. J., Lentati, L., Angelini, L., Davies, R. L., Gallagher, J., Kalogera, V., Kim, D.-W., King, A. R., Kundu, A., Pellegrini, S., Richings, A. J., Trinchieri, G., Zezas, A., & Zepf, S. 2010, ApJ, 725, 1824

Fabbiano, G., Zezas, A., & Murray, S. S. 2001, ApJ, 554, 1035

Fabian, A. C., Pringle, J. E., & Rees, M. J. 1975, MNRAS, 172, 15P

Farr, W. M., Sravan, N., Cantrell, A., Kreidberg, L., Bailyn, C. D., Mandel, I., & Kalogera, V. 2011, ApJ, 741, 103

Farrell, S. A., Webb, N. A., Barret, D., Godet, O., & Rodrigues, J. M. 2009, Nature, 460, 73

Fender, R. 2006, Jets from X-ray binaries, ed. W. H. G. Lewin & M. van der Klis, 381–419

Fender, R. P., Belloni, T. M., & Gallo, E. 2004, MNRAS, 355, 1105

Feng, H. & Kaaret, P. 2005, ApJ, 633, 1052

Feng, H. & Kaaret, P. 2007, The Astrophysical Journal, 668, 941

Feng, H. & Soria, R. 2011, NewAR, 55, 166

Ferrarese, L., Mould, J. R., Stetson, P. B., Tonry, J. L., Blakeslee, J. P., & Ajhar, E. A. 2007, ApJ, 654, 186

Ferrigno, C., Bozzo, E., Rodriguez, J., & Gibaud, L. 2011, The Astronomer's Telegram, 3566, 1

Foschini, L., Rodriguez, J., Fuchs, Y., Ho, L. C., Dadina, M., Di Cocco, G., Courvoisier, T. J.-L., & Malaguti, G. 2004, A&A, 416, 529

Frank, J., King, A., & Raine, D. J. 2002, Accretion Power in Astrophysics: Third Edition

Fruscione, A., McDowell, J. C., Allen, G. E., Brickhouse, N. S., Burke, D. J., Davis, J. E., Durham, N., Elvis, M., Galle, E. C., Harris, D. E., Huenemoerder, D. P., Houck, J. C., Ishibashi, B., Karovska, M., Nicastro, F., Noble, M. S., Nowak, M. A., Primini, F. A., Siemiginowska, A., Smith, R. K., & Wise, M. 2006, in Society of Photo-Optical Instrumentation Engineers (SPIE) Conference Series, Vol. 6270, Society of Photo-Optical Instrumentation Engineers (SPIE) Conference Series

Ghosh, K. K., Finger, M. H., Swartz, D. A., Tennant, A. F., & Wu, K. 2006, ApJ, 640, 459

Giacconi, R., Gursky, H., Paolini, F. R., & Rossi, B. B. 1962, Physical Review Letters, 9, 439

Gierliński, M. & Done, C. 2004, MNRAS, 347, 885

Gierliński, M., Zdziarski, A. A., Poutanen, J., Coppi, P. S., Ebisawa, K., & Johnson, W. N. 1999, MNRAS, 309, 496

Gilfanov, M., Revnivtsev, M., & Molkov, S. 2003, A&A, 410, 217

Gladstone, J. C., Copperwheat, C., Heinke, C. O., Roberts, T. P., Cartwright, T. F., Levan, A. J., Goad, M. R., & . 2013, ArXiv e-prints

Gladstone, J. C., Roberts, T. P., & Done, C. 2009, MNRAS, 397, 1836

Gnedin, O. Y., Maccarone, T. J., Psaltis, D., & Zepf, S. E. 2009, ApJL, 705, L168

Gonçalves, A. C. & Soria, R. 2006, MNRAS, 371, 673

Goodger, J. L., Hardcastle, M. J., Croston, J. H., Kraft, R. P., Birkinshaw, M., Evans, D. A., Jordán, A., Nulsen, P. E. J., Sivakoff, G. R., Worrall, D. M., Brassington, N. J., Forman, W. R., Gilfanov, M., Jones, C., Murray, S. S., Raychaudhury, S., Sarazin, C. L., Voss, R., & Woodley, K. A. 2010, ApJ, 708, 675

Graham, J. A. 1979, ApJ, 232, 60

Gregory, P. C. & Loredo, T. J. 1992, ApJ, 398, 146

Grimm, H.-J., Gilfanov, M., & Sunyaev, R. 2002, A&A, 391, 923

—. 2003, MNRAS, 339, 793

Grindlay, J. E., Heinke, C., Edmonds, P. D., & Murray, S. S. 2001, Science, 292, 2290

Grove, J. E., Johnson, W. N., Kroeger, R. A., McNaron-Brown, K., Skibo, J. G., & Phlips, B. F. 1998, ApJ, 500, 899

Güdel, M., Audard, M., Reale, F., Skinner, S. L., & Linsky, J. L. 2004, A&A, 416, 713

Güver, T. & Özel, F. 2009, MNRAS, 400, 2050

Hardcastle, M. J., Kraft, R. P., Sivakoff, G. R., Goodger, J. L., Croston, J. H., Jordán, A., Evans, D. A., Worrall, D. M., Birkinshaw, M., Raychaudhury, S., Brassington, N. J., Forman, W. R., Harris, W. E., Jones, C., Juett, A. M., Murray, S. S., Nulsen, P. E. J., Sarazin, C. L., & Woodley, K. A. 2007, ApJL, 670, L81

Harris, G. L. H., Gómez, M., Harris, W. E., Johnston, K., Kazemzadeh, F., Kerzendorf, W., Geisler, D., & Woodley, K. A. 2012, AJ, 143, 84

Harris, W. E., Spitler, L. R., Forbes, D. A., & Bailin, J. 2010, MNRAS, 401, 1965

Harry, G. M. & LIGO Scientific Collaboration. 2010, Classical and Quantum Gravity, 27, 084006

Hasinger, G. & van der Klis, M. 1989, A&A, 225, 79

Hastings, W. K. 1970, Biometrika, 57, 97

Heggie, D. C., Hut, P., & McMillan, S. L. W. 1996, ApJ, 467, 359

Heise, J. & in't Zand, J. 2006, Fast X-ray transients and X-ray flashes, ed. W. H. G. Lewin & M. van der Klis, 267–278

Heiselberg, H. & Pandharipande, V. 2000, Annual Review of Nuclear and Particle Science, 50, 481

Homan, J., Kaplan, D. L., van den Berg, M., & Young, A. J. 2009, ApJ, 692, 73

Homan, J., van der Klis, M., Wijnands, R., Belloni, T., Fender, R., Klein-Wolt, M., Casella, P., Méndez, M., Gallo, E., Lewin, W. H. G., & Gehrels, N. 2007, ApJ, 656, 420

Homan, J., Wijnands, R., van der Klis, M., Belloni, T., van Paradijs, J., Klein-Wolt, M., Fender, R., & Méndez, M. 2001, ApJS, 132, 377

Hong, J., Schlegel, E. M., & Grindlay, J. E. 2004, ApJ, 614, 508

Hong, J. S., van den Berg, M., Grindlay, J. E., & Laycock, S. 2009, ApJ, 706, 223

Humphrey, P. J., Buote, D. A., Gastaldello, F., Zappacosta, L., Bullock, J. S., Brighenti, F., & Mathews, W. G. 2006, ApJ, 646, 899

Hut, P., McMillan, S., Goodman, J., Mateo, M., Phinney, E. S., Pryor, C., Richer, H. B., Verbunt, F., & Weinberg, M. 1992, PASP, 104, 981

Ibragimov, A., Poutanen, J., Gilfanov, M., Zdziarski, A. A., & Shrader, C. R. 2005, MNRAS, 362, 1435

Irwin, J. A. 2006, MNRAS, 371, 1903

Israel, F. P. 1998, A&AR, 8, 237

Jeffreys, H. 1998, Theory of probability, Oxford Classic Texts in the Physical Sciences (New York: The Clarendon Press Oxford University Press), xii+459, reprint of the 1983 edition

Jin, J., Feng, H., & Kaaret, P. 2010, ApJ, 716, 181

Jordán, A., Sivakoff, G. R., McLaughlin, D. E., Blakeslee, J. P., Evans, D. A., Kraft, R. P., Hardcastle, M. J., Peng, E. W., Côté, P., Croston, J. H., Juett, A. M., Minniti, D., Raychaudhury, S., Sarazin, C. L., Worrall,

D. M., Harris, W. E., Woodley, K. A., Birkinshaw, M., Brassington, N. J., Forman, W. R., Jones, C., & Murray, S. S. 2007, ApJL, 671, L117

Judge, P. G., Solomon, S. C., & Ayres, T. R. 2003, ApJ, 593, 534

Kahabka, P. & van den Heuvel, E. P. J. 1997, ARA&A, 35, 69

Kainulainen, J. T., Alves, J. F., Beletsky, Y., Ascenso, J., Kainulainen, J. M., Amorim, A., Lima, J., Marques, R., Moitinho, A., Pinhão, J., Rebordão, J., & Santos, F. D. 2009, A&A, 502, L5

Kalogera, V., Henninger, M., Ivanova, N., & King, A. R. 2004a, ApJL, 603, L41

Kalogera, V., King, A. R., & Rasio, F. A. 2004b, ApJL, 601, L171

Kato, M., Saio, H., & Hachisu, I. 1989, ApJ, 340, 509

Kato, T., Kanatsu, K., Takamizawa, K., Takao, A., & Stubbings, R. 2000, IAU Circ., 7552, 1

Kaur, A., Henze, M., Haberl, F., Pietsch, W., Greiner, J., Rau, A., Hartmann, D. H., Sala, G., & Hernanz, M. 2012, A&A, 538, A49

Kim, D.-W. & Fabbiano, G. 2003, ApJ, 586, 826

—. 2004, ApJ, 611, 846

—. 2010, ApJ, 721, 1523

Kim, D.-W., Fabbiano, G., Ivanova, N., Fragos, T., Jordán, A., Sivakoff, G. R., & Voss, R. 2013, ApJ, 764, 98

King, A. R. 1988, QJRAS, 29, 1

King, A. R., Davies, M. B., Ward, M. J., Fabbiano, G., & Elvis, M. 2001, ApJL, 552, L109

King, A. R., Kolb, U., & Burderi, L. 1996, ApJL, 464, L127

King, I. 1962, AJ, 67, 471

Komossa, S. & Schulz, H. 1998, A&A, 339, 345

Kong, A. K. H. & Di Stefano, R. 2005, ApJL, 632, L107

Kong, A. K. H., Di Stefano, R., & Yuan, F. 2004, ApJL, 617, L49

Kraft, R. P., Hardcastle, M. J., Sivakoff, G. R., Jordán, A., Nulsen, P. E. J., Birkinshaw, M., Forman, W. R., Jones, C., Worrall, D. M., Croston, J. H., Evans, D. A., Raychaudhury, S., Murray, S. S., Brassington, N. J., Goodger, J. L., Harris, W. E., Juett, A. M., Sarazin, C. L., & Woodley, K. A. 2008, ApJL, 677, L97

Kraft, R. P., Kregenow, J. M., Forman, W. R., Jones, C., & Murray, S. S. 2001, ApJ, 560, 675

Kraus, A. L. & Hillenbrand, L. A. 2007, AJ, 134, 2340

Kreidberg, L., Bailyn, C. D., Farr, W. M., & Kalogera, V. 2012, ApJ, 757, 36

Kroupa, P. 2001, MNRAS, 322, 231

Kundu, A., Maccarone, T. J., & Zepf, S. E. 2002, ApJL, 574, L5

Kuntz, K. D., Gruendl, R. A., Chu, Y.-H., Chen, C.-H. R., Still, M., Mukai, K., & Mushotzky, R. F. 2005, ApJL, 620, L31

Lasota, J.-P. 2001, NAR, 45, 449

Leigh, N. W. C., Böker, T., Maccarone, T. J., & Perets, H. B. 2013, MNRAS, 429, 2997

Leitherer, C., Ortiz Otálvaro, P. A., Bresolin, F., Kudritzki, R.-P., Lo Faro, B., Pauldrach, A. W. A., Pettini, M., & Rix, S. A. 2010, ApJS, 189, 309

Leitherer, C., Schaerer, D., Goldader, J. D., González Delgado, R. M., Robert, C., Kune, D. F., de Mello, D. F., Devost, D., & Heckman, T. M. 1999, ApJS, 123, 3

Lewin, W. & van der Klis, M. 2010, Compact Stellar X-ray Sources

Lin, D., Remillard, R. A., & Homan, J. 2007, ApJ, 667, 1073

—. 2009, ApJ, 696, 1257

Lin, D., Remillard, R. A., Homan, J., & Barret, D. 2012, ApJ, 756, 34

Linares, M., Watts, A., Altamirano, D., Soleri, P., Degenaar, N., Yang, Y., Wijnands, R., Casella, P., Homan, J., Chakrabarty, D., Rea, N., Armas-Padilla, M., Cavecchi, Y., Kalamkar, M., Kaur, R., Patruno, A., & van der Klis, M. 2010, ApJL, 719, L84

Liu, J. 2009, ApJ, 704, 1628

Liu, J.-F., Bregman, J. N., & Irwin, J. 2006, ApJ, 642, 171

Liu, J.-F., Bregman, J. N., & Seitzer, P. 2004, ApJ, 602, 249

Long, K. S. & van Speybroeck, L. P. 1983, in Accretion-Driven Stellar X-ray Sources, ed. W. H. G. Lewin & E. P. J. van den Heuvel, 117–146

Maartens, R. & Koyama, K. 2010, Living Reviews in Relativity, 13

Maccarone, T. J. 2003, A&A, 409, 697

Maccarone, T. J. & Coppi, P. S. 2003, A&A, 399, 1151

Maccarone, T. J., Gallo, E., & Fender, R. 2003, MNRAS, 345, L19

Maccarone, T. J., Kundu, A., Zepf, S. E., & Rhode, K. L. 2007, Nature, 445, 183

—. 2010a, MNRAS, 409, L84

—. 2011, MNRAS, 410, 1655

Maccarone, T. J., Long, K. S., Knigge, C., Dieball, A., & Zurek, D. R. 2010b, MNRAS, 406, 2087

Maraschi, L., Treves, A., & van den Heuvel, E. P. J. 1976, Nature, 259, 292

Marconi, A., Schreier, E. J., Koekemoer, A., Capetti, A., Axon, D., Macchetto, D., & Caon, N. 2000, ApJ, 528, 276

Marquardt, D. 1963, Journal of the Society for Industrial and Applied Mathematics, 11, 431

Massey, F. J. 1951, Journal of the American Statistical Association, 46, 68

Matsumoto, H., Tsuru, T. G., Koyama, K., Awaki, H., Canizares, C. R., Kawai, N., Matsushita, S., & Kawabe, R. 2001, ApJL, 547, L25

McClintock, J. E. & Remillard, R. A. 2006, Black hole binaries, ed. W. H. G. Lewin & M. van der Klis, 157–213

Melia, F. 2009, High-Energy Astrophysics

Middleton, M. J., Sutton, A. D., Roberts, T. P., Jackson, F. E., & Done, C. 2012, MNRAS, 420, 2969

Mihara, T., Nakajima, M., Sugizaki, M., Serino, M., Matsuoka, M., Kohama, M., Kawasaki, K., Tomida, H., Ueno, S., Kawai, N., Kataoka, J., Morii, M., Yoshida, A., Yamaoka, K., Nakahira, S., Negoro, H., Isobe, N., Yamauchi, M., & Sakurai, I. 2011, PASJ, 63, 623

Miller, J. M., Fabbiano, G., Miller, M. C., & Fabian, A. C. 2003, ApJL, 585, L37

Miller, J. M., Fabian, A. C., & Miller, M. C. 2004, ApJL, 614, L117

Moretti, A., Campana, S., Lazzati, D., & Tagliaferri, G. 2003, ApJ, 588, 696

Morscher, M., Umbreit, S., Farr, W. M., & Rasio, F. A. 2013, ApJL, 763, L15

Muñoz-Darias, T., de Ugarte Postigo, A., Russell, D. M., Guziy, S., Gorosabel, J., Casares, J., Armas Padilla, M., Charles, P. A., Fender, R. P., Belloni, T. M., Lewis, F., Motta, S., Castro-Tirado, A., Mundell, C. G., Sánchez-Ramírez, R., & Thöne, C. C. 2013, ArXiv e-prints

Mukai, K., Still, M., Corbet, R. H. D., Kuntz, K. D., & Barnard, R. 2005, ApJ, 634, 1085

Murdin, P., Jauncey, D. L., Lerche, I., Nicolson, G. D., Kaluzienski, L. J., Holt, S. S., & Haynes, R. F. 1980, A&A, 87, 292

Okada, K., Dotani, T., Makishima, K., Mitsuda, K., & Mihara, T. 1998, PASJ, 50, 25

Oosterbroek, T., van der Klis, M., van Paradijs, J., Vaughan, B., Rutledge, R., Lewin, W. H. G., Tanaka, Y., Nagase, F., Dotani, T., Mitsuda, K., & Miyamoto, S. 1997, A&A, 321, 776

Oppenheimer, J. R. & Volkoff, G. M. 1939, Physical Review, 55, 374

Özel, F., Psaltis, D., Narayan, R., & McClintock, J. E. 2010, ApJ, 725, 1918

Park, T., Kashyap, V. L., Siemiginowska, A., van Dyk, D. A., Zezas, A., Heinke, C., & Wargelin, B. J. 2006, ApJ, 652, 610

Paul, B., Dotani, T., Nagase, F., Mukherjee, U., & Naik, S. 2005, ApJ, 627, 915

Peacock, M. B., Zepf, S. E., Kundu, A., Maccarone, T. J., Rhode, K. L., Salzer, J. J., Waters, C. Z., Ciardullo, R., Gronwall, C., & Stern, D. 2012, ApJ, 759, 126

Pearson, K. 1900, Philosophical Magazine Series 5, 50, 157

Piro, A. L. & Bildsten, L. 2002, ApJL, 571, L103

Portegies Zwart, S. F., Dewi, J., & Maccarone, T. 2004, MNRAS, 355, 413

Poutanen, J., Lipunova, G., Fabrika, S., Butkevich, A. G., & Abolmasov, P. 2007, MNRAS, 377, 1187

Prestwich, A. H., Kilgard, R. E., Primini, F., McDowell, J. C., & Zezas, A. 2009, ApJ, 705, 1632

Pringle, J. E. 1981, ARA&A, 19, 137

Protassov, R., van Dyk, D. A., Connors, A., Kashyap, V. L., & Siemiginowska, A. 2002, ApJ, 571, 545

Psaltis, D. 2006, Accreting neutron stars and black holes: a decade of discoveries, ed. W. H. G. Lewin & M. van der Klis, 1–38

Quillen, A. C., Brookes, M. H., Keene, J., Stern, D., Lawrence, C. R., & Werner, M. W. 2006, ApJ, 645, 1092

Randall, L. & Sundrum, R. 1999, Physical Review Letters, 83, 4690

Raymond, J. C. & Smith, B. W. 1977, ApJS, 35, 419

Redmount, I. H. & Rees, M. J. 1989, Comments on Astrophysics, 14, 165

Reig, P., Belloni, T., & van der Klis, M. 2003, A&A, 412, 229

Rejkuba, M., Harris, W. E., Greggio, L., & Harris, G. L. H. 2011, A&A, 526, A123

Remillard, R. A. & McClintock, J. E. 2006, ARA&A, 44, 49

Revnivtsev, M. G. & Gilfanov, M. R. 2006, A&A, 453, 253

Roberts, T. P. 2007, Ap&SS, 311, 203

Roberts, T. P., Fabbiano, G., Luo, B., Kim, D.-W., Strader, J., Middleton, M. J., Brodie, J. P., Fragos, T., Gallagher, J. S., Kalogera, V., King, A. R., & Zezas, A. 2012, ApJ, 760, 135

Roberts, T. P., Gladstone, J. C., Hetf, L. M., Done, C., & Vaughan, S. A. 2010, X-ray Astronomy 2009; Present Status, Multi-Wavelength Approach and Future Perspectives, 1248, 123

Roberts, T. P., Levan, A. J., & Goad, M. R. 2008, MNRAS, 387, 73

Rybicki, G. B. & Lightman, A. P. 1986, Radiative Processes in Astrophysics

Sandage, A., Osmer, P., Giacconi, R., Gorenstein, P., Gursky, H., Waters, J., Bradt, H., Garmire, G., Sreekantan, B. V., Oda, M., Osawa, K., & Jugaku, J. 1966, ApJ, 146, 316

Sanna, A., Méndez, M., Altamirano, D., Homan, J., Casella, P., Belloni, T., Lin, D., van der Klis, M., & Wijnands, R. 2010, MNRAS, 408, 622

Sarazin, C. L., Irwin, J. A., & Bregman, J. N. 2000, ApJL, 544, L101

—. 2001, ApJ, 556, 533

Schreier, E., Levinson, R., Gursky, H., Kellogg, E., Tananbaum, H., & Giacconi, R. 1972, ApJL, 172, L79

Schreier, E. J., Capetti, A., Macchetto, F., Sparks, W. B., & Ford, H. J. 1996, ApJ, 459, 535

Servillat, M., Farrell, S. A., Lin, D., Godet, O., Barret, D., & Webb, N. A. 2011, ApJ, 743, 6

Shahbaz, T., Charles, P. A., & King, A. R. 1998, MNRAS, 301, 382

Shakura, N. I. & Sunyaev, R. A. 1973, A&A, 24, 337

Shapiro, S. L., Lightman, A. P., & Eardley, D. M. 1976, ApJ, 204, 187

Shih, I. C., Kundu, A., Maccarone, T. J., Zepf, S. E., & Joseph, T. D. 2010, ApJ, 721, 323

Shimura, T. & Takahara, F. 1995, ApJ, 445, 780

Shklovsky, I. S. 1967, ApJL, 148, L1

Shrader, C. R., Titarchuk, L., & Shaposhnikov, N. 2010, ApJ, 718, 488

Sivakoff, G. R., Kraft, R. P., Jordán, A., Juett, A. M., Evans, D. A., Forman, W. R., Hardcastle, M. J., Sarazin, C. L., Birkinshaw, M., Brassington, N. J., Croston, J. H., Harris, W. E., Jones, C., Murray, S. S., Raychaudhury, S., Woodley, K. A., & Worrall, D. M. 2008, ApJL, 677, L27

Smak, J. 1984, PASP, 96, 5

Sobczak, G. J., McClintock, J. E., Remillard, R. A., Cui, W., Levine, A. M., Morgan, E. H., Orosz, J. A., & Bailyn, C. D. 2000, ApJ, 544, 993

Soleri, P., Muñoz-Darias, T., Motta, S., Belloni, T., Casella, P., Méndez, M., Altamirano, D., Linares, M., Wijnands, R., Fender, R., & van der Klis, M. 2012, MNRAS, 336

Soria, R., Broderick, J. W., Hao, J., Hannikainen, D. C., Mehdipour, M., Pottschmidt, K., & Zhang, S.-N. 2011, MNRAS, 415, 410

Soria, R., Kuntz, K. D., Winkler, P. F., Blair, W. P., Long, K. S., Plucinsky, P. P., & Whitmore, B. C. 2012, ApJ, 750, 152

Soria, R., Risaliti, G., Elvis, M., Fabbiano, G., Bianchi, S., & Kuncic, Z. 2009, ApJ, 695, 1614

Spitzer, Jr., L. 1969, ApJL, 158, L139

Steele, M. M., Zepf, S. E., Kundu, A., Maccarone, T. J., Rhode, K. L., & Salzer, J. J. 2011, ApJ, 739, 95

Steinle, H., Dennerl, K., & Englhauser, J. 2000, A&A, 357, L57

Stiele, H., Pietsch, W., Haberl, F., Hatzidimitriou, D., Barnard, R., Williams, B. F., Kong, A. K. H., & Kolb, U. 2011, A&A, 534, A55

Strohmayer, T. & Bildsten, L. 2006, New views of thermonuclear bursts, ed. W. H. G. Lewin & M. van der Klis, 113–156

Swartz, D. A., Tennant, A. F., & Soria, R. 2009, ApJ, 703, 159

Tennant, A. F., Fabian, A. C., & Shafer, R. A. 1986, MNRAS, 219, 871

Tennant, A. F., Wu, K., Ghosh, K. K., Kolodziejczak, J. J., & Swartz, D. A. 2001, ApJL, 549, L43

Thorne, K. S. & Price, R. H. 1975, ApJL, 195, L101

Tolman, R. C. 1939, Physical Review, 55, 364

Trudolyubov, S., Priedhorsky, W., & Cordova, F. 2006, ApJ, 645, 277

Tully, R. B., Shaya, E. J., Karachentsev, I. D., Courtois, H. M., Kocevski, D. D., Rizzi, L., & Peel, A. 2008, ApJ, 676, 184

van den Heuvel, E. P. J., Bhattacharya, D., Nomoto, K., & Rappaport, S. A. 1992, A&A, 262, 97

van der Klis, M. 1994, ApJS, 92, 511

—. 2006, Rapid X-ray Variability, ed. W. H. G. Lewin & M. van der Klis, 39–112

van Haaften, L. M., Nelemans, G., Voss, R., Wood, M. A., & Kuijpers, J. 2012, A&A, 537, A104

van Paradijs, J. 1996, ApJL, 464, L139

Vázquez, G. A. & Leitherer, C. 2005, ApJ, 621, 695

Voss, R. & Gilfanov, M. 2006, A&A, 447, 71

—. 2007, A&A, 468, 49

Voss, R., Gilfanov, M., Sivakoff, G. R., Kraft, R. P., Jordán, A., Raychaudhury, S., Birkinshaw, M., Brassington, N. J., Croston, J. H., Evans, D. A., Forman, W. R., Hardcastle, M. J., Harris, W. E., Jones, C., Juett, A. M., Murray, S. S., Sarazin, C. L., Woodley, K. A., & Worrall, D. M. 2009, ApJ, 701, 471

Webbink, R. F., Rappaport, S., & Savonije, G. J. 1983, ApJ, 270, 678

Webster, B. L. & Murdin, P. 1972, Nature, 235, 37

Weinberg, M. D. 2009, ArXiv e-prints

Weisskopf, M. C., Tananbaum, H. D., Van Speybroeck, L. P., & O'Dell, S. L. 2000, in Society of Photo-Optical Instrumentation Engineers (SPIE) Conference Series, Vol. 4012, Society of Photo-Optical Instrumentation Engineers (SPIE) Conference Series, ed. J. E. Truemper & B. Aschenbach, 2–16

White, N. E. & Marshall, F. E. 1984, ApJ, 281, 354

Whittet, D. C. B. 1992, Dust in the galactic environment

Wijnands, R. & van der Klis, M. 1999, ApJ, 522, 965

Williams, B. F., Gaetz, T. J., Haberl, F., Pietsch, W., Shporer, A., Ghavamian, P., Plucinsky, P. P., Mazeh, T., Sasaki, M., & Pannuti, T. G. 2008, ApJ, 680, 1120

Williams, B. F., Naik, S., Garcia, M. R., & Callanan, P. J. 2006, ApJ, 643, 356

Winter, L. M., Mushotzky, R. F., & Reynolds, C. S. 2006, ApJ, 649, 730

Woodley, K. A., Raychaudhury, S., Kraft, R. P., Harris, W. E., Jordán, A., Whitaker, K. E., Jones, C., Forman, W. R., & Murray, S. S. 2008, ApJ, 682, 199

Worrall, D. M., Birkinshaw, M., Kraft, R. P., Sivakoff, G. R., Jordán, A., Hardcastle, M. J., Brassington, N. J., Croston, J. H., Evans, D. A., Forman, W. R., Harris, W. E., Jones, C., Juett, A. M., Murray, S. S., Nulsen, P. E. J., Raychaudhury, S., Sarazin, C. L., & Woodley, K. A. 2008, ApJL, 673, L135

Wu, Q. & Gu, M. 2008, ApJ, 682, 212

Wu, Y. X., Yu, W., Li, T. P., Maccarone, T. J., & Li, X. D. 2010, ApJ, 718, 620

Zeldovich, Y. B. & Guseynov, O. H. 1966, ApJ, 144, 840

Zepf, S. E., Maccarone, T. J., Bergond, G., Kundu, A., Rhode, K. L., & Salzer, J. J. 2007, ApJL, 669, L69

Zepf, S. E., Stern, D., Maccarone, T. J., Kundu, A., Kamionkowski, M., Rhode, K. L., Salzer, J. J., Ciardullo, R., & Gronwall, C. 2008, ApJL, 683, L139

Zhang, S. N., Cui, W., & Chen, W. 1997, ApJL, 482, L155

Zhang, Z., Gilfanov, M., & Bogdán, Á. 2012, A&A, 546, A36

Zhang, Z., Gilfanov, M., Voss, R., Sivakoff, G. R., Kraft, R. P., Brassington, N. J., Kundu, A., Jordán, A., & Sarazin, C. 2011, A&A, 533, A33